TECHNISCHE UNIVERSITÄT MÜNCHEN
TUM School of Engineering and Design

The Natural Passive Aerodynamic Load Alleviation Characteristic of Swept High Aspect Ratio Transport Aircraft Wings

Andreas Hermanutz

Vollständiger Abdruck der von der TUM School of Engineering and Design der Technischen Universität München zur Erlangung eines

Doktors der Ingenieurwissenschaften (Dr.-Ing.)

genehmigten Dissertation.

Vorsitz: Prof. Dr.-Ing. Fernaß Daoud

Prüfer*innen der Dissertation:

1. Prof. Dr.-Ing. Mirko Hornung
2. Prof. Dr. Roeland De Breuker
3. Prof. Dr.-Ing. Horst Baier

Die Dissertation wurde am 01.12.2022 bei der Technischen Universität München eingereicht und durch die TUM School of Engineering and Design am 04.09.2023 angenommen.

Acknowledgments

I have been privileged to work with many exceptional people during my doctoral studies, all of whom have made essential contributions through valuable discussions, encouraging me and giving me the joy and motivation I have in my work. Therefore, writing this last part is probably the hardest. Not because the rest of the work is so straightforward, but because the contribution of colleagues and friends is priceless and I can only attempt to express my sincere thanks here.

I want to express my sincere gratitude to my two supervisors. Horst Baier for the cornerstones that led to this work and Mirko Hornung who supported me in finalizing it. I am very grateful to both of them for the unlimited trust and the opportunity to work independently on my ideas. I would like to thank both of them for always having a sympathetic ear and standing by my side with advice and support in difficult situations. I also want to thank Roeland de Breuker for supporting the work as an external reviewer.

Furthermore, a huge thanks goes to my colleagues for all the fruitful discussions, the constant encouragement to continue my research in difficult times, and for the great working environment. From the Chair of Lightweight Structures, I would like to express my special thanks to Martin Mahl, Luiz da Rocha-Schmidt, Markus Schatz and Felix Stroscher. From the Chair of Aircraft Design my two office colleagues Sebastian Oberschwendtner and Thomas Seren. Philipp Stahl and Franz Sendner for working together in a challenging project. Likewise, my thanks also goes to the many other supporters. Vladislav Rozov and Maximilian Winter, who have often given me aerodynamic modeling advice. Matteo Moioli, Ralf Heinrich and Stefan Platzer who shared their experience in TAU with me. I want to thank my former project partner Thiemo Kier for the many interesting discussions on aircraft load modeling. My study colleague and friend Markus Rinker for the critical review of this thesis.

Finally, I would like to thank my family. My parents, my sister and friends for their constant moral support and encouragement over the past years. A very warm thanks goes to Jocelyn. Especially in the last phase of my work, you had to put aside many hours, evenings and weekends. You went with me trough the ups and downs. Thank you for your constant patience, encouragement and support.

Singapore, August 2022 Andreas Hermanutz

Abstract

To achieve the goals of a sustainable aviation industry, there is a need for new and innovative aircraft technologies that are superior to today's transport aircraft in terms of performance and environmental impact. A developing trend for new aircraft configurations is using higher aspect ratio wings to minimize the induced drag. Owing to their design, these new wings are inherently more flexible. This leads to more wing deflection, especially during high load situations from maneuvering flights or gust encounters.

This study investigates the effect of structural flexibility on the passive load alleviation performance of backward-swept wings. For this purpose, the influence parameters are analyzed using a reduced-order academic demonstrator example. In the second part, a transport aircraft with a wing aspect ratio of 10 and a novel configuration with an aspect ratio of 13 are designed and analyzed under varying stiffness effects in maneuver and gust load conditions.

Due to the large wing deformations, an aeroelastic framework is presented that allows simulation including nonlinearities, such as large structural deformations, using nonlinear Finite Element (FE) methods. Because the simulations are carried out in the transonic flow regime, Reynolds-averaged Navier–Stokes methods are used for aerodynamic modeling to gain insight into the underlying flow physics. Both computational techniques are combined into a coupled fluid-structure interaction framework to perform aeroelastic simulations. The Field-Velocity-Approach (FVA) is applied to account for 1-cos gusts in aerodynamic modeling.

The results of the analyses showed that the bending deflection of the wings strongly influences the passive load reduction characteristic. Due to the kinematic coupling between the bending and wing twist, a local reduction in the angle of attack can be initiated. In particular, in the case of steady-state maneuver loads or gusts with a long gust length, the load reduction due to wing bending is predominant. With short impulsive gust excitations, inertia effects dominate, and no advantages can be achieved. Only the torsionally stiff wing configurations provided improved load reduction characteristics in these load cases. The results of the gust response analysis are summarized in terms of their passive load alleviation characteristics and limiting effects are highlighted specifically for wings with increased structural flexibility.

Kurzfassung

Um die Ziele einer nachhaltigen Luftfahrtindustrie zu erreichen, bedarf es neuer und innovativer Flugzeugtechnologien, die jene heutiger Verkehrsflugzeuge in Bezug auf Leistung und Umweltverträglichkeit übertreffen. Ein sich abzeichnender Trend bei neuen Flugzeugkonfigurationen ist die Verwendung von Flügeln mit einem höheren Streckungsverhältnis, um den induzierten Widerstand zu minimieren. Aufgrund ihrer Konstruktion sind diese neuen Flügel von Natur aus flexibler. Dies führt zu einer stärkeren Durchbiegung der Flügel, insbesondere bei zusätzlichen Belastungen durch Manöverflüge oder Böen.

In dieser Studie wird die Auswirkung der strukturellen Flexibilität auf das passive Lastabminderungsverhalten von rückwärtsgepfeilten Tragflächen untersucht. Zu diesem Zweck werden die Einflussparameter anhand eines akademischen Demonstrationsbeispiels reduzierter Ordnung analysiert. Im zweiten Teil wird ein Transportflugzeug mit einer Flügelstreckung von 10 und eine neuartige Konfiguration mit einer Streckung von 13 entworfen und unter verschiedenen Steifigkeitseffekten unter Manöver- und Böenlastbedingungen analysiert.

Da die Tragflächen große Verformungen aufweisen, wird ein aeroelastischer Simulationsansatz vorgestellt, der die Simulation von Nichtlinearitäten, wie z.B. große strukturelle Verformungen, mit Hilfe nichtlinearer Finite-Elemente-Methoden (FE) ermöglicht. Da die Simulationen im transsonischen Strömungsbereich durchgeführt werden, werden für die aerodynamische Modellierung Reynolds-gemittelte Navier-Stokes-Methoden verwendet, um einen Einblick in die zugrunde liegende Strömungsphysik zu erhalten. Beide Berechnungsmethoden werden in einem gekoppelten Fluid-Struktur-Interaktionsmodell zusammengeführt, um aeroelastische Simulationen durchzuführen. Der Field-Velocity-Approach (FVA) wird verwendet, um 1-cos-Böen bei der aerodynamischen Modellierung zu berücksichtigen.

Die Ergebnisse der Analysen zeigten, dass die Biegung der Flügel die Charakteristik der passiven Lastreduktion stark beeinflusst. Durch die kinematische Kopplung zwischen Biegung und Flügelverwindung kann eine lokale Reduzierung des Anstellwinkels eingeleitet werden. Insbesondere bei stationären Manöverlasten oder Böen mit großer Böenlänge überwiegt die Lastreduktion durch die Flügelbiegung. Bei kurzen impulsiven Böenanregungen dominieren Trägheitseffekte, und es können keine Vorteile erzielt werden. Nur die verwindungssteifen Flügelkonfigurationen zeigten in diesen Lastfällen bessere Lastminderungseigenschaften. Die Ergebnisse der Böenanalyse werden hinsichtlich ihrer passiven Lastminderungseigenschaften zusammengefasst und begrenzende Effekte speziell für Flügel mit erhöhter Strukturflexibilität aufgezeigt.

Contents

List of Figures

List of Tables

List of Symbols and Abbreviations

Abbreviations

ALE	Arbitrary Lagrangian-Eulerian
AoA	Angel of attack
AR	Aspect ratio
C.G.	Center of Gravity
CFD	Computational fluid dynamics
CFRP	Carbon-fiber-reinforced polymers
CLT	Classical laminate theory
CO2	Carbon dioxide
DLM	Doublet-lattice method
DoF	Degree of freedom
EASA	European union aviation safety agency
FEM	Finite elemente method
FI	Failure index
FL	Flight level
FRP	Fibre-reinforced-polymers
FT	Fuel tank
FVA	Field Velocity Approach
FVM	Finite volume method
HALE	High altitude long endurance
LE	Leading edge
Ma	Mach number
MAC	Mean aerodynamic chord
MDO	Multidisciplinary design optimization
MTOW	Maximum take-off weight
NASA	National aeronautics and space administration
NOx	Nitrogen oxides
SR	Strength index
TE	Trailing edge
uCRM, CRM	Undeflected, Common Research Model
UD	Unidirectional
uRANS, RANS	Unsteady, Reynolds-averaged Navier–Stokes equations
uVLM, VLM	Unsteady, Vortex-lattice method

Greek Symbols

α, α_1, α_2	Angle of attack, Rayleigh damping constants
ϵ	Increment per step
ϵ_0, ϵ_x	Strain in fibre, x-direction

ϵ_1, ϵ_y	Strain orthogonal to fibre, y-direction
Γ	Domain interface, also gradient of $\frac{\partial \alpha_{eff}}{\partial AoA}$
γ	Specific heat ratio
γ_{12}, γ_{xy}	In plane shear strain
κ_x, κ_y	Out-of-plane bending curvature
κ_f	Thermal conductivity
κ_{xy}	Out-of-plane twisting curvature
Λ, Λ_i	Wing sweep, also logarithmic decrement
μ_F	Dynamic viscosity
ν_{12}, ν_{21}	Poissons's Ratio in 1-2 plane
Ω	Computational domain
ω_h, ω_θ	Rotational frequency
Φ	Rotational DoF
Φ	Scalar quantity
φ	Stiffness ratio
ρ, ρ_0	Density, material density
τ, τ_{12}	Normalized time, shear stress in 1-2 plane
θ	Torsional DoF, also composite ply angle
Roman Symbols	
A, A_0	Area, Area in referenz configuration
C_f	Friction coefficient
C_L, C_l, $C_{l,max}$, $\bar{C}_l$	Total, sectional lift coefficient, maximum lift coefficient, mean sectional lift coefficient
C_M, C_m	Total, sectional pitch coefficient
D_v	Damping Ratio
E_1	Youngs modulus in fibre direction
E_2	Youngs modulus orthogonal to fibre direction
F_{12}	Tsai-Wu stress interacton parameter
G_{12}	Shear modulus in 1-2 plane
I_y, I_G, I_E	Inertia around y-axis, Inertia around C.G., Inertia around shear center
K_θ	Torsional stiffness
K_h	Translational stiffness
l_m	Reference length
m_x, m_y, m_{xy}	Line moments
n_x, n_y, n_{xy}	Line forces
n_z	Load factor
V, V_0, V_v	Volume, Volume in referenz configuration, design gust velocity
X_c, Y_c	Stress allowable in compression
X_t, Y_t	Stress allowable in tension
A	Amplitude
b, (b)	Wing span, also bending laminate
c	Chord length
E	Total energy, also shear center
f	Natural eigenfrequency

g	Gravitational constant
H	Gust length
h	Laminate or shell thickness, also translational displacment or gust gradient
I	Second moment of area
J	Jacobian of $\underline{F}$, also torsion constant
L	Lift force
l	Length of beam
M	Bending moment, also aerodynamic moment
m	Mass
p	Pressure
q	Pitch rate
S	Wing reference area, also transverse force or shear stress allowable
s,(s)	Distance mass-elastic axis, also shear laminate
T	Temperature
T	Torsional moment
t	time
W	Work

Vectors and Tensors

$\underline{\sigma}$	Cauchy, true stress tensor
$\underline{A}$	Membrane stiffness matrix, also fluid system coefficient matrix or mapping matrix
$\underline{B}$	Coupling stiffness matrix
$\underline{C}$	Material tensor
$\underline{D}$	Damping matrix, also dending stiffness matrix
$\underline{E}$	Green-Lagrange strain tensor
$\underline{F}$	Deformation gradient
$\underline{I}$	Identity tensor
$\underline{K}$	Stiffness matrix
$\underline{M}$	Mass matrix
$\underline{N}$	Shape function matrix
$\underline{P}$	Fist Piola-Kirchhoff stess tensor
$\underline{Q}$, $\breve{\underline{Q}}$	Stiffness tensor in UD coordinate system, tensor in CLT coordinate system
$\underline{S}$	Second Piola-Kirchhoff stess tensor
$\underline{T}$	Stiffness transformation matrix
$\vec{\Phi}$	Fluid solution vector
$\vec{b}$, $\vec{b}_0$	Boundary vector, body forces
$\vec{F}_{crit}$, $\vec{F}_{applied}$	Critical force, applied force
$\vec{F}_{int}$, $\vec{F}_{ext}$	Internal force, external force
$\vec{n}$, $\vec{n}_p$	Interface normal vector, pseude normal vector
$\vec{q}$	Heat flow
$\vec{u}$	Displacements
$\vec{v}$	Modal eigenvector
$\vec{V}$, $\vec{V}_g$, $\vec{V}_\Gamma$, $\vec{V}_{gust}$	Velocity, grid velocity, interface velocity, gust upwind velocity
$\vec{x}^p$	Predicted interface position vector

1 Introduction

The first part of this thesis describes the objectives of this study and outlines the core idea and the main motivation. The subsequent section presents a brief overview of the current research and the dynamics of this topic. Finally, the objectives and the structure of this thesis are presented.

Contents

1.1. Motivation and Scope of Thesis

The development of sustainable, new aircraft technologies and designs with improved energy efficiency is an increasingly demanding objective in the aviation industry [41]. With an estimated contribution of $2.4\,\%$ of anthropogenic CO_2 emission, the environmental footprint is receiving increasing attention in aircraft development and operation [36]. Therefore, the European aviation vision has set ambitious environmental objectives for future air transport in the coming decades. The Flightpath 2050 vision aims to reduce CO_2 emissions per passenger kilometer by 75% and the total NO_x emissions by 90% compared with technologies existing in the year 2000 [40]. As the environmental requirements for the aviation industry increase, the need to develop aircraft with low amounts of emission has increased. Therefore, next-generation aircraft concepts feature improvements in propulsion, optimized aerodynamics, structures and hybrid solutions [1, 62, 93, 98].

An observed trend towards the development of new advanced aircraft concepts is to increase the aerodynamic performance by using wings with high aspect ratios to reduce the lift induced drag, as shown in Abbas [2] and Schlichting [49]. Consequently, the direct operating costs of aircraft can be lowered through an improved fuel consumption. Figure 1.1a and Figure 1.1b show two examples of new aircraft concepts with slender wings. A further possibility is the installation of modified wing tip devices to increase the wings span. The Boeing 777x with a folding wing tip, as shown in Figure 1.1c, is an example of re-designing an existing configuration to increase the span to $71.75\,\mathrm{m}$ [11].

(a) Airbus ZeroE turbofan concept [8]

(b) Boeing Truss-Braced Wing [13]

(c) Boeing 777x folding wing tip [12]

Figure 1.1.: Novel aircraft concepts with wings of increased aspect ratio.

Structural design and aerodynamics are closely related for the development of wings. Challenges arise as the wings become more flexible with increased aspect ratios and higher deflections occur under

the same operating conditions. Changes in wing shape can considerably affect the aerodynamics of the aircraft, which is particularly important in the case of swept wings.

Most backward swept wings have an inherent bending-torsion coupling due to their design, which depends on the structural stiffness. Due to this coupling, the wing bending caused by lift directly affects the twist distribution of the wing [52]. One of the main features of this coupling effect is that the span wise distribution of the lift can be shifted towards the wing root as a result of the wing deflection and the associated local change in the angle of attack.

A particular problem with increasing aspect ratio is the higher internal loads resulting from the inherently increasing bending and torsional moments. Additional loads, such as those occurring during maneuver or gust encounter, can therefore significantly increase the internal loading. Sufficient load-bearing ability of the structure leads accordingly to heavier wing structures. The motivation to realize swept transport aircraft wings with a better lift-to-drag ratio leads to a conflict of objectives with regard to the overall performance of the aircraft due to the higher structural weight. With increasing structural flexibility of the wing, an increase in the natural bending-torsion kinematic coupling is to be expected. How these effects influence the natural passive load reduction characteristic of backward swept wings under flight conditions with higher load factors needs to be analyzed in more detail.

1.2. State of Research in the Development of Wing Structures

Passive structural technologies. New airframe technologies, designs and construction methods substantially contribute to the development of new wings. In recent years, the extensive use of composite materials, which has increased to over 50% in the currently in-service B787 and A350 aircraft [53, 92], has significantly influenced airframe technologies. The high specific stiffness, strength, good fatigue behavior, and orthotropic material properties of composite materials can be used to tailor the stiffness and strength in the direction of the main load paths, making these materials ideal for lightweight structural design. As the potential of composites has not been fully utilized to date, researchers are focusing on the adaptation of the wing's stiffness distribution by the ply angle and the number of plies, as well as fiber placement in complex paths, known as tow-steered composites [9, 100]. Another research field is structures with active functional integration, such as morphing wings. For example, Fujiwara [45] investigated how a continuous trailing edge flap with variable camber can be used on transport aircraft wings. Burdette [33] demonstrates how morphing trailing edge devices in combination with active control can help improve aircraft performance. The *Smart Droop Nose* [51] of the German Aerospace Center is used as an example to investigate how continuous wings can be realized by employing a morphing leading edge. To improve the aerodynamic performance of a wing, the design and development of wings with higher aspect ratio is another important research topic.

Active control technologies. The research fields mentioned are mostly passive technologies, which implies that their characteristics such as deformation or dynamic response are determined by the design. This is distinct from passive technologies in terms of actively influencing the structure by applying additional forces through flaps or spoilers to influence the shape of the wing. For example Schlemmer [23] presented various concepts of different wing control surface devices for active gust load alleviation. Pattinson [61] investigated, if folding wing tips as presented in Figure 1.1c, can be used as active control surfaces. Binder [96] developed an aircraft pre-design process to study passive aeroelastic tailoring combined with active load reduction system of an elastic free flying aircraft. In addition to active load alleviation methods, there are a number of research activities on active flutter suppression. Wings with high aspect ratio exhibit a reduced critical flutter speed so that technologies to prevent the aeroelastic instability is of particular interest. A comprehensive overview of the state-of-art developments is presented by Livne [37].

Virtual aircraft model. Today, simulation tools are used intensively in the development of new structural technologies. This is also favored by the fact that computing capacity has continued to increase since the first computers appeared in the 1960s. Computational methods, such as the Finite Element Method (FEM), have been developed for describing advanced structural mechanics problems in the aerospace industry. Likewise, in the field of aerodynamics, increasingly precise methods for describing complex flow processes have been established. This development continues, as demonstrated at NASAs *CFD Vision 2030* [64]. Simulation-based technology assessment is being integrated into the airframe design process to analyse new technologies such as passive and active load alleviation in highly flexible wings [103]. The project *VitAM* [68] shows that the research is motivated to minimize costs and risks during development by conducting virtual simulations. Challenges arising from a lack of understanding or the financial inefficiency of numerous tests on prototypes are to be solved using simulations. Further physical insight can be gained by using advanced computational methods and new simulation tools are helping to explore new improved technologies.

In general, load calculation is a critical step in the development of airframes, as it influences the dimensioning of structural components. Basic approval regulations which accompany the development and certification process are specified in Europe by the European Union Aviation Safety Agency (EASA). In the case of loads for civil transport aircraft, the relevant regulation is specified in the certification specification CS-25 section C [38]. Based on the requirements for accuracy, computing time and the overall complexity of the problem being investigated, several different models are defined and applied during the development process.

Medium fidelity model. In both structural mechanics and aerodynamics, linearized computational models have become state-of-the-art simulation methods, which involve structures discretized by beam or shell elements under linear elastic and kinematic assumptions. For aerodynamic modeling, lifting-line methods or methods based on the linear potential theory, such as VLM, uVLM, and DLM, are often used. However, the lack in theory to describe important physical phenomena such as shocks or viscous effects is a disadvantage of the aerodynamic modeling approach [58]. Nonetheless, they are advantageous in terms of the short computing time and, hence, are used in many scientific research problems pertaining to aircraft design in an early or exploratory development stage. For example, Kier [72–74] demonstrated how such models can be used to describe the dynamic behavior and structural loads on elastic aircraft, including flight control. Cook [94] and Szczyglowski [28] used potential theory based methods to describe aircraft gust loads. Klimmek [102] developed an approach for aircraft pre-design, load calculation, and structural sizing. Krueger [106] and Bordogna [78] used the aforementioned methods to investigate the passive aeroelastic tailoring of composite wings.

High fidelity model. Palacios [14] reviewed the criticality of linearized computational methods for very flexible wing structures and studied the relevant physical effects using a High Altitude Long Endurance (HALE) configuration with highly flexible high-aspect ratio wings as an example. The main focus was on structural mechanical modeling, particularly on the description of geometric nonlinearities due to large deformations, as these have a considerable effect on structural mechanical modeling, especially in dynamic gust load calculations. Afonso [43] summarizes the current state-of-the-art in high-aspect ratio wing design, and underlines the nonlinear aeroelastic characteristics due to large structural deformations. The nonlinearity of transonic flows requires methods with higher fidelity to capture important physical effects, which is not modeled trough linearized methods. As a result, modern aircraft experience aeroelastic problems that cannot be effectively predicted using these methods [31].

The development of new wing concepts for transport aircraft has been further advanced in recent years through projects such as *NASAs Fixed Wing* [90] or the *CleanSky Smart Fixed-Wing Aircraft* [42]. For example, Kenway [46] coupled an Euler Computational Fluid Dynamics solver with an structural FE method and optimized the NASA Common Research Model (CRM) for fuel-burn and maximum take-off weight (MTOW) using multi-disciplinary design optimization tools. Based on the objective

function, a high-aspect ratio wing was developed to achieve a low-fuel-consumption configuration. In these studies, the structural weight is increased compared to the initial configuration in order to support the increased loads at the wing. If the take-off weight of the aircraft is chosen as the objective function of the optimization, configurations with smaller aspect ratio are found. In both cases, the wing washout shifted the lift distribution further towards the wing root at higher maneuver loads, making passive load reduction possible. In the case of the high-aspect ratio configuration, a larger washout was observed than in the stiffer MTOW-optimized configuration.

Kennedy [59] continued this research using multi-objective optimization and shows that the preferred wing aspect ratio varies for the two objectives of minimum-fuel consumption and minimum take-off weight. Further, the influence of different materials, such as aluminum and carbon fiber reinforced plastic (CFRP), for the wing's primary structure is investigated. For the aerodynamic modeling, computational methods that solve the Reynolds-average Navier-Stokes (RANS) equations are used to consider viscous effects, such as flow separation. The decrease in the lift owing to the stall is identified as an effective measure of load reduction in the optimization task.

Higher-precision gust loads. The potential of methods with higher accuracy in the calculation of loads must be further utilized to develop new improved technologies [80]. To consider transonic effects, Raveh [30] compared different approaches to simulate the direct gust response of an aircraft. A fully resolved RANS CFD simulation and a hybrid method were compared by determining the impulse response (sharp edge gust) of a transport aircraft, which was then assembled into an arbitrary gust signal by convolution. Once the impulse response is determined, the method is distinguished because of its short computing times. Raveh demonstrated that a deviation of up to 10% occurred and that the approach was suitable for identifying critical load cases; however, the exact loads must be recalculated by using sophisticated full resolution methods.

Heinrich [89] compared a completely resolved RANS gust response with a simplified method based on induced disturbance velocities, as part of the *AeroGust* project [27]. The results show that for gust gradients larger than twice the mean aerodynamic chord, c_{ref}, good agreement is observed with the fully resolved simulations. Reimer [70] successfully applied the same approach on a transport aircraft to compare the gust behavior with that of a potential-based DLM gust model. In particular, distinct differences in the absolute load peaks were identified. Wales [24] investigated gust simulations using DLM and uVLM with different steady-state and transient CFD based correction factors. Improvements in the load prediction are achieved, but depending on the gust profile and flight conditions, the peak loads are over- or underestimated. Reimer [71] shows the advantage of the disturbance velocity approach in accuracy and simulation effort and, hence, its suitability for detailed and accurate aeroelastic design analyses.

1.3. Aims and Structure of the Thesis

To optimise the aerodynamic efficiency, wings with a higher aspect ratio show an advantage. At the same time, the wing becomes structurally more flexible. Through increased structural deflection and torsion, the lift distribution is also influenced. The use of passive load reduction by systematically changing the lift distribution to achieve smaller bending and torsional loads is being investigated in the development of new wing airframe technologies. A key consideration with regard to higher elastic wings is the influence of structural stiffness. This results in the following research question:

- How does the flow over the wing react to large wing deformations - to what extent can the local angle of attack be influenced.
- How does the wing stiffness generally affect the passive load alleviation performance?
- How does possible flow separation reduce the wing load?

In this study, the general effect of the wings structural flexibility on load alleviation characteristics is investigated to gain a deeper understanding of increased wing flexibility. Wings with the same planform but increased flexibility and those inherently more flexible, such as wings with increased aspect ratios, are studied under steady maneuver flight loads and transient loads due to gust exposure. Furthermore, higher-precision, high-fidelity methods are used to capture relevant physical phenomena. The application of computational aeroelasticity is still a challenging topic and is mainly applied in the academic research context. The work will therefore also contribute to demonstrate the applicability, flexibility and robustness of new methods for industry-relevant use cases. In order to answer the research questions, the work is divided into two sections with different demonstration examples:

- First, the properties that influence the wing flexibility are classified. A two-degree of freedom example is used to show the impact of the changing wing stiffness regardless of the material stiffness or geometric aspects, abstractly by discrete springs. To study individual impacts, which are often difficult to identify in complex real-world problems, the two-degree of freedom model is reduced to the most basic characteristics. The study is further categorized into structural and aerodynamic effects. These are influences caused by structural stiffness, as well as load reduction through flow separation.
- In the second part, a generic transport aircraft with different wing configurations is studied. The first wing configuration has an aspect ratio of $AR = 10$. With the same aircraft requirements and wing size, the second wing has an aspect ratio of $AR = 13$. For both configurations, wings with varying stiffness are set up and their characteristics under a quasi-steady maneuver and gust loads are investigated.

The essential aspects of this work and the links between the demonstration examples are shown in Figure 1.2.

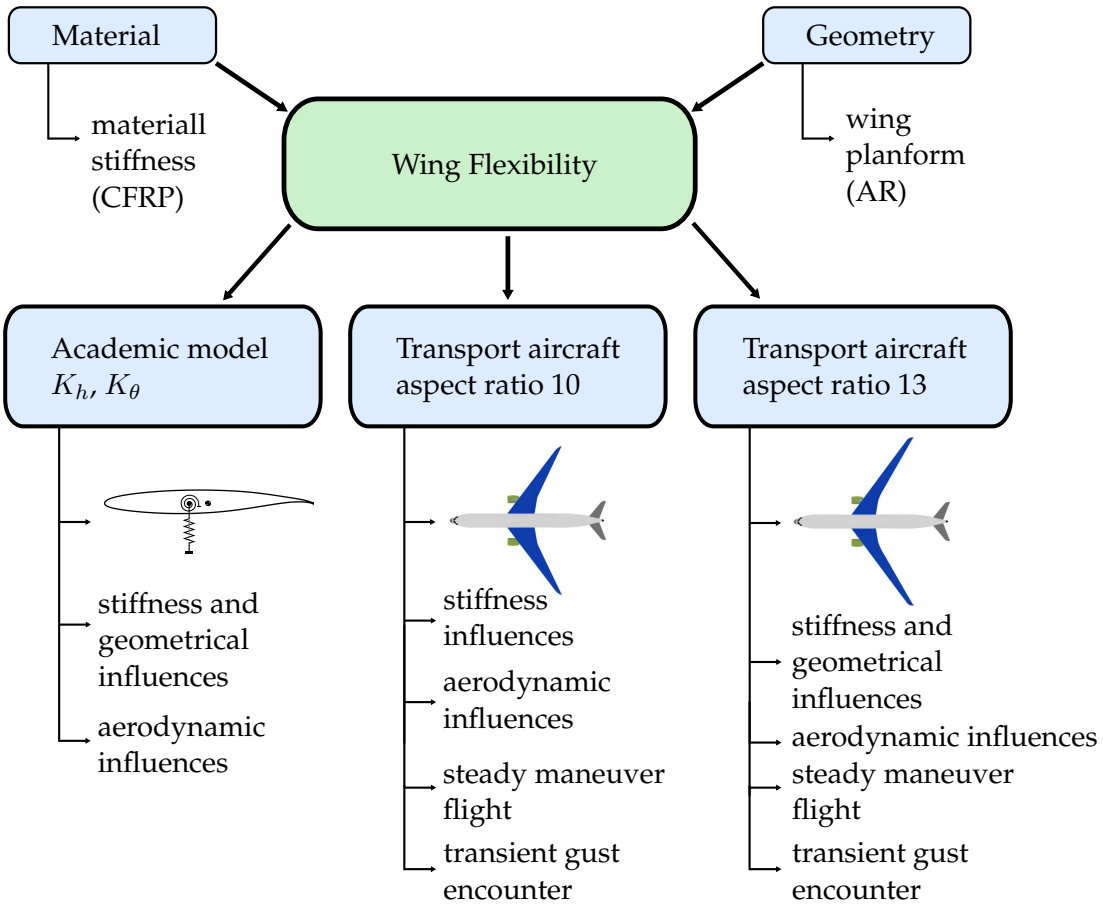

Figure 1.2.: Classification of the study and the three main elements of the computational models.

The thesis is organized in seven chapters, with Chapter 1 providing the introduction. Chapter 2 presents the necessary foundations and the computational framework that was developed to conduct the studies. Chapter 3 describes the development of a two-degree of freedom model, numerical experiments, and analysis of the results. Chapter 4 details the generic full-scale transport aircraft configuration, which includes the individual steps of the computational model development and the design simulations, such as structure sizing and jig-shape design. Chapter 5 provides the numerical results of quasi-stationary maneuver loads. Chapter 6 presents the transient gust encounter results. Chapter 7 underlines the relevance of the derived approaches and outlined ideas and summarizes the results and their scope.

2 Aeroelastic Modeling and Simulation Methodology

This chapter highlights the computational aeroelasticity fundamentals applied in this thesis. A summary of the governing continuum mechanics models for fluids and solids, is presented first, followed by the description of the computational gust modeling method using the Field-Velocity-Approach. Some aspects of composite modeling are briefly discussed to make the airframe structure sizing introduced later more transparent. Finally, the numerical methods used for solving continuum mechanical single-field problems and the developed framework for coupled Fluid-Structure-Interaction (FSI) simulations are described.

Contents

2.1. Computational Structural Dynamics Framework

The computational domain $\Omega = \Omega_F \cup \Omega_S$ consists of two non-overlapping computational subdomains Ω_S and Ω_F. Subsequently, the subscript F is used for the fluid and S for the solid continuum. The common interface between the two domains is denoted as $\Gamma = \Omega_F \cap \Omega_S$.

2.1.1. Continuum Mechanics of Solids

In aeroelastic calculations, it is essential to assess the structural deformation and the internal loads of the airframe due to external loads. The computational structural subdomain Ω_S is governed by the linear momentum balance with respect to the undeformed reference configuration. The linear momentum balance refers to the balance between inertia, internal, and external forces, and in its local form, is given by

$$\rho_0 \frac{\partial^2 \vec{u}}{\partial t^2} = \nabla \cdot (\underline{F} \cdot \underline{S}) + \vec{b}_0 \quad \text{in } \Omega_S, \tag{2.1}$$

where $\vec{u}$ represents the vector of unknown displacements, ρ_0 is the material density, and $\vec{b}_0$ is the vector of body forces. The internal forces are described by the first Piola-Kirchhoff stress tensor $\underline{P} = \underline{F} \cdot \underline{S}$, which is expressed in terms of the deformation gradient $\underline{F}$, and the second Piola-Kirchhoff stress tensor $\underline{S}$. The deformation is quantified using the Green-Lagrange strain tensor $\underline{E}$

$$\underline{E} = \frac{1}{2}(\underline{F} \cdot \underline{F}^T - \underline{I}), \tag{2.2}$$

which forms an energy conjugate pair with the stress tensor $\underline{S}$. The kinematic relationship described by Equation 2.2 and the balance Equation 2.1 are related by a constitutive law, which takes the form

$$\underline{S} = \underline{C} : \underline{E}. \tag{2.3}$$

The material tensor $\underline{C}$ is of fourth order, and its structure depends on the material model, as discussed in a later subsection. The Cauchy stress tensor σ_S, which describes the spatial dependence of the constitutive law and is often called the *true stress* tensor, is introduced as:

$$\underline{\sigma}_S = \frac{1}{J}\underline{P} \cdot \underline{F}^T = \frac{1}{J}(\underline{F} \cdot \underline{S}) \cdot \underline{F}^T, \tag{2.4}$$

where $J = det(\underline{F})$ is the Jacobian.

2.1.2. Structural Mechanics of Composites

The use of composite materials in the aerospace industry has increased since 1960. Composites have replaced aluminum as the primary material for modern commercial aircraft, contributing to more than $50\,\%$ [53] [92]. As this trend is expected to continue, this work considers composite materials for the primary wing structures. The following chapter summarizes the most important aspects of modeling composite structures in this thesis. Further details of composites are provided in [95].

Fiber reinforced polymers (FRP) consist of fibers, polymers, and coatings. Owing to the high specific stiffness and strength of the fibers, their volume content of approximately 60% is generally the largest among all three materials. However, high stiffness and strength are only exhibited along the fiber direction, and diminished along the orthogonal direction. Typical fiber materials include carbon, glass, and aramid. The matrix material consists of much softer polymers and possesses lower strength. Its main purpose is to support the fibers to withstand shear and pressure loads. The coating is included for manufacturability reasons and is neglected in the micromechanical modeling.

Unidirectional Composite Ply

The relationship between the stresses and strains in Equation 2.3 is given by the constitutive law. In unidirectional (UD) composite plies, an in-plane stress-strain relationship applies because of the

small perpendicular geometric dimension compared with the other dimensions. The relationship for a linearly elastic anisotropic material can generally be expressed in matrix notation as follows:

$$\begin{Bmatrix} \sigma_1 \\ \sigma_2 \\ \tau_{12} \end{Bmatrix} = \underline{Q} \begin{Bmatrix} \epsilon_1 \\ \epsilon_2 \\ \gamma_{12} \end{Bmatrix}, \tag{2.5}$$

$$\text{with:} \quad \underline{Q} = \frac{1}{1-\nu_{12}\nu_{21}} \begin{bmatrix} E_1 & \nu_{21}E_1 & 0 \\ \nu_{12}E_2 & E_2 & 0 \\ 0 & 0 & G_{12}(1-\nu_{12}\nu_{21}) \end{bmatrix}$$

where E_1 and E_2 describe the modulus of elasticity in the fiber direction and perpendicular to it, respectively. The material constants ν_{ij} and G_{ij} stand for the Poisson's ratio and shear modulus, respectively.

2.1.3. Structural Mechanics of Composite Laminates

The composite laminate is designed by determining the number of UD plies, their thicknesses, and fiber orientations. For the UD ply orientation, the coordinate system (0-1) with reference to the global material system (x-y) is used. The fiber direction is defined by the 0-axis, as indicated in Figure 2.1a.

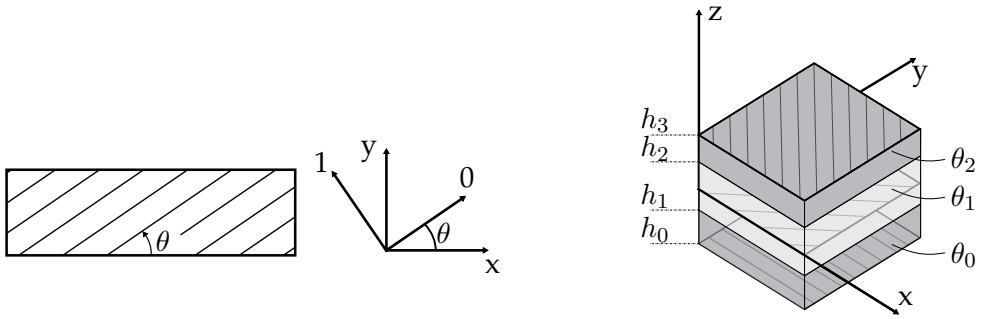

(a) UD coordinate system (b) CLT coordinate system

Figure 2.1.: Definition of material coordinate system for UD composite and laminate.

The constitutive law of Equation 2.5 can be transformed into the material system (x-y) by applying the coordinate transformation

$$\breve{\underline{Q}} = \underline{T}\underline{Q}\underline{T}^T, \tag{2.6}$$

$$\text{with:} \quad \underline{T} = \begin{bmatrix} cos^2(\theta) & sin^2(\theta) & -2cos(\theta)sin(\theta) \\ sin^2(\theta) & cos^2(\theta) & 2cos(\theta)sin(\theta) \\ cos(\theta)sin(\theta) & -cos(\theta)sin(\theta) & cos^2(\theta) - sin^2(\theta) \end{bmatrix}.$$

The mechanical properties of the laminate are described using the Classical Laminate Theory (CLT). According to the Kirchhoff-Love plate theory, the strain across the plate thickness is given by

$$\vec{\epsilon}(z) = \vec{\epsilon}_0 + z \cdot \vec{\kappa} = \begin{Bmatrix} \epsilon_x^0 \\ \epsilon_y^0 \\ \gamma_{xy}^0 \end{Bmatrix} + z \cdot \begin{Bmatrix} \kappa_x \\ \kappa_y \\ \kappa_{xy} \end{Bmatrix}, \tag{2.7}$$

with $\vec{\epsilon}_0$ being the strain in the reference plane and $\vec{\kappa}$ the curvature of the composite plate. The correlation between external and internal loads is obtained by integration over the laminate thickness

t. For the applied in-plain line force n_i it follows the relation

$$\begin{Bmatrix} n_x \\ n_y \\ n_{xy} \end{Bmatrix} = \sum_{k=1}^{N} \int_{h_{k-1}}^{h_k} \vec{\sigma}(z) dz = \sum_{k=1}^{N} \int_{h_{k-1}}^{h_k} \breve{\underline{Q}}(z) \{\vec{\epsilon}_0 + z \cdot \vec{\kappa}\} dz, \tag{2.8}$$

and for the line moments m_i, it follows that

$$\begin{Bmatrix} m_x \\ m_y \\ m_{xy} \end{Bmatrix} = \sum_{k=1}^{N} \int_{h_{k-1}}^{h_k} \vec{\sigma}(z) z dz = \sum_{k=1}^{N} \int_{h_{k-1}}^{h_k} \breve{\underline{Q}}(z) \{z\vec{\epsilon}_0 + z^2 \cdot \vec{\kappa}\} dz. \tag{2.9}$$

Equation 2.8 and Equation 2.9 represent the material law for composite panels by linking the force and moment fluxes with strains and curvatures. This can be further condensed to the commonly used ABD-matrix notation, that is

$$\begin{Bmatrix} n_x \\ n_y \\ n_{xy} \\ m_x \\ m_y \\ m_{xy} \end{Bmatrix} = \begin{bmatrix} \underline{A} & \underline{B} \\ \underline{B} & \underline{D} \end{bmatrix} \begin{Bmatrix} \epsilon_x \\ \epsilon_y \\ \gamma_{xy} \\ \kappa_x \\ \kappa_y \\ \kappa_{xy} \end{Bmatrix}. \tag{2.10}$$

$$\begin{aligned} \text{with:} \quad A_{ij} &= \textstyle\sum_{k=1}^{N} \breve{Q}_{ij}^{k} \{h_k - h_{k-1}\} \\ B_{ij} &= \textstyle\sum_{k=1}^{N} \breve{Q}_{ij}^{k} \{h_k^2 - h_{k-1}^2\} \\ C_{ij} &= \textstyle\sum_{k=1}^{N} \breve{Q}_{ij}^{k} \{h_k^3 - h_{k-1}^3\} \end{aligned}$$

2.1.4. Composite Failure Modeling

Compared with metals, composites exhibit a more complex failure behavior. This is mainly because the definition of failure cannot be defined based on a fracture criterion alone. Additional damage mechanisms such as delamination, fiber fracture, and matrix failure must also be considered. A number of different failure criteria exists to assess failure, such as Tsai–Wu, Tsai–Hill, Hashin and Cuntze. Most theories attempt to evaluate the internal stress in different plies of a laminate and assign it to a failure index $\mathcal{FI}$. The failure index is based on the stress measure $\underline{\sigma}$ and material strength data $\vec{X}_R, \vec{Y}_R$. Generally, the principles are expressed as follows:

$$\mathcal{FI}(\underline{\sigma}, \vec{X}_R, \vec{Y}_R) \begin{Bmatrix} < 1 & \text{No failure} \\ = 1 & \text{Critical loading} \\ > 1 & \text{Failure according to failure theory} \end{Bmatrix}. \tag{2.11}$$

In this thesis, the failure theory by Tsai-Wu [97] is applied, expressed as

$$\mathcal{FI}(\underline{\sigma}, \vec{X}_R, \vec{Y}_R) = \frac{\sigma_1^2}{X_t X_c} + \frac{\sigma_2^2}{Y_t Y_c} + 2F_{12}\sigma_1\sigma_2 + \frac{\tau_{12}^2}{S^2} + \sigma_1 \left[\frac{1}{X_t} - \frac{1}{X_c}\right] + \sigma_2 \left[\frac{1}{Y_t} - \frac{1}{Y_c}\right]. \tag{2.12}$$

Here, X_t and X_c represent the tensile and compressive strengths in the direction of the fiber, respectively. Y_t, Y_c represents the tensile and compressive properties orthogonal to the fiber, respectively. Parameter F_{12} describes the interaction of the normal stresses σ_i and is determined by a biaxial tensile test. If no test data is available, according to Wu, F_{12} can be determined using the correlation:

$$F_{12} = f^* \sqrt{F_{11} F_{22}} = -\frac{1}{2\sqrt{X_t X_c Y_t Y_c}}. \tag{2.13}$$

$$\begin{aligned} \text{with:} \quad f^* &= -0.5 \\ \text{and Tsai-Wu coeffizient:} \quad F_{11} &= -\frac{1}{X_t X_c} \\ F_{22} &= -\frac{1}{Y_t Y_c} \end{aligned}$$

Equation 2.12 shows that a nonlinear relationship between $\mathcal{FI}$ and the stresses does exist. To obtain a direct measure between the composite failure and applied external loads, the strength quotient $\mathcal{SR} = \frac{\vec{F}_{allowed}}{\vec{F}_{applied}}$ is introduced [82]. Substituting Equation 2.14 into Equation 2.12, and solving the same for $\mathcal{FI} = 1.0$ gives the implicit form:

$$1.0 = \left[\frac{\sigma_1^2}{X_t X_c} + \frac{\sigma_2^2}{Y_t Y_c} + 2F_{12}\sigma_1\sigma_2 + \frac{\tau_{12}^2}{S^2}\right]\mathcal{SR}^2 + \left[\sigma_1\left[\frac{1}{X_t} - \frac{1}{X_c}\right] + \sigma_2\left[\frac{1}{Y_t} - \frac{1}{Y_c}\right]\right]\mathcal{SR}\,. \tag{2.14}$$

By finding the roots of Equation 2.14, the critical load $\vec{F}_{crit}$ can be determined by

$$\vec{F}_{crit} = \mathcal{SR} \cdot \vec{F}_{applied}. \tag{2.15}$$

2.1.5. Discretization and Numerical Solution

The Finite Element (FE) method is a discretization method for an approximate solution of partial differential equations. This method is commonly used in structural mechanics calculations to solve for the displacement field $\vec{u}$ over the solution domain Ω_S. This section summarizes the FE method focused on Bathe and Wriggers [69, 86].

The starting point is the weak form of the equilibrium equation, which is obtained by calculating the weighted residuals of Equation 2.1 using virtual displacements δu. In structural mechanics, this approach is known as the *principle of virtual work*. In matrix notation, the weak form of the equilibrium equation is

$$\int_{\Omega_S} \delta\vec{u}^T \rho_0 \ddot{\vec{u}}\, dV_0 + \int_{\Omega_S} \delta\underline{E}^T \underline{S}\, dV_0 - \int_{\Omega_S} \delta\vec{u}^T \vec{b}_0\, dV_0 - \int_{\Gamma_S} \delta\vec{u}^T \vec{t}_0\, dA_0 = 0, \tag{2.16}$$

where dV_0 and dA_0 are the infinitesimal volume and surface elements, respectively. The variation in the Green-Lagrange strain tensor $\delta\underline{E}$ is obtained from Equation 2.2 and is expressed as

$$\delta\underline{E} = \frac{1}{2}\left[(\nabla\delta\vec{u})^T \cdot \underline{F} + \underline{F}^T \cdot (\nabla\delta\vec{u})\right]. \tag{2.17}$$

The weak form is first approached by discretizing the domain Ω_S into N^e elements. With the associated standard shape functions N_i, the approximated displacement field is

$$\vec{u}^{(e)} = \sum_i N_i^{(e)} \vec{\vec{u}}_i \quad \text{on } \Omega^{(e)}, \tag{2.18}$$

wherein $\vec{\vec{u}}_i$ stands for the nodal displacement of the element. For the virtual displacement, the same shape function $N_i^{(e)}$ is used as the node displacement. The final element-wise displacement approach of the virtual work, expressed in matrix notation, is as follows:

$$\delta\vec{u}^T \left\{\int_{\Omega^{(e)}} \underline{N}^T \rho_0 \underline{N}\, dV\, \ddot{\vec{u}} + \int_{\Omega^{(e)}} (\frac{\partial\underline{E}}{\partial\vec{u}})^T \underline{S}\, dV - \int_{\Omega^{(e)}} \underline{N}^T \vec{b}_0\, dV - \int_{\Gamma^{(e)}} \underline{N}^T \vec{t}_0\, dA\right\} = 0. \tag{2.19}$$

By assembling all elements, the compact form of the *ndof*-dimensional semi-discrete equation of motion

$$\underline{M}\ddot{\vec{u}} + \vec{f}_{int}(\vec{u}) - \vec{f}_{ext}(\vec{u}) = \vec{0}, \tag{2.20}$$

is obtained. Here, $\underline{M}$ denotes the mass matrix, and $\ddot{\vec{u}}, \vec{u}$ denote the nodal acceleration and displacement, respectively. The discrete force vectors are split into internal forces $\vec{f}_{S,int}(\vec{u})$ and external applied forces $\vec{f}_{S,ext}(\vec{u})$. Equation 2.20 is generally a thin-banded system of algebraic equations that can be solved using established numerical methods.

Damping Model

In this study, influence of structural damping is represented by applying Rayleigh's damping model [69, p. 948]. An additional viscous damping matrix $\underline{D}$ is established as follows:

$$\underline{D} = \alpha_1 \underline{M} + \alpha_2 \underline{K}. \tag{2.21}$$

A constant modal damping is assumed for this study. For the i^{th} DoF, the Rayleigh damping is formulated as a function of the damping ratio, $D_{\nu,i}$, and the rotation frequency, ω_i, such that Equation 2.22 holds.

$$D_{\nu,i} = \frac{1}{2}\left(\frac{\alpha_1}{\omega_i} + \alpha_2 \omega_i\right) \tag{2.22}$$

The first natural bending and torsional eigenmode (ω_h, ω_θ) are considered as the relevant motions, and parameters α_1 and α_2 are obtained by solving the linear system, given as

$$\frac{1}{2}\begin{bmatrix} \frac{1}{\omega_h} & \omega_h \\ \frac{1}{\omega_\theta} & \omega_\theta \end{bmatrix}\begin{Bmatrix}\alpha_1 \\ \alpha_2\end{Bmatrix} = \begin{Bmatrix} D_{\nu,h} \\ D_{\nu,\theta}\end{Bmatrix}. \tag{2.23}$$

Here, the damping ratios are assumed to be $D_{v,i} << 1$. Thus, the definition of $D_{\nu,i} \approx \frac{\Lambda_i}{2\pi}$ can be used, where $\Lambda_i = ln(\frac{A(t)}{A(t+T_d)})$ is the logarithmic decrement [48]. The two parameters α_1 and α_2 are selected later such that a specific modal damping for individual vibration modes is achieved. The final semi-discrete equation of motion is as follows:

$$\underline{M}\ddot{\vec{u}} + \underline{D}\dot{\vec{u}} + \vec{f}_{int}(\vec{u}) - \vec{f}_{ext}(\vec{u}) = \vec{0}. \tag{2.24}$$

Discretization in Time

The semi-discrete Equation 2.24 is discretized in time using the Newmark β-method [77]. The generalized form of the Newmark-beta operator is as follows:

$$\ddot{\vec{u}}_{n+1} = \frac{1}{\beta\Delta t^2}(\vec{u}_{n+1} - \vec{u}_n) - \frac{1}{\beta\Delta t}\dot{\vec{u}}_n - \frac{1-2\beta}{2\beta}\ddot{\vec{u}}_n, \tag{2.25}$$

$$\dot{\vec{u}}_{n+1} = \dot{\vec{u}}_n + \gamma\Delta t\ddot{\vec{u}}_{n+1} + (1-\gamma)\ddot{\vec{u}}_n.$$

The force balance Equation 2.24 at a new time step t_{n+1} with $\vec{f}_{int} = \underline{K}\vec{u}$ is

$$\underline{M}\ddot{\vec{u}}_{n+1} + \underline{D}\dot{\vec{u}}_{n+1} + \underline{K}\vec{u}_{n+1} = \vec{f}_{ext}(\vec{u})_{n+1}. \tag{2.26}$$

Inserting the Newmark-beta operators in Equation 2.26 will result in

$$\begin{aligned} \left\{\tfrac{1}{\beta\Delta t^2}\underline{M} + \tfrac{\gamma}{\beta\Delta t}\underline{D}\right\} &\quad \vec{u}_n + \\ \left\{\tfrac{1}{\beta\Delta t}\underline{M} + (\tfrac{\gamma}{\beta} - 1)\underline{D}\right\} &\quad \dot{\vec{u}}_n + \\ \left\{\tfrac{1-2\beta}{2\beta}\underline{M} + \Delta t(\tfrac{\gamma-2\beta}{2\beta})\underline{D}\right\} &\quad \ddot{\vec{u}}_n + \\ &\quad \vec{f}_{n+1} = \left\{\tfrac{1}{\beta\Delta t^2}\underline{M} + \tfrac{\gamma}{\beta\Delta t}\underline{D} + \underline{K}\right\}\vec{u}_{n+1} \end{aligned} \tag{2.27}$$

which is solved for the displacement $\vec{u}_{n+1}$. The two Newmark parameters are set as $\beta = \frac{1}{4}$ and $\gamma = \frac{1}{2}$, which corresponds to a constant average acceleration within a time step. In this thesis, unless otherwise stated, the FE solver MSC-NASTRAN-SOL400 [81] is used to solve computational structural mechanics problems in statics and dynamics.

2.2. Computational Fluid Dynamics Framework

In aeroelastic studies, the aerodynamic forces and moments acting on the airframe must be calculated. Considering transonic flow conditions, including shocks and viscous effects, the three-dimensional Navier-Stokes equations without body forces are used to describe the flow on the domain Ω_F. The fundamentals used in this thesis for fluid mechanical modeling are outlined in the following section.

2.2.1. Continuum Mechanics of Fluids

As presented by Hirsch [20, Chapter 1.1] and Ferziger [66, Chapter 1.2] , the conservation law for a scalar quantity Φ in its differential form without diffusion can be expressed as:

$$\frac{\partial \Phi}{\partial t} + \nabla \cdot (\Phi \vec{V}) = S_\Phi \quad \text{in } \Omega_F. \tag{2.28}$$

The conservation quantities Φ of compressible fluids are mass, momentum, and energy. Thus, Φ is the density ρ_F, momentum $\rho_F \vec{V} = \rho_F \{V_1, V_2, V_3\}^T$ and total energy E. The right-sight S_Φ of Equation 2.28 describes the source terms for the three conservation quantities, and is expressed as:

$$S_{\Phi=\rho} = 0 \tag{2.29}$$

$$\vec{S}_{\Phi=\rho\vec{V}} = \{S_{\Phi=\rho V_1}, S_{\Phi=\rho V_2}, S_{\Phi=\rho V_3}\}^T = \nabla \cdot (\underline{\sigma}_F)$$

$$S_{\Phi=E} = \nabla \cdot (\underline{\sigma}_F \vec{V} - \vec{q})$$

For a Newtonian fluid based on Stoke's hypothesis ($\lambda_F = -\frac{2}{3}\mu_F$), the Cauchy stress tensor σ_F can be expressed as:

$$\underline{\sigma}_F = -p\underline{I} + \mu_F[(\nabla \vec{V} + \nabla \vec{V}^T) - \frac{2}{3}\nabla \cdot \vec{V}\underline{I}], \tag{2.30}$$

where p is the pressure and μ_F is the dynamic viscosity. The heat flow due to heat conduction is determined according to Fourier's law:

$$\vec{q} = -\kappa_F \nabla T, \tag{2.31}$$

where T denotes the temperature, and κ_F is the coefficient of thermal conductivity. In this work, air is considered as an ideal gas with a specific heat ratio of $\gamma = 1.4$ and a specific gas constant $\mathcal{R} = 287.05\,\mathrm{J/(kgK)}$. Pressure p and temperature T are described by the equation of state for ideal gases, which is expressed as follows:

$$p = \rho_F \mathcal{R} T. \tag{2.32}$$

The definition of the total energy is

$$E = \rho_F(e + \frac{1}{2}\vec{V}^2) = \frac{p}{\gamma - 1} + \frac{1}{2}\rho_F \vec{V}^2, \tag{2.33}$$

with the approximation $p = \rho(1-\gamma)e$ for a caloric perfect gas.

ALE-Formulation

The Arbitrary-Lagrangian-Eulerian (ALE) method provides a description of the flow equilibrium equation in time-dependent domains [21, 56]. An essential characteristic of the ALE approach is the arbitrary reference frame, which is no longer fixed to the movement of the continuum (Lagrange) or in space (Eulerian). The approach involves a mesh movement algorithm that moves the computational fluid dynamics (CFD) mesh with the time-varying FSI interface so that the fluid domain is adapted to the body at each time. The change in the arbitrary moving domain is described by the grid velocity $\vec{V}_g$. The Eulerian form of the conservation law for scalar Φ is given in Equation 2.28. Considering Gauss theorem and inclusion of the ALE kinematics on an arbitrary moving grid (see for instance Donea [57]), the conservation law in its integral form is expressed as:

$$\frac{d}{dt}\int_{\Omega_F} \Phi \, dV + \int_{\partial\Omega_F} \Phi(\vec{V} - \vec{V}_g) \, d\vec{A} = \int_{\Omega_F} S_\Phi \, dV. \tag{2.34}$$

It should be noted that an additional flux term appears because of domain movement. The special case of a Eulerian frame is obtained by setting $\vec{V}_g = 0$. Similarly, one obtains the Lagrange description by setting the grid velocity to the particle velocity $\vec{V}_g = \vec{V}$. The latter is useful as it simplifies the handling of the interface wall boundary conditions, because the motion can be directly considered in the conservation laws.

2.2.2. Gust Modeling

The direct way to introduce a gust into a CFD simulation is through a transient boundary condition in the far-field of the domain. However, it must be ensured that the gust between the far-field and body surface is preserved, and the accuracy is not affected by numerical diffusion. Consequently, high-order numerical discretization methods or very fine grid resolutions must be applied to the entire domain. In this study, a 2^{nd} order discretization method is used to solve the governing equation of the fluid domain. Therefore, a high grid resolution is necessary, resulting in an unavoidably high computing effort.

In this study, the *Field-Velocity-Approach* (FVA), as described in [63, 91], is used instead to circumvent this major drawback. The approach uses an additional superposed disturbance velocity field, V_{gust}, as the vertical velocity induced by a gust. The problem is then handled as if the wing is moving at the speed of the gust but in the opposite direction. The modification in the equilibrium equation results in an additional flux term, which is similar to the change in the grid time metrics in a moving mesh. The ALE formulation of the conservation laws can be used to implement this approach by modifying the mesh velocity with an artificially superimposed gust velocity field. The modified ALE formulation is as follows:

$$\frac{d}{dt}\int_{\Omega_F} \Phi \, dV + \int_{\partial\Omega_F} \Phi(\vec{V} - (\vec{V}_\Gamma + \vec{V}_{gust})) \, d\vec{A} = \int_{\Omega_F} S_\Phi \, dV. \tag{2.35}$$

This approach is demonstrated in [27, 88, 89] and shows good validity when the influence of the body surface on the gust can be neglected. This is the case when the gust gradients are more than twice the mean aerodynamic chord c_{ref} [88, 89].

2.2.3. Turbulence Modeling

Despite increasing computing capacities, direct numerical simulation of the Navier-Stokes equations for aircraft aerodynamics is practically infeasible [20, 66]. For this reason, the approximation by splitting the conservation variables into an average and turbulent part is applied for the flow simulation.

The idea originally introduced by Reynolds results in the so called Reynolds-averaged Navier-Stokes (RANS) equations [20, section 2.2.2][66, section 10.3.5]. Turbulent random fluctuations are inherently suppressed, and only the time-variant flow phenomena are modeled. The underlying turbulent fluxes emerge in the form of the Reynolds stress tensor, which is a symmetric tensor with six unknowns [34]. As a result of the Reynolds stress tensor, the system of equations can no longer be solved in a closed form. Thus, an additional approximation to model the turbulence is necessary. Numerous turbulence models with varying degrees of complexity have been developed for different fields of application. A general classification of these models is presented in [54]. In this study, the eddy-viscosity turbulence modeling according to Spalart-Allmaras (SA) [85] is used. As a single-equation turbulence model, an additional transport equation for the eddy viscosity must be solved.

2.2.4. Surface Friction - Flow Separation

In a later detailed evaluation of the flow along the wing surface, a measurement is required to detect possible flow separation. For this purpose, the surface friction coefficient C_f along the lifting surface is determined, given as follows:

$$C_f = \frac{\tau_w}{0.5 \cdot \rho \cdot V^2} = \frac{\mu \frac{\partial u}{\partial n}}{0.5 \cdot \rho \cdot V^2}, \tag{2.36}$$

where $\frac{\partial u}{\partial n}$ denotes the flow velocity derivative normal to the wall. From the theory of boundary layer flow, it follows that at the flow separation point $\frac{\partial u}{\partial n} = 0$ applies [50, section 13.0]. Therefore, this implies that at the flow separation point $C_f = 0$ and in the following recirculating zone, $C_f < 0$ applies.

2.2.5. Discretization and Numerical Solution

For the discretization of Equation 2.28 and Equation 2.34 the Finite Volume Method (FVM) is applied. The FVM integrates the transport equation for each control volume, which provides a discrete equation expressing the conservation law on a control volume basis. The integral form of the equilibrium Equation 2.28 for an arbitrary volume $\Omega_F^{(e)}$ is

$$\int_{\Omega_F^{(e)}} \frac{\partial \Phi}{\partial t}\, dV + \int_{\partial\Omega_F^{(e)}} \Phi \vec{V}\, d\vec{A} = \int_{\Omega_F^{(e)}} S_\Phi\, dV. \tag{2.37}$$

The discretization on a given cell yields

$$\frac{\partial \Phi}{\partial t}\Omega_F^{(e)} + \sum_i^{N_f} \Phi_i \vec{V}_i \vec{A}_i = S_\Phi \Omega_F^{(e)}. \tag{2.38}$$

The functional values are approximated by difference quotients, which differ in their order of termination. Together with suitable boundary conditions, an algebraic system of equations in the form

$$\underline{A}\vec{\Phi} = \vec{b}, \tag{2.39}$$

with the coefficient matrix $\underline{A}$, the solution vector $\vec{\Phi}$ and the applied boundary condition $\vec{b}$ is obtained, which is usually solved iteratively. In this study, the FVM-based flow solver TAU [32] is used on an unstructured vortex-centered dual-mesh approach, providing second-order accuracy in time and space [101].

Boundary Conditions

Various boundary conditions are available in the context of the CFD methods. Three boundary conditions are essential for this study, and the implementation details can be found in [35].

Viscous turbulent wall: Viscous surfaces are used to model the wings and fuselage. The boundary condition is assumed to be turbulent with a fully resolved boundary layer, meaning no wall functions are applied.

Far-field: An inflow and outflow boundary condition is selected at the outer boundary of the computational domain (farfield). By definition, all gradients are zero and viscous effects are not considered; thus, the boundary condition is placed far from the simulated object.

Symmetry: The symmetry boundary condition is used to reduce the computational cost of the model to a symmetric subrange of the domain. Therefore, the symmetrical geometry and flow pattern of the aircraft is exploited. The conditions at the symmetric boundary are zero normal velocity at the symmetry plane and zero normal gradients for all variables. Under these conditions, the flux through the symmetry plane is zero.

Discretization in Time

For time-accurate calculations, an implicit second-order backward Euler scheme is applied, where every physical time step is transformed into a pseudo-stationary problem using dual-time stepping. As described in [6, 54], the partial differential equations are solved in each time step by a combination of physical time and pseudo time steps, resulting in a series of nonlinear steady-state problems [35]. Furthermore, numerical techniques can be applied to accelerate convergence, such as implicit schemes, local time steps, and multigrid methods. In this study, a three-stage W-cycle multigrid scheme is used with an additional step on the coarser grid level. The maximum Courant-Friedrichs-Lewy number is set as 2.0.

2.3. Computational Aeroelastic Modeling

The structural and fluid mechanical model are subsequently combined to form a aeroelastic model. This subsection addresses the computational FSI framework used in aeroelastic studies. These include the fluid-structure interface conditions and a technique for load and motion transfer across nonuniform grids. In addition, the applied domain-coupling methods are discussed in detail.

2.3.1. Fluid-Solid Interface Conditions

The integrity between the two subdomains Ω_S and Ω_F is established by enforcing the dynamic and kinematic coupling conditions at the interface Γ. To achieve dynamic equilibrium, the forces must be balanced, resulting in

$$\underline{\sigma}_S^\Gamma \cdot \vec{n}^\Gamma = \underline{\sigma}_F^\Gamma \cdot \vec{n}^\Gamma, \tag{2.40}$$

with $\vec{n}$ being the interface normal vector. The Cauchy stress tensor is given by Equation 2.4 and Equation 2.30. Furthermore, a kinematic non-slip boundary condition is applied, so that for the normal speeds at the interface, the condition

$$\frac{\partial u}{\partial t} \cdot \vec{n}^\Gamma = \vec{V}^\Gamma \cdot \vec{n}^\Gamma, \tag{2.41}$$

must apply.

2.3.2. Interface Load and Motion Transfer

For FSI problems, the load and motion transfer at the interface Γ must be defined. No special treatment is necessary with the same discretization on the solid and fluid domains. However, different discretization requirements and different types of grids lead to a non-matching interface, as illustrated in Figure 2.2.

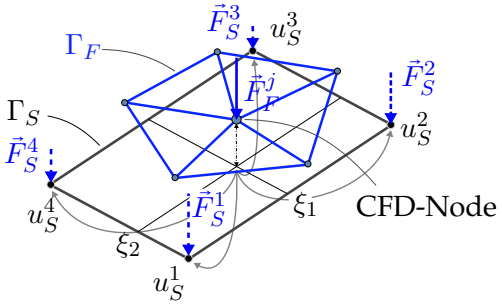

(a) Non-matching interface grid

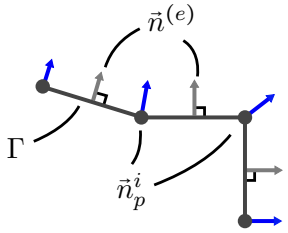

(b) Pseudo node normals

Figure 2.2.: FSI load and motion transfer mapping scheme.

In this study, a bilinear mapping method based on the FE shape function presented by Farhat [17] is applied. The displacement transfer of a single grid node is expressed as:

$$\vec{u}_F^j = \sum_i N_i^{(e)}(\xi_1, \xi_2)\vec{u}_S^i, \tag{2.42}$$

where $N_i^{(e)}$ represents the i^{th} shape function of the finite element. The projection is based on a continuous field of normal vectors $\vec{n}$. To obtain a $\mathcal{C}^0$-continuous field, the pseudo-normal vector $\vec{n}_p$ is interpolated by means of the FE formulation:

$$\vec{n} = \sum_i N_i^{(e)}(\xi_1, \xi_2)\vec{n}_p^i. \tag{2.43}$$

As suggested by Yang [10], the pseudo normal vector $\vec{n}_p$ as shown in Figure 2.2b, is obtained by averaging the element normal vector of the adjacent elements in the following form:

$$\vec{n}_p = \frac{\sum_{i=1}^{adj} \vec{n}_i^{(e)}}{\left\| \sum_{i=1}^{adj} \vec{n}_i^{(e)} \right\|}. \tag{2.44}$$

By assembling the individual element mapping parameters, the overall mapping matrix $\underline{A}$ is obtained, which maps the displacement vector $\vec{u}_S^\Gamma$ to the CFD node displacement $\vec{u}_F^\Gamma$, which is expressed as follows:

$$\vec{u}_F^\Gamma = \underline{A}_{F,S}\, \vec{u}_S^\Gamma. \tag{2.45}$$

For the transfer of the loads, the following condition applies:

$$\vec{f}_S^\Gamma = \underline{A}_{F,S}^T\, \vec{f}_F^\Gamma. \tag{2.46}$$

2.3.3. FSI Coupling Framework

The classification of FSI algorithms can be grouped into monolithic and partitioned approaches. Monolithic methods consist of a single system of equations that contain complete information regarding the coupled problem. In contrast, partitioned algorithms solve the different disciplines in a sequential or parallel manner and offer problem-specific efficient coupling of different single-field solvers [3].

Partitioned algorithms are additionally differentiated into loose and strongly coupled approaches, which refer to whether the coupling conditions at each time step are exactly fulfilled. Loosely coupled methods can typically be found in aeroelasticity [15, 16], where due to low fluid-solid density ratios, instabilities caused by the added mass effect do not apply [84].

Staggered Coupling Scheme

The two subdomains Ω_S and Ω_F are loosely coupled using a staggered coupling algorithm, as presented by Farhat [16]. In this approach, the fluid transfers forces at the interface as a Neumann boundary condition, and the structure defines the kinematic constraint (displacements and velocities) in terms of a Dirichlet boundary condition. The main steps to advance the coupled system from time step t_n to $t_{n+1} = t_n + \Delta t$ are illustrated in Figure 2.3.

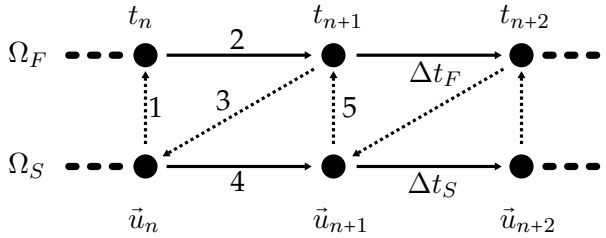

Figure 2.3.: Staggered FSI coupling algorithm.

The steps are as follows:

1. Transfer the structural interface displacements $\vec{u}$ and velocities $\dot{\vec{u}}$ at time step t_n to the flow solver. In the case of non-matching grids, interpolation in the form of Equation 2.45 is required to transfer structural displacements to the fluid interface.
2. Predict the new interface position Γ_F with

$$\vec{x}^p_{n+1} = \vec{u}_n + \frac{\Delta t}{2}(3.0 \cdot \dot{\vec{u}}_n - \dot{\vec{u}}_{n-1}), \tag{2.47}$$

   and advance the fluid system in time from t_n to t_{n+1}
3. Transmission of fluid forces $\vec{f}_F^{n+1}$ to the structural solver. In the case of non-matching grids, interpolation in the form of Equation 2.46 is required to transfer fluid forces to the solid interface.
4. Advance the structural system in time from t_n to t_{n+1} with the interface force $\vec{f}_S^{n+1}$.
5. Continue with next time step.

The proposed staggered solution method has the advantage of straightforward implementation, and its computational efficiency enables realistic engineering applications [18].

Strong Coupling Scheme

Owing to the large deformations, a strong coupling scheme is used for steady-state aeroelastic analysis. The initial state is an undeformed structure on which aerodynamic loads are applied. The numerical solution is implemented by means of a fixed-point iteration, in which the change in the interface variables is considered as the convergence criterion. A schematic workflow is shown in Figure 2.4, and summarizes as:

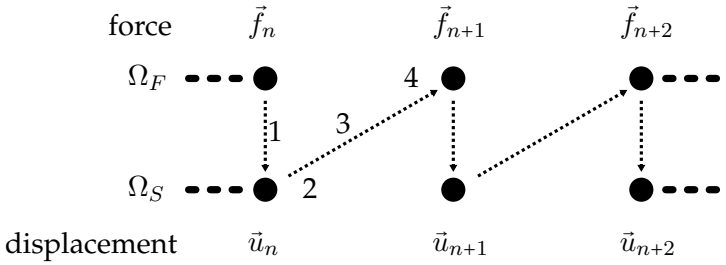

Figure 2.4.: Strong FSI coupling algorithm.

1. Calculate interface fluid force $\vec{f}_F^n$ and transfer the under-relaxed force

$$\vec{f}_S^n = \vec{f}_S^{n-1} + \alpha_f \cdot (\vec{f}_F^n - \vec{f}_F^{n-1}), \tag{2.48}$$

   to the structure solver. In the case of non-matching grids, interpolation in the form of Equation 2.46 is required to transfer fluid forces to the structural interface.

2. Calculate the new interface displacement $\vec{u}_S^n$ on Γ_S

3. Check interface convergence condition, $\vec{f}_F^n - \vec{f}_F^{n-1} < \epsilon_{\vec{f}}$ and $\vec{u}_S^n - \vec{f}_S^{n-1} < \epsilon_{\vec{u}}$. If convergence is fulfilled, stop the coupling process; otherwise proceed to the next step.

4. Transmission of structural displacement $\vec{u}_S^n$, under relaxed to the fluid solver

$$\vec{u}_F^{n+1} = \vec{u}_F^n + \alpha_u \cdot (\vec{u}_F^n - \vec{u}_F^{n-1}). \tag{2.49}$$

   In the case of non-matching grids, interpolation in the form of Equation 2.45 is required to transfer structural displacements to the fluid interface.

5. Interface convergence check. Continue with next iteration step.

The under-relaxation parameters α_f and α_u are typically set within the interval of $[0.5, 0.9]$. In comparison with the staggered algorithm, the interface balance is checked at the coupling iteration end and re-iterated until convergence is achieved.

3 Quantitative Assessment of Passive Gust Load Alleviation

This chapter presents a quantitative assessment of passive gust alleviation. A simplified model of the problem is presented to explain the main aeroelastic characteristics of an elastic swept wing, using a structural system with two degrees of freedom. The aerodynamic loading is obtained by solving the unsteady RANS equation. Loads due to gusts are simulated by employing the Field-Velocity-Approach, as described in subsection 2.2.2. Then, the model is used to investigate the influence of the structural bending and torsional stiffness with respect to a possible aerodynamic load reduction.

Contents

3.1. Aeroelastic Two-Degree-of-Freedom (2-DoF) Model

To investigate the fundamental effects of passive load alleviation and its dependency on the structural stiffness, an infinite wing cross-section, dl, located at 65% of the semi-wing-span, $\frac{b}{2}$, as shown in Figure 3.1a, of a swept wing is considered. The elastic axis is assumed to be a straight line with sweep angle Λ. This model simplification is generally not the case for finite 3D wing structures [83], however, for this study reasonable, as only a single wing segment is considered for the analysis. For the aerodynamic modeling, Nasa's Common Research Model *CRM.65* airfoil is used. The configuration in the structural coordinate system, x-y (green), of the 2-DoF model is shown in Figure 3.1b. The basic concept of the following aeroelastic modeling approach is adapted from Miles [60] and Weisshaar [7].

The motion of the wing section is described by two generalized coordinates: h for plunge and θ for rotational motion. The structural stiffness is considered idealized by two discrete linear springs, K_h

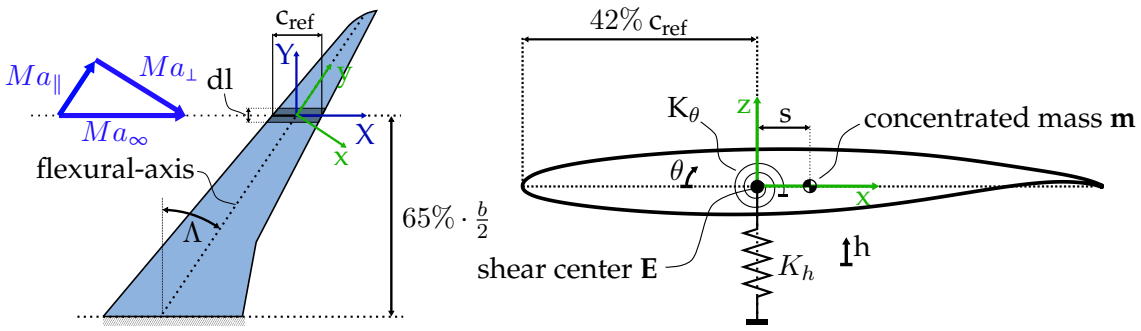

(a) Swept wing geometry.

(b) Wing section 2-DoF structural model.

Figure 3.1.: Schematic representation of the 2-DoF swept wing model.

and K_θ, which are located on the elastic axis, where K_h is the bending stiffness and K_θ is the torsional stiffness of the wing section.

3.1.1. Structural Model Setup

The motion of the wing section is described by the differential equation derived from Lagrange's equation in the discrete form, given by Equation 3.1 [69, p. 166]. In this context, vector $\vec{U}$ represents the structural displacement and matrices $\underline{M}$, $\underline{D}$, and $\underline{K}$ denote the corresponding mass, damping, and stiffness matrix of the system, respectively. Vectors $\ddot{\vec{U}}$ and $\dot{\vec{U}}$ represent the derivatives in time $\vec{U}$. The imposed external forces are described by the aerodynamic load vector, $\vec{f}_{aero}$.

$$\underline{M}\ddot{\vec{U}} + \underline{D}\dot{\vec{U}} + \underline{K}\vec{U} = \vec{f}_{aero} \tag{3.1}$$

Stiffness Matrix Assembly

The structural stiffness is presented by a beam and a torsion element with the arrangement of the nodal degrees of freedom, $\vec{U}^{(e)}_{node-2} = \begin{bmatrix} h & \phi & \theta \end{bmatrix}^T$, as shown in Figure 3.2. The beam-torsion element is considered to be clamped on one side. To obtain a clearer representation, the corresponding element matrices are presented by considering the applied boundary conditions. Including the fixed-support at node-1, the degrees of freedom are correspondingly $\vec{U}^{(e)}_{node-1} \begin{bmatrix} 0.0 & 0.0 & 0.0 \end{bmatrix}^T$.

Based on Hermitian cubic deflections and the local DoFs, arranged as $\vec{U}^{(e)}_{node-2} = \begin{bmatrix} h & \phi \end{bmatrix}^T$, the stiffness for an Euler-Bernoulli beam element is given as

$$\underline{k}_{beam} = K_h \begin{bmatrix} 12.0 & -6.0l \\ -6.0l & 4.0l^2 \end{bmatrix}, \tag{3.2}$$

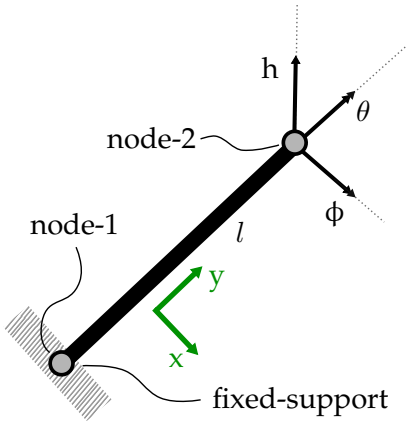

Figure 3.2.: Schematic wing beam model.

with $K_h = \frac{EI}{l^3}$. For the torsional element, a linear shape function is applied. The resulting stiffness matrix, with with $\vec{U}^{(e)}_{node-2} = \begin{bmatrix} \theta \end{bmatrix}$, is given in Equation 3.3 with $K_\theta = \frac{GJ}{l}$. A more detailed discussion can be found in Felippa [19] and Cooper [65].

$$\underline{k}_{torsion} = K_\theta \begin{bmatrix} 1.0 \end{bmatrix} \tag{3.3}$$

The two element stiffness matrices in the structural x-z coordinate system are assembled to express the global stiffness matrix, $\underline{K}$, as follows:

$$\underline{K} = \begin{bmatrix} 12.0 \cdot K_h & -6.0l \cdot K_h & 0 \\ -6.0l \cdot K_h & 4.0l^2 \cdot K_h & 0 \\ 0 & 0 & K_\theta \end{bmatrix}. \tag{3.4}$$

Side Comment: Structural Bending-Torsion Coupling
In this study, no structural coupling between the bending $[h, \phi]$ and torsion $[\theta]$ is considered. In terms of modeling, the entries of the stiffness matrices $K_{1,3}$ and $K_{2,3}$ are zero in the x-y system of the structure. The modeling approach used is selected intentionally to reduce the complexity of the overall system, although in general, most wings exhibit structural couplings. The reasons for this are geometric design anisotropies due to varying stringer distributions, asymmetric wing boxes, or swept wings. The second source is the use of materials with anisotropic properties such as composites [55]. However, despite the simplification due to the wing sweep and the necessary transformation into the aerodynamic coordinate system, fully populated system matrices occur (see subsection 3.1.3).

Mass Matrix Assembly

The mass of the wing section is considered as a discrete structural mass, represented by m and its inertia I_y. As shown in [3] the bar element mass matrix with the DoFs, $\vec{U}^{(e)}_{node-2} = \begin{bmatrix} h & \phi \end{bmatrix}^T$, is given as

$$\underline{m}_{beam} = \frac{m^{(e)}}{420} \begin{bmatrix} 156 & -22l \\ -22l & 4l^2 \end{bmatrix}. \tag{3.5}$$

The element mass, $m^{(e)}$, is specified so that the translational mass of the degree of freedom, h, is equal to the point mass, m. Thus, $m^{(e)} = \frac{420}{156} \cdot m$. The offset distance from m to the shear center, E, is s, which results in an additional inertia coupling between displacement h and wing twist θ. The discrete mass is included as a lumped mass representation, where the arrangement is $\vec{U}^{(e)}_{node-2} = \begin{bmatrix} h & \theta \end{bmatrix}$. The mass matrix can be expressed as

$$\underline{m}_{lumped} = \begin{bmatrix} m & m \cdot s \cdot cos(\theta) \\ m \cdot s \cdot cos(\theta) & I_E \end{bmatrix}, \tag{3.6}$$

with $I_E = I_{y,m} + m \cdot s^2$. The two element mass matrices are combined to obtain the global system mass matrix as

$$\underline{M} = \begin{bmatrix} m & -\frac{11}{78}l \cdot m & m \cdot s \cdot cos(\theta) \\ -\frac{11}{78}l \cdot m & \frac{1}{39}l^2 \cdot m & 0 \\ m \cdot s \cdot cos(\theta) & 0 & I_E \end{bmatrix}. \tag{3.7}$$

The two remaining mass parameters, m and I_G, with $I_E = I_G - m \cdot s^2$, are specified such that for a given stiffness, the bending and torsional natural frequencies meet specified reference values.

3.1.2. Computational Aerodynamic Model Setup

The flow is described and the occurring aerodynamic forces, $\vec{f}^{XYZ}_{aero}$, are calculated by solving the steady and unsteady RANS equations. The applied forces in the aerodynamic X-Z system are given by Equation 3.8, where L is the lift force and M_{aero} is the pitch moment in reference to the shear center, **E**.

$$\vec{f}^{XYZ}_{aero} = \begin{Bmatrix} 0 & 0 & L & 0 & M_{aero} & 0 \end{Bmatrix}^T \tag{3.8}$$

To consider the effects caused by wing sweep Λ, the infinite swept wing theory, proposed by Busemann, with a constant airfoil section is used. Further, the flow is assumed to be frictionless in the span-wise direction, and thus, span-wise flow boundary layer effects are neglected. The wing segment can be characterized as a swept oblique wing with infinite span. As described by Busemann, only the speed component perpendicular to the leading edge contributes to the lift [67], resulting in a difference between the profile parallel to the airflow and that normal to the leading edge of the wing, which is mainly responsible for the lift. As depicted in the velocity diagram of Figure 3.1a, the effective normal wing-section velocity depends on wing sweep Λ, such that $U_\perp = cos(\Lambda) \cdot U_\infty$ applies. The effective Mach number, $Ma_{eff.}$, at the wing section is given as

$$Ma_{eff.} = cos(\Lambda) \cdot Ma_\infty. \tag{3.9}$$

If the wing has a global AoA of α, the relationship between free flow V_∞ and vertical flow V_z applies to $tan(\alpha) = \frac{V_z}{V_\infty}$. Based on Equation 3.9 for the swept wing, the effective AoA is given as

$$tan(\alpha_{eff.}) = \frac{V_z}{V_\perp} = \frac{tan(\alpha)}{cos(\Lambda)}. \tag{3.10}$$

Computational Domain and Boundary Conditions

The flow around the wing normal cross-section is described by the RANS equations, which are solved using the finite volume based solver *TAU*. A cylindrical domain with a diameter of $\emptyset \approx 38 \cdot c_{ref}$ discretized with an unstructured hex cell mesh, as shown in Figure 3.3, is used as computational domain. The outer boundary is treated as farfield boundary condition and the airfoil as viscose wall. The flow is considered to be two-dimensional. Therefore, a spatial discretisation of one cell is used in the y-direction, and symmetry conditions are defined on both sides. The effect of the boundary layer is directly resolved by applying sufficient discretization. For this purpose, the grid density at the wall is increased, and the first cell height adjusted to achieve reasonable $y+ \approx 1.0$ values. The 1-equation model by Spalart-Allmaras [85] is used as turbulence model. To ensure independence from the grid resolution, a grid sensitivity study is conducted, whose results are described in the appendix A.1.

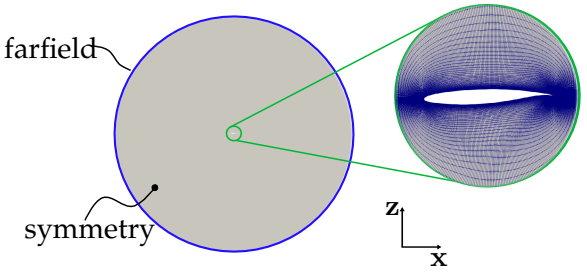

Figure 3.3.: Fluid-domain and mesh topology.

For this study, two flow cases within the flight envelope are covered. The first represents the *cruise-flight* condition at flight level $FL = 350$ with a free stream Mach number of $Ma_\infty = 0.86$, whereas the second condition represents an aircraft *approach-flight* with a free stream Mach number of $Ma_\infty = 0.5$ at mean sea level. The reduced free stream Mach numbers are calculated according to Equation 3.9, considering the 3-dimensional sweep effect in the 2-dimensional flow domain. The reduced Mach numbers in *cruise-* and *approach-flight* scenario are $Ma_\perp = 0.745$ and $Ma_\perp = 0.433$, respectively. The pressure contour plot and the C_P distribution along the wing section for trimmed flight at *cruise* and *approach* are shown in Figure 3.4 and Figure 3.5, respectively. The *cruise* flight represents a transonic flow condition, in which subsonic and supersonic flows occur, including a compression shock. A summary for the computational aerodynamic setup is given in Table 3.1.

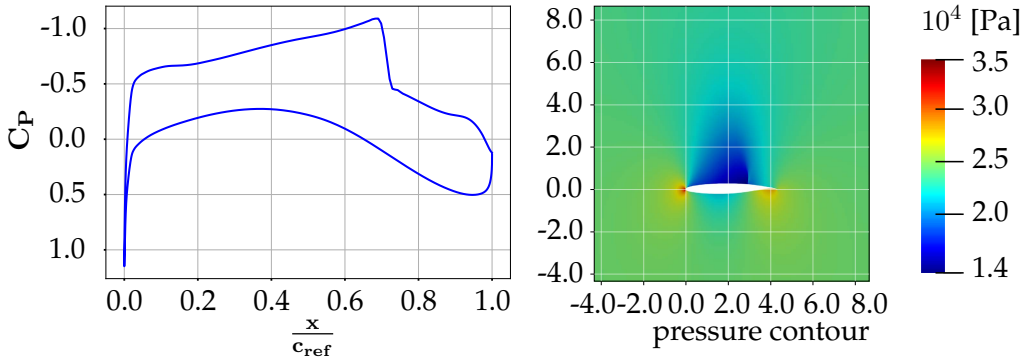

Figure 3.4.: Airfoil pressure distribution at cruise flight.

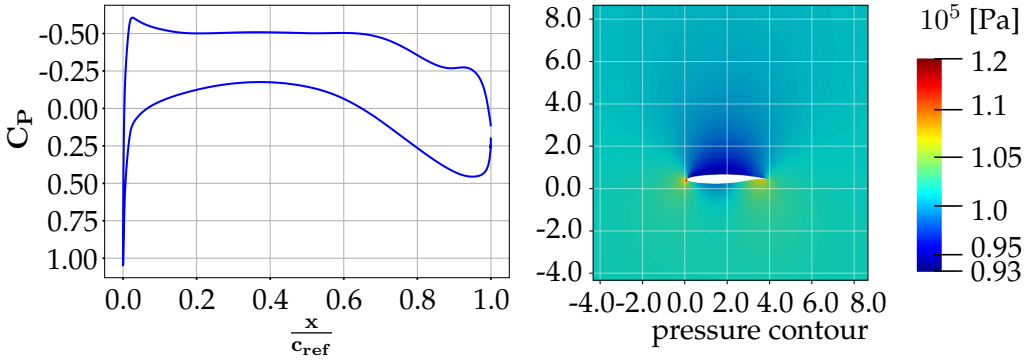

Figure 3.5.: Airfoil pressure distribution at approach flight.

Table 3.1.: Summary computational aerodynamic model setup.

			cruise :	**approach** :
c_{ref}	4.325 m	Ma_∞	0.86	0.5
S_{ref}	$4.325\,\mathrm{m}^2$	$Ma_\perp$	0.745	0.433
domain size Ø	$38 \cdot c_{ref}$	FL	350	0
cell count	97486	ρ_∞	$0.380\,45\,\mathrm{kg\,m^{-3}}$	$1.225\,\mathrm{kg\,m^{-3}}$
$y+_{cruise}$	0.688	T_∞	218.92 K	288.15 K
$y+_{approach}$	1.238	C_l	0.3537	0.2450
		AoA	0.0 deg	−0.148 deg

3.1.3. Aeroelastic Model Setup

The aerodynamic and structural models are combined to develop an aeroelastic model, which is then solved in the time domain. Attention should be paid to the different coordinate systems in which the conservation equations of the structure and aerodynamic model are formulated. The resulting displacements are transferred from the x-z system to the aerodynamic X-Z coordinates by means of the coordinate transformation, given as

$$\tilde{\vec{U}}^{XZ}_{aero} = \begin{bmatrix} 1 & 0 & 0 \\ 0 & cos(\Lambda) & sin(\Lambda) \\ 0 & -sin(\Lambda) & cos(\Lambda) \end{bmatrix} \begin{Bmatrix} h + h_{jig} \\ \phi \\ \theta + \theta_{jig} \end{Bmatrix}_{xz} , \tag{3.11}$$

where h_{jig} and θ_{jig} are the initial deformation in jig-shape, that is, the stress-free initial state in reference to the x-z system. As the rotation ϕ is not represented in the aerodynamic model (pure 2-d

analysis, $\phi_{aero} = 0.0$), the displacement vector of the wing section in the aerodynamic system is given as

$$\vec{U}_{aero}^{XZ} = \begin{Bmatrix} h \\ \theta \end{Bmatrix}_{XZ} = \begin{bmatrix} 1 & 0 & 0 \\ 0 & 0 & 1 \end{bmatrix} \vec{\tilde{U}}_{aero}^{XZ} = \begin{Bmatrix} h + h_{jig} \\ cos(\Lambda) \cdot (\theta_{jig} + \theta) - sin(\Lambda) \cdot \phi \end{Bmatrix}. \tag{3.12}$$

Elastic twist θ has the same effect on the aerodynamics as a local change in α. Therefore, θ must be corrected according to the infinite swept wing theory, as described in the previous chapter. If α is assumed to be small, the small-angle approximation can be applied so that $tan(\alpha) \approx \alpha$ and Equation 3.10 can be simplified to

$$\alpha_{eff.} \approx \frac{V_z}{V_\perp} \approx \frac{\alpha}{cos(\Lambda)}. \tag{3.13}$$

The translational degree of freedom h remains unaffected by the twist correction in Equation 3.13. The effective displacement vector is the superposition of the elastic deformation and the global AoA. If no external wind is considered, the effective displacement vector is expressed as

$$\vec{U}_{aero,eff}^{XZ} = \begin{Bmatrix} h + h_{jig} \\ \frac{\alpha_{global}}{cos(\Lambda)} + (\theta_{jig} + \theta) - tan(\Lambda) \cdot \phi. \end{Bmatrix} \tag{3.14}$$

Accordingly, the aerodynamic forces must be transformed from the X-Z to the structural x-z coordinate system. The structural force vector is given in Equation 3.15. With the three components, namely, lift force L, bending moment M, and torsional moment T, vector $\vec{f}_{aero}$ is defined as

$$\vec{f}_{aero} = \begin{Bmatrix} L \\ M \\ T \end{Bmatrix}_{xz} = \begin{Bmatrix} L \\ M_{aero} \cdot sin(\Lambda) \\ M_{aero} \cdot cos(\Lambda) \end{Bmatrix}. \tag{3.15}$$

To provide a better understanding of the entire aeroelastic model, a schematic chart of the model is presented in Figure 3.6 along with the corresponding transformations.

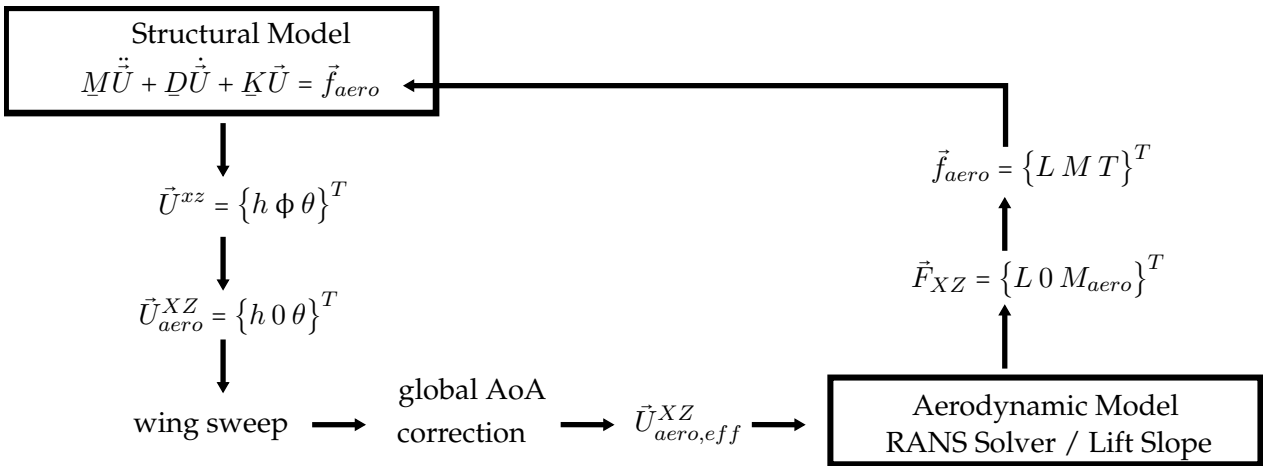

Figure 3.6.: Schematic representation of the aeroelastic model setup.

Aircraft Trim Setup

In this study, a constant lift is assumed for *cruise-* and *approach-flight*. In case of changing flow conditions, α_{global} in Equation 3.14 must be adjusted accordingly. As the aeroelastic system shown in Figure 3.6 has geometrical non-linearities, the static system is solved numerically by means of a minimization problem of the form:

$$min\{\left|\vec{f}_{intern}(h,\varphi,\theta) - \vec{f}_{extern}(h,\varphi,\theta,\alpha_{global})\right|\} \tag{3.16}$$

$$\text{with:} \quad L_{approach} = L_{cruise}$$

When simplifying the aeroelastic model to a 2-DoF system, it must be considered that the two degrees of freedom h and ϕ are merged. With the same total lift (*approach-*, *cruise-flight*), different displacement results occur with the same trim conditions, resulting from different aerodynamic pitch moments.

Interface Coupling Setup

To deflect the wing cross-section in the CFD model, the movement of the shear centre $\mathbf{E}$ must be transferred to the wetted nodes through a kinematic correlation. The same applies for the inverse transfer from fluid to structural forces. As the wing shape remains constant, the resulting lift force and pitch moment can be transferred directly to the shear center $\mathbf{E}$ by integration over the wing surface. For the discrete model, this leads to the following summation

$$L = \sum_i F_{i,z} \qquad M_{aero} = \sum_i (x_i - \mathbf{E_x}) \cdot F_{i,z} - (z_i - \mathbf{E_z}) \cdot F_{i,x}. \tag{3.17}$$

with:	i	interface node index
	$F_{i,x}, F_{i,z}$	x, z-component of i^{th} node force
	x_i, z_i	x, z-coordinate of i^{th} interface node
	$\mathbf{E}_x, \mathbf{E}_z$	x, z-coordinate of shear center $\mathbf{E}$

The displacement of the CFD grid nodes is calculated by the kinematic rigid body motion, given by Equation 3.18, where X_i, Z_i are the reference coordinates at the beginning of the simulation at time $t = 0$. Coordinates x_i, z_i are the coordinates for the current configuration at time $t = t_i$.

$$\begin{Bmatrix} x_i \\ z_i \end{Bmatrix}_{XZ} = \begin{bmatrix} cos(\theta) & sin(\theta) \\ -sin(\theta) & cos(\theta) \end{bmatrix} \begin{Bmatrix} X_i - \mathbf{E}_x \\ Z_i - \mathbf{E}_z \end{Bmatrix} + \begin{Bmatrix} \mathbf{E}_x \\ \mathbf{E}_z + h \end{Bmatrix} \tag{3.18}$$

with:	i	interface node index
	X_i, Z_i	reference ($t = 0$) x, z-component of i^{th} node
	x_i, z_i	x, z-coordinate of i^{th} interface node
	$\mathbf{E}_x, \mathbf{E}_z$	x, z-coordinate of shear center $\mathbf{E}$
	h, θ	structrual displacment, rotation in the XZ-System

Side Comment: Aerodynamic Washout Illustration

After the aeroelastic system is discussed, the term washout will be explained in more detail. Figure 3.7 shows the pure kinematic correlation obtained from Equation 3.14. The aerofoil translation and rotation at different displacements h are illustrated in blue. For reference purposes, the non-rotated profile indicating pure translation h is additionally plotted in gray. It can be noted that with increasing h, the leading edge of the aerofoil moves downward, which means that the local angle of attack is reduced. This effect depends directly on $\frac{dh}{dx} = \phi$, which can by obtained using Equation 3.4. Assuming that there is no applied bending moment, and $\tilde{h}$ is defined as the kinematic boundary condition, the correlation $\phi = -\frac{K_{21}}{K_{22}} \cdot \tilde{h}$ follows. The elastic twist is set to $\theta = 0$. In this example, the wing displacement is that of a backward-swept wing. For a forward-swept wing, the effect reverses such that with increasing h, the leading edge turns upward and the local angle of attack is increased.

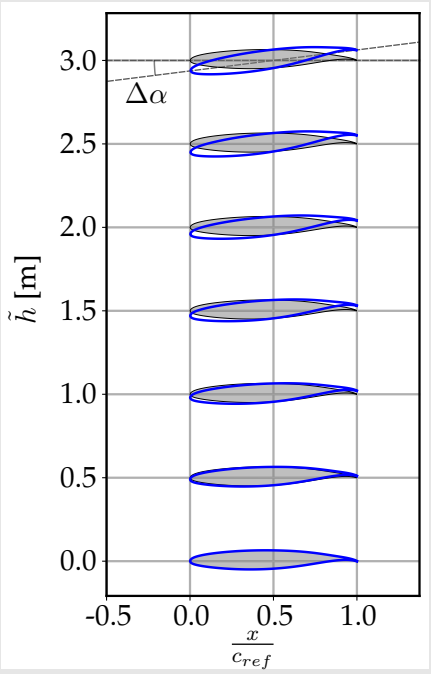

Figure 3.7.: Aerofoil kinematic washout illustration.

3.2. Effects of Structural Stiffness on Steady Load Alleviation

In the following chapter, the investigation of the basic aeroelastic behavior by means of the steady-state/static loading of the wing section is presented. The initial reference configuration is defined by specifying the undefined structural and geometric parameters. After the essential aeroelastic behavior is analyzed, the effect of increasing and decreasing the structural stiffness under a static loading is investigated.

3.2.1. Aeroelastic Response of the Initial Configuration

To reduce the computational effort, the C_l-α and C_m-α slopes are calculated for *cruise-* and *approach-flight*, which are plotted in Figure 3.8. The support points are calculated at intervals of $\Delta\alpha = 0.25\,\mathrm{deg}$ and stored in the aerodynamic model as a lookup table. All further values for α are interpolated linearly between the support points.

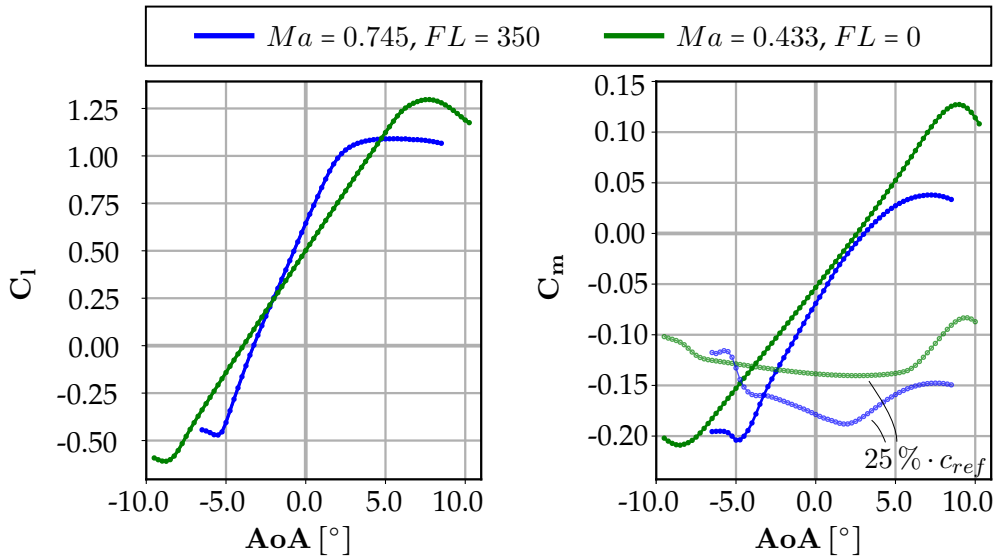

Figure 3.8.: C_l and C_m slope with respect to the shear centre **E** and $25\,\% \cdot c_{ref}$ line as reference, for cruise and approach flight condition.

Initial Configuration Setup

To specify the stiffness matrix and kinematic coupling, the geometrical parameters element length l and wing sweep Λ must be specified. Both are determined generically on the basis of common wing layouts. The sweep and length of the flexural-axis is set to $30\,\mathrm{m}$ and $30\,\mathrm{deg}$, respectively, which corresponds to $65\% \cdot \frac{b}{2}$ half span position of $15\,\mathrm{m}$.

The flight shape for the present investigations is fixed at a deflection of $0.8\,\mathrm{m}$ and an effective AoA of $\alpha_{eff} = -1.5\,\mathrm{deg}$. Furthermore, the stiffness of the jig-shape displacement h_0 and the torsional stiffness K_θ of the structural model are pre-assigned. The two remaining parameters, bending stiffness K_h and the jig-hape incidence θ_0, are determined in a way that the given boundary conditions are fulfilled under aerodynamic loading. A summary of the initial structural configuration is given in the following Table 3.2.

Table 3.2.: Summary of the initial structural model.

predefined (independent parameters)							calculated		
$\mathbf{\Lambda}$	**l**	**AoA**	$\boldsymbol{\alpha_{eff}}$	$\mathbf{h_0}$	$\mathbf{\Delta h}$	$\mathbf{K_\theta}$	$\mathbf{K_h}$	$\boldsymbol{\theta_0}$	$\boldsymbol{\Delta\theta}$
$30\,\mathrm{deg}$	$30\,\mathrm{m}$	$0.0\,\mathrm{deg}$	$-1.5\,\mathrm{deg}$	$0.0\,\mathrm{m}$	$0.8\,\mathrm{m}$	$600.0\,\frac{\mathrm{kN\,m}}{\mathrm{rad}}$	$5.671\,\frac{\mathrm{kN}}{\mathrm{m}}$	$1.375\,\mathrm{deg}$	$-1.567\,\mathrm{deg}$

Aeroelastic Analysis

The system response for *cruise-* and *approach-flight* for different global AoA is shown in Figure 3.9. Here, the blue and green graphs represent displacement h and the effective AoA α_{eff} in dependency of the global AoA, respectively. As the lift is directly related to α_{eff}, the latter is used as an evaluation criterion. In addition to the response of the elastic wing section, that of a rigid aerofoil is plotted in black as reference. In the *approach-flight* case, the requirement for the same flight shape can no longer be satisfied as it inevitably leads to different structural stiffnesses, and the corresponding configurations no longer have a common reference. Instead, the structural model from the *cruise-flight* configuration is used for the *approach-flight* scenario, and a flight condition with same constant lift as in *cruise-flight* is requested. As the flight condition changes, an adjustment of the global AoA is necessary. For the initial configuration, the corresponding stationary flight design points are marked at the corresponding global AoA of $\alpha = 0.0\,\mathrm{deg}$ for *cruise-flight* and $\alpha = -0.148\,\mathrm{deg}$ for *approach-flight*. The associated jig-shape parameters are indicated by h_0 and θ_0.

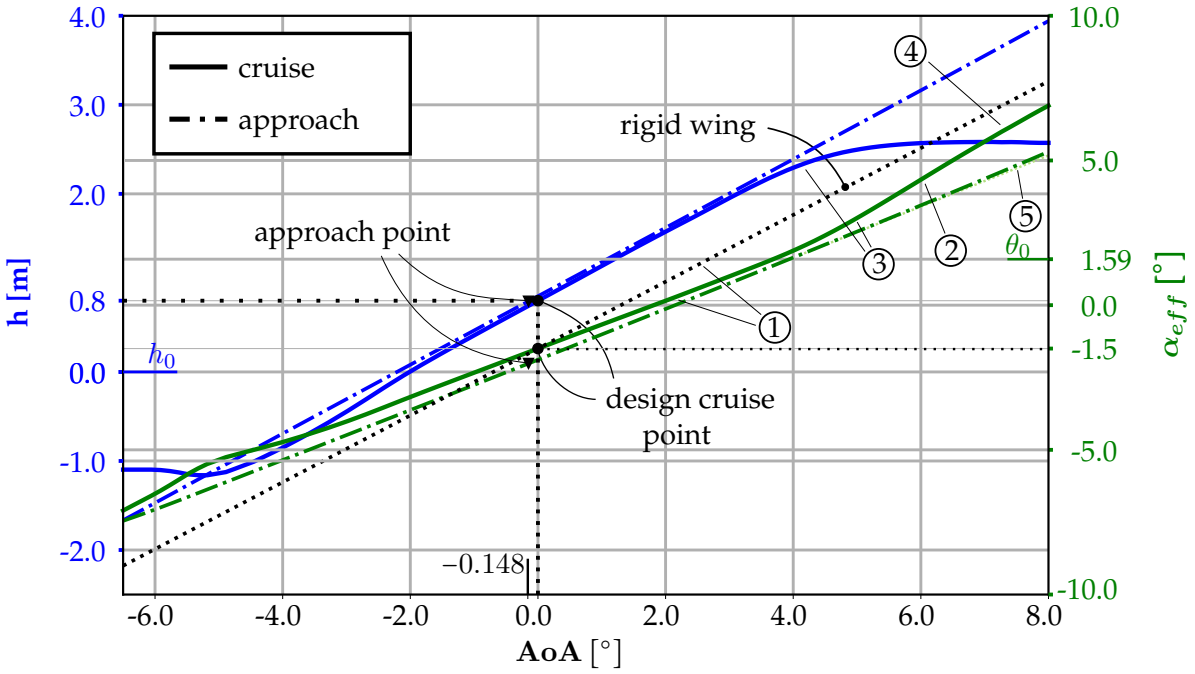

Figure 3.9.: Aeroelastic response due to different global AoA for cruise- (solid line) and approach-flight (dashed line) condition, blue: bending deflection h, green: torsional deflection, α_{eff}, black: rigid body for reference.

The assessment of the results gives the following listed observations:

1. For both *cruise-* and *approach-flight*, the effective α_{eff} gradient is lower than that for the rigid case. The increase in α_{eff} due to an increase in global AoA, caused by factors such as vertical gusts, therefore decreases.

2. In the *cruise* flight conditions, the gradient starts to increase at a global AoA of $\approx 4.5\,\mathrm{deg}$ and degrades compared to the rigid-body wing. At the same time, the maximum lift $C_{l,max}$, as shown in Figure 3.8, is achieved for *cruise*.

3. As the lift cannot be increased any further, the bending of the wing and the corresponding washout resulting from the bending kinematic are stopped.

4. Additionally, as the global AoA continues to increase, the pitch moment increases and reverses its effect (refer to Figure 3.8), causing the wing to turn further up, which explains the increased gradient of the effective α_{eff}.

5. For the *approach-flight* case, higher $C_{l,max}$ values can be achieved. This also results in a considerably improved washout. At around $6.5\,\mathrm{deg}$, an increase in the effective α_{eff} gradient can likewise be observed in this case.

3.2.2. Dependency of Bending and Torsional Wing Stiffness

Based on the previous results, the influence of wing bending stiffness K_h and torsional stiffness K_θ on the deformation behavior is analyzed separately. The initial configuration is used as the starting design and its stiffnesses are increased and decreased by $25\,\%$, respectively. To observe the influence of the individual DoF, the limiting case of infinite stiffness, hence rigid, is additionally considered. To achieve the same flight shape in the *cruise* flight condition, the jig-shape parameters h_{jig} and θ_{jig} are adjusted accordingly when the stiffness is changed. Furthermore, different stiffness values result in different trim conditions, which can be found in detail for all cases in appendix A.2.

Torsional Stiffness Variation

Figure 3.10 shows the result of varying torsional stiffnesses, K_θ, with a constant bending stiffness, $K_{h,ref}$, in *cruise-flight* condition under different AoA. The effective AoA α_{eff} is again used to evaluate the load reduction characteristics.

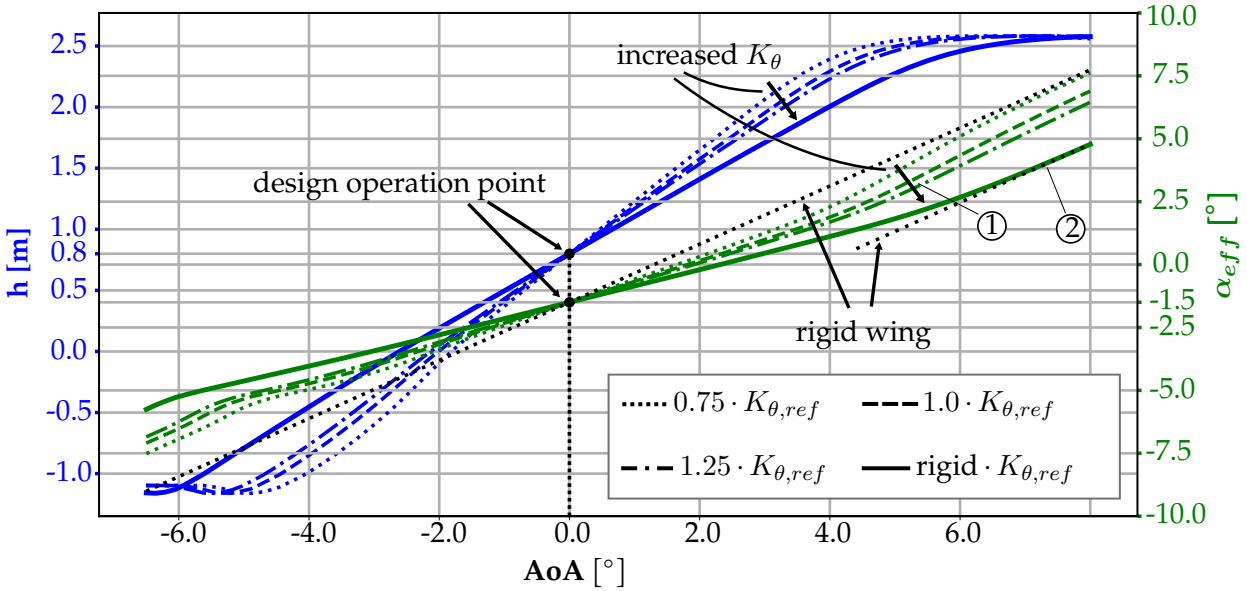

Figure 3.10.: Aeroelastic response at cruise-flight for different torsional stiffnesses K_θ, with constant bending stiffness K_h, blue: bending deflection h, green: torsional deflection, α_{eff}, black: rigid body for reference.

The following observations can be derived from the analysis:

1. The increased torsional stiffness gives an improved possibilities for load reduction by reducing the steepness of α_{eff}. The highest load reduction is achieved for infinite torsional stiffness, that is, rigidity in rotation. Therefore, the remaining load reduction at $K_{\theta,\infty}$ is caused by the washout due to wing bending.

2. As in the initial study, when $C_{L,max}$ is reached, the deflection stops at a global AoA of ≈6.0 deg ($\alpha_{eff} \approx 2.5\,\text{deg}$) and the elastic wing section shows no difference from a rigid wing.

The results for the *approach-flight* case are shown in Figure 3.11. The essential characteristics as identified for the *cruise-flight* study are likewise reflected in the *approach-flight* study. The most significant difference observed are:

1. During *cruise-flight*, the total lift is approximately constant when $C_{L,max}$ is reached, whereas it decreases at low air speeds owing to flow separation. Therefore the wing shows a difference in the stall behavior. This is reflected in the structural displacement response of h.

2. As in the case of the *cruise-flight*, the gradient in the effective α_{eff} increases when the maximum deflection is achieved. Similar the load reduction decreases.

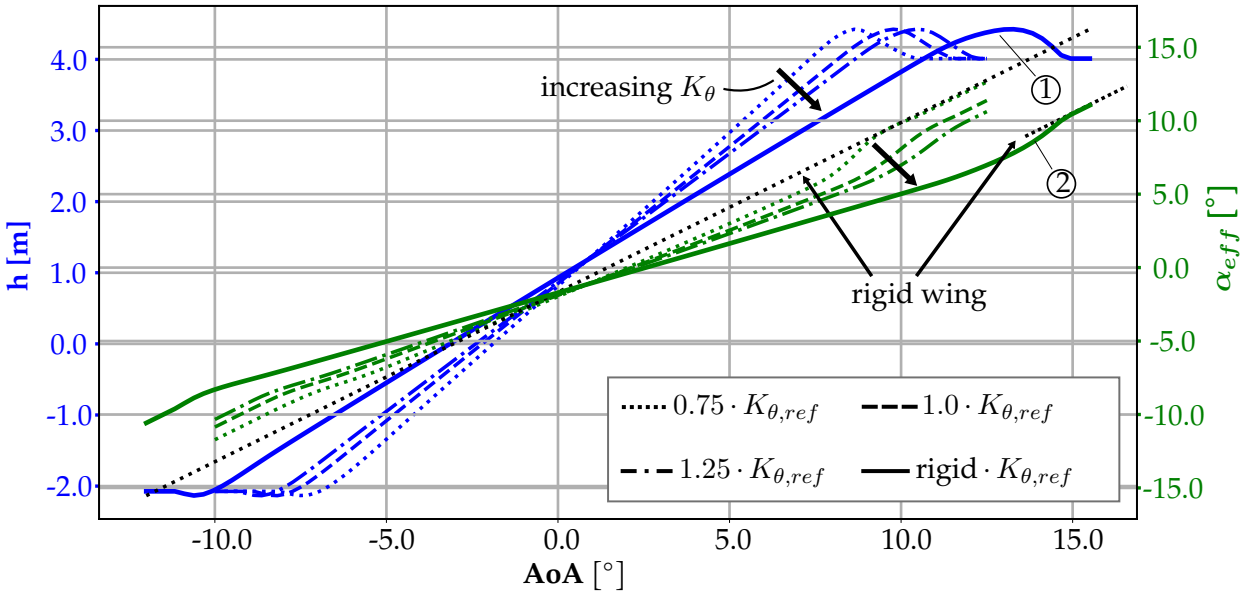

Figure 3.11.: Aeroelastic response at approach for different torsional stiffnesses K_θ, with constant bending stiffness K_h, blue: bending deflection h, green: torsional deflection, α_{eff}, black: rigid body for reference.

Bending Stiffness Variation

Figure 3.12 shows the results of varying bending stiffness K_h and constant torsional stiffness K_θ for *cruise-flight*.

1. The elastic wing section provides a higher load reduction at reduced bending stiffness K_h.

2. This is consistent with Equation 3.14, because ϕ increases as K_h decreases, and hence, α_{eff} decreases. If K_h is assumed to be rigid, the influence on α_{eff} is considerably worse compared with the rigid wing segment. As discussed in the torsional stiffness study, this is due to the vanishing bending deformation (h = 0) and pitch moment pre-loading.

3. After achieving the maximum lift $C_{L,max}$, the bending deflection h stops and the load reduction potential decreases.

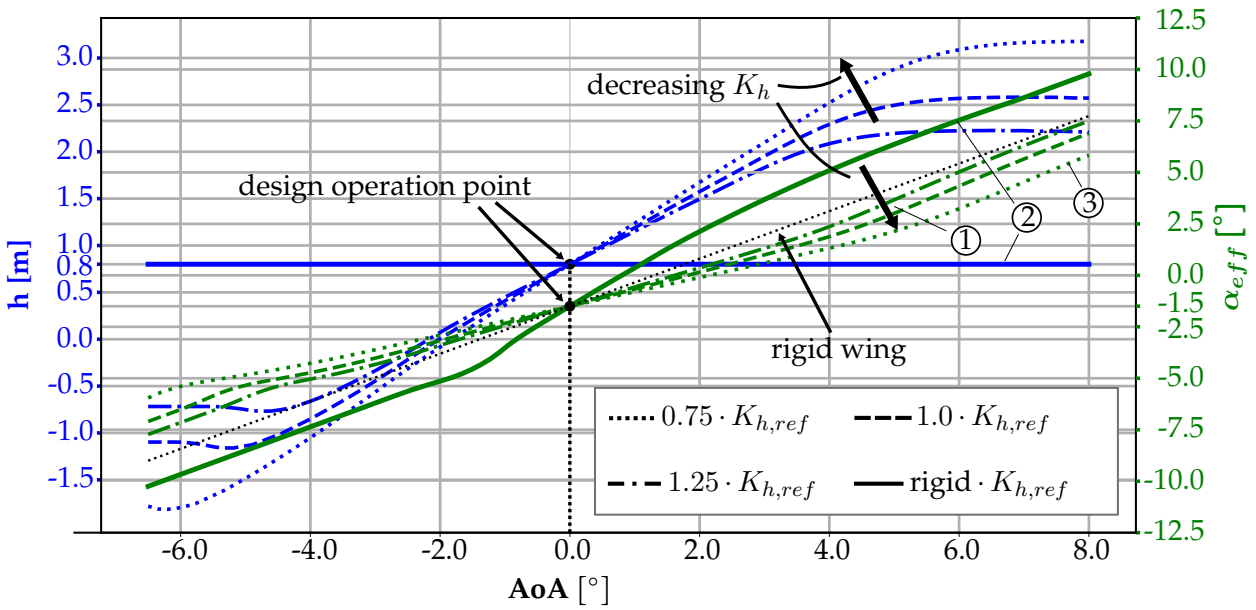

Figure 3.12.: Aeroelastic response due to different bending stiffnesses K_h at cruise, blue: bending deflection h, green: torsional deflection, α_{eff}, black: rigid body for reference.

The same can be observed for the *approach-flight* case, as depicted in Figure 3.13. Generally, the same behavior can be observed, that is:

1. A more bending flexible wing section has the higher load reduction potential.
2. Likewise, when the maximum lift is achieved the reduction potential is reduced.
3. In case of rigid bending stiffness, no washout effect can be achieved and the wing section shows the worst load reduction potential. This is in turn due to the pitch moment, which causes the wing leading edge to twist up.

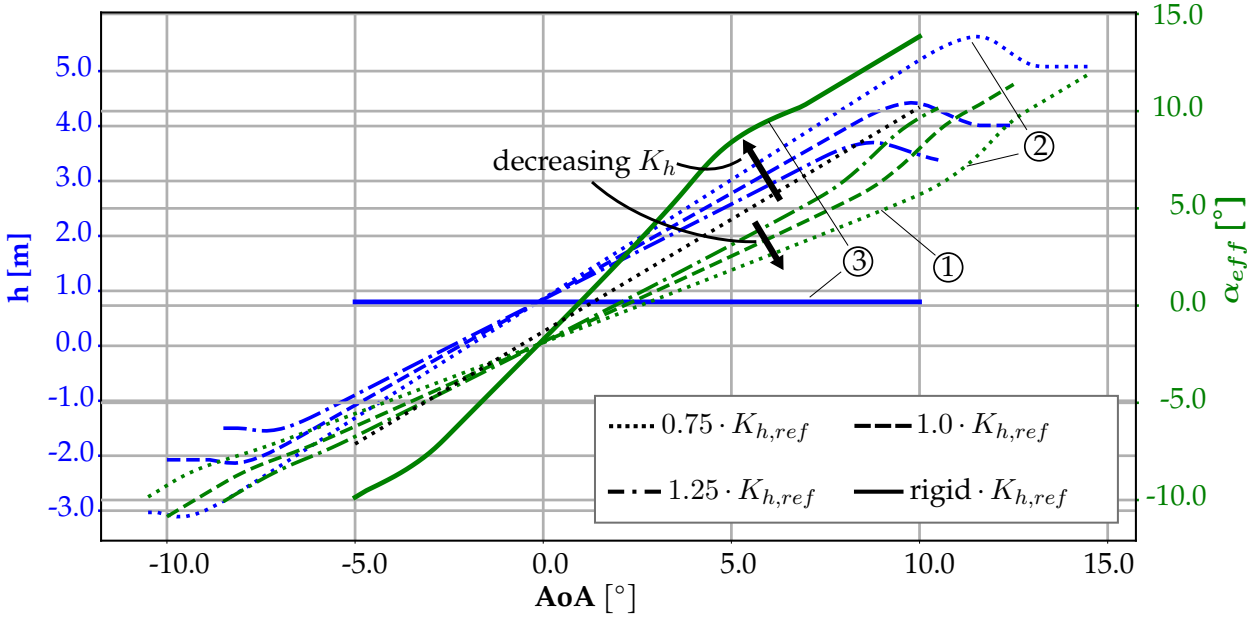

Figure 3.13.: Aeroelastic response due to different bending stiffnesses K_h at approach-flight, blue: bending deflection h, green: torsional deflection, α_{eff}, black: rigid body for reference.

Direct Comparison

To obtain a direct comparison between bending and torsional stiffness, α_{eff} for varying AoA is compared for the *cruise-flight* case, as shown in Figure 3.14. The initial configuration, highlighted in yellow, is used as a reference. The case with rigid torsional stiffness shows the strongest influence on α_{eff}, closely followed by a wing with low bending stiffness.

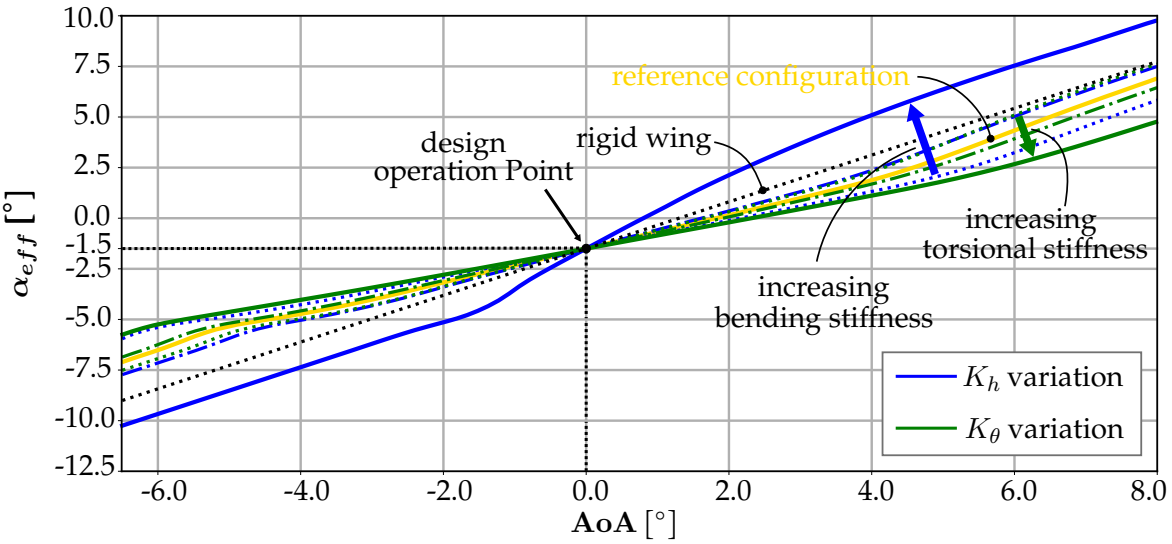

Figure 3.14.: Stiffness influence on α_{eff} for different K_h and K_θ in cruise flight.

Due to the linearity around the design point, the load reduction potential is evaluated in the form of the gradient $\Gamma = \frac{\partial \alpha_{eff}}{\partial AoA}$. Therefore, Γ describes the extent to which a change in the global AoA is reflected in the effective α_{eff}, which includes both, the effects of sweep and the elastic deformation. The results of all configurations around the respective trim point for *cruise-flight* and *approach-flight* with the variations in K_h and K_θ are shown in Figure 3.15. From the results, it can be concluded that a moderately better reduction can be achieved for the *approach-flight* condition.

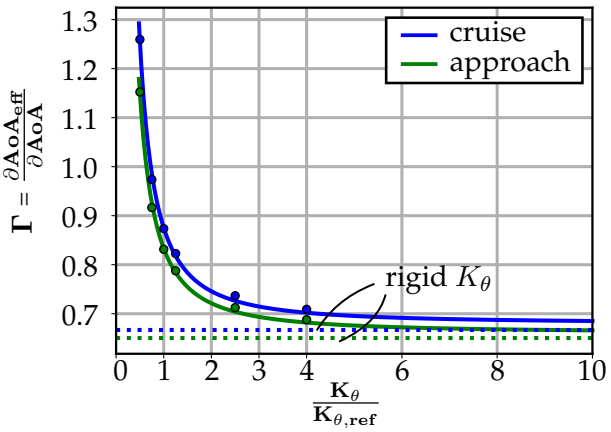

(a) Stiffness influence of K_θ.

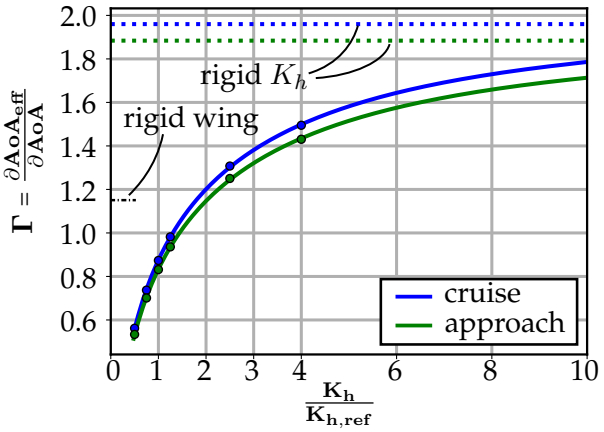

(b) Stiffness influence of K_h.

Figure 3.15.: Γ for different K_θ and K_h at cruise and approach flight, including approximation of the form $a \cdot e^{-b \cdot x^c} + d$.

The influence of the simultaneous change of both stiffnesses K_θ and K_h in *cruise-flight* scenario is shown in Figure 3.16. Around the reference position, changes two lower bending stiffness result in considerable load reduction potential. In this stiffness ratio range, the bending stiffness K_h dominates over the torsional stiffness K_θ. With increasing bending stiffness, improvements can be achieved by increasing the torsional stiffness. The limit case of being rigid in bending is shown as asymptotes of the interpolation, indicated by dashed lines.

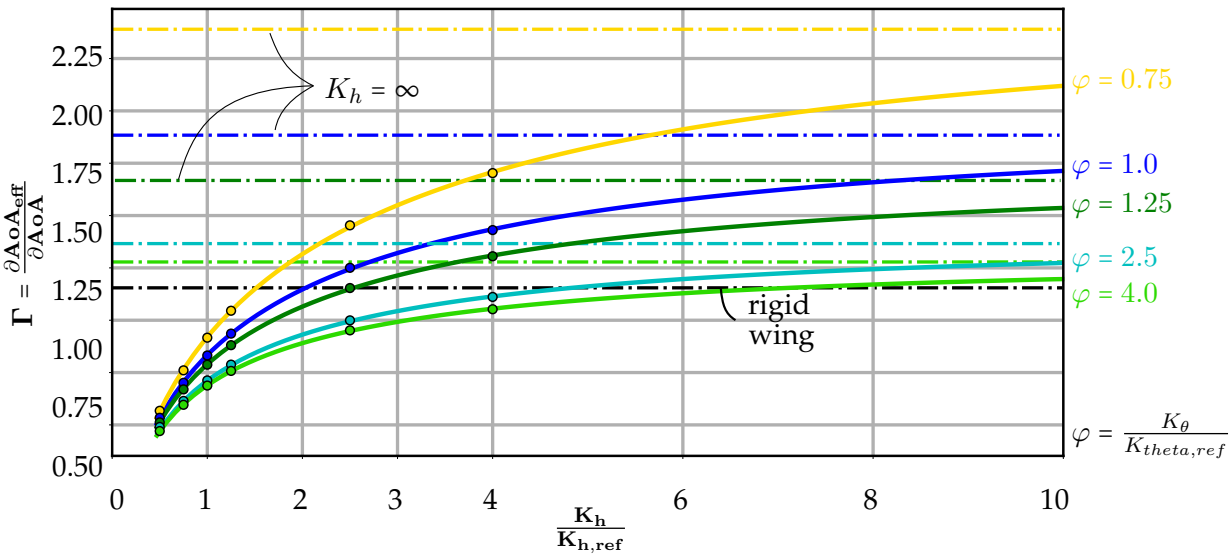

Figure 3.16.: Stiffness comparison between K_h and K_θ in cruise flight.

Interim conclusion

Based on the results of the static analysis, it can be found that a swept wing that is more torsionally stiff but flexible in bending has a positive effect on load reduction. In general, the amount of local α_{eff} reduction by bending has a stronger influence than that resulting from torsional stiffness. The load reduction is dominated by the kinematic coupling, especially by the bending component in combination with the wing sweep.

Side Discussion: Sweep Influence - Natural Laminar Flow

Natural laminar flow is being pursued and researched in numerous studies for further reduction of drag (see Chambell [87]). One reason for the current limits is that modern transport aircraft wings are swept to allow for higher *cruise* speeds. The sweep has a negative effect as the boundary layer near the leading edge increases by the cross flow to an extent that laminarity cannot be maintained. For this reason, research is being carried out, especially in this context, to design wings with less sweep. As shown in the previous examples, load reduction is mainly enabled by the kinematic coupling resulting from the sweep. Therefore, the question arises to what extent a reduction in wing sweep influences the kinematic coupling. The following diagram shows the influence of varying sweep Λ and variable bending stiffness K_h at constant $K_{\theta,ref}$ = 1.0 with same flight shape on Γ. It can be observed that Γ increases accordingly with decreasing Λ. With small sweep angles, values below $\Gamma_{rigid} = \frac{1.0}{cos(\Lambda)}$ can only be achieved using low bending stiffness configurations. Furthermore, it can be noted that with increasing sweep Λ the local torsional load increases and the wing twist accordingly. This effect is noticeable in configurations with high bending stiffness ratios, where torsional stiffness dominates the result.

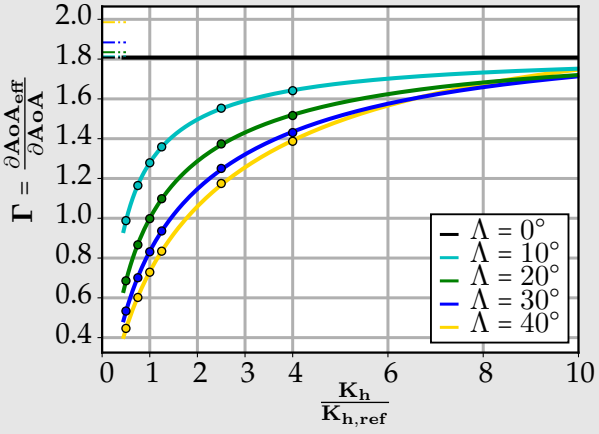

3.3. Effects of the Structural Stiffness on the Gust Load Alleviation

In the previous section 3.2, the basic displacement response of the elastic mounted aerofoil with different stiffness values is characterized under the assumption of a steady equilibrium state. To investigate the influence of gusts, a computational study with fully resolved transient simulations is performed next. The dynamic equations of motion of the elastic wing profile are solved using the Newmark-β time integration method (see subsection 2.1.5). The analysis scenario is the aeroelastic response of a discrete 1-cos gust, as described in the CS-25.341 [29] or FAA-25.341-1 [44] certification regulations. The vertical gust speed field $V(x)$ is

$$\begin{aligned} V(x) &= \tfrac{V_v}{2}[1 - cos(\tfrac{\pi \cdot x}{h})] \qquad 0 \le x \le 2h \\ V(x) &= 0 \qquad\qquad\qquad\qquad\quad x > 2h \end{aligned} \tag{3.19}$$

with:
- V_v design gust velocity
- h gust gradient, distance to reach V_v peak velocity
- H gust length $(2 \cdot h)$
- x position

For the transient simulation, different gust scenarios are defined, as summarized in Table 3.3. The gust load cases Gust-A for *cruise-flight* and Gust-B for *approach-flight* are assumed to be the design load cases for general gust response studies. The gust scenarios Gust-C to Gust-E describe the load cases with increased design gust velocity. These gust scenarios are considered for investigations close to the limit of the maximum aerodynamic lift $C_{l,max}$.

Table 3.3.: 1-cos gust load scenarios.

	Design Gust Velocity		**Increased Gust Velocity Cases**		
	V_v Gust-A cruise	**V_v Gust-B** approach	**V_v Gust-C** cruise/approach	**V_v Gust-D** cruise	**V_v Gust-E** approach
case-1: $H = 18.29\,\mathrm{m}$	$11.24\,\frac{\mathrm{m}}{\mathrm{s}}$	$8.82\,\frac{\mathrm{m}}{\mathrm{s}}$	$15.17\,\frac{\mathrm{m}}{\mathrm{s}}$	$19.05\,\frac{\mathrm{m}}{\mathrm{s}}$	$21.52\,\frac{\mathrm{m}}{\mathrm{s}}$
case-2: $H = 91.44\,\mathrm{m}$	$14.7\,\frac{\mathrm{m}}{\mathrm{s}}$	$11.54\,\frac{\mathrm{m}}{\mathrm{s}}$	$19.84\,\frac{\mathrm{m}}{\mathrm{s}}$	$24.98\,\frac{\mathrm{m}}{\mathrm{s}}$	$28.14\,\frac{\mathrm{m}}{\mathrm{s}}$
case-3: $H = 213.36\,\mathrm{m}$	$16.94\,\frac{\mathrm{m}}{\mathrm{s}}$	$13.29\,\frac{\mathrm{m}}{\mathrm{s}}$	$22.85\,\frac{\mathrm{m}}{\mathrm{s}}$	$28.76\,\frac{\mathrm{m}}{\mathrm{s}}$	$32.41\,\frac{\mathrm{m}}{\mathrm{s}}$

Three gust gradient cases 1–3, are considered for the respective gust models. The gust profiles for case-A over the normalized time τ are illustrated in Figure 3.17. In the selection of the gust gradients, case-1 represents a short excitation. In case-2 and case-3, the vertical velocity acts over a longer period. As a result of the different interaction times between the gust and wing section, varying influences from inertia effects are studied. Further information on the specifications of the test cases from Table 3.3 is given in the Appendix A.3.

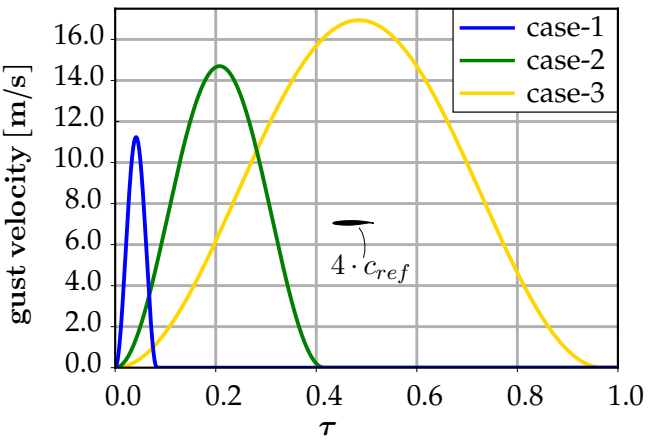

Figure 3.17.: 1-cos design gust gradients, Gust-A.

Mass and Damping Properties

The main structural model parameters for the static analysis are defined in subsubsection 3.2.1. The structural model is extended to a dynamic model, in which the inertial effects are considered by a discrete mass m. Following the work of [76], the position of the shear center **E** is consider in the center of the wing box. Due to additional trailing edge subsystems, the mass m is assumed behind the elastic axis towards the rear spar. The distance between the mass m and the elastic axis is defined to $s = 0.05 \cdot c_{ref}$. The inertia properties m and I_G are defined such that the 1^{st} bending and torsion modes have a natural frequency of $f_1 = 2.5\,\text{Hz}$ and $f_2 = 7.5\,\text{Hz}$, respectively. These assumptions are derived from the NASA CRM wing structure model. The modal properties of the reference model are summarized in Table 3.4, where the eigenvectors $\vec{v}_i$ are scaled such that the degree of freedom with the largest deflection is 1.0.

Table 3.4.: Modal properties of the initial configuration.

$\mathbf{f_1}$	$\mathbf{f_2}$	$\mathbf{f_3}$
1st bending	1st torsion	-
$2.5\,\text{Hz}$	$7.5\,\text{Hz}$	$25.4\,\text{Hz}$
$\vec{v}_1 = \begin{Bmatrix} -0.67 \\ 0.1 \\ 1.0 \end{Bmatrix}$	$\vec{v}_2 = \begin{Bmatrix} -0.125 \\ 0.0 \\ 1.0 \end{Bmatrix}$	$\vec{v}_3 = \begin{Bmatrix} -0.02 \\ 1.0 \\ 0.26 \end{Bmatrix}$

To fulfill the described dynamic characteristic, the discrete mass properties are set to $m = 106\,\text{kg}$ and $I_E = 277.1\,\text{kg}\,\text{m}^2$. For all further parametric studies of varying stiffness, it is assumed that these properties are constant.

The damping matrix can be described as presented in subsection 2.1.5. To determine the vector $\{\alpha_1, \alpha_2\}$, the natural eigenfrequencies f_1 and f_2 from Table 3.4 are also used. As can be seen from Equation 2.21, a change in the stiffness also modifies the damping model. To ensure that the results are not influenced by different structural damping effects, the damping matrix and mass matrix derived from the reference model are considered constant for all further simulations.

3.3.1. Unsteady FSI Coupling Evaluation

Prior to the investigation of the transient aeroelastic characteristics, the influence of time-step discretization on the simulation result is analyzed. For this purpose, the gust response at the rigid-wing section is considered. Therefore, the time step size is determined by the number of time steps $\mathcal{C}$ in which a disturbance needs to pass the length c_{ref}. The initial value of Δx is the uniform distribution of the spatial chord-wise discretization of the airfoil. As a function of $\mathcal{C}$, the physical time-step size is

$$\Delta t = \frac{[\Delta x] \cdot \mathcal{C}}{V_{gust}} = \frac{\left[\frac{c_{ref}}{300}\right] \cdot \mathcal{C}}{V_{gust}}. \tag{3.20}$$

As convergence criterion, the lift coefficient C_l and pitch coefficient C_m with an absolute change of $\epsilon < 10^{-5}$ over 30 iteration steps are used within one time step. The corresponding physical time-step sizes for the discretization of $\mathcal{C} = [8, 4, 2, 1]$ is listed in Table 3.5.

Table 3.5.: Physical time step discretization for cruise flight.

$\mathcal{C}$	8	4	2	1
$\Delta t\,[s]$	$5.2 \cdot 10^{-4}$	$2.6 \cdot 10^{-4}$	$1.3 \cdot 10^{-4}$	$0.7 \cdot 10^{-4}$

A change in C_l and C_m of $epsilon < 10^{-4}$ is considered sufficient which is achieved with a time discretization of $\mathcal{C} = 2$. The detailed results for the gust gradient cases 1-3 are presented in the Appendix A.4. From a structural dynamics perspective, the highest natural eigenfrequency of the reference configuration is $f = 7.5\,\text{Hz}$. This results in $N \approx 1025$ time steps per period for harmonic oscillation, which ensures sufficient resolution of the natural structural vibration for the cases studied.

FSI Interface Evaluation

As described in subsection 2.3.3, a loosely coupled system is used for the unsteady aeroelastic gust load simulations. To ensure that the selected time increment $\mathcal{C} = 2$ is sufficiently accurate for the coupling scheme, the interface work on both sides Γ_F and Γ_S is analyzed. The comparison of the work increment $\Delta W_{t_i} = L_{t_i} \cdot (h_i - h_{i-1}) + M_{t_i} \cdot (\theta_i - \theta_{i-1})$ for two consecutive time steps of the three gust gradients is plotted separately for the fluid and structural interface sides in Figure 3.18.

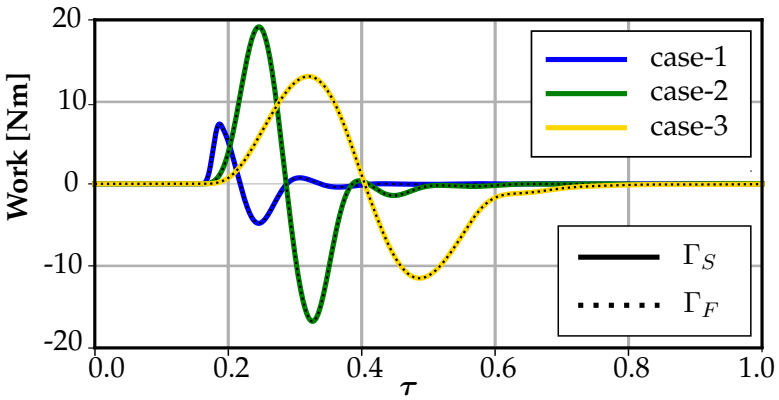

Figure 3.18.: Interface work between two time steps for the fluid and structural subdomain.

The interface work on both sides Γ_F and Γ_S does not show significant deviations, which is verified by the maximum error in Table 3.6. The second criterion is the accumulated error over the simulation time. It should be noted that the error increases with time. Compared with the total interface work, the errors are orders of magnitude smaller; this minor relative violation of the work transmission is considered negligible. Therefore, the model setup is for this study sufficiently accurate to investigate the influence of different stiffnesses under gust loads.

Table 3.6.: Domain interface, max and accumulated error.

	case-1	**case-2**	**case-3**
Max Error [Nm]	$3.54 \cdot 10^{-5}$	$4.9 \cdot 10^{-6}$	$1.83 \cdot 10^{-5}$
$\sum_i \Delta W_{t_i}$ [Nm]	$1.00 \cdot 10^{-3}$	$1.95 \cdot 10^{-3}$	$2.53 \cdot 10^{-3}$

3.3.2. Aeroelastic Response Due to 1-Cos Gusts

The passive load reduction and its dependency on the bending and torsional stiffness are analyzed by using unsteady simulations. As in the quasi-steady analysis, the stiffness K_h and K_θ of the reference configuration are varied to investigate their influence. For the gust model, the three gust gradients case 1-3 and the vertical gust speed for *cruise* (Gust-A) and *approach* (Gust-B) are applied.

Cruise Flight Condition

The gust response of the reference configurations for the three load cases 1-3 under gust-A from Table 3.3 is used as the starting point of the analysis. The C_l and C_m time progressions over the normalized time τ and the gust position relative to the airfoil are shown in Figure 3.19.

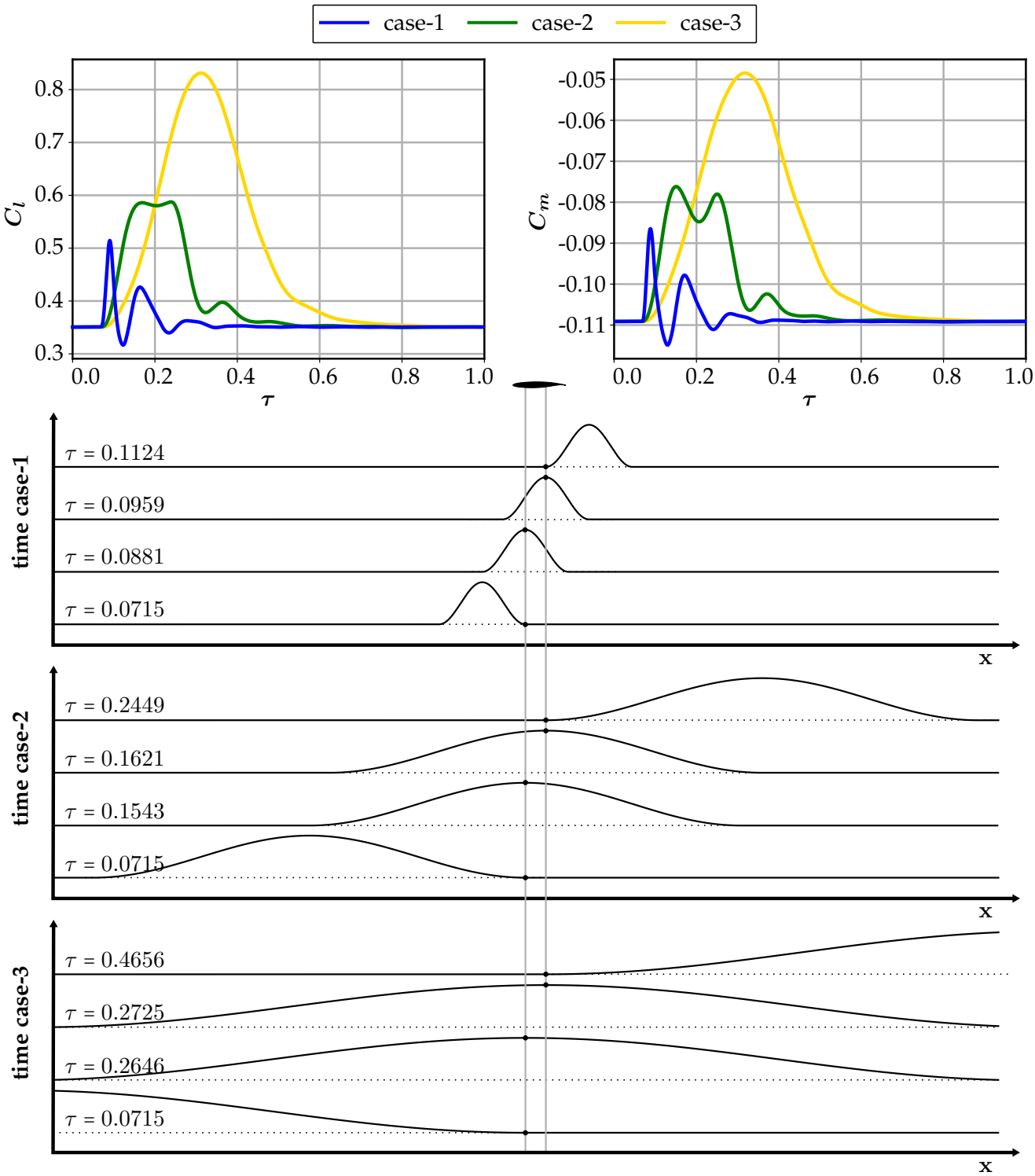

Figure 3.19.: C_l and C_m gust response of the reference model in cruise flight condition.

Case-1 shows an impulse-like excitation in C_l and C_m, while in case-3 the profile is more heavily loaded. In accordance with the gust gradient, the loading gradient is gradually distributed over time.

The corresponding progression of the structural degrees of freedom h and θ is shown in Figure 3.20. In gust case-1, it can be noted that θ is excited to a higher frequency pitch vibration, while the plunge degree of freedom h quickly decays with a short overshoot. Gust load case-3 causes the largest deflections, where the structure is not excited to vibrate. The load case-2 represents an in-between condition where the gust initially uniformly interacts with the elastic structure, similar to case-3. However, a moderate structural vibration excitation due to a varying pitch moment can be observed towards the end of the gust encounter.

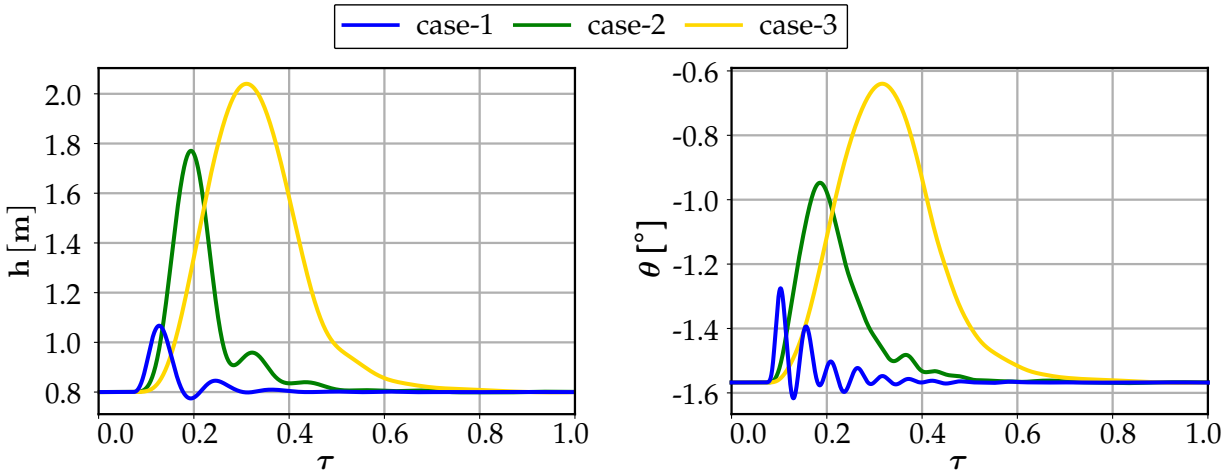

(a) Displacement h. (b) Rotation θ.

Figure 3.20.: Structural displacement h and rotation θ progression at cruise flight for case-1 to case-3.

A direct comparison of the lift curves with varying bending stiffness K_h is shown in Figure 3.20. Similar to the steady case, configurations with lower bending stiffness show an improved reduction performance compared to those with higher bending stiffness. In case-3 with infinite bending stiffness, a special condition occurs when the steady maximum lift is exceeded, and accordingly, C_l drops due to flow separation.

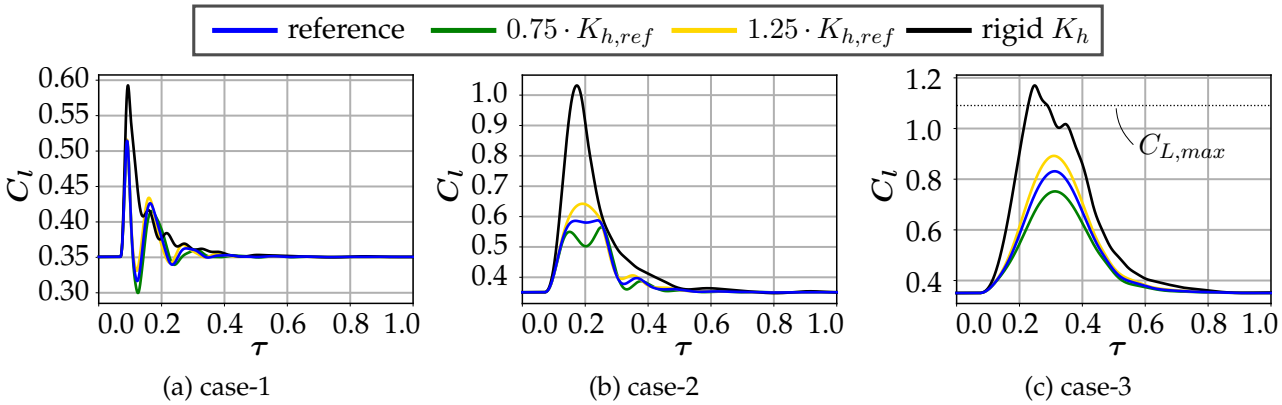

(a) case-1 (b) case-2 (c) case-3

Figure 3.21.: C_l progression for different K_h in cruise flight condition for case-1 to case-3.

The respective study with variation in torsional stiffness K_θ is shown in Figure 3.22. As in the steady-state analysis, torsional stiff configurations in particular show improved characteristics.

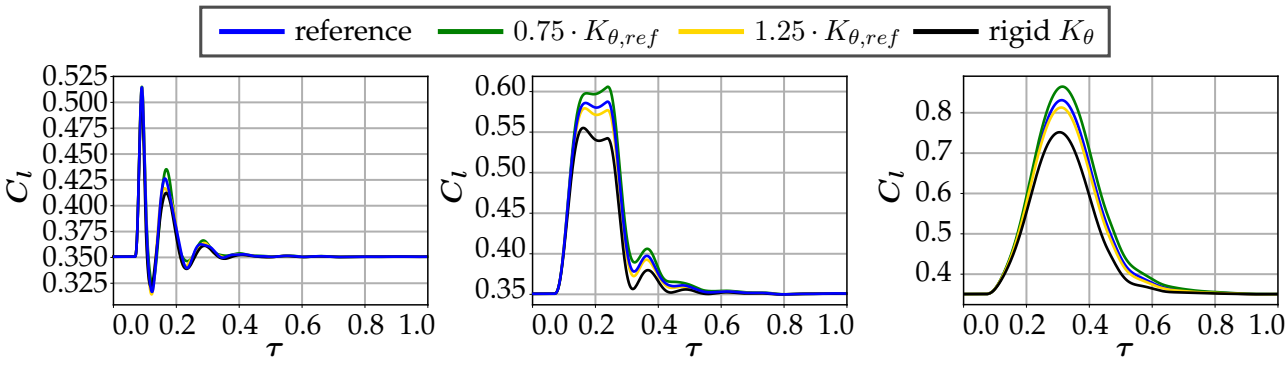

(a) case-1 (b) case-2 (c) case-3

Figure 3.22.: C_l progression for different K_θ in cruise condition for case-1 to case-3.

In Figure 3.23, the maximum lift value occurring over time is used as the assessment criterion to compare the different configurations. The results are plotted as individual markers, with the approximation $a \cdot e^{-b \cdot x^d} + c$ given as an indication of the trends in the results. Different load levels can be observed for the three load cases 1-3, converging towards the rigid solutions with increasing stiffness. It can be noted that, in general, gusts with a longer half-length (case-3) provide more reduction potential. It can be further observed that the increased torsional stiffness and reduced bending stiffness have a positive effect on the load reduction capacity. Thus, the behavior of the quasi-steady analysis can be confirmed in the transient analysis. Similarly it can be confirmed that the load reduction is dominated by the bending stiffness of the wing as a higher reduction of $C_{l,max}$ is possible. This can also be verified by comparing the $C_{l,max}$ values of the rigid profile to $K_{h=\infty}$ and $K_{\theta=\infty}$ configurations.

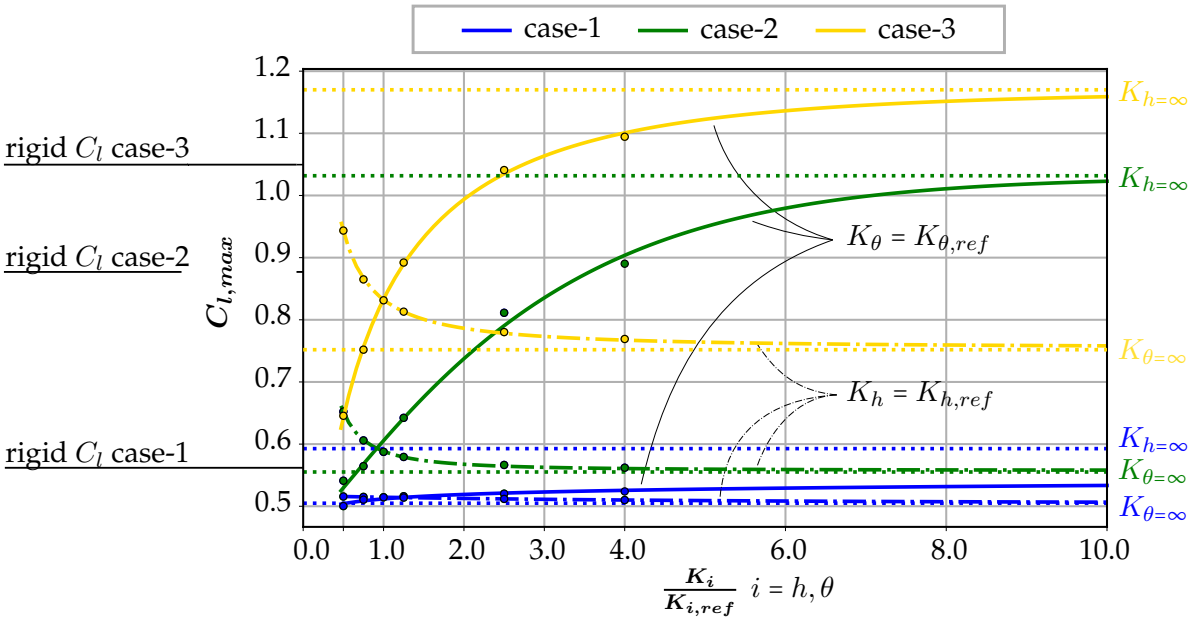

Figure 3.23.: Reference model gust response in cruise flight condition for different stiffness values K_h, K_θ.

Simultaneous Change of Bending and Torsional Stiffness in Cruise

The listed results in Figure 3.23 take into account the change in a single stiffness parameter. The simultaneous variation in both structural stiffness parameters K_h and K_θ around the reference

configuration is shown in Figure 3.24. For clarity, the three gust load cases are plotted separately. The x-axis shows the variation in the bending stiffness K_h normalized with $K_{h,ref}$. The green curves show the variation in the torsional stiffness ratio $\varphi = \frac{K_\theta}{K_{\theta,ref}} = [0.5, 0.75, 1.0, 1.25, 2.5, 4.0, \infty]$. The reference configuration $\varphi = 1.0$ is highlighted in blue, and the calculated support points are plotted as individual markers. The main conclusion from the study of the stiffness variation is that the basic characteristics remain the same, independent of the selected stiffness of the reference configuration. Thus, the previous statements regarding load reduction capacity remain valid.

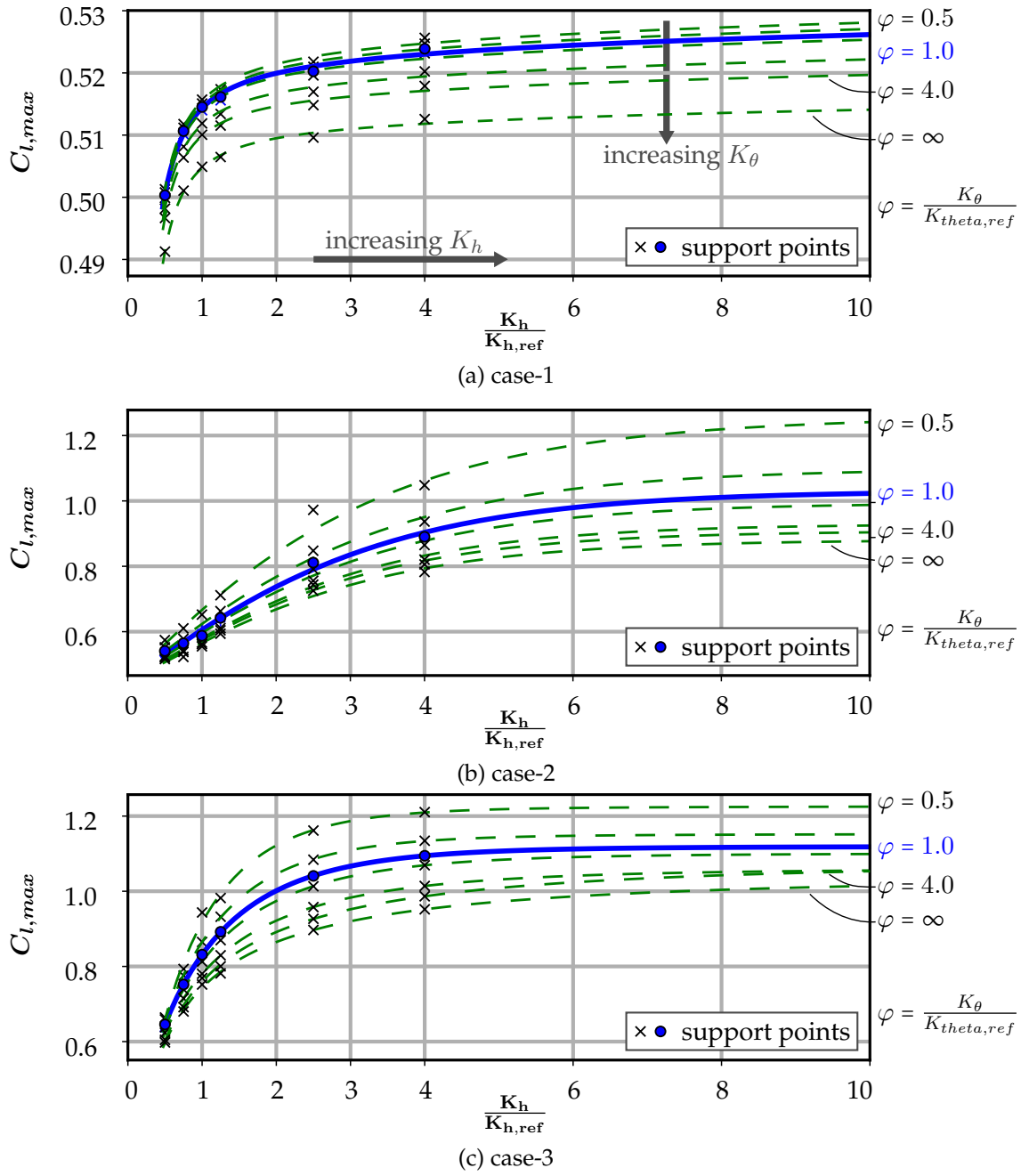

Figure 3.24.: C_l progression for different structural stiffnesses in cruise condition for case-1 to case-3.

Approach Flight Condition

The C_l and C_m results over the normalized time τ of the reference configuration in *approach-flight* are shown in Figure 3.25. The gust responses are calculated with the same steady-state lift as in the *cruise-flight* case. Because of the higher dynamic pressure, the flight is at a lower C_l and the AoA is adjusted by a trim calculation, as introduced in the steady-state investigations of section 3.2.

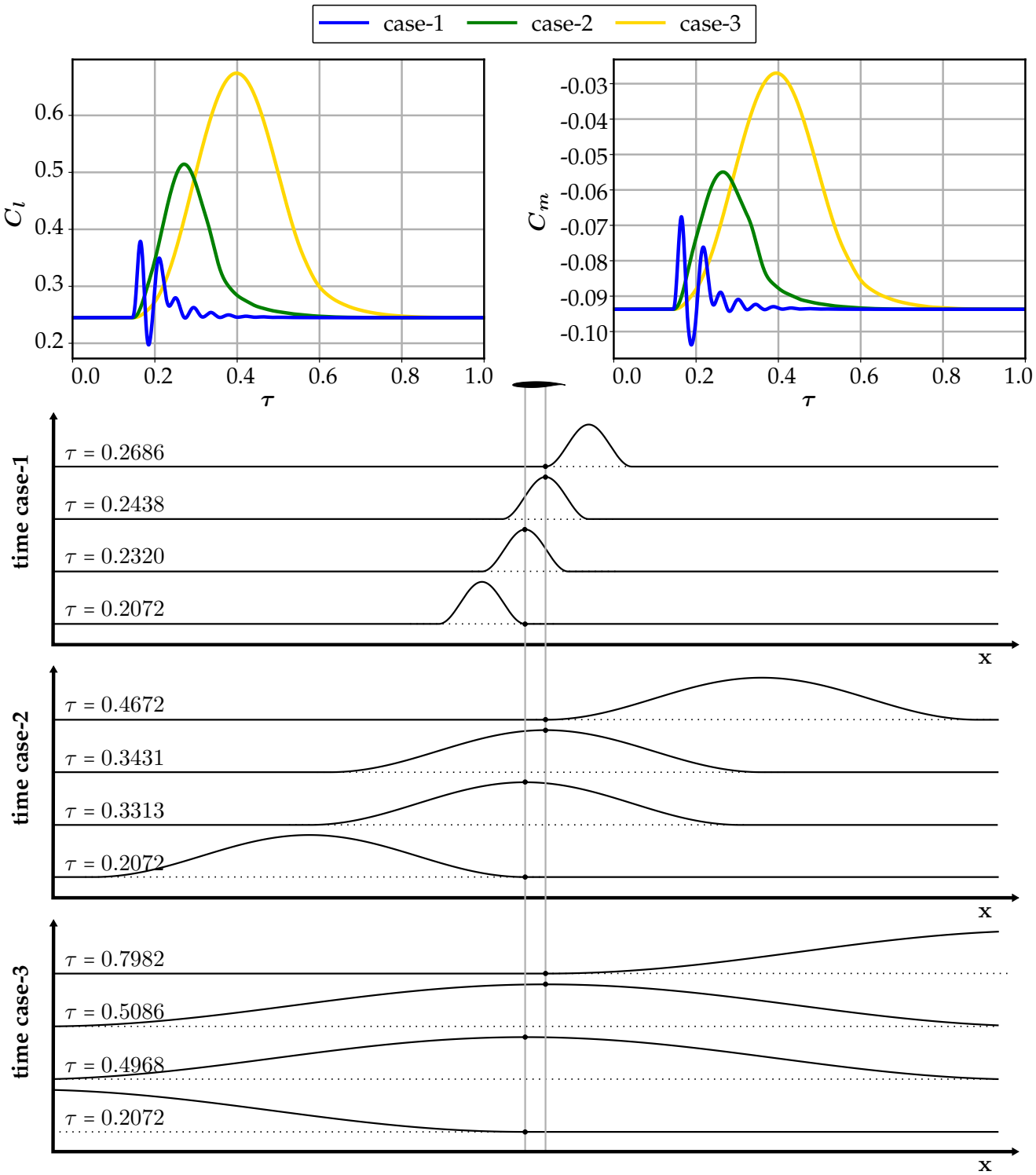

Figure 3.25.: C_l and C_m gust response of the reference model in approach flight condition.

Compared with *cruise* flight, the response to gusts in *approach-flight* condition shows a similar

characteristic. Differences can be observed in gust load case-1 and case-2, where a stronger excitation is encountered. Furthermore, no fluctuations in pitch moment are observed. In *cruise* flight, this can be attributed to the transonic flow conditions, which shift the position of the compression shock when the induced angle of attack increases due to the gust. Because of the lower Mach number, compression shocks do not occur in the *approach-flight* case. Additionally, a higher air density leads to increased aerodynamic damping. The associated structural displacements are presented in Figure 3.26. The resulting higher dynamic pressure leads to different C_l values and AoA, resulting in different pressure distributions. Because the total lift is, by definition, the same as in the *cruise-flight* case, both flight conditions have a similar steady-state deflection h which, as already described, varies slightly owing to the change in external aerodynamic moments. A stronger influence of this effect can be observed in the elastic twist θ of the airfoil section. In addition to the different steady-state conditions, it can be noted that in gust case-1, the torsional degree of freedom is particularly excited to considerable vibrations.

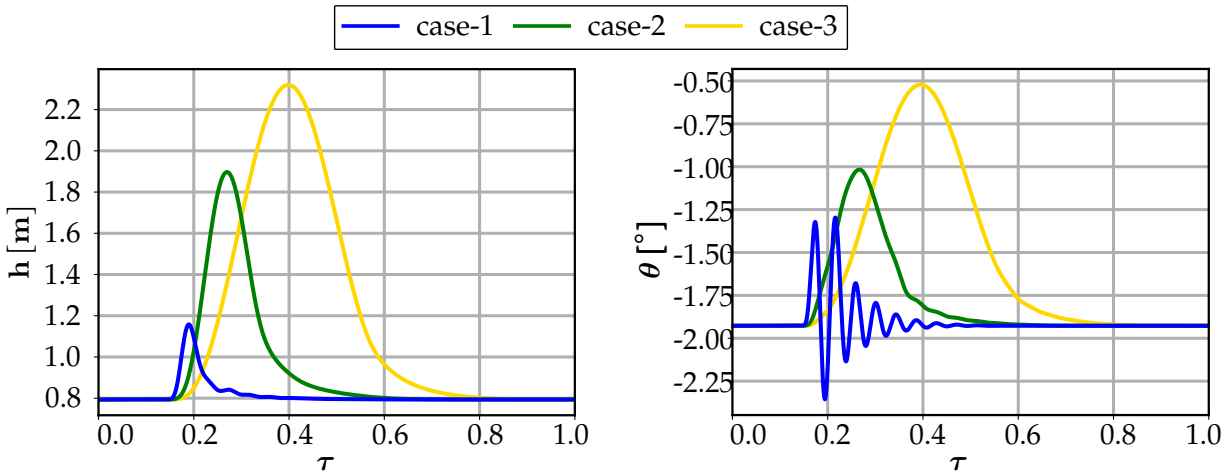

(a) Displacement h.

(b) Rotation θ.

Figure 3.26.: structural displacement h and rotation θ progression at approach flight for case-1 to case-3.

A comparison of the lift progression over time with varying bending stiffness K_h is shown in Figure 3.27a and varying torsional stiffness K_θ in Figure 3.28. As with the previous results, configurations with lower bending stiffness show better reduction capability than those with higher bending stiffness. The same holds true for configurations with increased torsional stiffness.

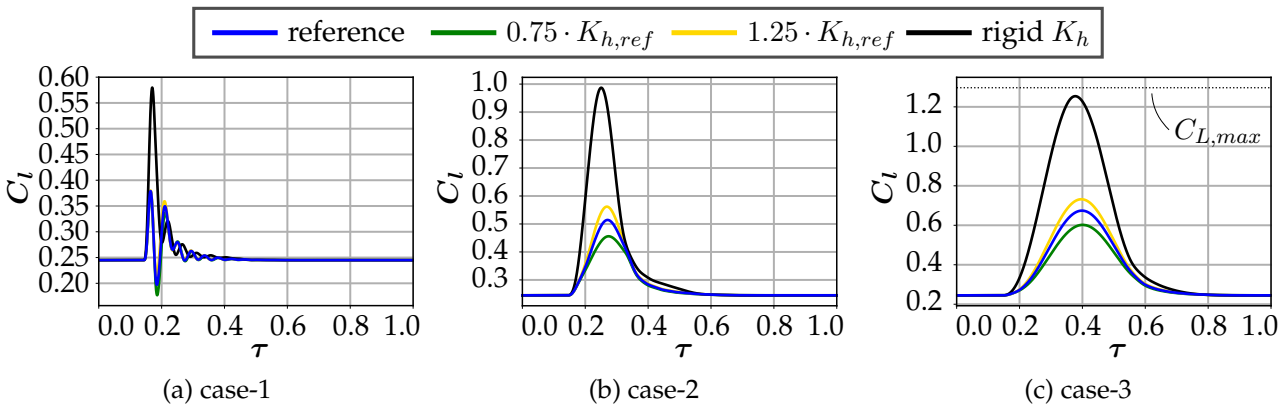

(a) case-1

(b) case-2

(c) case-3

Figure 3.27.: C_l progression for different K_h in approach condition for case-1 to case-3.

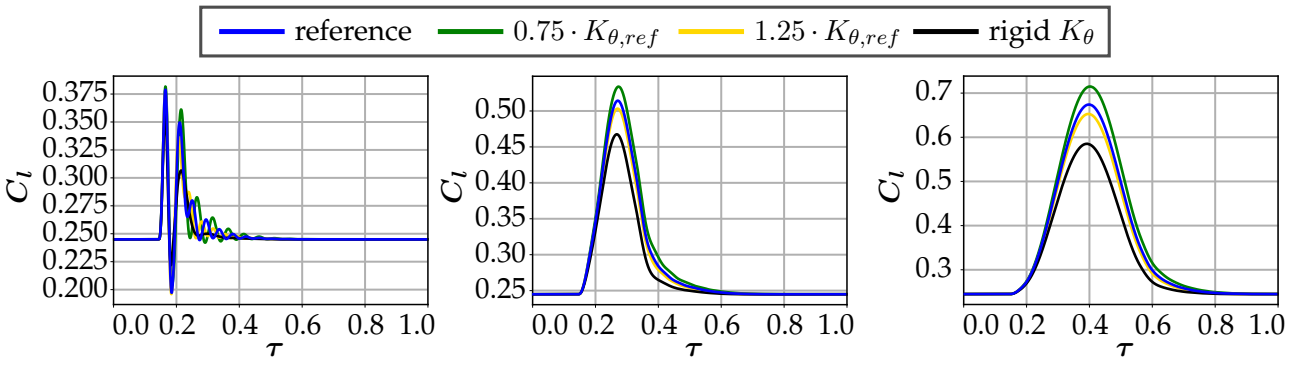

(a) case-1 (b) case-2 (c) case-3

Figure 3.28.: C_l progression for different K_θ in approach condition for case-1 to case-3.

A comparison of all *approach-flight* configurations is shown in Figure 3.29. As in the previous *cruise-flight* study, $C_{l,max}$ is used for assessment, with the support points shown as markers. The curve-fitting approximation is performed once more in the form $a \cdot e^{-b \cdot x^d} + c$. The results of *cruise-* and *approach-flight* show similar characteristics, differing essentially in scale or magnitude.

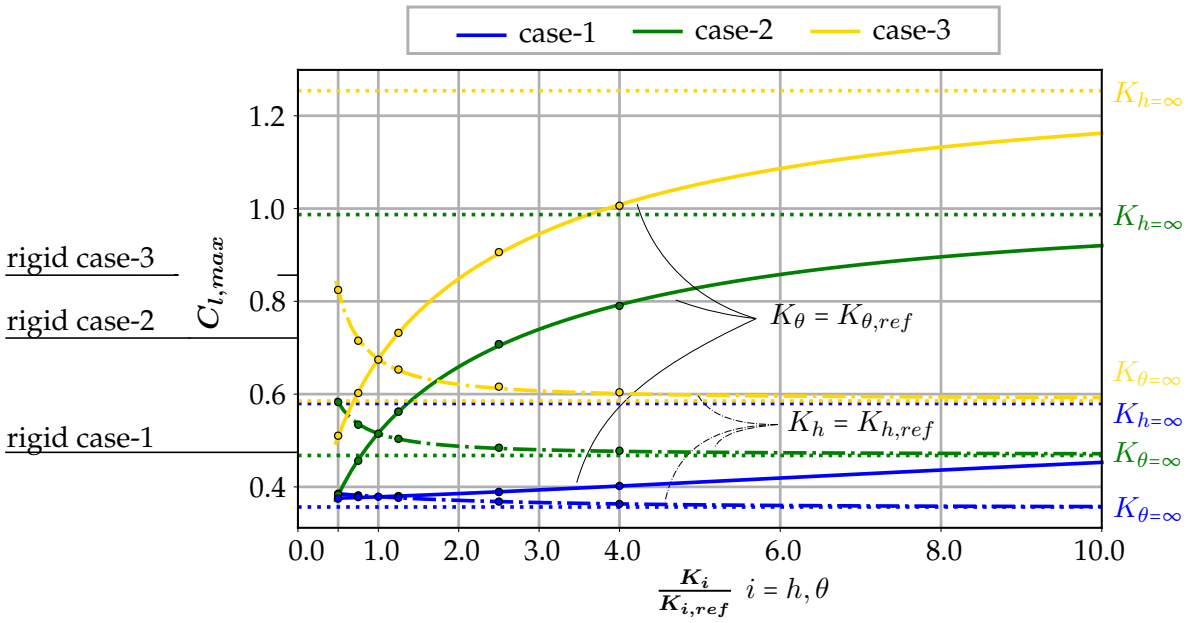

Figure 3.29.: Reference model gust response in approach flight for different stiffness values K_h, K_θ.

Simultaneous Change of Bending and Torsional Stiffness in Approach

Both parameters K_h and K_θ are varied simultaneously to exclude influences from the selected reference stiffness configuration. The results of the analysis for *approach-flight* are shown in Figure 3.30. Load case-2 and case-3 show a steep decrease in $C_{l,max}$ at low bending stiffnesses. A difference can be observed in case 1, where $C_{l,max}$ asymptotically approaches a constant value for low bending stiffnesses ratios. This is mainly due to the decreased deflection, which prevents the washout necessary for load reduction. In this case of small gust lengths, $C_{l,max}$ is dominated by the torsional stiffness.

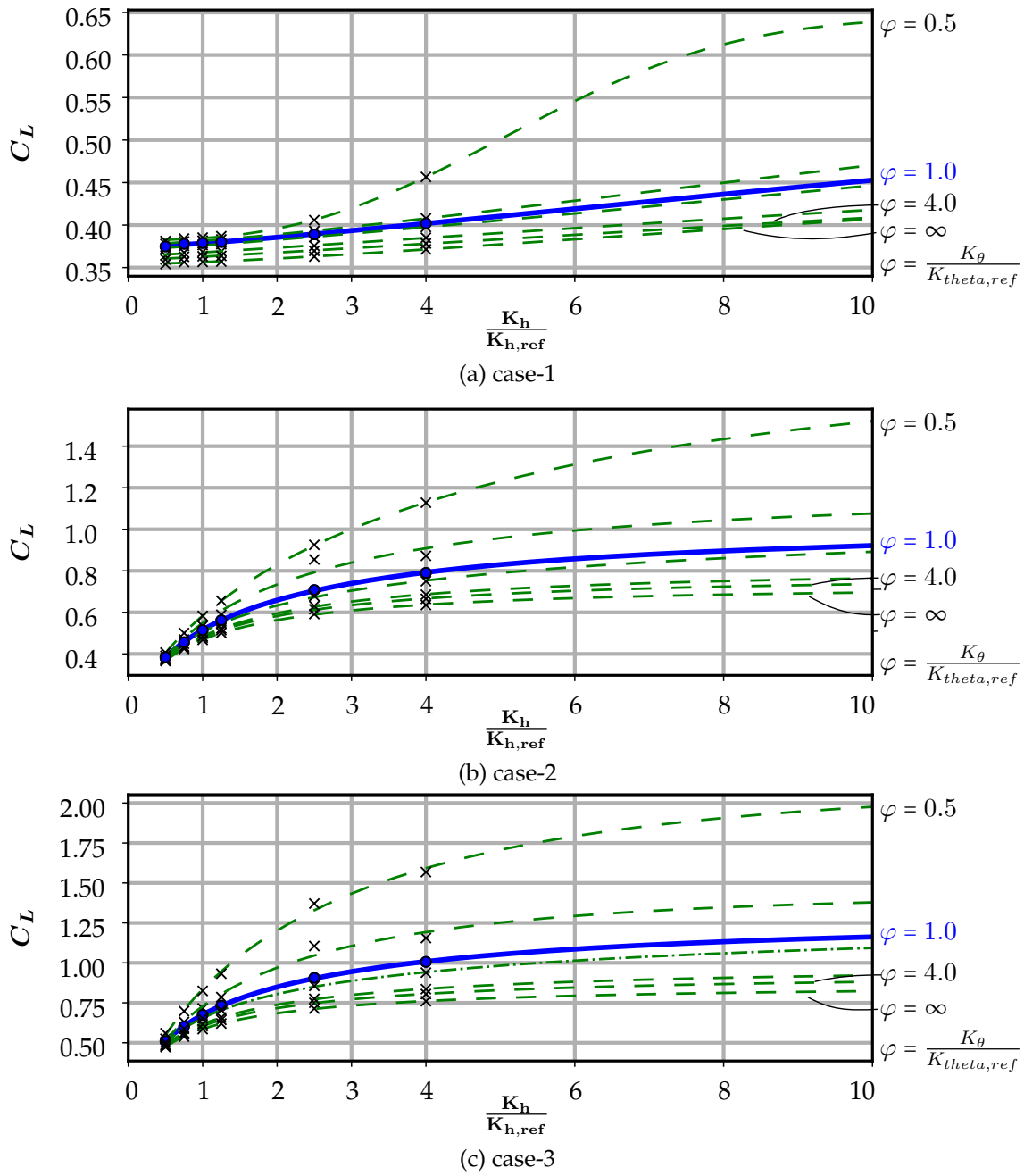

Figure 3.30.: C_l progression for different structural stiffnesses in approach condition for case-1 to case-3.

Summary and Interim Conclusion

In the dynamic study, the results of the static analysis are confirmed. In addition to the insights gained regarding the different structural stiffnesses K_h and K_θ, further transient dependencies can be identified. This includes the duration of gust exposure and unsteady effects, such as oscillating shocks. To summarize the most important statements in this chapter, all partial results are shown in Figure 3.31a for *cruise-* and for *approach-flight* in Figure 3.31b. The plot $\Delta C_{l,max} = \frac{C_{l,max} - C^{ref}_{l,max}}{C^{ref}_{l,max}}$ is compared with the reference configuration over the relative deflection $\Delta h = h_{max} - h_{ref,t_0}$ from the trimmed flight condition. The elastic torsion $\delta\theta = \theta_{max} - \theta_{ref,t_0}$ is represented by the color code of

the markers. The area marked in green is of particular interest because in these cases, $C_{l,max}$ can be reduced relative to the selected reference configuration.

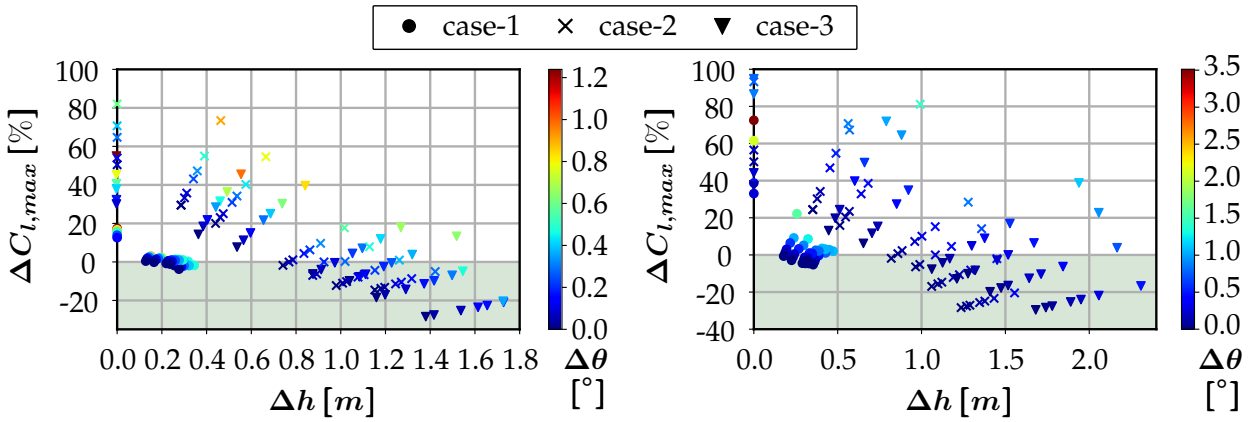

(a) cruise (b) approach

Figure 3.31.: $\Delta C_{l,max}$ reduction over relative structural deflection Δh.

The results obtained from the academic model cannot be transferred to an aircraft on a one-to-one basis. However, the following conclusions can be drawn from this study:

- To achieve a significant load reduction in $C_{l,max}$, the wing must deflect (bend) sufficiently. This is due to the kinematic coupling between Δh and α_{eff}. More flexible wings in bending favor this.
- Configurations with a low elastic twist show better load alleviation potential. The explanation for this is that the aerodynamic center is located in front of the elastic axis. Therefore, an increase in lift will lead to an up-twist of the profile. A sufficiently high K_θ value can counteract this problem.
- Gusts with a long duration have better load alleviation potential than gusts with a short duration. This is due to the short gust encounter time together with the inertia of the wing, which in turn leads to less deflection. Short gusts tend to initiate stronger structural oscillations.
- In the *approach-flight* scenario, higher load reduction potential is identified, compared to *cruise-flight*. This is related to the gust duration exposure. With *approach-flight* speed, the gust is transported more slowly and the wing remains longer in the disturbance field. Consequently, the gust forces can act longer, and higher deflections are achieved for all the gust load cases.

3.4. Aerodynamic Load Alleviation Effects During Gust Encounter

In the previous study subsection 3.3.2, the influence of the structural stiffness parameters, K_θ and K_h on the load reduction behavior have been studied. In the following, effects dominated by aerodynamic factors will be assessed in more detail. For this purpose, the influence of flow separation and the consequent limitation of $C_{l,max}$ is assessed. For this purpose, two scenarios are considered: flight at increased mean aerodynamic $\bar{C}_l$ and flow separation induced through increased gust magnitude.

3.4.1. Flight at Increased Aerodynamic Loading

To demonstrate the behavior in the aerodynamic limit region, the steady mean aerodynamic load of the wing section is increased so that the trimmed flight state is closer to the steady $C_{l,max}$, as shown in Figure 3.8. For this purpose, the steady lift of the initial configuration is scaled using the factor n_{C_l}. For the new steady flight derivative, $\bar{C}_l = n_{C_l} \cdot \bar{C}_{l,ref}$ applies and the AoA are adjusted accordingly. The structural stiffness parameters of the reference configuration are applied and the airfoil exposed to Gust-A and Gust-B scenarios.

Cruise Flight Condition

The results of the *cruise-flight* configuration for the three different gust load cases with increased steady lift are shown in Figure 3.32. To provide a better comparison of the C_l magnitudes, steady $C_{l,max}$ is depicted as a black dashed line. For case-1, it can be seen that all gust responses, except $3.0 \cdot \bar{C}_l$, are in the linear range of the lift slope. Thus, the response is shifted by the steady increase in the lift. A similar response can be observed in case-2, where for the case with $C_l = 2.5 \cdot \bar{C}_{l,ref}$, first deviations in the response occur and getting more significant with an increased C_l, as can be seen for the load case with $C_l = 3.0 \cdot \bar{C}_{l,ref}$. The same applies to case-3, where the lift cannot be further increased when the stationary value $C_{l,max}$ is noticeably exceeded.

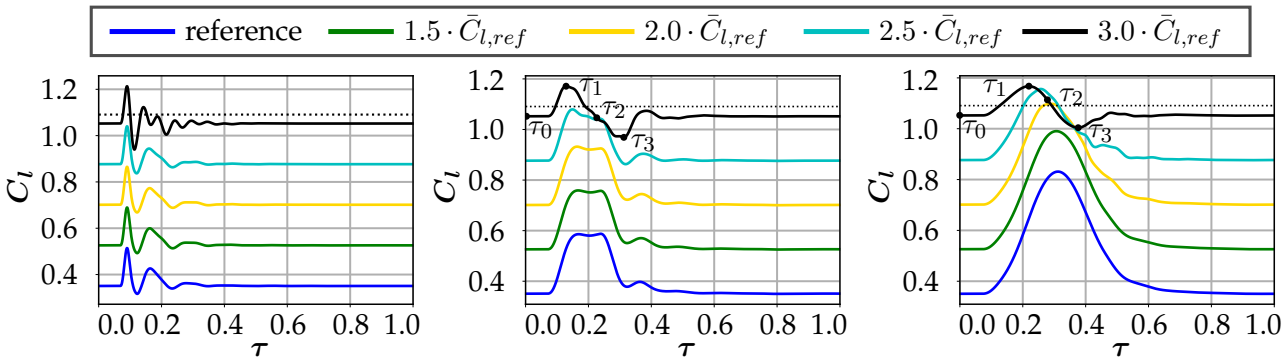

(a) case-1 (b) case-2 (c) case-3

Figure 3.32.: C_l progression for different $\bar{C}_l$ in cruise condition for case-1 to case-3.

A contour plot of the Mach number at four different time steps τ_i is shown for case-2 in Figure 3.32. At time τ_0, a steady undisturbed flow is observed. In the following time steps, it can be noted that the strength of the shock increases, followed by flow separation in time step τ_1 and τ_2. Accordingly, the reduction in lift is caused by the detached flow, which reattaches after time step τ_3 before the steady lift $\bar{C}_l$ is recovered. The same can be stated for gust load case-3 with the corresponding Mach number contour plot given in Figure 3.34.

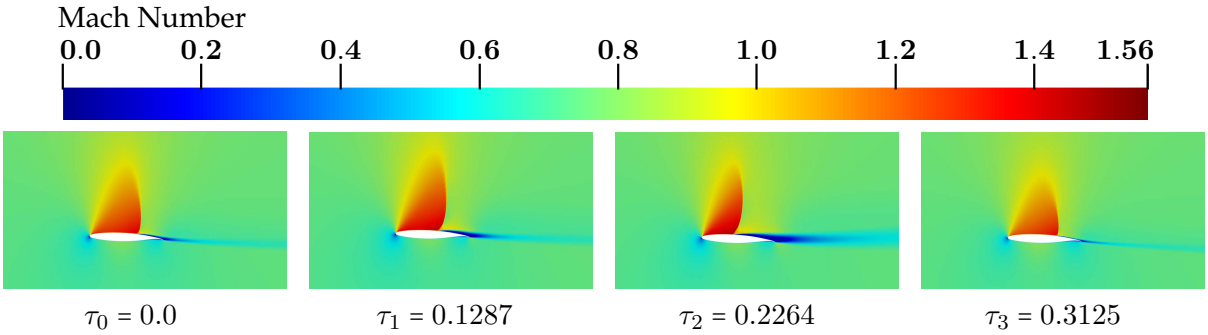

Figure 3.33.: *Ma* contour plot for time step τ_i at cruise, gust case-2, $3.0 \cdot \bar{C}_{l,ref}$.

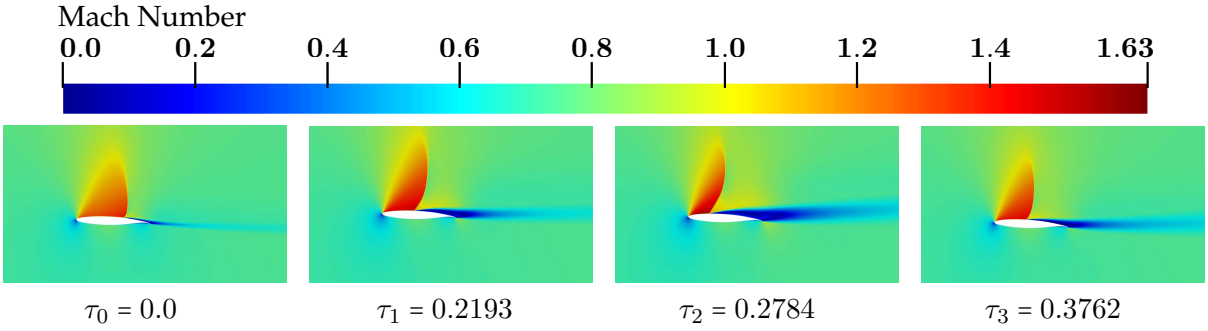

Figure 3.34.: *Ma* contour plot for time step τ_i at cruise, gust case-3, $3.0 \cdot \bar{C}_{l,ref}$.

In both gust load cases-2 and -3, it can be observed that an upper limit of C_l is reached at a steady $\bar{C}_l$ of $2.5 \cdot \bar{C}_l$ and $3.0 \cdot \bar{C}_l$. This implies that no further lift and no higher loads are generated. Furthermore, case $3.0 \cdot \bar{C}_l$ shows that after the stall, the lift drops below the required level for a steady horizontal flight. In contrast, the flow can stabilize fast enough and return to the stationary lift without a major collapse in $2.5 \cdot \bar{C}_l$.

The effects on the structural dynamics can be seen from the deflection h and θ time plots in Figure 3.35 and Figure 3.36, respectively. As can be noted, for small gust lengths, the torsional degree of freedom is primarily excited by vibrations. For gust case-2 and case-3, the loss of lift is also noticeable in the vertical deflection h. In both cases, an overshoot around the static equilibrium position for $3.0 \cdot \bar{C}_l$ is observed. In the lower $2.5 \cdot \bar{C}_l$ scenario, this effect could be avoided.

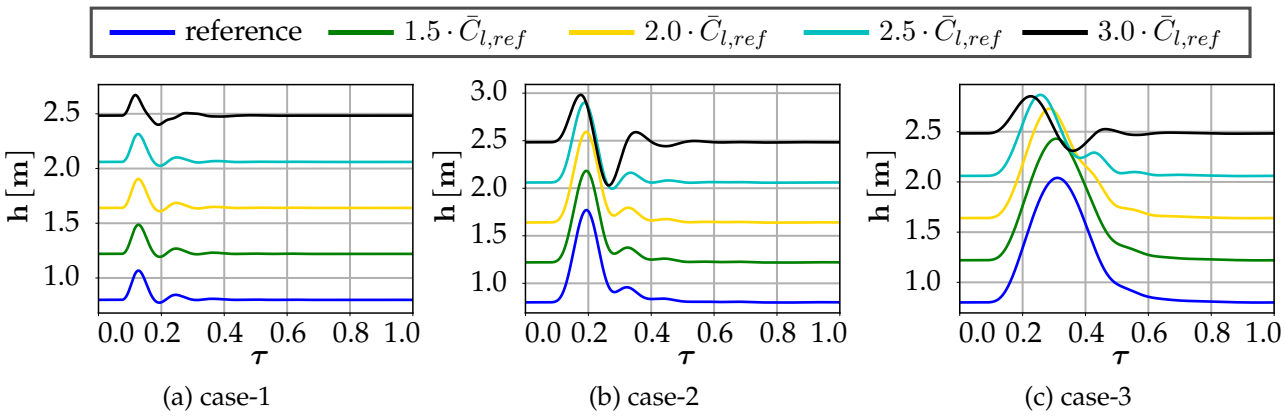

(a) case-1 (b) case-2 (c) case-3

Figure 3.35.: h progression for different $\bar{C}_l$ in cruise condition for case-1 to case-3.

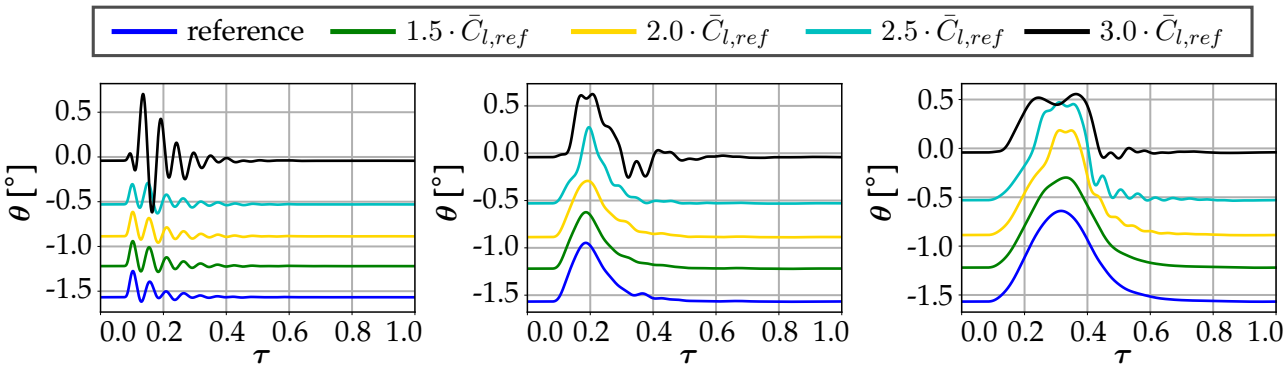

(a) case-1 (b) case-2 (c) case-3

Figure 3.36.: θ progression for different $\bar{C}_l$ in cruise condition for case-1 to case-3.

Approach Flight Condition

The results of the C_l progression for the *approach-flight* condition are shown in Figure 3.37. The steady lift is indicated by the dashed line. As a much higher steady $C_{L,max}$ is possible for *approach-flight* conditions compared with *cruise-flight*, the mean $\bar{C}_l$ is increased accordingly. Essentially, the same linear gust response behavior as in the *cruise-flight* condition is found for both gust loads in case-1 and case-2. The most significant difference can be noted for the case with $4.5 \cdot \bar{C}_l$ in gust case-3. After reaching the maximum lift, it drops abruptly below the steady flight value, accompanied by strong oscillations.

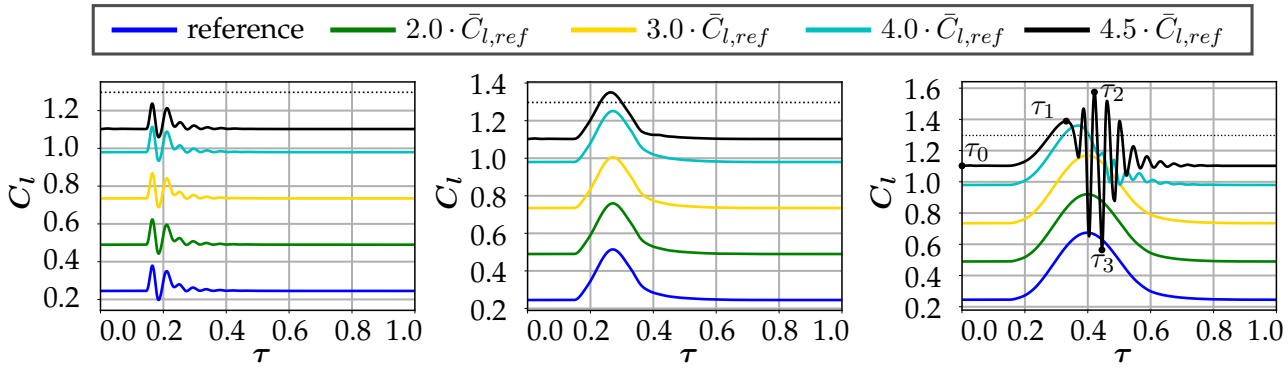

(a) case-1 (b) case-2 (c) case-3

Figure 3.37.: C_l progression for different $\bar{C}_l$ in approach condition for case-1 to case-3.

The visualization of the flow field for different time steps τ_i is shown in Figure 3.38. It is observed, that after reaching time step τ_1, noticeable flow separations along the entire wing section occur.

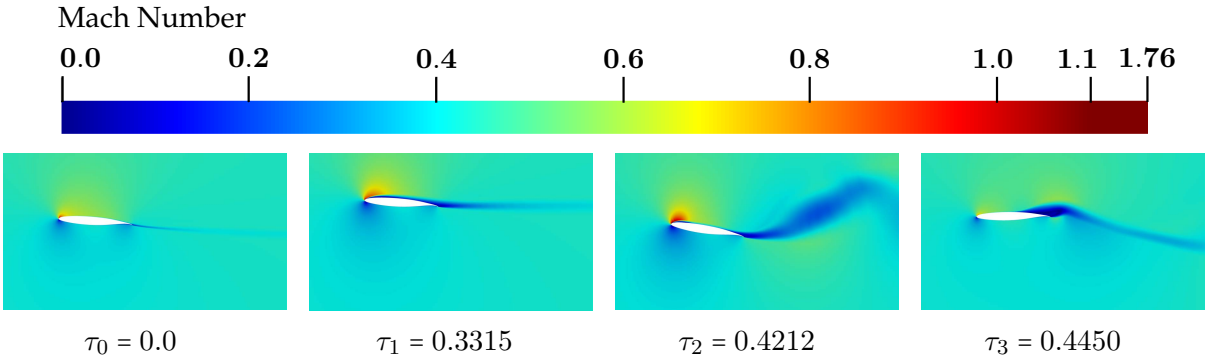

τ_0 = 0.0 τ_1 = 0.3315 τ_2 = 0.4212 τ_3 = 0.4450

Figure 3.38.: Ma contour plot for time step τ_i at approach flight, gust case-3, $4.5 \cdot \bar{C}_{l,ref}$.

Compared with the *cruise-flight* condition, the flow stabilizes only at a slow rate. As can be seen in Figure 3.39 and Figure 3.40, strong structural excitation especially in the torsional degree of freedom θ are induced for load case $C_l = 4.5 \cdot \bar{C}_{l,ref}$.

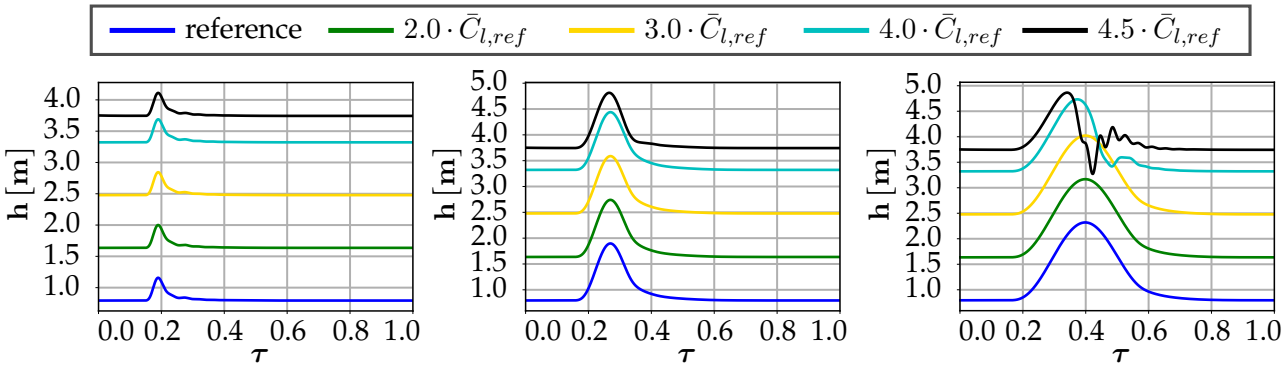

(a) case-1 (b) case-2 (c) case-3

Figure 3.39.: h progression for different $\bar{C}_l$ in approach condition for case-1 to case-3.

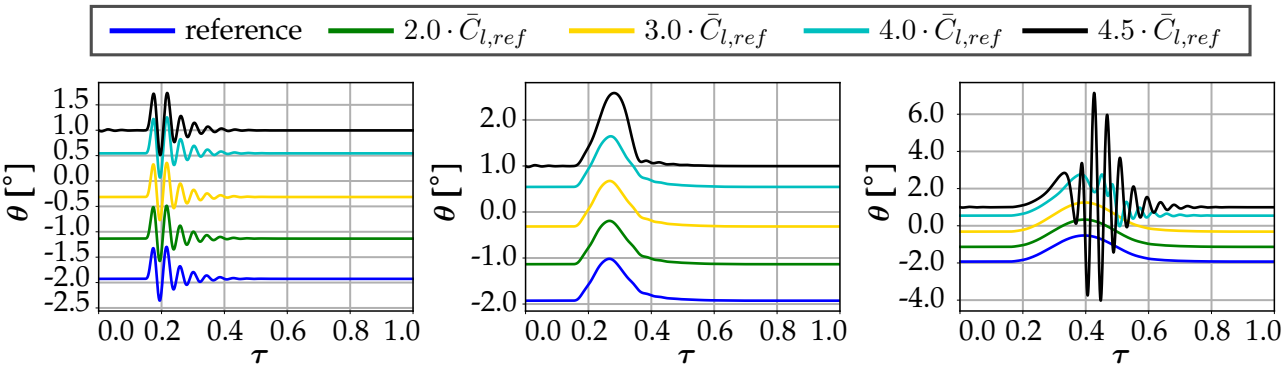

(a) case-1 (b) case-2 (c) case-3

Figure 3.40.: θ progression for different $\bar{C}_l$ in approach condition for case-1 to case-3.

If the aerodynamic load is increased further, that is, the steady flight takes place at further increased AoA, a phenomenon known as stall flutter appears. More details on this instability have been investigated and described by Dowell [39]. The characteristic is lift oscillation, as shown in Figure 3.41, caused by cyclic flow separations. This is depicted in Figure 3.42 as a Mach contour plot for case-1. The Mach contours at four different time steps within a single oscillation period, as indicated in Figure 3.40a, are shown.

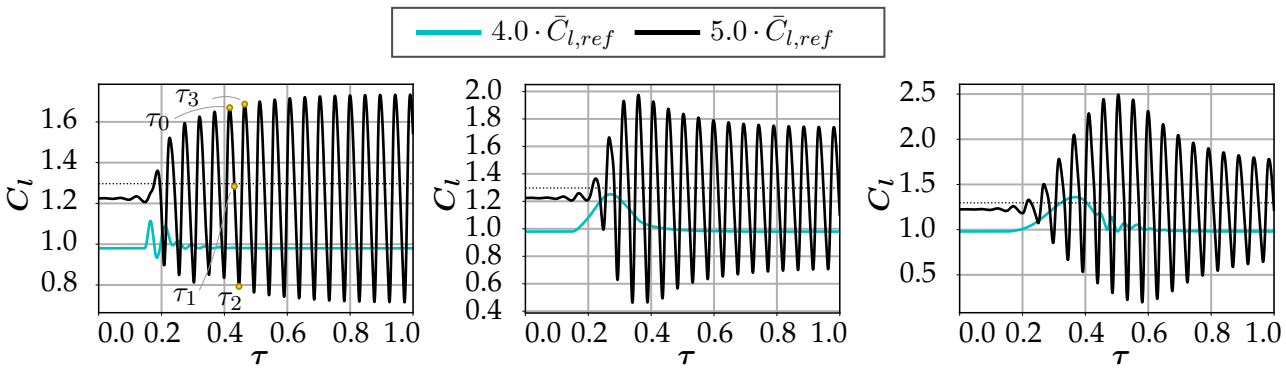

(a) case-1 (b) case-2 (c) case-3

Figure 3.41.: C_l progression for $4.0 \cdot \bar{C}_l$ and $5.0 \cdot \bar{C}_l$ in approach flight condition for gust case-1 to case-3.

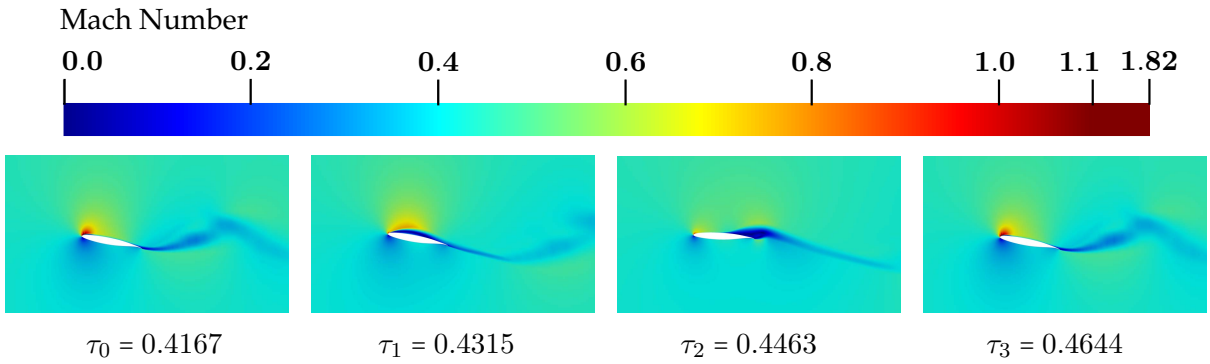

Figure 3.42.: Mach-Number contour plot for time step τ_i at approach, gust case-3, $5.0 \cdot \bar{C}_{l,ref}$.

The progression of the two structural degrees of freedom over time is shown in Figure 3.43. It can be observed that the oscillations are superimposed, but not induced by the gusts.

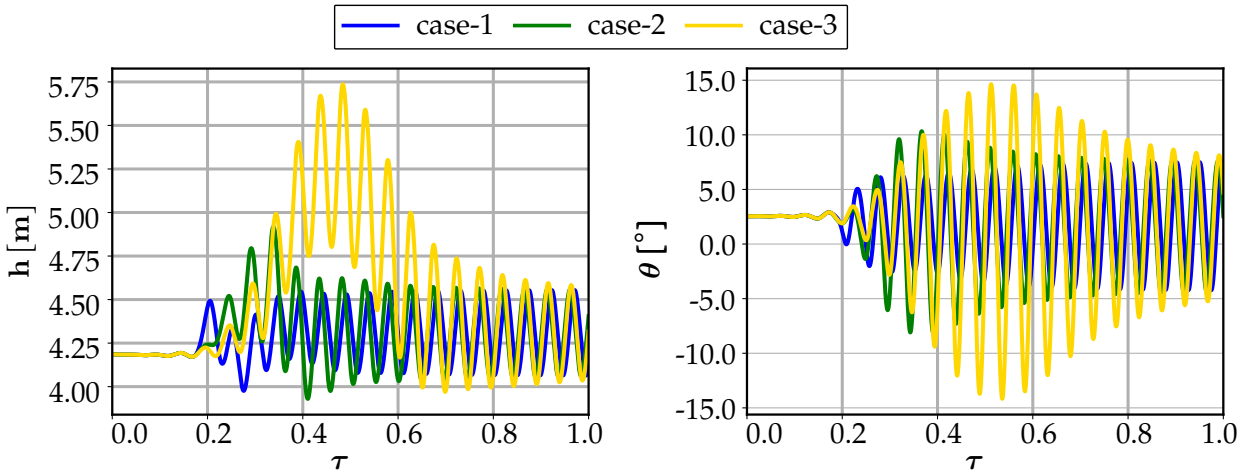

(a) Displacement h.

(b) Rotation θ.

Figure 3.43.: Structural displacement h and rotation θ progression at cruise flight for case-1 to case-3, 5.0 mean $\bar{C}_{l,ref}$.

The investigations presented here are primarily carried out to identify possible load and operation scenarios. A constant flight close to $C_{l,max}$, or with a corresponding high load factor n_z, is considered challenging for application in the commercial aircraft sector. Further detailed studies on this specific aspect will therefore not be addressed in this work.

Summary and Interim Conclusion

The purpose of this section is to understand how flow separation, as a lift-limiting factor, can contribute to passive load reduction. For this study, under flow conditions with increased aerodynamic lift C_l, the following conclusions can be drawn:

- It can be observed that in *cruise-flight* $C_{l,max}$ is limited independent of varying aerodynamic steady C_l level. This means that irrespective of the additionally induced gust loads, no additional lift amplitude is generated due to flow separation.
- After flow separation occurs, the speed at which the flow reattaches to the wing is essential. This is related to whether the average C_l falls below the level required for a steady-state flight. If the

drop is too large, the deflection falls below the stationary equilibrium position and the structure is excited to vibrate.

- The *approach-flight* condition shows abrupt flow separation and collapse of the lift. Simultaneously, a strong structural excitation in the torsional degree of freedom is observed.
- Another limiting case in *approach-flight* is stall flutter within flight at a significantly high steady-state C_l.

3.4.2. Gust Response at Varying Design Gust Profiles

In the following section, the influence of the gust design velocity V_v of the 1-cos gust profile on the load reduction behavior is analyzed in more detail. Compared to flight at higher mean C_l, the aerodynamic effect of flow separation due to an induced higher AoA will be analyzed. As V_v is indirectly linearly adjustable via the flight profile alleviation factor F_g, the design gust speed also increases linearly. The resulting gust models for *cruise-* and *approach-flight* conditions are listed in Table 3.3. The variation of the profile alleviation factor F_g simultaneously allows an investigation of the extent to which the load reduction behavior depends on the gust profile.

Cruise Flight Condition

For the gust response under *cruise-flight*, the C_l progression for the three cases $1-3$ with increased design speed is shown in Figure 3.44. Apart of gust-D, similar C_l profiles are obtained and scaled to larger response amplitudes in accordance with the vertical design gust velocities V_v. For gust scenario D, gust length case-3, the steady-state $C_{l,max}$ is exceeded and C_l is limited by flow separation.

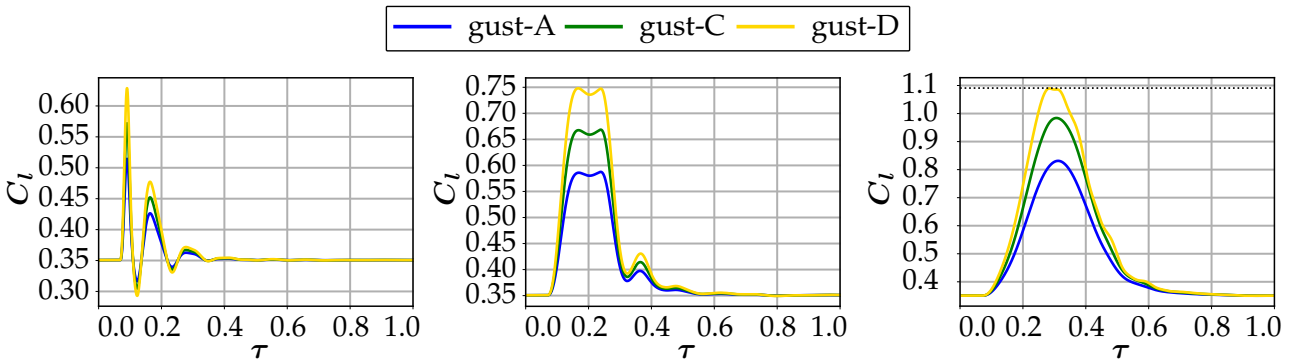

(a) case-1 (b) case-2 (c) case-3

Figure 3.44.: C_L progression for different gust design speed V_v in cruise flight condition for case-1 to case-3.

The $C_{l,max}$ results for different gust lengths H and gust speeds V_v is shown in Figure 3.45. In order to reflect the influence of different structural stiffnesses, the evaluation is carried out for the reference (solid line) and $0.75 \cdot K_h$ stiffness configuration (dashed line). The following conclusions can be obtained:

1. The $C_{l,max}$ results do not show any decisive reduction for small gust lengths.
2. For gust lengths of $H \approx 50\,\mathrm{m}$, the more flexible configuration shows a better washout performance,
3. which is most significant between $90\,\mathrm{m}$-$110\,\mathrm{m}$ gust length.

4. For gust lengths $H > 125\,\mathrm{m}$, the reference configuration shows flow separation in the Gust-D scenario.
5. The $C_{l,max}$ of the flexible configuration, however, remains approximately at the C_l level of the reference configuration with smaller gust velocity V_v (Gust-C).

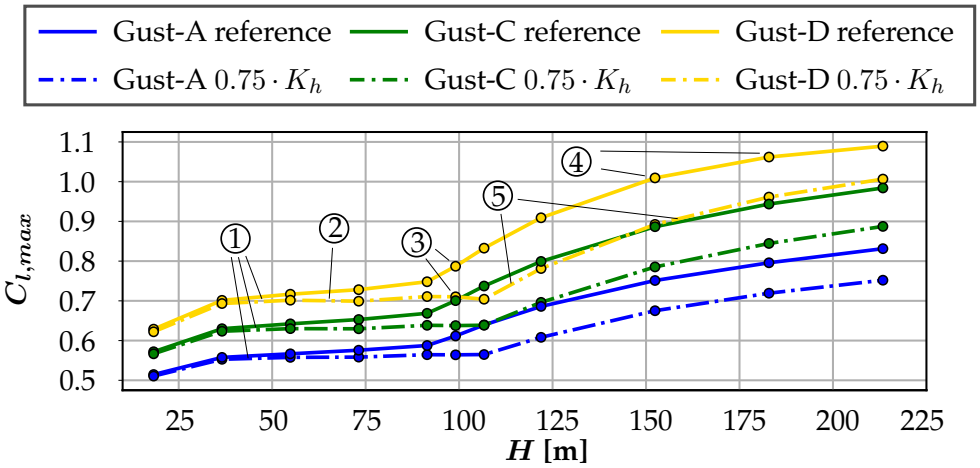

Figure 3.45.: Design gust velocity analysis results at cruise flight for different gust lengths H.

An important finding is, that the load alleviation by washout is more effective than the load limiting induced by stall. The difference in ΔC_l between the two assessed stiffness configurations at different gust velocities V_v can be found in annex A.5.

Approach Flight Condition

The results of the C_l progression for the *approach-flight* condition are shown in Figure 3.46. Similar to *cruise-flight* condition, a linear dependency is observed for all three gust load cases.

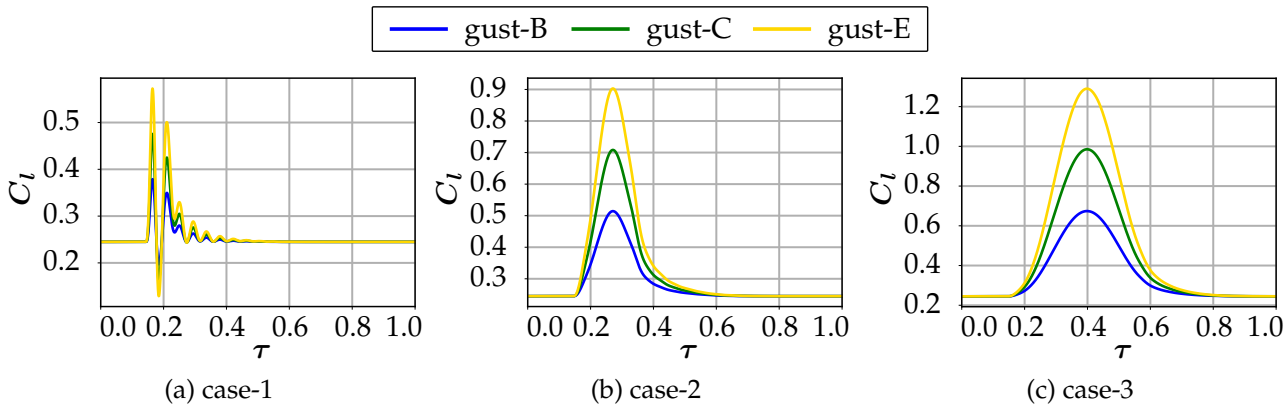

(a) case-1 (b) case-2 (c) case-3

Figure 3.46.: C_L progression for design gust velocities in approach condition for case-1 to case-3.

A comparison of $C_{l,max}$ at different gust lengths H is shown in Figure 3.47. As in *cruise-flight*, load reduction characteristics can be classified into different sections:

1. Small gust lengths shows minimal reduction potential,
2. followed by gust lengths where the reduction comes mainly from the washout of the flexible configuration.

3. The reduction increases slightly until, similar to the *cruise-flight* case, a significant reduction in $C_{l,max}$ around $H \approx 60\,\mathrm{m}$ occurs.

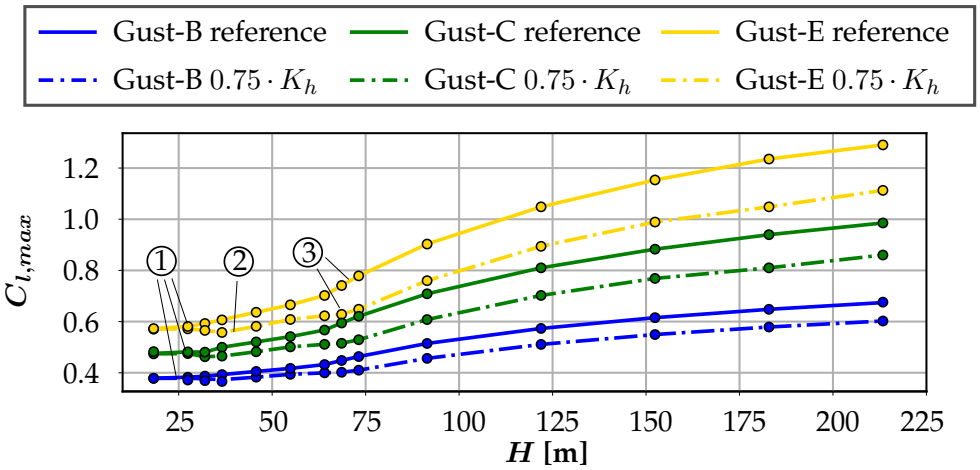

Figure 3.47.: Design gust velocity results at approach flight for different gust lengths.

Compared to *cruise-flight*, no flow separations can be identified. With increasing gust velocity V_v, the load alleviation potential scales linearly, as described in more detail in annex A.5.

Summary and Interim Conclusion

In this section, the influence of the gust length and varying vertical gust speed of the 1-cos gust is analyzed. For this purpose, the structural reference configuration is compared with a reduced stiffness. The findings of this study are as follows:

- For both *cruise-* and *approach-flight*, small gust lengths have lower potential for passive gust load reduction.
- The more flexible wing section has a lower absolute $C_{l,max}$ over the entire gust length spectrum.
- For *cruise-flight* with long gust lengths and increase gust design velocity, flow separation is a lift-limiting factor.
- In *approach-flight*, the reduction in $C_{l,max}$ can be scaled linearly with the gust speed. However, a nonlinear dependency is observed for *cruise* and long gust lengths.

3.5. Summary and Discussion of the 2-DoF Results

In this chapter, a 2-DoF model is described to investigate the dominant influence mechanisms of passive aerodynamic load alleviation of flexible swept wings. The structural model is reduced to a 2-DoF system, which represents the bending and torsional stiffness of the wing. The aerodynamic model is considered under the assumption of a quasi-2D representation, and the interaction with gusts is investigated using the *Field-Velocity-Approach*.

3.5.1. Results Summary

First, the general influence of the two structural stiffnesses on the load reduction behavior is investigated by considering the static behavior under steady aerodynamic forces without structural inertia. Next, the dynamic behavior is considered by means of transient aerodynamic forces and structural inertia. For this purpose, different gust load cases with different half-wave lengths and design gust velocities are used. In both cases, the bending stiffness dominates over the torsion stiffness. A more bending flexible wing proves to be more efficient in the sense of load reduction, because it can effectively compensate for the additionally induced AoA by the kinematic coupling. Since the center of pressure is usually located in front of the elastic axis, the wing's lift causes a moment turning it up. A sufficiently high torsional stiffness can counteract this. Thus, a wing that is as torsionally stiff as possible is advantageous. To ensure independence from the selected reference stiffness configuration, the stiffness parameters are varied. The findings obtained could be confirmed independently of this.

Second, two studies in the operational aerodynamic limit range are considered: flight at increased mean aerodynamic lift and gusts with increased design gust speeds. Under this consideration, aerodynamic effect for load reduction are analysed. The gust response shows a linear correlation with the increase in the mean aerodynamic lift. When steady-state $C_{l,max}$ is reached, nonlinearities resulting form flow separation become evident. In case of *cruise-flight*, the response behavior is classified into two categories. The first is lift collapse with quick recovery of the flow, in which the lift required for a steady equilibrium flight does not fall below the stationary C_l, and the second is where the mean C_l decreases and the airfoil no longer provides the necessary lift. These phenomena could be demonstrated in the hypothetical $n_z = 2.5 \cdot \bar{C}_{l,ref}$ load case. However, in the *approach-flight* scenario, the influence of the flow detachment could only be identified at excessively high aerodynamic loads. In this case, stall flutter is identified as the limiting phenomenon. Conversely, in the *approach-flight* scenario, it ends in an unmanageable instability. It must be noted that stationary flight must take place at an unrealistically high mean $\bar{C}_l$ in *flight approach*.

Finally, the extent to which the gust interaction responds to different design gust speeds and lengths is evaluated. In contrast to the previous analysis, $C_{l,max}$ is achieved by increasing the design gust velocity. Here, nonlinearity is confirmed to occur only at *cruise-flight*. In the *approach-flight* case, no influence of flow separation is identified, even at extremely excessive design gust speeds. Similarly, the passive load reduction behavior only reaches its full potential in the case of increased gust lengths.

3.5.2. Findings and Discussion

The results obtained thus far have been used in the sense of a simplified study, while considering extreme conditions. Here, the results are discussed in the context of engineering feasibility and other research areas.

General Structural Design

The first finding of having a torsional stiff wing is considered advantageous, as it has a positive effect on other aeroelastic problems such as flutter or aileron effectiveness. The feasibility is usually limited by the fact that the corresponding stiffness is achieved at the expense of additional weight or new, more expensive materials. The lowered bending stiffness is mainly limited by dynamic aspects. A more flexible wing, particularly with short gust lengths, excites the structure to strong vibrations. Therefore, preventing the structural vibrations from interacting with the rigid body motion of the aircraft is increasingly difficult.

The investigations do not provide the extent to which structural vibrations can be permitted. Considering active gust load alleviation [26, 105], a smoother and therefore more passenger comfortable flight can be achieved, as well as improve airframe fatigue under normal operating conditions by reducing the alternating load amplitudes. However, in the event of failure of the active system, the passive load reduction behavior is still be available for the large gust lengths, ensuring that the safety of the overall system is still given. Passive technologies as backup solutions thus influence the certification and authorization of future active technologies.

Flow Separation

A further research question is to investigate whether flow separation can be used specifically for passive dynamic load reduction. A key criterion is whether the necessary lift for a stationary flight can be guaranteed. A drop below this level is considered critical. As shown in the investigations, states with moderate flow separation can be identified in the *cruise-flight* case, which fulfill this condition. The post stall characteristics are significant in whether the flow recovers fast enough or the lift falls below that necessary to maintain flight attitude.

For *approach-flight* conditions, flow separation is technically difficult to achieve as a means of load reduction. To achieve the $C_{l,max}$ range, extreme flow conditions at high AoA must be achieved. If such extreme boundary conditions should be achieved from a design perspective, the instability of stall flutter must be controlled.

For completeness, the 2D model can show possible tendencies or limits, but does not allow any conclusions to be stated about a finite 3D wing and its stall characteristic. The collapse of lift in the 2D model cannot be compared to that of an entire aircraft, which is unacceptable. The flow separation is not expected to start on the entire wing. Therefore, it must be discussed whether a partial flow separation can be tolerated, which is undertaken in the subsequent chapters, taking into account a finite 3D wing.

Modeling Reliability and Limits

Structural coupling between bending and torsional deformation is intentionally not considered in this study to keep the complexity of the structural and aeroelastic model as low as possible. For the 2-DoF system as presented in this study, the coupling can be modeled by assigning the entries K_{13} and K_{23} of Equation 3.4 accordingly [47]. The decision is motivated through the possibility to investigate the bending and torsional deformation independently. However, a non-existent bending-torsion coupling is generally not the case for wing structures. Wing structures designed with isotropic materials such as aluminum may show such characteristics. In this case, one speaks of designed anisotropy, which is caused by different stringer arrangements, ribs, cut outs, or different cross section geometries. Further, the coupling between bending and torsional deflection can be specifically induced by aeroelastic tailoring by means of the stacking sequence of composite materials. In summary, the non-existent coupling demonstrated here is suitable for a general study, but cannot represent complex finite 3D wing structures.

A further reduction of the computational complexity is achieved by the quasi two-dimensional analysis of the flow with known physical laws. It was obvious and common knowledge that these reductions cannot represent the aerodynamic characteristics of a finite 3D wing. However, the applied approaches describe the problem sufficiently for efficient general investigations. In order to further investigate the finding, the subsequent chapters deal with the set-up and the investigation of representative, industry relevant, aircraft 3D wing models.

4 Transport Aircraft Design and Computational Modeling

In this chapter, the design and computational aeroelastic modeling of a generic transport aircraft with two different wing configurations are described. As illustrated in Figure 4.1, a wing with an aspect ratio of 10 and a future wing with an aspect ratio of 13 are set up for detailed aeroelastic investigations. First, configuration and design of the aircraft are described, followed by the structural design and sizing method. As a substep of the structural design process, a procedure for determining the wing jig-shape such that a predefined target *cruise-flight* shape can be achieved is introduced. Finally, the effects of changing structural stiffness on the inherent deformation characteristic of the wings are analyzed.

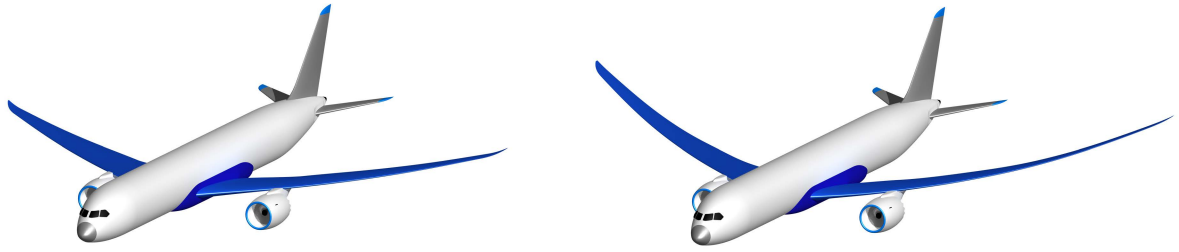

(a) Reference Aspect Ratio 10 configuration. (b) Novel Aspect Ratio 13 configuration.

Figure 4.1.: Transport aircraft demonstration example.

Contents

4.1. Description of the Aircraft Configurations

To investigate the influence of gusts on different wing geometries with varying structural stiffness, a transport aircraft configuration is designed to provide a common demonstration example. The configurations have the same fuselage cell, but different wing layouts. The aircraft design point for the configurations is $C_L = 0.5$ at *cruise-flight* with $Ma = 0.86$, $FL = 350$. It must be considered that the present work does not claim to present a fully optimized aircraft design concept. To give the work significant informative value, the aim is to ensure that the models used are sophisticated enough to capture most of the relevant physical phenomena. The models developed for this work are based on the content of the NASA Common Research Model (CRM) and undeflected (uCRM) models developed by Brooks [99, 104]. In addition to adjusting the wing area, specific modifications are made to the wing tip and root airfoil, including an adjustment of the twisting distribution along the span to achieve a suitable lift distribution for both configurations.

4.1.1. Aspect Ratio 10 Configuration

The first configuration serves as a reference and has an aspect ratio of 10.1, as can be found in modern commercial aircraft. Figure 4.2 presents an overview of the designed configuration. The wing has a size of $362\,\mathrm{m}^2$ with a design maximum takeoff weight (MTOW) of $230\,\mathrm{t}$. The wing geometric model is designed in its flight shape and is used to derive aerodynamic and structural models. A summary of all design parameters is provided in Table 4.1.

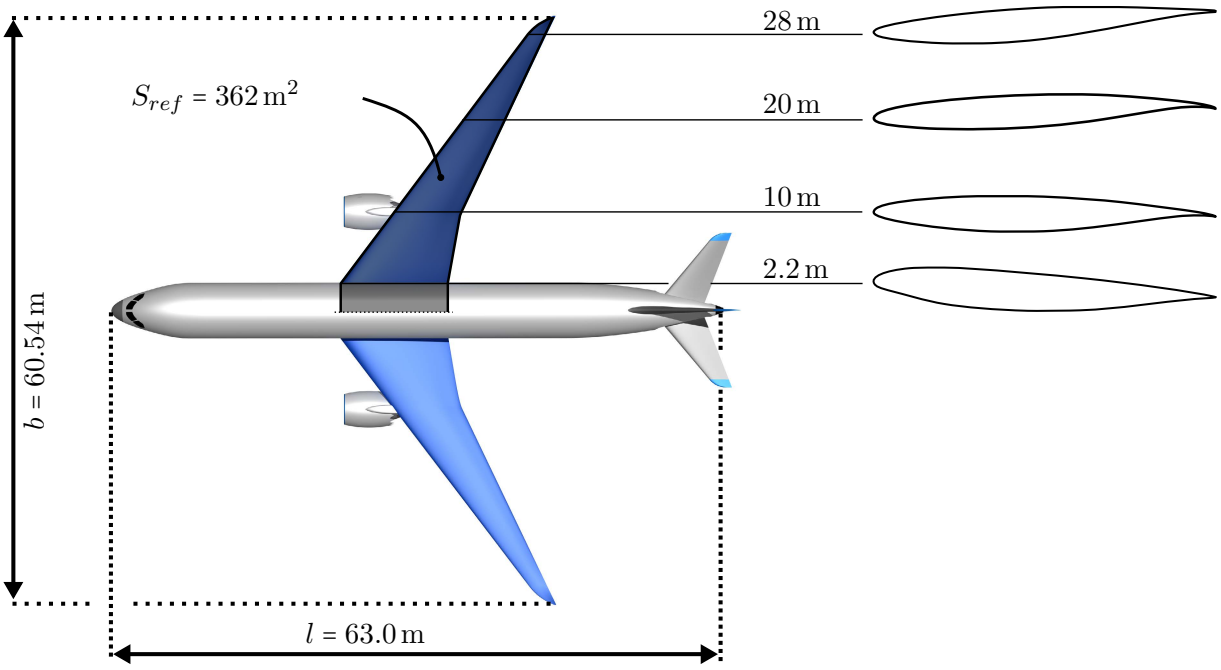

Figure 4.2.: Dimensions transport aircraft AR-10 configuration.

4.1.2. Aspect Ratio 13 Configuration

The second configuration in this study is based on the reference configuration, except that a slender wing with an aspect ratio of 13 is used. The other design parameters are kept constant to compare the two configurations with regard to the differences in wing shapes. The wing profiles shown in Figure 4.3 are adopted from the uCRM model [99, 104]. The wing tip twist is adjusted such that the

Table 4.1.: AR-10 aircraft specification.

Aspect Ratio	10.1		Reference area	362	m^2
Span	60.54	m	Root chord	11.584	m
Tip chord	1.867	m	MAC	6.34	m
1/4 chord Sweep	34.0	deg	fuselage length	63.0	m
MTOW	228	t	Design C_L	0.5	
Design Ma	0.86		Design altitude	FL 350	

scaled wing still achieves a smooth lift distribution. Additionally, the wing incidence is changed so that at the design point, the aircraft design C_L and wings $C_{L,wing}$ of the AR-10 and AR-13 configuration are coincident. This implies that both configurations have the same vertical wing root force. A summary of all design parameters is provided in Table 4.2.

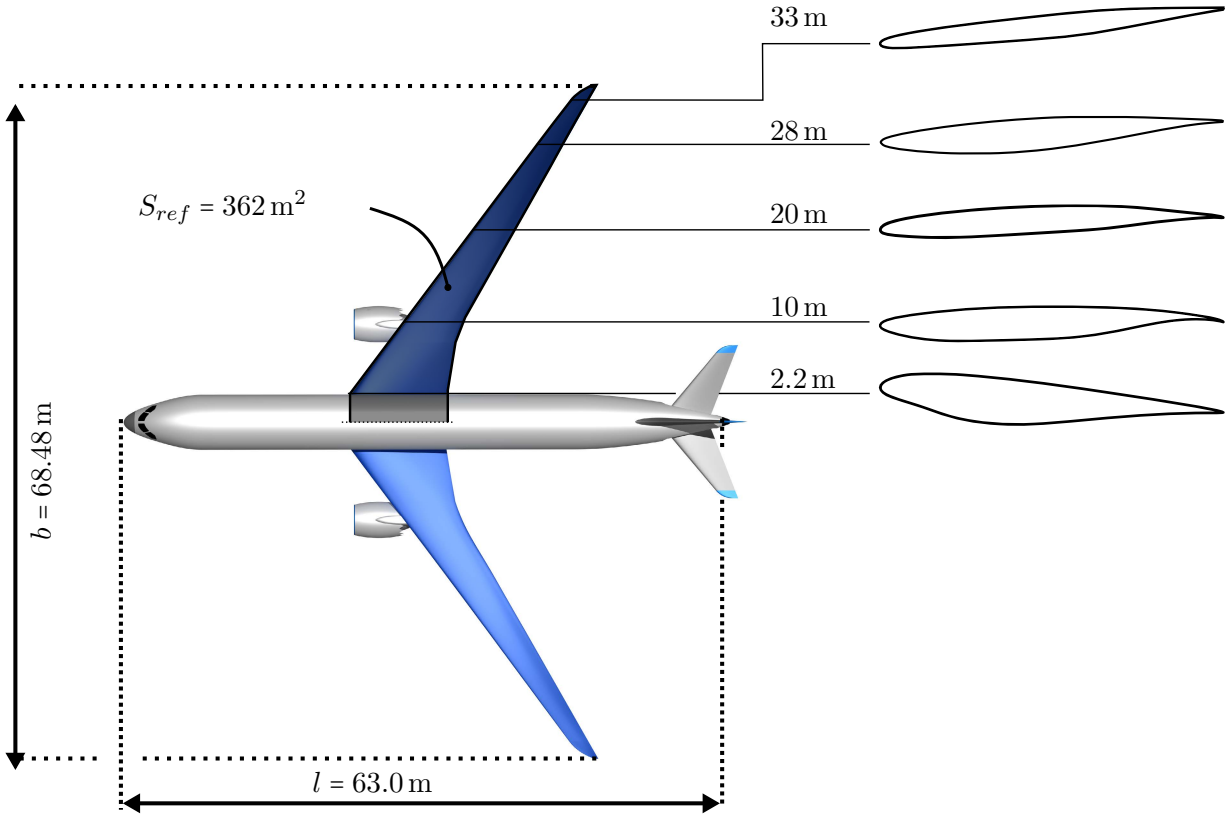

Figure 4.3.: Dimensions transport aircraft AR-13 configuration.

Table 4.2.: AR-13 aircraft specification.

Aspect Ratio	12.95		Reference area	362	m^2
Span	68.48	m	Root chord	10.466	m
Tip chord	1.800	m	MAC	5.25	m
1/4 chord Sweep	34.0	deg	fuselage length	63.0	m
MTOW	228	t	Design C_L	0.5	
Design Ma	0.86		Design altitude	FL 350	

4.2. Aerodynamic Modeling Setup

The lift forces of the predefined flight shapes are used for the structural design, that is why the computational setup starts with the aerodynamic model. The geometrical model developed in section 4.1 is used as a starting point. As described in the previous section, the aerodynamic load is determined by solving the RANS equation using CFD methods. Owing to the increasing geometric complexity, an unstructured tetrahedral computational mesh is selected as the discretization strategy. The computational domain and its dimensions are illustrated in Figure 4.4a. The volume mesh used for the far-field is shown in Figure 4.4b and the near-field with a higher cell density is shown in Figure 4.4c. In the aerodynamic modeling, the wing and fuselage are considered. Because the pitch moment of the aircraft is not explicitly trimmed by the empennage, it is not considered in the aerodynamic model. The same applies to the influence of the engine and its nacelle. To achieve efficient computational times, the model is set up as a half-model with a symmetrical boundary condition. The wing and fuselage surfaces are specified as non-slip walls. All other domain boundaries are handled as a far-field boundary conditions.

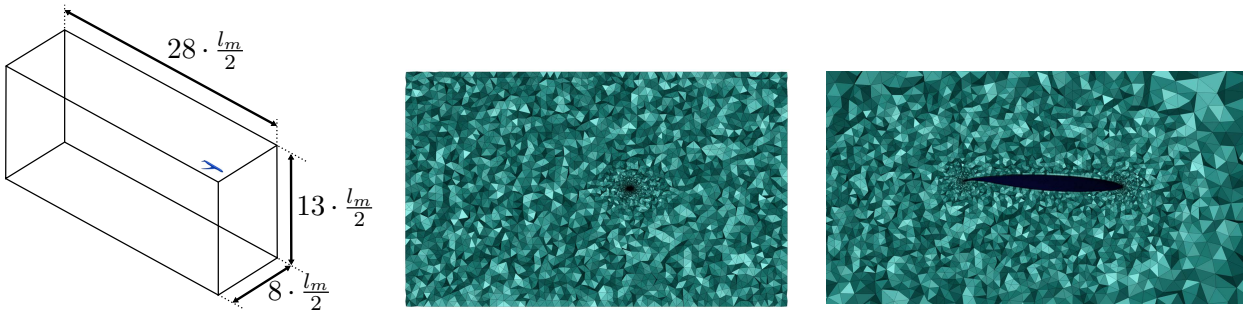

(a) Computational domain.

(b) Farfield mesh.

(c) Nearfield mesh.

Figure 4.4.: Computational domain and unstructured volume mesh.

To evaluate the appropriate grid resolution required to capture most aerodynamic characteristics, a grid convergence study is conducted. For this purpose, different volume meshes with different resolutions are set up. The lift coefficient C_l at an AoA of $\alpha = 1.5\,\mathrm{deg}$ under *cruise-flight* condition is used as an assessment criterion. The changes in C_l with increasing mesh size for the two aircraft configurations with AR-10 and AR-13 wings are shown in Figure 4.5a. Extensive transient simulation requires a compromise to obtain sufficient accuracy with reasonable computational effort. The grids used for the simulation are marked with a circle, comprising $N_{\text{AR-10}} \approx 30.7 \cdot 10^6$ and $N_{\text{AR-13}} \approx 34.9 \cdot 10^6$ cells. The *Spalart-Allmaras* turbulence model is also used in this study. To cover the boundary layer effects, a mesh inflation comprising 15 layers, with a first cell height of $0.004\,\mathrm{mm}$ is created. With this setup, the maximum y-plus values for the AR-10 and AR-13 configurations are $y^+_{\text{AR-10}} = 1.391$ and $y^+_{\text{AR-13}} = 1.397$, respectively.

The lift curve slopes of the rigid-body configurations during *cruise-flight* are shown in Figure 4.5b. The fuselages are identical for both configurations, and as already mentioned, both wing configurations have the same $C_{L,wing}$ at the design point. Thus, the vertical wing root shear load is identical, which is not true for bending and torsional moments, due to the different wing planforms. Although the two fuselages are identical, they have different lift contributions due to the different velocity downwash fields of the two wings. Therefore, to ensure the same overall lift, the trimmed AoA must be adjusted accordingly. With the design $C_l = 0.5$, the trimmed AoA is $\alpha_{trim} = 2.099\,\mathrm{deg}$ for the AR-10 configuration and $\alpha_{trim} = 2.567\,\mathrm{deg}$ for AR-13. The results refer to the rigid-body configuration and are therefore only valid for the design points. Hence, the analysis of the elastic wing structure and its interaction with aerodynamics are discussed in more detail in section 5.1.

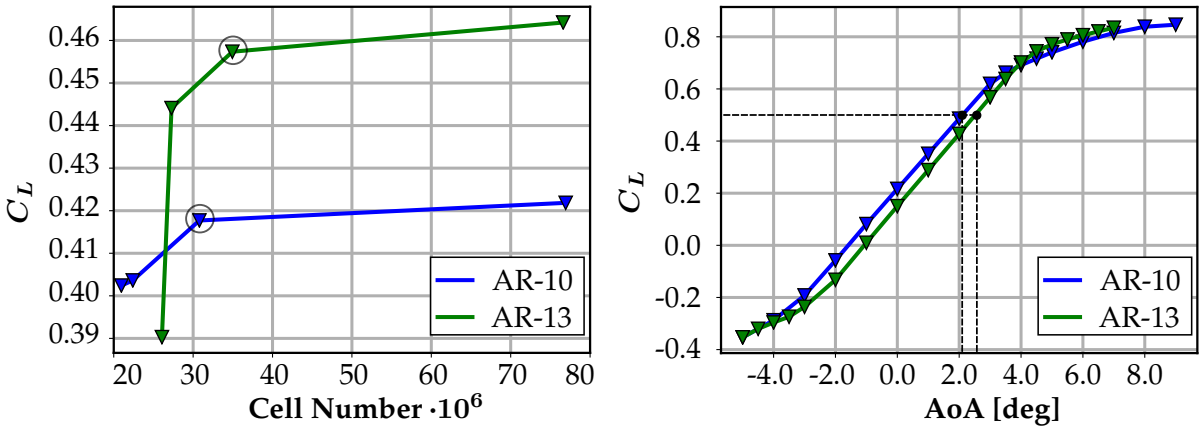

(a) Tau-RANS mesh convergence study.

(b) Lift slope in cruise flight condition.

Figure 4.5.: C_L results of the AR-10 and AR-13 rigid aircraft configuration.

4.2.1. Steady Aerodynamic Assessment in Flight Shape

Because wings feature different planforms, they also inherently differ in their aerodynamic characteristics. Figure 4.6 shows the lift distribution of both configurations in trimmed *cruise-flight*, which means $C_L = 0.5$, $Ma = 0.86$ at $FL = 350$. The respective elliptical distributions are indicated by dashed lines as references. Although the total lift is identical, a higher root bending moment is obtained for the AR-13 wing owing to its larger span.

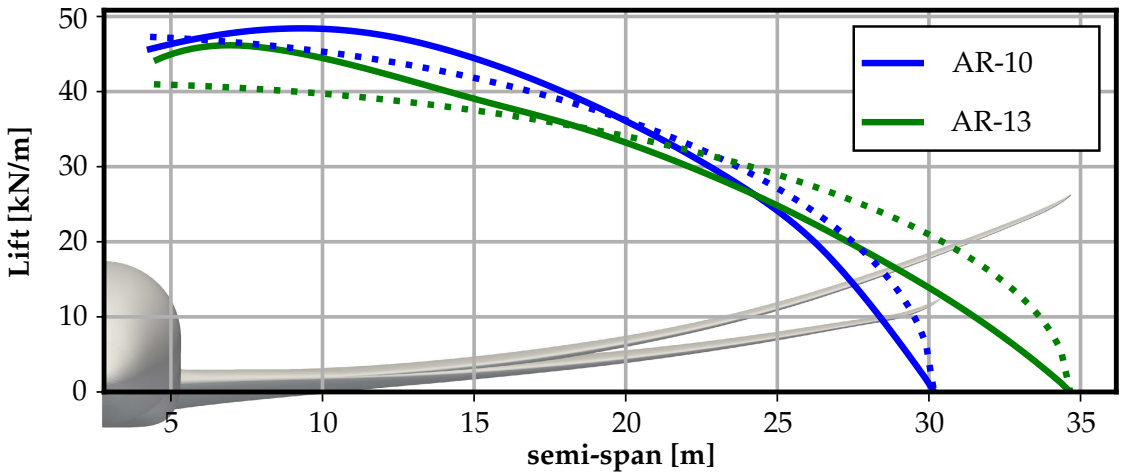

Figure 4.6.: Lift distribution in cruise flight at $Ma = 0.86$, $FL = 350$, theoretical elliptical distribution depicted as dashed lines.

All loads are related to the wing-root reference point to calculate the internal loads at the wing root. Because of different root chord lengths, the latter is $\vec{X}_{ref}^{root} = \begin{bmatrix} 4.874\,\mathrm{m} & 2.52\,\mathrm{m} & -0.3\,\mathrm{m} \end{bmatrix}^T$ for the AR-10 and $\vec{X}_{ref}^{root} = \begin{bmatrix} 4.462\,\mathrm{m} & 2.52\,\mathrm{m} & -0.3\,\mathrm{m} \end{bmatrix}^T$ for the AR-13 configuration.

The aerodynamic root section loads at the *cruise-flight* design point evaluated in the global system are listed in Table 4.3. The difference in the vertical shear force (S) in the AR-13 configuration is in order of $0.3\,\%$, which is considered sufficient for the subsequent investigations.

Table 4.3.: Wing root section forces at cruise flight.

	Vertical Shear Force **(S)**	Bending Moment **(M)**	Torque Moment **(T)**
#AR-10	$997.050\,\mathrm{kN}$	$11.401\,318 \cdot 10^6\,\mathrm{N\,m}$	$-6.771\,026 \cdot 10^6\,\mathrm{N\,m}$
#AR-13	$996.517\,\mathrm{kN}$	$12.696\,222 \cdot 10^6\,\mathrm{N\,m}$	$-7.988\,907 \cdot 10^6\,\mathrm{N\,m}$

Figure 4.7 and Figure 4.8 show the pressure distributions of the two configurations from which the aerodynamic loads are calculated. Based on the profile cuttings, the transonic flow region are identified in both configurations, which are bound by compression shocks.

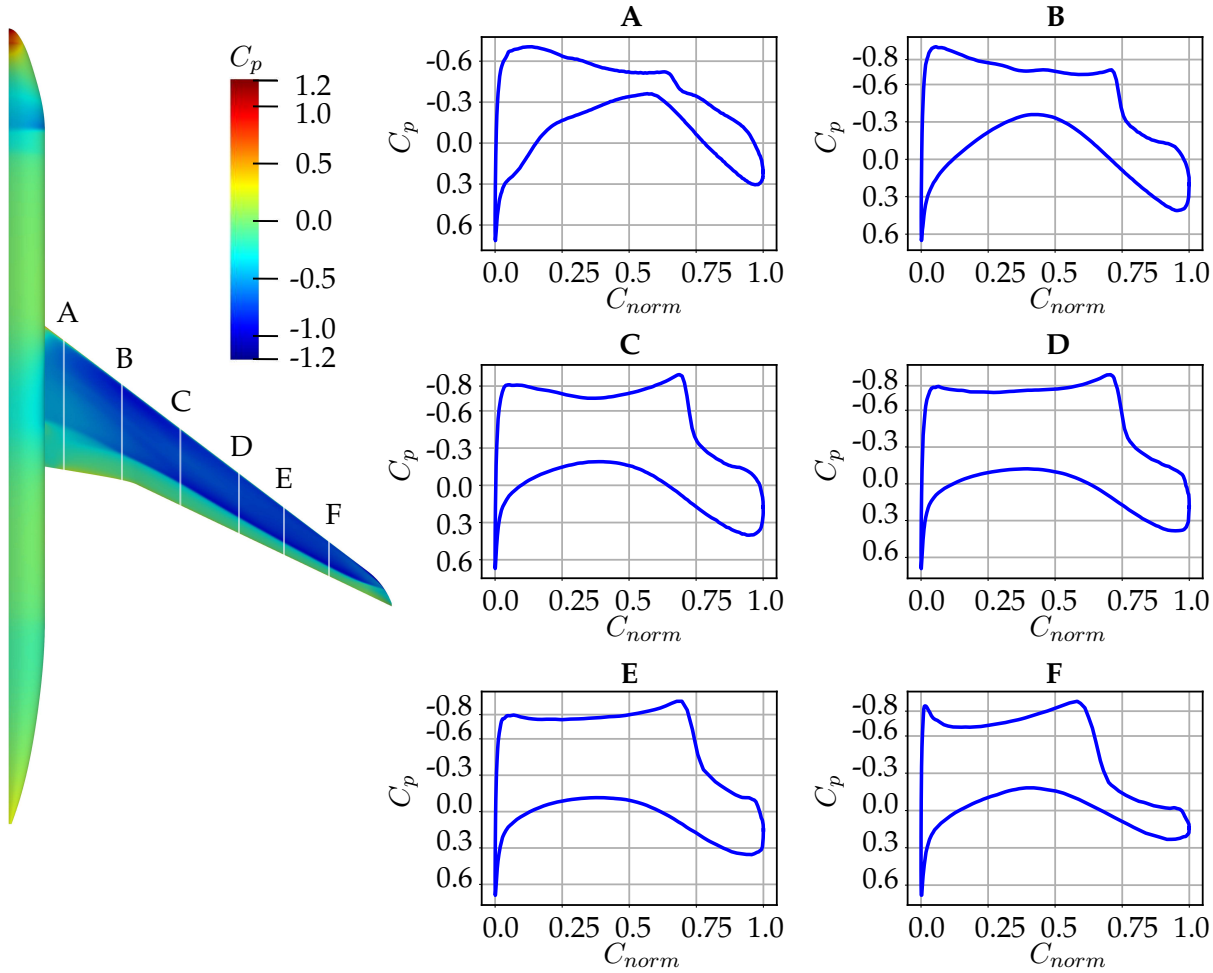

Figure 4.7.: C_p distribution of the AR-10 configuration at $Ma = 0.86$, $FL = 350$.

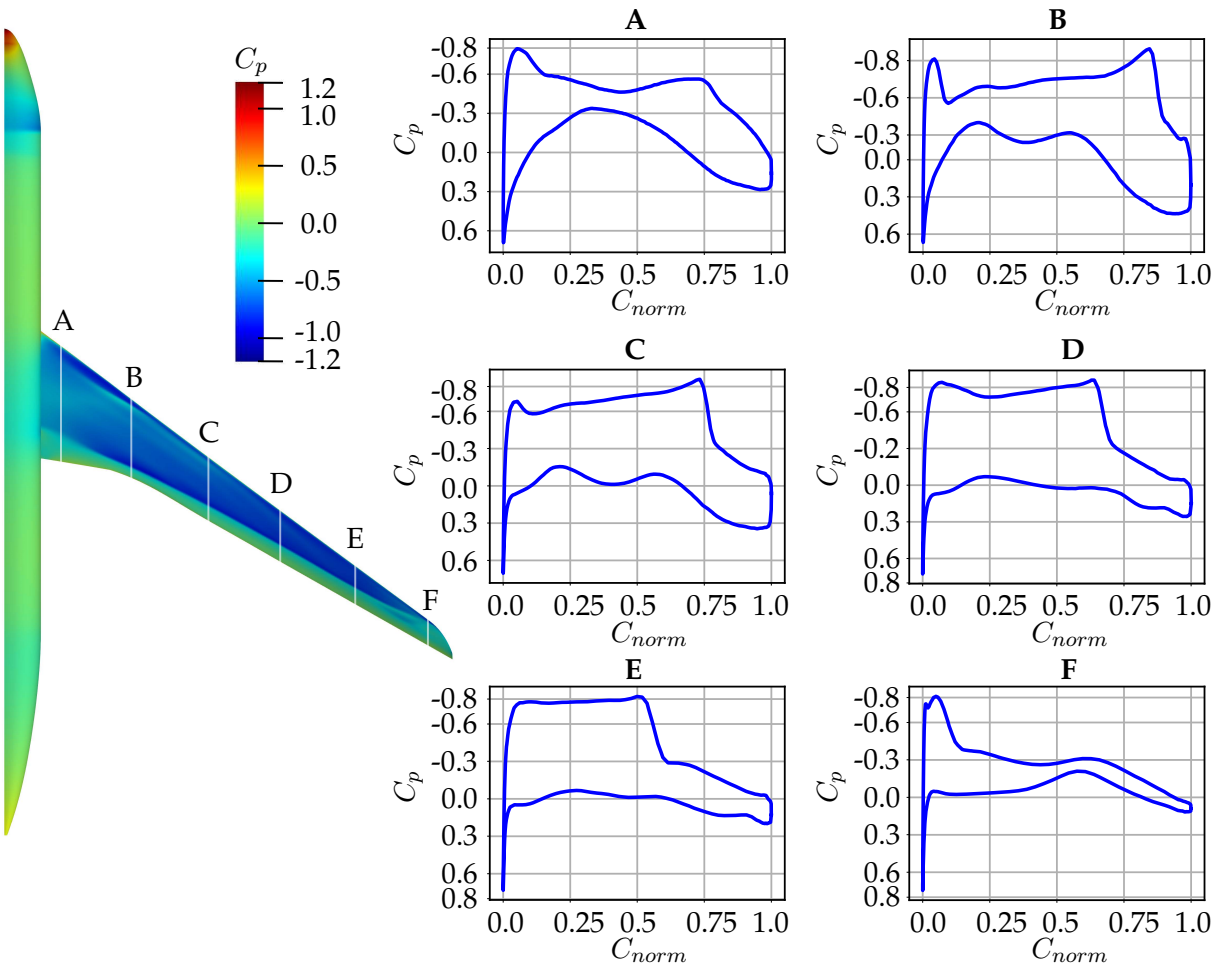

Figure 4.8.: C_p distribution of the AR-13 configuration at $Ma = 0.86$, $FL = 350$.

4.3. Structural Design and Modeling

Since the early days of aviation, load bearing wing box design has become a standard in the structural wing design of transport aircraft. The main components are the front and rear spar together with a stringer-stiffened upper and lower shell. The main added feature of the stringers is the reduction of the free buckling length of the wing shell. Moreover, they contribute to the bending stiffness of the wing. In addition, ribs are used to define the cross-section of the wing, serving both structural and aerodynamic functions. An overview of aircraft structural design is provided in Sensmeier [75] and Niu [25]. The basic structural design for both wing configurations is selected similarly, but there are variations in the number of ribs and stringers due to the different wing planforms. As previously mentioned, the flight shape is used as the starting point from which the internal structure is designed.

The deformations and internal structural loads are calculated using the FE method, as implemented in *NASTRAN SOL400*. The starting point for structural modeling is the geometric wing model of the flight shape. The discretization is carried out using shell elements (CQUAD4 and TRIA3) for all thin-walled components, such as shells, spars, and ribs. The modeling of the stringers is done using 1d beam elements (CBEAM). Because the focus of this study is on aircraft wings, the fuselage is assumed to be rigid and thus not explicitly modeled.

4.3.1. Structural Layout of the Aspect Ratio 10 Configuration

The structural model of the wing for AR-10 configuration is illustrated in Figure 4.9. Each half wing consists of 37 wing ribs with stiffening elements, as shown in Figure 4.10b. The upper and lower wing shells have 13 and 8 sizing patch zones, respectively. In addition, both shells are supported by 21 stringers, which have a T-section of constant thickness and variable web height. The engine inertia is considered with seven discrete mass points and connected to the wing box trough an rigid interpolation element (RBE3).

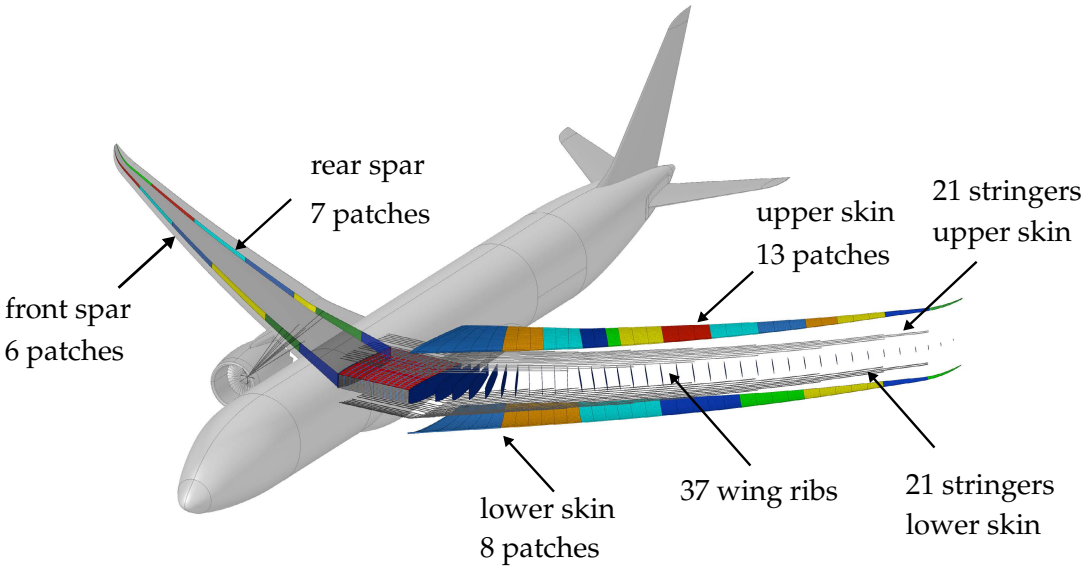

Figure 4.9.: General view of the structural layout of the AR-10 wing configuration, included patch zone definition for structural sizing.

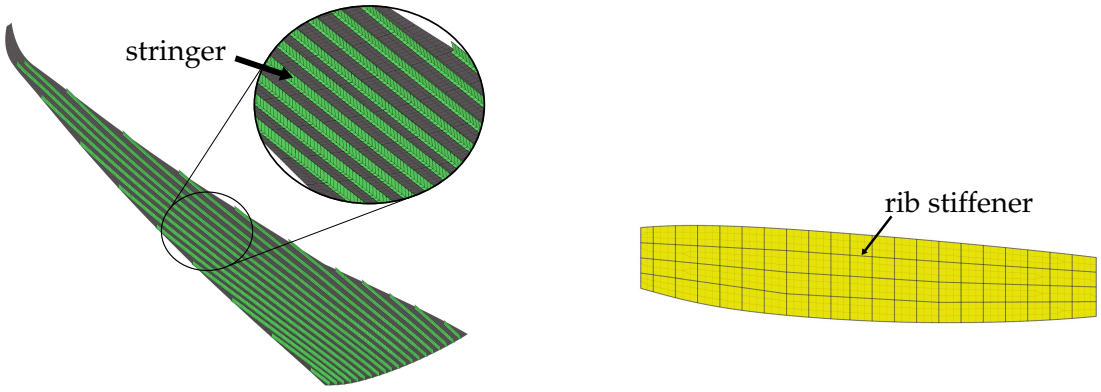

(a) Lower wing shell and stringer.

(b) Wing rib including rib stiffener.

Figure 4.10.: Detailed view of the AR-10 FEM model, wing and ribs as shell elements, stringer and stiffener as beam elements respectively. The cross-section of the beam elements is displayed for illustration purposes.

4.3.2. Structural Layout of the Aspect Ratio 13 Configuration

A structural model of the AR-13 wing is shown in Figure 4.11. In general, the same structural layout concept is used, as shown in Figure 4.10b. However, due to the slender wing, there are different numbers of individual components. With the same spacing, this results in 17 stringers for the upper

and lower shells, which in turn are assumed to have *T*-section. The shell shape is supported by 46 ribs. For structural sizing, the upper and lower shells are divided into 13 and 8 design zones, respectively.

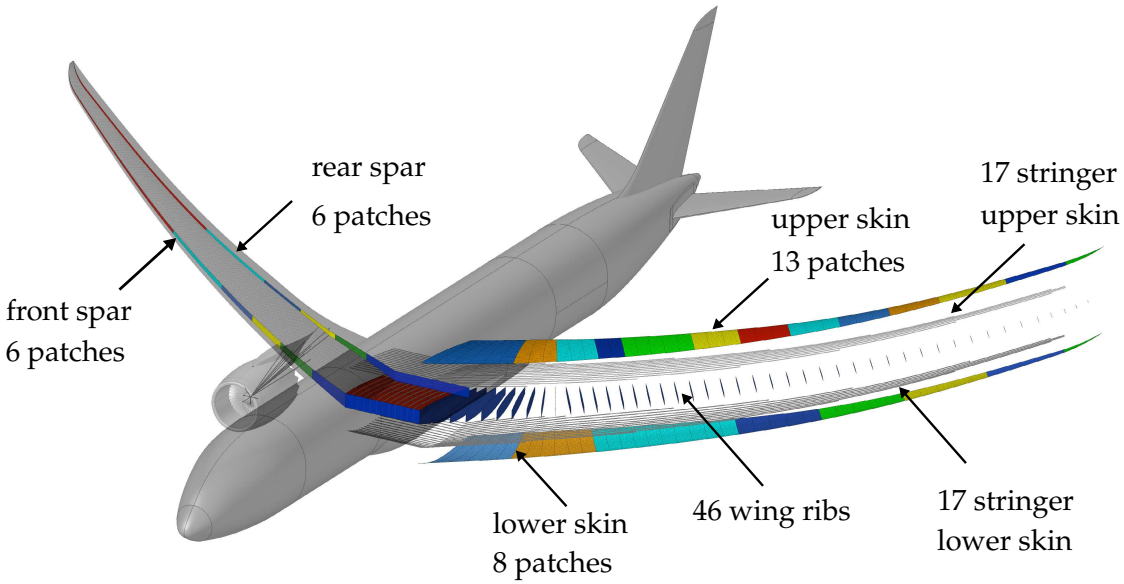

Figure 4.11.: General view of the structural layout of the AR-13 wing configuration, included patch zone definition for structural sizing.

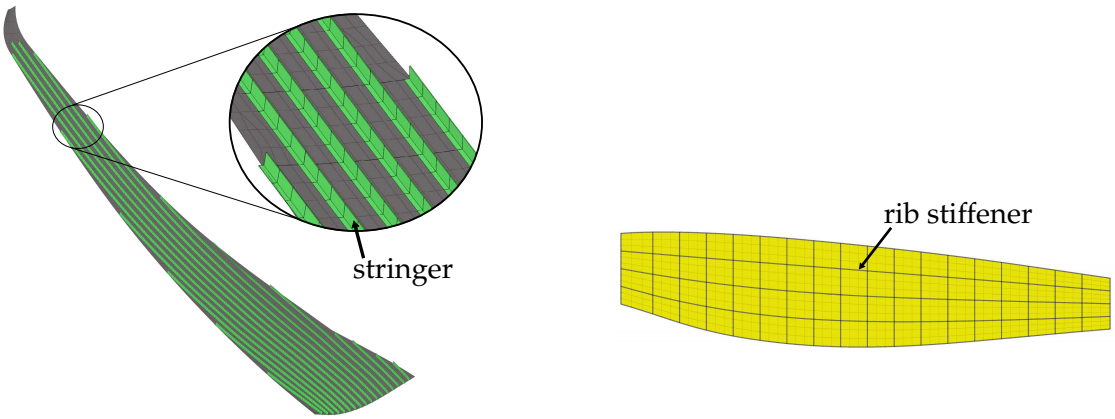

(a) Lower wing shell and stringer.

(b) Wing rib including rib stiffener.

Figure 4.12.: Detailed view of the AR-13 FEM model, wing and ribs as shell elements, stringer and stiffener as beam elements respectively. The cross-section of the beam elements is displayed for illustration purposes.

4.3.3. FEM Boundary Conditions

The fuselage attachment is modeled by displacement boundary conditions, as shown in Figure 4.13. To reduce the computational time, only half of the wing is modeled, and symmetry boundary conditions on the symmetry plane are applied. The connection to the fuselage is modeled at the wing root and corner nodes between the rib and lower wing shell. Rigid-body motions are not considered under the given boundary conditions. This is justified in terms of a quasi-steady simulation in the trimmed flight condition. For the transient gust simulation, this simplification allows investigations of the structural wing flexibility without considering the influence of the horizontal tail and control commands of the pilot or autopilot.

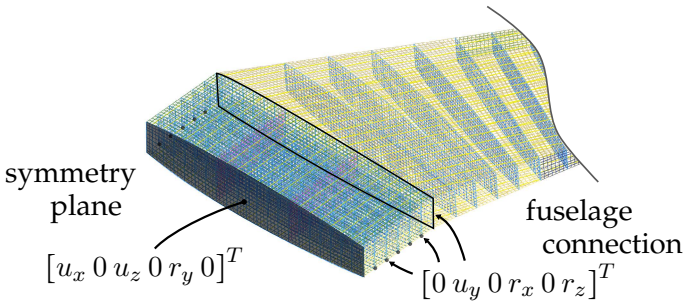

Figure 4.13.: FEM boundary condition, center wing box, structural support and fuselage connection.

4.3.4. Composite Material Properties

The composite structures are modeled as described in subsection 2.1.3. For the initial design, the reference material *AS4* (#mat-ref), with the single ply data listed in Table 4.4, is used.

Table 4.4.: Single ply properties: **reference material**.

$\mathbf{E_{11}}$	$\mathbf{E_{22}}$	$\mathbf{G_{12}}$	$\mathbf{G_{13}}$	$\boldsymbol{\nu_{12}}$	$\boldsymbol{\rho}$
138 GPa	10.05 GPa	4.7 GPa	3.36 GPa	0.31	$1620\,\mathrm{kg\,m^{-3}}$
$\mathbf{X_t}$	$\mathbf{X_c}$	$\mathbf{Y_t}$	$\mathbf{Y_c}$	$\mathbf{S}$	
2.328 GPa	1.568 GPa	0.056 GPa	0.351 GPa	0.117 GPa	

The *ABD*-matrix is calculated by defining the stacking sequence, ply thickness, and fiber orientation angle to describe the laminate stiffness. In this study, two standard laminates are defined. The first layup is selected such that a higher in-plane stiffness in $0\,\mathrm{deg}$ direction is achieved. The second layup is characterized by an increased contribution to shear stiffness. The stacking sequence of both laminates can be seen in Table 4.5, where the index represents the percentage of total thickness.

Table 4.5.: Layup definition of bending (b) and shear (s) laminate.

bending laminate (b):	$[0.0_{70.0}, \pm 45.0_{20.0}, 90.0_{10.0}]_S$
shear laminate (s):	$[0.0_{20.0}, \pm 45.0_{70.0}, 90.0_{10.0}]_S$

In Figure 4.14, the in-plane stiffness distribution of $\tilde{A}_{11}$ is shown as a polar diagram, with the main stiffness direction $0\,\mathrm{deg}$ for bending in blue and $\pm 45\,\mathrm{deg}$ for shear in green. The stiffness values are normalized with the largest value of the single ply, which is in $0\,\mathrm{deg}$ for the bending laminate.

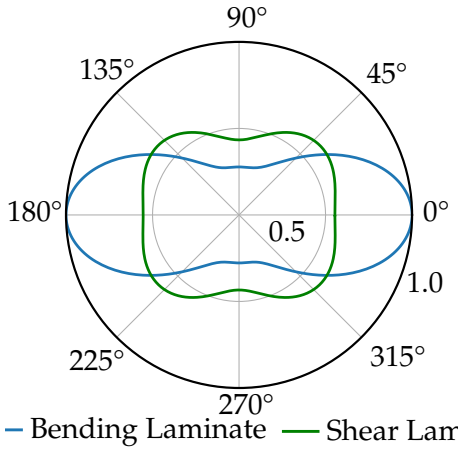

Figure 4.14.: Normalized $\tilde{A}_{11}(\theta)$ stiffness distribution of the bending and shear laminate.

Stringer and Stiffener Properties

The stringers, rib stiffeners, and flanges are modeled using beam elements with a constant thickness. Due to the dominant in-plane load, they are built by means of the previously defined bending laminate (b). Using beam elements, laminate failure is related to normal stresses in the direction of the stiffening elements. The corresponding material properties and allowable stress ranges are determined using laminate analysis in *elamX2* [4]. The resulting material model is listed in Table 4.6. The failure stress is defined as the stress in $0\,\mathrm{deg}$ direction at which the first laminate ply fails. For tensile stress, using the Tsai-Wu failure theory, these are the $\pm 45\,\mathrm{deg}$ plies. In the case of compressive loads, the limited failure case for many thin-walled sections is not the strength but rather the structural stability. Therefore, the maximum compressive stress corresponds to the critical buckling load. For this purpose, an average length of $350\,\mathrm{mm}$ and height of $80\,\mathrm{mm}$ is used to determine the critical buckling stress.

Table 4.6.: Stringer material properties: **reference material**.

$\mathbf{E_{11}}$	$\boldsymbol{\nu_{12}}$	$\mathbf{X_t}$	$\mathbf{X_c}$	$\boldsymbol{\rho}$
$104\,\mathrm{GPa}$	$0.35\,\mathrm{GPa}$	$512.7\,\mathrm{MPa}$	$-265.1\,\mathrm{MPa}$	$1620\,\mathrm{kg\,m^{-3}}$

The modeling of the stringers and stiffening elements described here represents a simplification. However, because the influence of stiffness is of primary interest, this assumption is reasonable for the case investigated here.

Generic Material Properties

In addition to the reference material, generic materials that do not exist technically are introduced; however, they are used in the simulation for stiffness variation. These materials are essentially different in terms of material stiffness. For these materials, the following assumptions are made:

- The generic material strengths are assumed to be identical to those of the reference material (AS4).
- To avoid structural configurations with significant deviations in the structural mass distribution, all materials have the same density, $\rho_i = \rho_{\#mat-ref}$.

Three additional generic material models are implemented, as listed in Table 4.7. In comparison with the reference, one is assigned with an increased material stiffness (#mat-1), another is provided with a reduced stiffness (#mat-2), and one with below-average soft material stiffness (#mat-3). As mentioned, these materials are purely hypothetical in nature but essentially adapted from existing materials (*IM6*, *T600SC*, *S-ply*). Their properties are summarized in Table 4.7.

4.3.5. Wing Shell Composite Layup Definition

The predefined bending (b) and shear (s) laminates are used to define the load-carrying structural components of the wing. Each shell is designed in layers along the span with the length specified by the wing patches. The definition of the patches and the corresponding layup of the upper and lower wing shells are depicted in Figure 4.15 and Figure 4.16 for the AR-10 configuration. The composite layer definition of the AR-13 configuration is specified using the same concept as that of the AR-10 wing. However, due to the geometrical layout, the designed patch zones have different sizes. The upper and lower wing shells are shown in Figure 4.17 and Figure 4.18, respectively. Layer-11 and -12 serve a particular function in determining the stiffness distribution. Layer-11 provides additional reinforcement for the engine support, and layer-12 provides an independent, non-root-dominated

Table 4.7.: Surrogate-material properties.

	#mat-1	#mat-ref	#mat-2	#mat-3
$\mathbf{E_1}$	203 GPa	138 GPa	109 GPa	60 GPa
$\mathbf{E_2}$	11.2 GPa	10.05 GPa	7.7 GPa	25.0 GPa
$\mathbf{G_{12}}$	8.4 GPa	4.7 GPa	4.5 GPa	4.7 GPa
$\mathbf{G_{13}}$	6.0 GPa	3.36 GPa	3.2 GPa	3.36 GPa
$\boldsymbol{\nu_{12}}$	0.32	0.31	0.28	0.23
$\boldsymbol{\rho}$	$1620\,\mathrm{kg\,m^{-3}}$			
$\mathbf{X_t}$, $\mathbf{X_c}$	2.328 GPa, 1.568 GPa			
$\mathbf{Y_t}$, $\mathbf{Y_c}$, $\mathbf{S}$	56.0 MPa, 351.0 MPa, 117 MPa			
$\mathbf{E_{11,stringer}}$	153.0 GPa	104.0 GPa	82.4 GPa	51.1 GPa
$\boldsymbol{\nu_{12,stringer}}$	0.32	0.315	0.296	0.231

outer wing reinforcement. The total layer thickness and thus the percentage of bending and shear laminate per layer is left variable, and defined in the subsequent sizing process. All other components, such as the ribs and spars are defined consistently by the shear laminate.

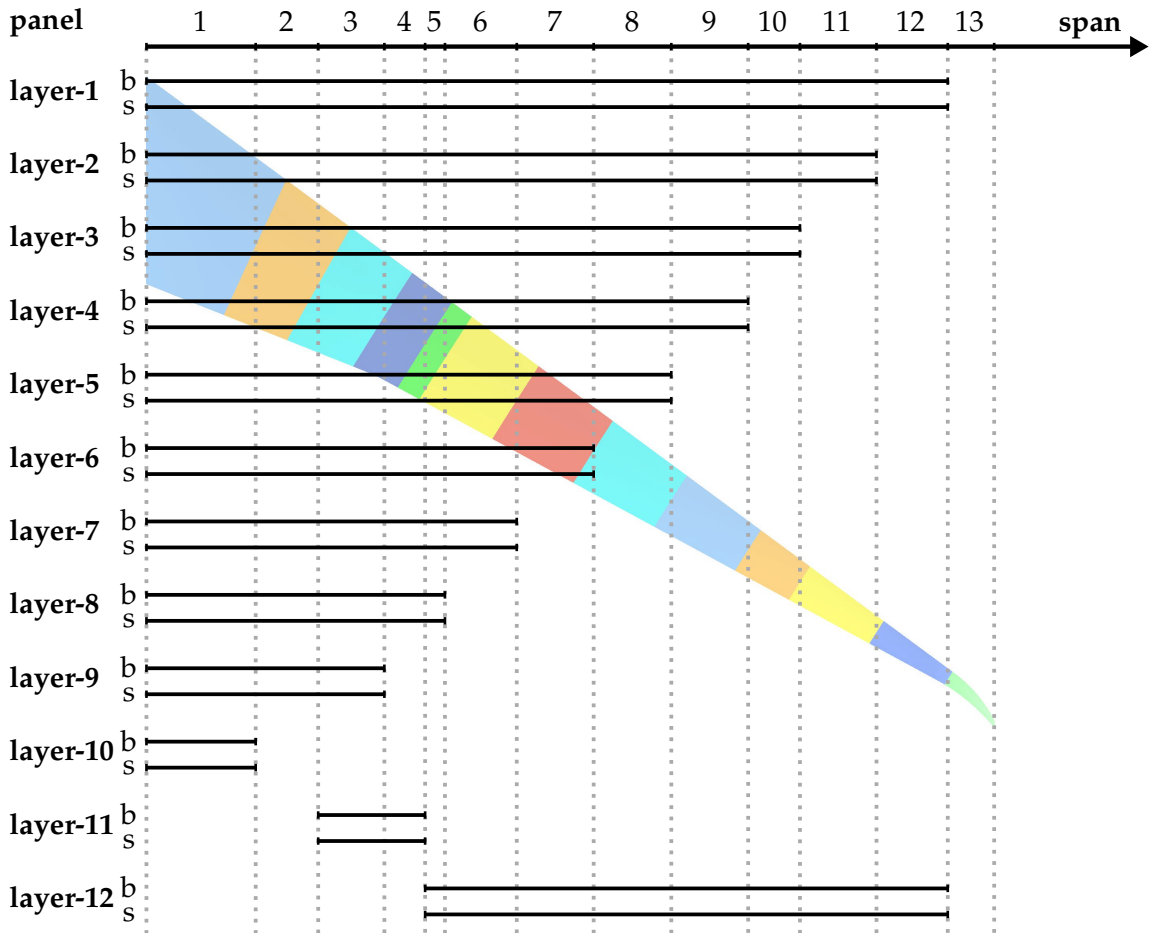

Figure 4.15.: AR-10 upper wing shell composite layup definition, layer consisting of variable thickness of (b) and (s) laminate, correlation to the FE Model patch definition.

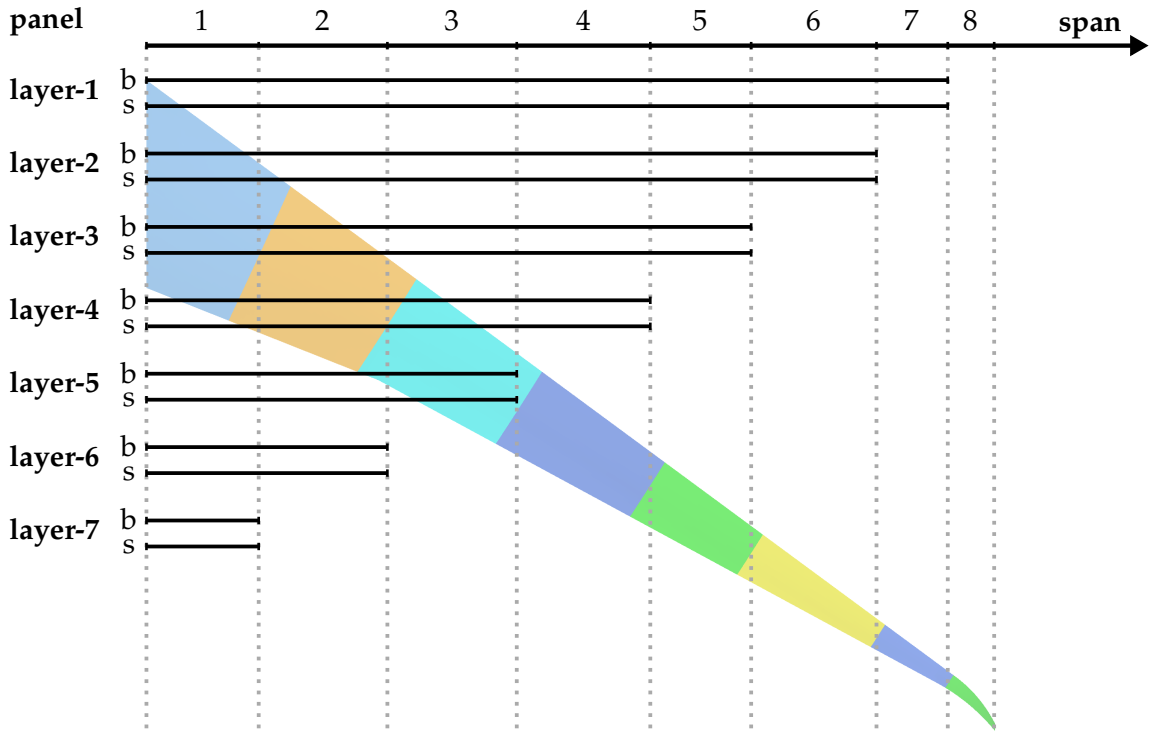

Figure 4.16.: AR-10 lower wing shell composite layup definition, layer consisting of variable thickness of (b) and (s) laminate, correlation to the FE Model patch definition.

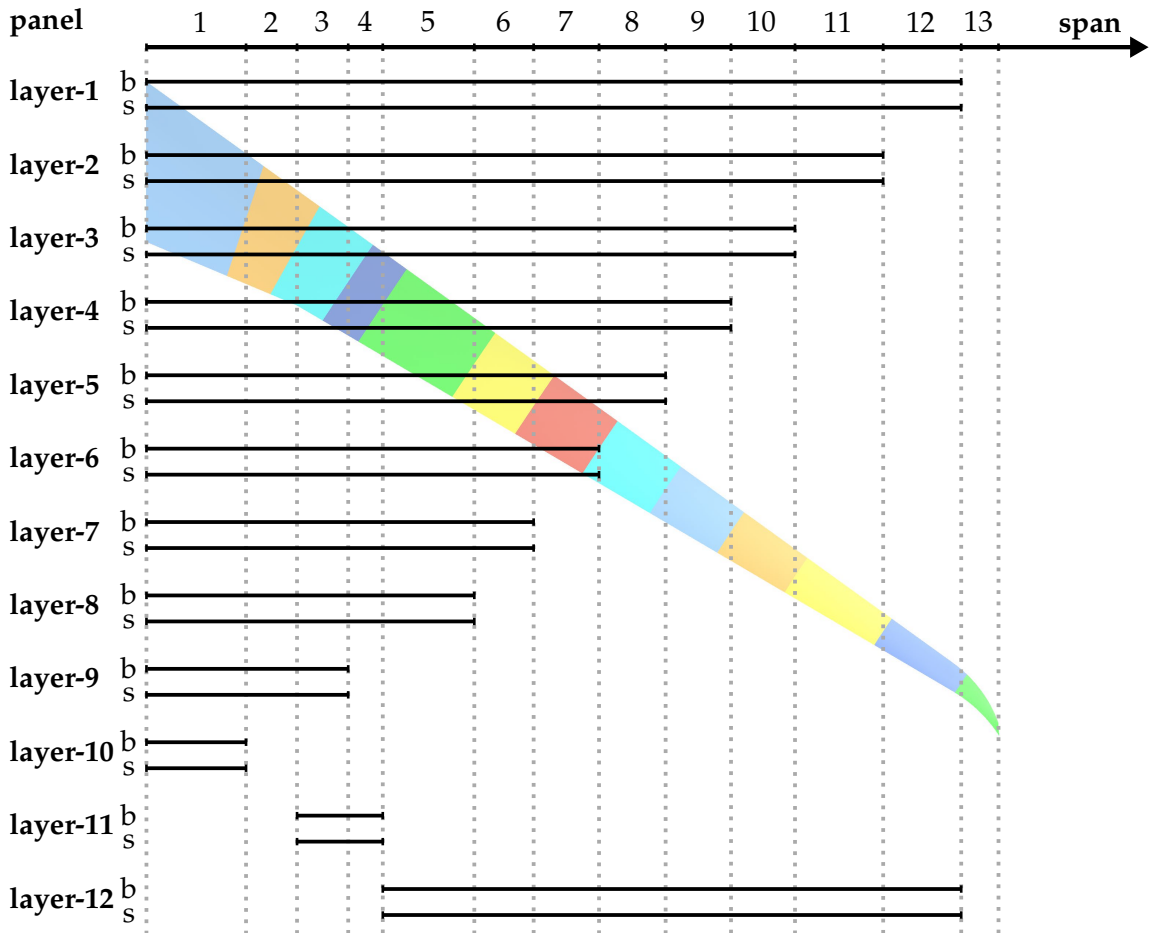

Figure 4.17.: AR-13 upper wing shell composite layup definition, layer consisting of variable thickness of (b) and (s) laminate, correlation to the FE Model patch definition.

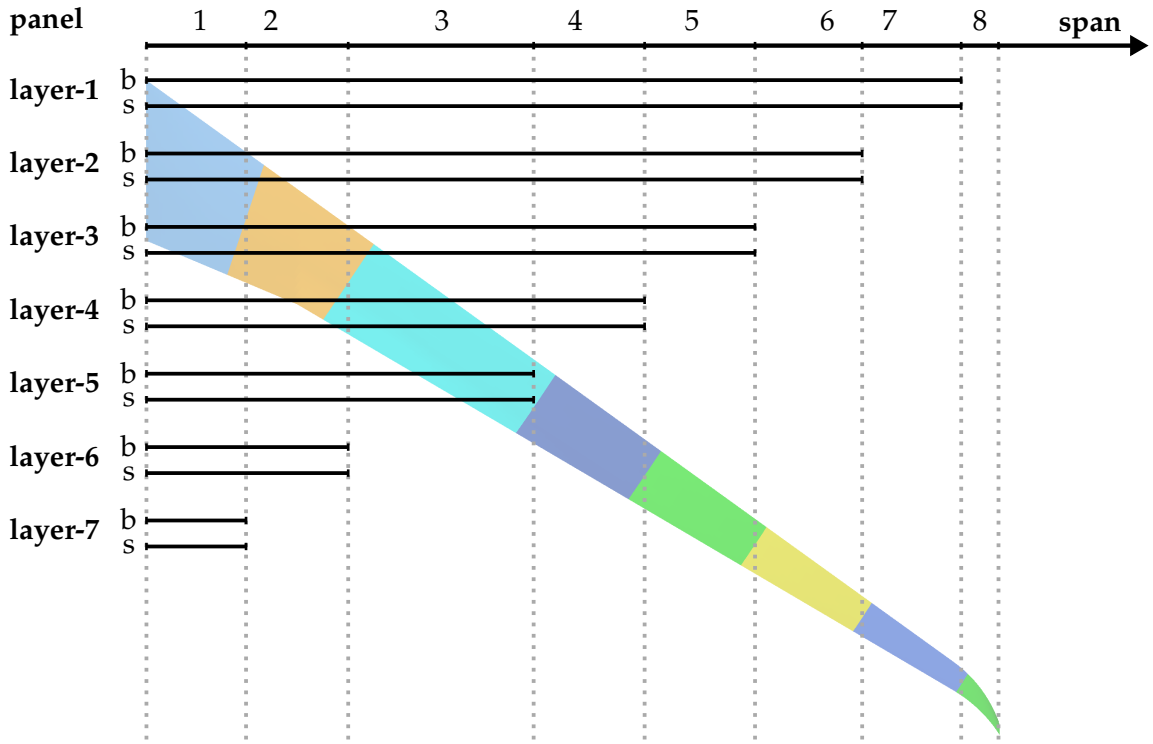

Figure 4.18.: AR-13 lower wing shell composite layup definition, layer consisting of variable thickness of (b) and (s) laminate, correlation to the FE Model patch definition.

4.3.6. Mass Modeling

The modeling of aircraft masses is an essential part of the overall aircraft model, as both aircraft dynamics and loads are considerably affected. Owing to unavailable information, a mass model is set up for the studies under certain assumptions. The mass model for the flexible wings consist of four parts:

1. **wing structural mass:** which is inherently determined by the material density in the FE model.
2. **non-structural wing mass:** comprising the weight of the subsystem, such as leading and trailing edge devices, landing gear, and engine.
3. **fuel mass:** wing tank fuel weight
4. **remaining mass:** structure components which are not explicitly modeled such as fuselage and payload.

The non-structural wing masses are modeled by discrete mass points, which are attached to the leading or trailing edge of the wing via *RBE3* elements. The same applies to the engine mass, which is applied to the underside of the wing via seven discrete masses as shown in Figure 4.9 and Figure 4.11.

Fuel Mass Model

The fuel tanks in the wing are defined by the rib bays, each extending from rib to rib and limited by spars. The exact volume and mass and inertia properties are determined by a separate FE volume model, as shown in Figure 4.19a. For the actual investigations, the volume model is not used, but rather a point mass model for each rib bay, as represented in Figure 4.19b. The corresponding mass

properties, such as mass m and inertia $\underline{I}$, are derived from the previously calculated fuel volume model. The point mass is located at the center of gravity of the rib bay and is attached to the main structure with *RBE3* elements.

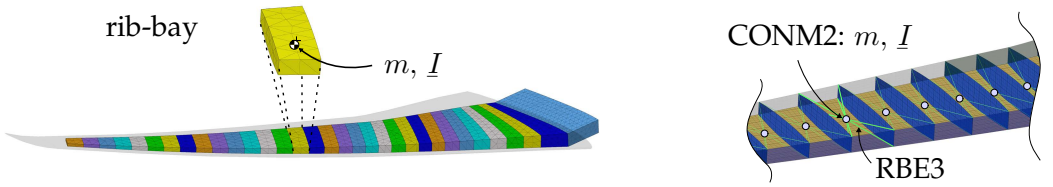

(a) Wing rib-bays FE volume model.

(b) Fuel model with FE concentrate mass model.

Figure 4.19.: Wing tank fuel mass model.

No detailed fuel burn scenario is available for the studies considered here. Therefore, the rib bays will later be combined into three main wing tanks, with the two fuel loading conditions assumed, as shown in Table 4.8. Fuel model-1 is used for the beginning *cruise-flight* and model-2, representing the *cruise-flight* end, meaning the beginning of *approach-flight*.

Table 4.8.: AR-10 and AR-13 aircraft fuel level models.

fuel model	**centre tank**	**wing fuel tank**			**description**
		FT-1	FT-2	FT-3	
model-1	100 %	100 %	100 %	100 %	MTOW
model-2	0 %	0 %	0 %	100 %	end cruise, start approach flight
model-3	100 %	0 %	0 %	0 %	structural sizing

AR-10 Mass Model

The distribution of the non-structural leading and trailing edge subsystems is shown in Figure 4.20a. It is assumed that these are linearly distributed along the span direction. The total weight of the leading edge and trailing edge systems are 1200 kg and 2189 kg, respectively. Further system masses, which are attached to the wing, are the main landing gear with 4077 kg and engine with 6118 kg.

Together with the center fuel tank, the configuration features a total fuel mass of 108.4 t. The wing tanks, which are distributed as shown in Figure 4.20b, hold a total of 92.472 t, distributed over the three tanks FT-1 to FT-3. A detailed summary of all the system masses is provided in the later comparison of the configurations.

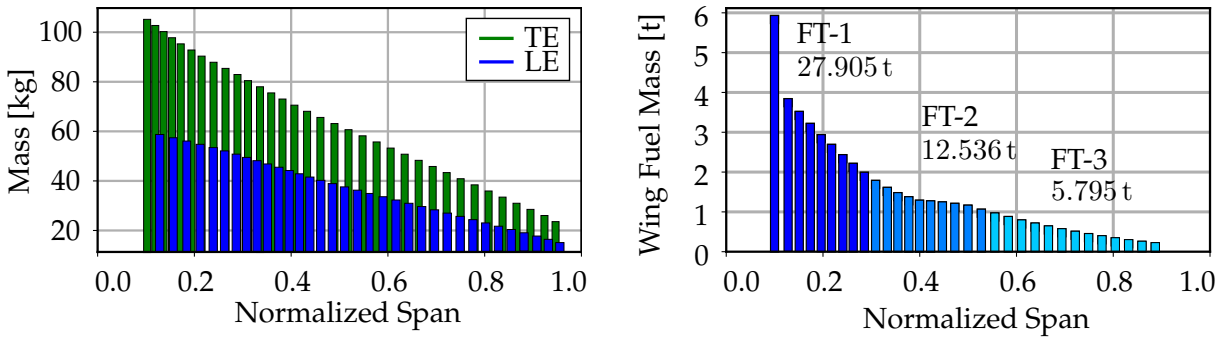

(a) AR-10 leading (LE) and trailing (TE) edge masses.

(b) AR-10 wing fuel tank masses.

Figure 4.20.: AR-10 non-structural discrete masses over normalized wing span.

AR-13 Mass Model

The wing leading edge and fuel mass are again modeled according to subsection 4.3.6. Due to the different geometric dimensions of the wing, the fuel tank volumes, and mass distributions are different from those of the AR-10 wing. As shown in Figure 4.21b, the fuel tanks are combined into three main tanks, with the outer tanks chosen to have approximately the same masses as in the AR-10 configuration. A linear distribution along the span is assumed for non-structural system masses.

The resulting distribution is shown in Figure 4.21a, with a total mass of $1440\,\mathrm{kg}$ and $2962\,\mathrm{kg}$ used for the leading edge and trailing edge, respectively. All the other system masses are assumed to be the same as those for the AR-10 configuration.

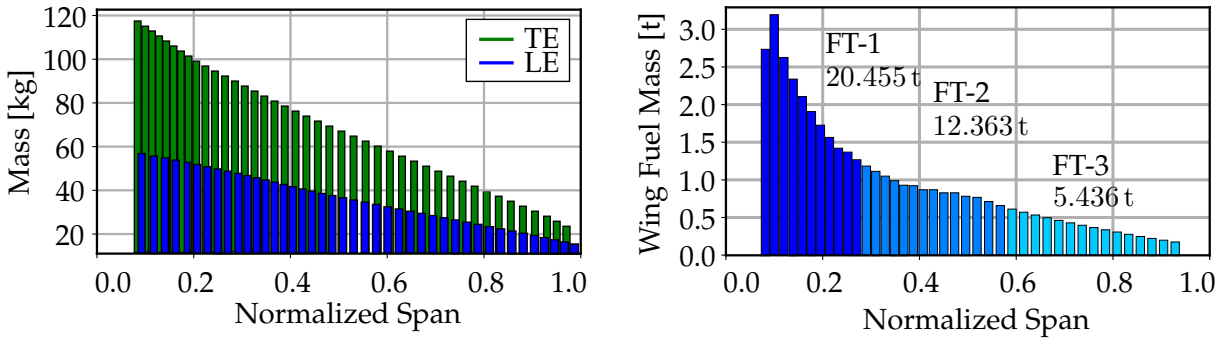

(a) AR-13 leading (LE) and trailing (TE) edge masses.

(b) AR-13 wing fuel tank masses

Figure 4.21.: AR-13 non-structural discrete masses over normalized wing span.

4.4. Structural Wing Sizing and Optimization Task

The selection of structural design variables, even if simplified, leads to the simultaneous consideration of many variables in the optimization process. The design of the wing is therefore formulated as an optimization task and is solved using the methods and algorithms provided by *NASTRAN-SOL200*.

In this study, all structural components are implemented using the same composite materials within one configuration, as defined in Table 4.7. Each patch zone, as described in the previous section, is associated with the corresponding layers which consist of the bending and shear laminates. Thee relative thickness is defined as the design variable. Depending on the loading, strength and stiffness is influenced accordingly. Details of the stacking sequence, such as those resulting from manufacturing restrictions, are not considered. Furthermore, the layer thickness is assumed to be a continuous variable, which means that discrete numbers of layers are not considered. The minimum wing structural weight is defined as the optimization objective, with additional strength and buckling restrictions. The applied safety factors are $SF_{buckling} = 1.4$ and $SF_{strength} = 1.4$, such that the optimization task is defined as

$$\begin{aligned} \underset{\vec{x}}{\text{minimize}} \quad & m(\vec{x}) \\ \text{subject to} \quad & g_{buckling}(\vec{x}) \geq 1.4 \\ & g_{strengthRatio}(\vec{x}) \geq 1.4, \end{aligned} \tag{4.1}$$

where $\vec{x}$ represents the design variables, $m(\vec{x})$ the total structural mass and $g(\vec{x})$ the constraints to be considered. The structural design process is performed using linear FE methods in the wing flight shape without prestressing effects. Thus, the aerodynamic forces for the structural design load cases are derived from the target flight shape, as introduced in section 4.2, distinguishing between maneuver

and quasi steady gust loads. In the case of maneuvering loads, this involves trimming the aircraft to achieve the desired lift at a specified load factor n_z. The aircraft is considered as a point mass, as explained in more detail in chapter 5. The effects of dynamic flight maneuvers are not considered in the sizing. In accordance with the certification standard CS-25 [38], the limit maneuver load factors of $n_z = 2.5$ and $n_z = -1.0$ are applied.

As a further load case, the lift distributions when reaching the maximum wing root cross-sectional load during a gust encounter are selected. These are obtained from a rigid-body aircraft through a transient gust simulation. For completeness, it is anticipated that gust load case-3 is applied as the gust sizing scenario. Further details are discussed in chapter 5. Altogether, 11 load cases with different flight states are considered in the sizing process, which are summarized in the following Table 4.9. Load cases #1-#5 are quasi-steady maneuver load cases, and load cases #6-#11 are those derived from the transient gust simulation. The maximum internal loads do not occur at the same time, which is why different pressure distributions are obtained for each simulation. Furthermore, AR-10 and AR-13 configurations must be distinguished because of the different wing planforms.

Table 4.9.: Structural design sizing load cases.

load case		n_z [–]	Ma [–]	q_∞ [Pa]	h [m]	C_L [–]	**fuel model**
#1	*sym. pull-up*	+2.5	0.64	29046	0.0	0.3172	3
#2	*sym. push-down*	−1.0	0.64	29046	0.0	−0.1269	3
#3	*sym. pull-up*	+2.5	0.86	12375	10668	0.7446	3
#4	*level flight*	+1.0	0.86	12375	10668	0.2978	3
#5	*parking*	+1.0	0.0	0.0	0.0	0.0	1
#6	*Gust* S_{max} $\begin{pmatrix} AR\text{-}10 \\ AR\text{-}13 \end{pmatrix}$	$\begin{pmatrix} +3.22 \\ +3.34 \end{pmatrix}$	0.5	17728	0.0	$\begin{pmatrix} 0.7265 \\ 0.7535 \end{pmatrix}$	3
#7	*Gust* M_{max} $\begin{pmatrix} AR\text{-}10 \\ AR\text{-}13 \end{pmatrix}$	$\begin{pmatrix} +3.20 \\ +3.34 \end{pmatrix}$	0.5	17728	0.0	$\begin{pmatrix} 0.7237 \\ 0.7529 \end{pmatrix}$	3
#8	*Gust* T_{max} $\begin{pmatrix} AR\text{-}10 \\ AR\text{-}13 \end{pmatrix}$	$\begin{pmatrix} +3.20 \\ +3.34 \end{pmatrix}$	0.5	17728	0.0	$\begin{pmatrix} 0.7229 \\ 0.7530 \end{pmatrix}$	3
#9	*Gust* S_{max} $\begin{pmatrix} AR\text{-}10 \\ AR\text{-}13 \end{pmatrix}$	$\begin{pmatrix} +2.73 \\ +2.87 \end{pmatrix}$	0.86	12375	10668	$\begin{pmatrix} 0.8125 \\ 0.8556 \end{pmatrix}$	3
#10	*Gust* M_{max} $\begin{pmatrix} AR\text{-}10 \\ AR\text{-}13 \end{pmatrix}$	$\begin{pmatrix} +2.66 \\ +2.84 \end{pmatrix}$	0.86	12375	10668	$\begin{pmatrix} 0.7926 \\ 0.8447 \end{pmatrix}$	3
#11	*Gust* T_{max} $\begin{pmatrix} AR\text{-}10 \\ AR\text{-}13 \end{pmatrix}$	$\begin{pmatrix} +2.64 \\ +2.83 \end{pmatrix}$	0.86	12375	10668	$\begin{pmatrix} 0.7859 \\ 0.8432 \end{pmatrix}$	3

Side Comment: Structural Initial Design Process

The modeling strategy and layout definition presented herein is a simplified initial design approach customized for this study. The selection of optimization parameters is reduced to a minimum; thus, it must be considered that the optimization potential is restricted as well. Additional constraints originating from the manufacturing processes, other maneuver loads, and aeroelastic instabilities (flutter and divergence) are not considered in the initial design. The layout is minimalistic, but fulfills the purpose of designing the structural wing layout to be able to perform load simulations on a representative example. More sophisticated and more efficient designs make special use of methods from aeroelastic tailoring or tow-steered composite wings, which are comprehensive research topics of their own.

4.4.1. Wing Jig Shape Design

The prerequisite for the wing configuration studied in this work is that all wings of the same planform, regardless of their structural stiffness, have the same lift distribution and flight shape. From a structural simulation perspective, this is an unconventional approach because the stress-free state is typically chosen as the reference configuration of the structural-mechanical equilibrium equation. In the case of the wing airframe, this corresponds to its jig-shape. To ensure the same flight-shape for the wings, each must have a different jig-shape when the stiffness is changed.

In this study, the flight shape was defined as the target. Therefore, the corresponding jig-shape must be determined. Thus, the structural model described in the previous section is adapted using a residual displacement approach. The implemented algorithm for this study is shown in Figure 4.22 and consists of the following steps:

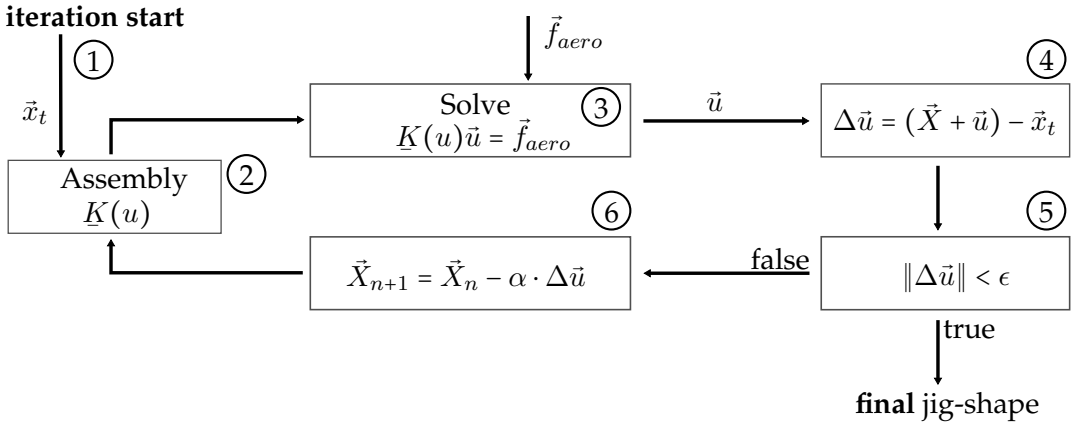

Figure 4.22.: Wing jig-shape design algorithm.

1. Iteration start: use target configuration $\vec{x}_t$ for initialization.

2. Assemble stiffness matrix $\underline{K}$

3. Solve a nonlinear structural system for the aerodynamic force $\vec{f}_{areo}$.

4. Calculate the difference vector $\Delta\vec{u}$ between target wing shape $\vec{x}_t$ and current configuration $(\vec{X} + \vec{u})$

5. Check the convergence condition. True if deviation of current and target configuration is less than ϵ.

6. Update jig-shape node vector $\vec{X}$ using the under-relaxed difference vector $\alpha \cdot \Delta\vec{u}$ where $\alpha \in [0, 1]$.

7. Continue with next iteration step.

Due to the large deformations, the simulation is performed nonlinearly. However, it is important to consider that the update of the jig-shape positions (Step 6) is linear. Therefore, the under-relaxation parameter α must be chosen to be sufficiently small such that the linearized assumption around the nonlinear reference state is valid. For the cases studied here, an under-relaxation of $\alpha = 0.5$ is shown to be sufficient.

Side example: Rotation of a bar

The described algorithm is applied to a rigid body bar with length $l = 1$, which is rotated around the z-axis with a predefined displacement load of $\theta = 45\,\mathrm{deg}$. The rigid body rotation from the jig shape $\vec{X}_{jig}$ to the current configuration $\vec{x}$ can be specified as follows

$$\vec{x} = \begin{bmatrix} cos(\theta) & -sin(\theta) \\ sin(\theta) & cos(\theta) \end{bmatrix} \begin{Bmatrix} X_{jig} \\ Y_{jig} \end{Bmatrix}, \tag{4.2}$$

as a result, the difference vector is

$$\Delta\vec{u} = \vec{x} - \vec{x}_t = \vec{x} - \begin{Bmatrix} cos(45°) \\ sin(45°) \end{Bmatrix}. \tag{4.3}$$

The iteration result from algorithm Figure 4.22 is shown below for the under-relaxation $\alpha = [0.8, 0.25, 0.01]$. The example shows a significant geometric nonlinearity, so that the results of the intermediate iterations are not physically meaningful. In case of convergence difficulties, the method can be stabilized by determining the solution in several load steps rather than in a single step.

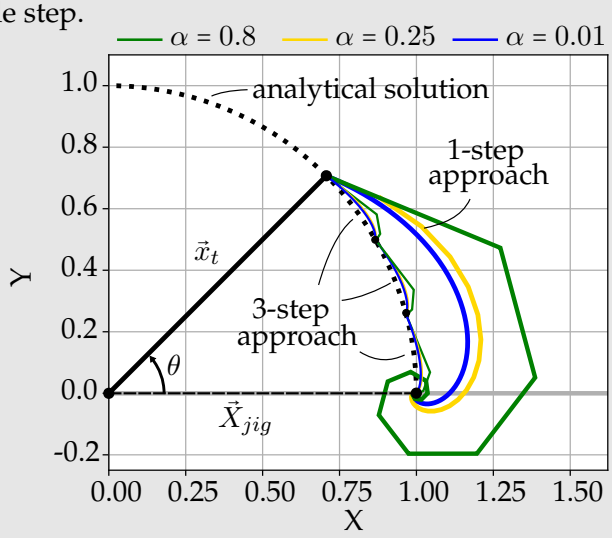

4.5. Structural Comparison of the Wings

The aim of this study is to investigate the influence of different wing stiffnesses on the passive load alleviation. For this purpose, wings with different structural stiffnesses are realized. Owing to the many degrees of freedom and complexity, the influence of stiffness can no longer be directly specified compared to the 2-DoF system presented in chapter 3. To achieve the intended result, the bending stiffness ($\frac{EI}{l}$) or torsional stiffness ($\frac{GJ}{l}$) of the structure is considered as an example. Influencing these leaves two possibilities: either geometric changes are applied, thus influencing I and J, or different material models are introduced, which allow E and G to be adjusted. The latter is achieved through the application of different materials as introduced in subsection 4.3.4. This implies that the overall stiffness of the structure is indirectly modified by the different generic materials.

A number of wing structures are realized using the modeling approach presented in chapter 4. The structural sizing is carried out separately for each configuration. Similar to changed stiffness, effects such as buckling must be assessed individually. This means that all implemented configurations fulfill the sizing load cases defined in Table 4.9.

Three configurations with increasing structural flexibility are set up for each wing planform. The different stiffness variations are denoted as **#ref**, **#red** and **#sft**. The #ref configuration is used as a reference, while the structural flexibility for #red and #sft progressively becomes more flexible. In the following section, the structural properties are compared to evaluate their influence on the aeroelastic characteristics.

4.5.1. Wing Stiffness Comparison

The stiffness distribution on the wing is evaluated at the nodes of the reference axis, which is shown for the AR-10 configuration in Figure 4.23. The relative z-deflection and y-rotation degrees of freedom under a predefined reference test load are used as assessment criteria. The evaluation is performed at each reference point in the flow parallel to the X-Y coordinate system. It should be noted that the twist of the rotational degree of freedom is not solely due to wing torsion but also wing bending (see section 3.1). This means that the twist in the Y-direction represents the washout of the wing and is an indirect measure of lift reduction. The influence of structural stiffness is of particular interest, and thus inertia forces are not considered. The lift distribution is therefore scaled to 20% of the *cruise-flight* condition and used as reference load, since no weight is presented which counteracts. The results of the relative and absolute displacement z, as well as rotation θ is shown separately for the AR-10 wing in Figure 4.24a and for the AR-13 wing in Figure 4.25a.

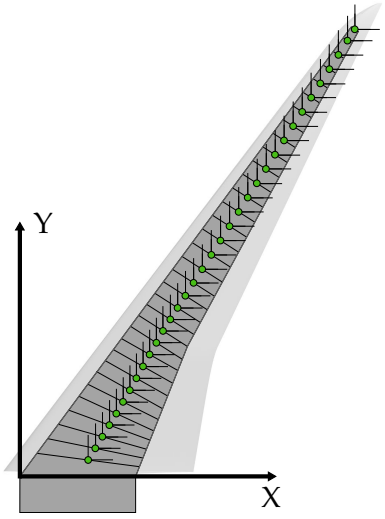

Figure 4.23.: Wing reference axis.

A comparison of the absolute displacement amplitudes of the AR-10 and AR-13 configurations shows that the wing with a higher AR is significantly more flexible. The different structural stiffnesses shows that the z-deflection and wing washout are higher when using a lower stiffness wing (#red, #sct). However, the absolute deflection is of secondary importance for load reduction. The slope $\frac{\delta(deflection)}{\delta(load)}$ is more significant, meaning the extent to which the washout is enhanced with an additional load increment δL. For this purpose, an additional lift increment δL of $[2\%, 4\%, 6\%]$ of the reference test load is added to the 20% *cruise-flight* load and the displacement difference $\Delta\theta = \theta_{+2\%} - \theta_{reference}$ is evaluated. It can be confirmed that more flexible wing structures allow for improved relative washout.

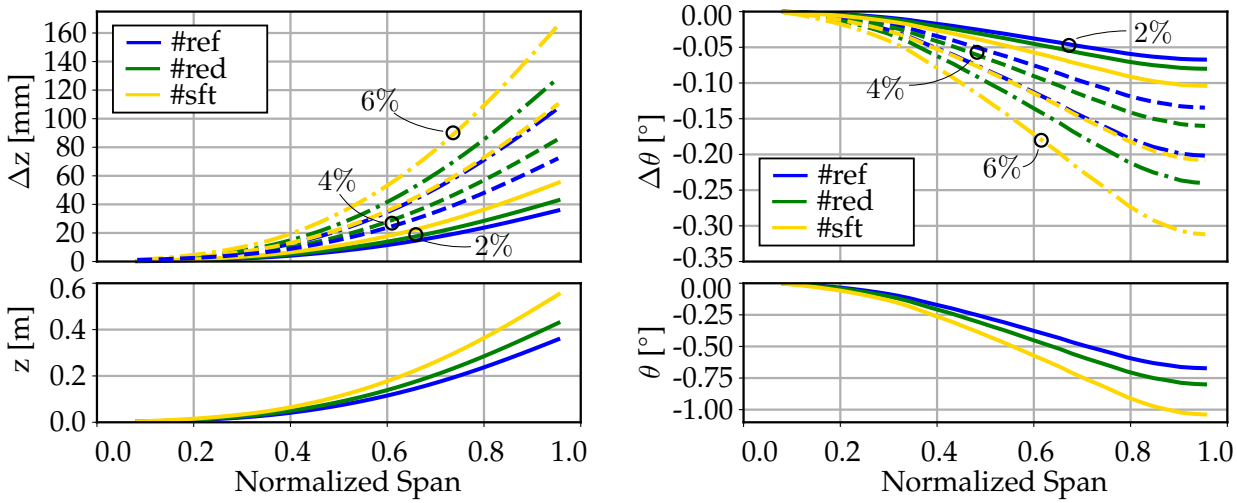

(a) Bending deflection difference Δz, and total z deflection.

(b) Twist deflection difference $\Delta\theta$, and total θ deflection.

Figure 4.24.: Comparison of the AR-10 wing deflection results in bending z and twist θ at varying lift increments and varying wing stiffness

.

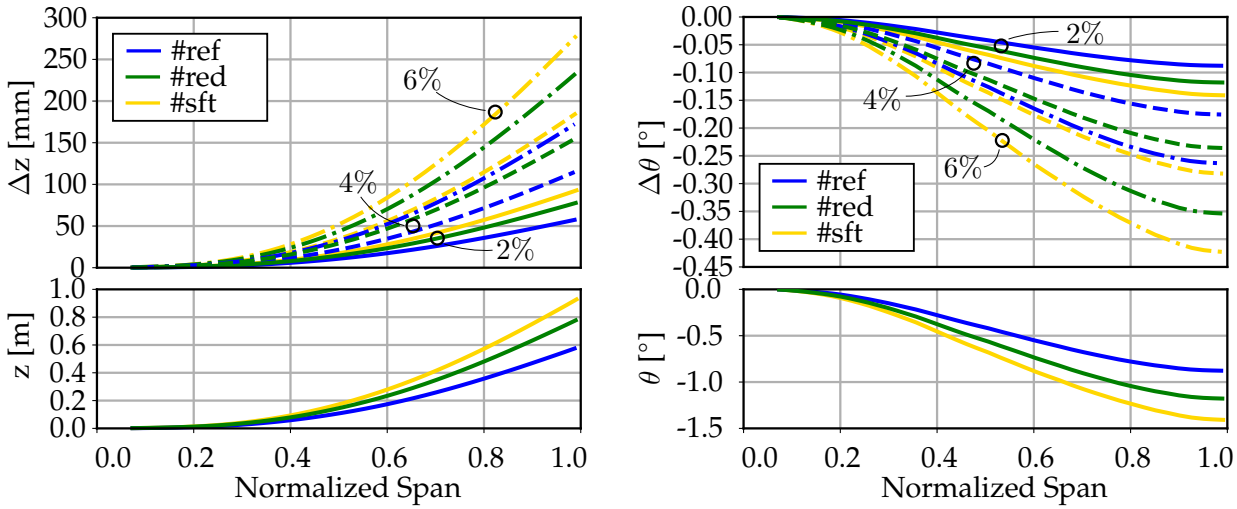

(a) Bending deflection difference Δz, and total z deflection.

(b) Twist deflection difference $\Delta\theta$, and total θ deflection.

Figure 4.25.: Comparison of the AR-13 wing deflection results in bending z and twist θ at varying lift increments and varying wing stiffness

.

4.5.2. Structural Dynamics and Mass Properties Summary

The designs of both wing structures are based on similar structural concepts. However, due to different wing configurations, there are still inherent differences between the aircraft configurations. These are:

- The wing fuel tank is shown in Figure 4.20b for AR-10 and Figure 4.21b for the AR-13 configuration. With a larger aspect ratio, the wing tank volume is reduced, and thus the fuel weight distribution in the wing. To achieve the same total aircraft fuel mass, the difference of the wing tanks in the AR-13 configurations is allocated to the center fuel tank.

- From subsection 4.2.1, it can be noted that the two wings have different load distributions due to their different geometries. This means that the individual components are also dimensioned accordingly; therefore, both structural configurations show different wing structural weights.

- In addition, the stiffness variation of the generic material models leads to different thickness distributions for the same wing configuration and to different structural masses. This has a particularly significant impact on the AR-10 #sft configuration, which is set up using the extremely soft #mat-3 property. To prevent buckling, the components must be thicker accordingly.

A final summary of all the systems and structural masses of the individual configurations is given in Table 4.10. AR-13 has an increased structural mass in all the configurations. Although in a different context, a similar result was obtained in Brooks' work [100], demonstrating that a lower structural wing weight can be achieved with wings of smaller AR.

Table 4.10.: AR-10 and AR-13 configuration mass summary.

component	**AR-10**	**AR-13**
centre fuel tank	$8.114\,\mathrm{t}\cdot 2$	$16.096\,\mathrm{t}\cdot 2$
wing tank 1	$27.905\,\mathrm{t}\cdot 2$	$20.455\,\mathrm{t}\cdot 2$
wing tank 2	$12.536\,\mathrm{t}\cdot 2$	$12.363\,\mathrm{t}\cdot 2$
wing tank 3	$5.795\,\mathrm{t}\cdot 2$	$5.436\,\mathrm{t}\cdot 2$
leading edge masses	$1.2\,\mathrm{t}\cdot 2$	$1.44\,\mathrm{t}\cdot 2$
trailing edge masses	$2.189\,\mathrm{t}\cdot 2$	$2.962\,\mathrm{t}\cdot 2$
engine	$6.118\,\mathrm{t}\cdot 2$	
main landing gear	$4.077\,\mathrm{t}\cdot 2$	
wing structure (#ref)	$23.357\,\mathrm{t}$	$31.579\,\mathrm{t}$
wing structure (#red)	$24.182\,\mathrm{t}$	$32.381\,\mathrm{t}$
wing structure (#sft)	$27.477\,\mathrm{t}$	$31.722\,\mathrm{t}$
fuselage, empennage, systems, payload (#ref)	$68.775\,\mathrm{t}$	$58.527\,\mathrm{t}$
fuselage, empennage, systems, payload (#red)	$67.950\,\mathrm{t}$	$57.725\,\mathrm{t}$
fuselage, empennage, systems, payload (#sft)	$64.654\,\mathrm{t}$	$58.383\,\mathrm{t}$
$\sum$ MTOW	$228.0\,\mathrm{t}$	$228.0\,\mathrm{t}$

Due to the different stiffness and mass distributions, the wings have different dynamic properties. The modal properties of the wing configurations are compared to understand the differences between the different mass and stiffness distributions. The dominant eigenmodes are depicted with scaled amplitudes in Figure 4.26 and the resulting eigenfrequencies are listed in Table 4.11. The natural frequencies of the two wing configurations with different stiffnesses #ref and #red in *cruise-flight* fuel model-1 and *approach-flight* fuel model-2 condition. As mentioned in the Introduction, the natural frequencies of the AR-13 configuration are noticeably lower than those of AR-10. Furthermore, the first bending mode is in a range in which rigid-body modes of the aircraft are expected. The difference between the two stiffness models also shows that the natural frequencies are reduced, which can be explained by the lower wing stiffness. The changes observed between *cruise-* and *approach-flight* configurations are due to changes in fuel masses.

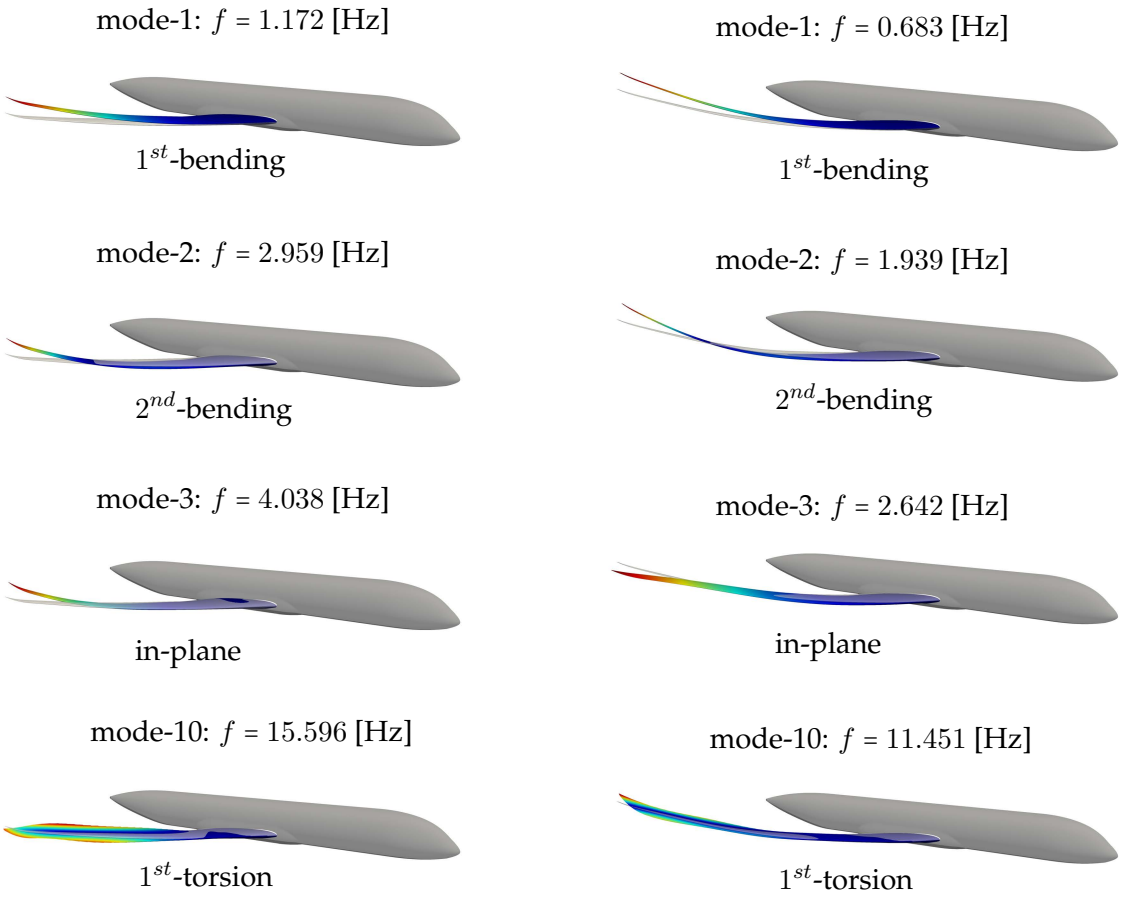

(a) AR-10 wing. (b) AR-13 wing.

Figure 4.26.: Visualisation of the symmetric structural eigenmodes of the AR-10 and AR-13 #ref cruise configuration.

The natural frequencies listed in Table 4.11 are obtained considering wing structural prestressing due to flight loads. A direct comparison of how prestressing affects the modal properties is given in A.7. Because the structural dynamic models in the next section are solved in the time domain considering structural nonlinearities, the influence of changing modes due to prestressing is considered automatically; therefore, no further details will be given in the following.

Table 4.11.: Structural (symmetric) eigenfrequencies for the #ref and #red stiffness configuration.

	AR-10				**AR-13**			
mode	cruise		approach		cruise		approach	
number	#ref	#red	#ref	#red	#ref	#red	#ref	#red
1	1.172	1.063	1.223	1.109	0.683	0.628	0.700	0.644
2	2.959	2.704	3.604	3.300	1.939	1.799	2.192	2.031
3	4.038	3.688	4.245	3.882	2.642	2.412	2.822	2.589
4	5.106	4.676	6.188	5.627	3.871	3.570	4.738	4.352
5	7.070	6.461	8.145	7.473	5.691	5.179	6.332	5.663
6	9.226	8.480	10.639	9.544	6.578	5.949	7.704	7.003
7	10.293	9.312	11.616	10.595	7.362	6.627	8.435	7.632
8	10.535	9.544	12.769	11.718	9.735	8.781	11.183	9.499
9	13.591	12.422	16.071	14.743	10.835	9.201	11.485	10.436
10	15.596	14.313	17.644	16.221	11.451	10.312	12.377	10.724
25	48.616	44.721	53.326	55.541	41.225	36.430	46.878	42.247

5 Steady Aircraft Maneuver Load Study

The aircraft models described in the previous chapter 4 are used to investigate the load reduction behavior under a quasi-steady pull-up maneuver, as displayed in Figure 5.1. Different flight conditions are considered, distinguishing between *cruise* and *low speed* flight. The simulation results of the AR-10 and AR-13 wing layout configurations are presented in detail. The aerodynamic properties, C_L, and the lift distribution are evaluated at different load factors of the reference configurations. In addition, the wing root section forces of the different structural stiffnesses at different load factors are presented. Finally, the results are compared and evaluated according to the potential of passive load alleviation under a quasi-steady pull-up maneuver load.

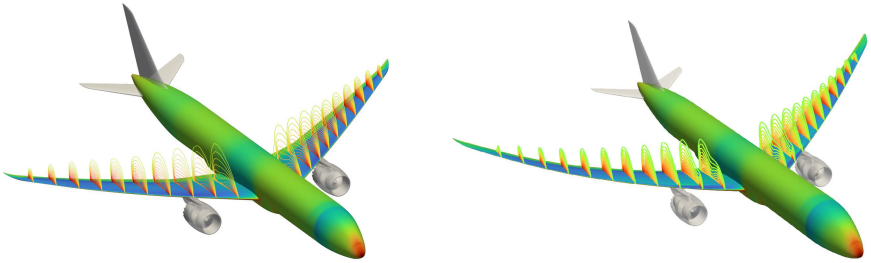

(a) Aspect ratio 10 (AR-10) configuration.

(b) Aspect ratio 13 (AR-13) configuration.

Figure 5.1.: Transport aircraft maneuver load study.

Contents

5.1. Steady Flight Condition and Computational Setup

In this analysis, main influences of the elastic wings are investigated under the assumption of a quasi-steady pull-up maneuver flight. The state can be considered quasi-steady because the acceleration induced by the movement is constant. For this purpose, the aircraft is considered in a trimmed equilibrium flight state, in which all forces and moments acting on the aircraft, including forces from lift, control surfaces, inertia, and elastic deformation, are in equilibrium.

As the focus is on the lift generated by the wings, the trim task is simplified in this study. Due to the assumed steady-state flight condition no transient effects are modeled. Furthermore, the aircraft is considered as a point mass, as shown in Figure 5.2, so that for a given load factor, $n_z \cdot mg = L$ applies.

The pitch moment of the aircraft is balanced by the structural boundary conditions and not by the empennage. For this study, different load factors n_z are defined and the corresponding AoA for the necessary lift is determined iteratively until equilibrium is achieved. The influence of pitch rate q is not considered, and hence, whether the AoA is of steady origin or induced by the dynamic motion of the aircraft is not differentiated. However, due to the small distance to the center of gravity, the influence is small, as discussed in the appendix section A.8.

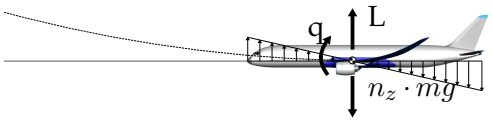

Figure 5.2.: Trim forces during maneuver flight.

To consider the influence of different flow conditions, *take-off*, *cruise-*, and *approach-flight* is studied individually. The individual flight scenarios are summarized in Table 5.1. In the subsequent analyses, as the final wing shape is initially unknown, a strong coupling scheme is used to determine the equilibrium state between aerodynamic forces and structural deformation, as described in subsection 2.3.3.

Table 5.1.: Summary maneuver flight scenarios.

flight condition		**Ma**	**FL**	ρ_∞	T_∞	**fuel model**
#1	take-off	0.5	0	$1.225\,\mathrm{kg\,m^{-3}}$	288.15 K	model-1
#2	start cruise flight	0.86	350	$0.380\,45\,\mathrm{kg\,m^{-3}}$	218.92 K	model-1
#3	end cruise flight	0.86	350	$0.380\,45\,\mathrm{kg\,m^{-3}}$	218.92 K	model-2
#4	approach flight	0.5	0	$1.225\,\mathrm{kg\,m^{-3}}$	288.15 K	model-2

5.2. Aeroelastic Analysis of the AR-10 Wings

Figure 5.3 shows load factor n_z and lift coefficient C_L-AoA slope of the elastic #ref AR-10 configuration for different flight and fuel loading conditions as defined in Table 5.1. The basic characteristics of the elastic wings are investigated in this context using the #ref wing structure. The corresponding n_z- and C_L-slope results of the #red and #sft wing structures can be found in section A.9.

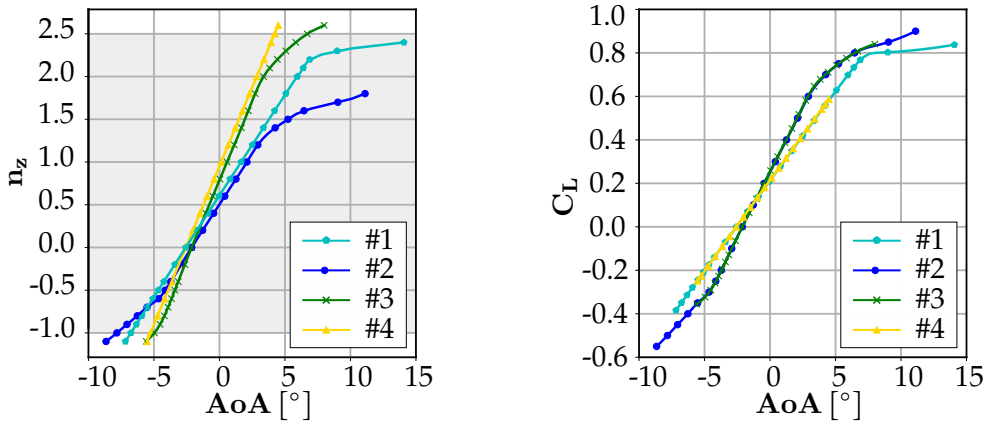

(a) n_z-slope.

(b) C_l-slope.

Figure 5.3.: Load Factor n_z and C_L-AoA slope, trimmed in quasi-steady maneuver loads of the AR-10 elastic aircraft configuration, wing structure #ref.

Differences in the flight scenarios can be recognized in the different C_L and n_z gradients, as well as in the characteristics at high AoA. The influence of the fuel loading conditions is present, but has only a minor effect on the C_L slope (comapre flight scenarios #1-#4 and #2-#3). However, when analyzing the dependency of the load factors, similarities emerge for the same fuel loading condition. The load cases with a full wing tank show a smaller n_z-AoA slope compared to that with an empty wing tank, such that the changes in AoA increases the load factor rapidly with empty wing tanks.

The two empty wing tanks scenarios (#3, #4) are the flight scenarios wherein the limit load is reached by a pull-up maneuver. However, the first signs of flow separation, are observed at the end of the *cruise-flight* scenario (#3). This is becomes more apparent for the two scenarios with full wing tanks (#1, #2). The *approach* scenario (#4) shows no separations, with a linear relationship between lift and AoA in the operational range. For flight scenario #2, the lack of further increase in lift on the wing owing to flow separation is shown in Figure 5.4. The surface friction coefficient C_f is depicted as the contour plot of the upper wing surface. It can be noted that flow separation occurs as the load factors n_z increases, which is indicated by areas with a low or negative C_f coefficient.

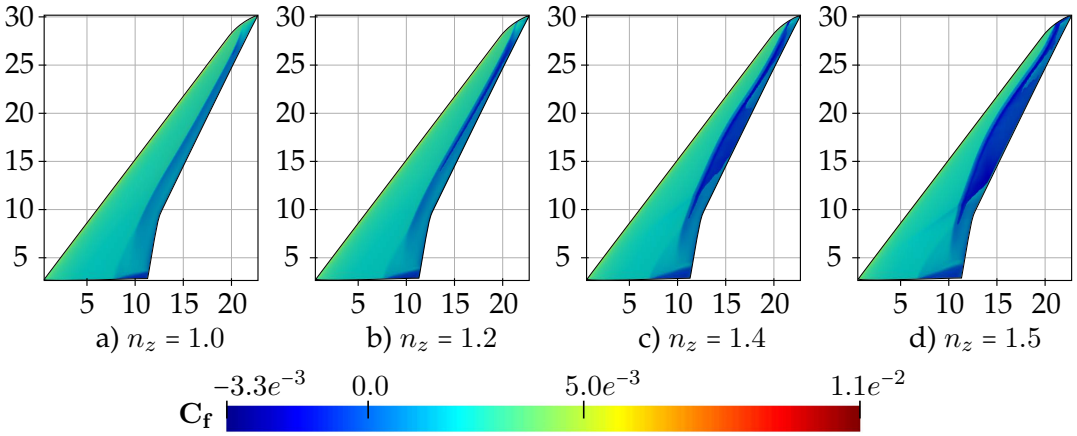

Figure 5.4.: Skin friction coefficient C_f for different load factors n_z at cruise #2.

5.2.1. External Wing Loads Investigation of the Reference Configuration

Analyzing integral values such as C_L provide a limited indication of the loads that occur, as the influence of the lift distribution is not considered. Therefore, the resulting aerodynamic section loads transverse force S, bending moment M, and torsional moment T at the wing root reference point are used as evaluation criteria. The different flight scenarios (#1-#4) are shown separately with changing load factors in Figure 5.5. For all cases, a linear behavior is observed around the steady flight state at n_z = 1.0. The effect of the already identified flow separation on the wing root section forces at higher load factors can be recognized by the vanishing gradient or dropping of the external loads.

Side Comment: External Loads
It should be noted that the plotted wing root loadings are the results of the aerodynamic section loads. Thus, the following assessment refer to the load reduction of the external forces. Additional loads from inertia are not represented. When assessing the internal structural loads, these come into effect as they can partially compensate the external loads. In this study, however, the focus is on the kinematic washout of swept wings and the associated lift distribution.

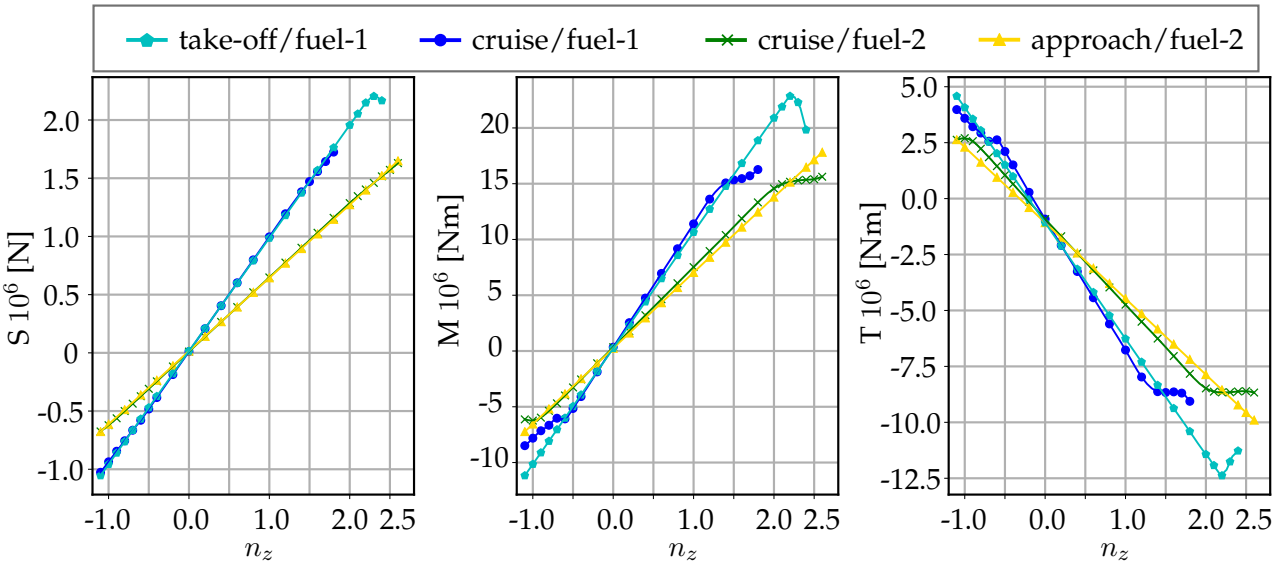

Figure 5.5.: AR-10 configuration wing root section forces for different flight and fuel loading scenarios.

To better understand the effects that causes the change in the root bending moment M and the torsional moment T, the lift distribution and wing deformation are analyzed at different load factors. The results for the different flight and fuel loading conditions for *cruise* and *low-speed* flight are shown in Figure 5.6 and Figure 5.7, respectively.

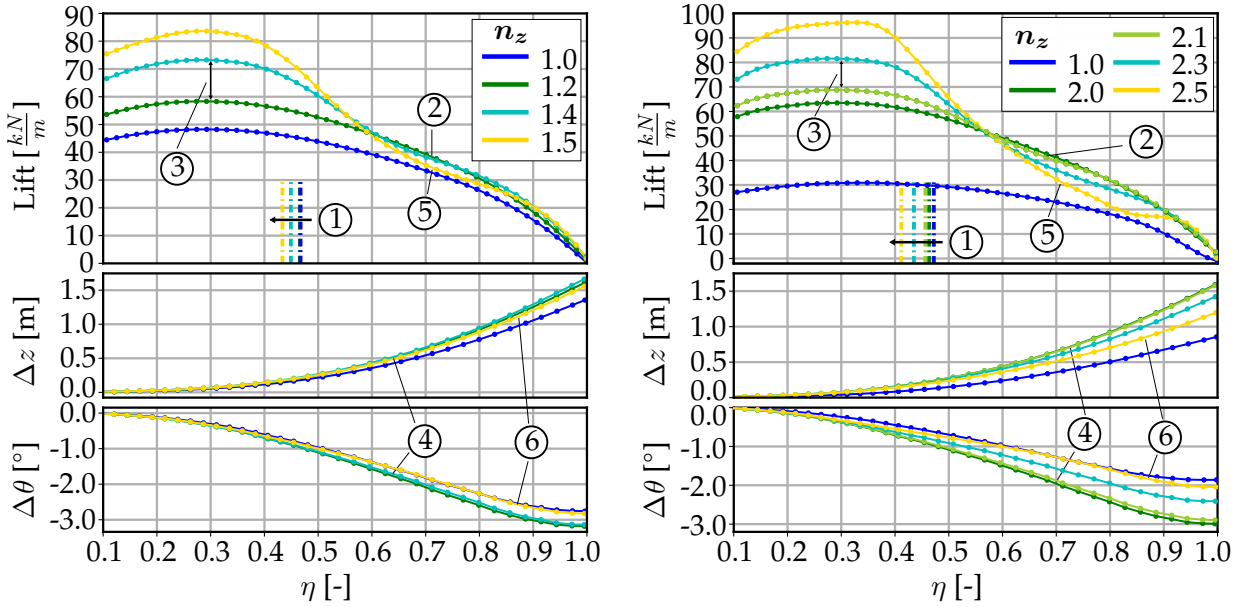

(a) Ma = 0.86, fuel model-1.

(b) Ma = 0.86, fuel model-2.

Figure 5.6.: Wing lift dirstribution and deformation at trimmed quasi-steady maneuver loads of the AR-10, #ref structural elastic aircraft configuration at cruise flight (#2, #3).

From the results, a number of correlations are identified that describe the essential characteristics:

1. The resulting load center of the lift distribution shown in Figure 5.6a is indicated by a dashed line for different n_z. In both *cruise* scenarios, the lift shifts towards the wing root for higher load factors n_z.

2. When increasing the load factor n_z, the gradient in the bending moment M and the torsional moment T decrease at a certain value, as observed in the lift distribution plot between n_z = 1.2

and $n_z = 1.4$ for fuel model-1 or between $n_z = 2.0$ and $n_z = 2.1$ for fuel model-2. First flow detachments are visible, which can also be seen in the C_f value given in Figure 5.4.

3. The lift increase at the wing root is proportionally higher due to the larger AoA. The moments increase proportionately less by shifting the lift towards the wing root.
4. Deflection Δz and twist $\Delta\theta$ on the wing are reduced, and the washout stops.
5. As the load factor increases further, a considerable reduction in lift is observed resulting from flow separation.
6. With a reduced lift, the deflection decreases and the wing begins to twist up, resulting in an increased local AoA. This means that the load reduction effect stops and the wing root moments continues to increase.

The low speed lift distribution for *take-off* and *approach-flight* scenario is shown in Figure 5.7. Similar fundamental principles can be identified from the results:

1. At higher load factors, n_z, the lift shifts towards the wing root.
2. With full wing tanks, flow separation occurs at higher load factors.
3. From a semi-span of $\eta = 0.65$, the flow is attached again owing to the washout.
4. As the load factor increases, the airflow over the entire wing starts to separate over a large section.
5. The loss of lift reduces the deflection and stops the washout.

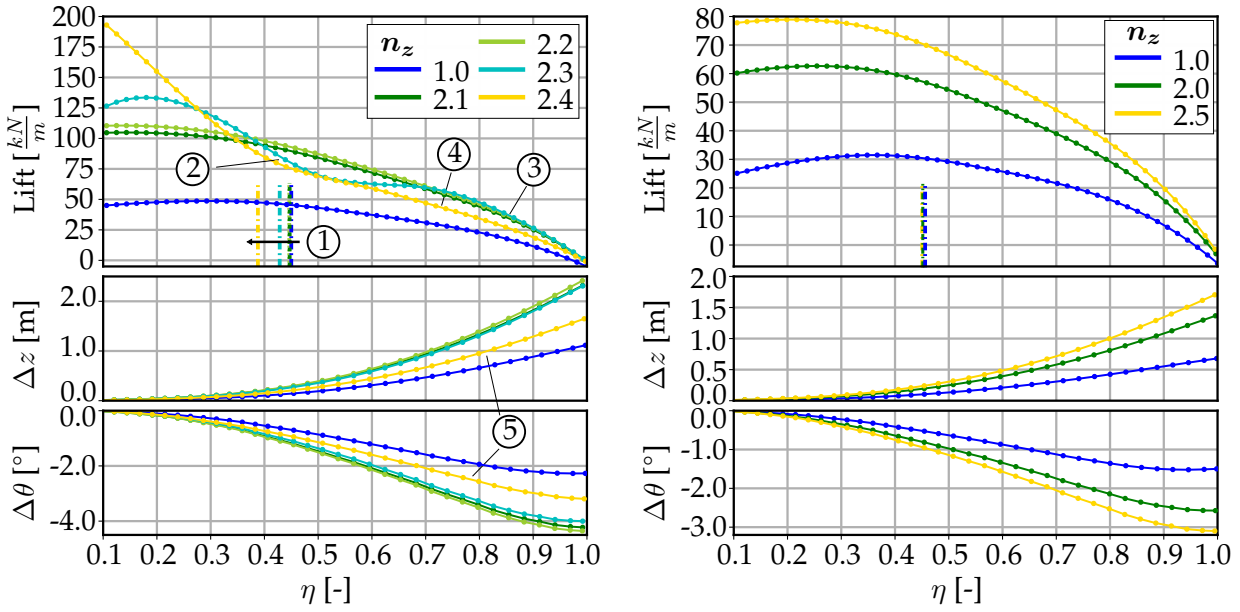

(a) $Ma = 0.5$, fuel model-1.

(b) $Ma = 0.5$, fuel model-2.

Figure 5.7.: Wing lift dirstribution and deformation at trimmed quasi-steady maneuver loads of the AR-10, #ref structural elastic aircraft configuration at approach (#1, #4).

The flight scenario at *low speed* with an empty wing tank, shown in Figure 5.7b, is important as it represents a pull-up maneuver study where enough lift can be generated to achieve the maximum load factor. In this case, the center loads (shown as dashed lines) only shift slightly in the direction of the wing root. This indicates that the load reduction by washout has only a minor effect. Even if possible, the load is not increased further at this point, because the limit load of $n_{z,max} = 2.5$ as defined in the sizing scenario is reached.

5.2.2. External Load Comparison at Different Wing Stiffnesses

The influence of the modified structural stiffness on the lift distribution and the wing washout with the possibility of load reduction is investigated, by comparing the wing root section loading of the three different flexible wings, #ref, #red, and #sft, under different flight scenarios. In particular, the load reduction at increased maneuver load factors is the primary interest of this study. Therefore, the difference of ΔS, ΔM, and ΔT between the #ref and #red,#sft is presented. More details about the absolute load values can be found in annex A.10.

Cruise Flight Scenarios

The variation of the section root forces compared to the #ref stiffness configuration at *cruise* flight with mass model-1 (#2) is shown in Figure 5.8a. A comparison of the transverse root sectional load, S, between the individual stiffness variants (#ref, #red, #sft) shows only small changes. The more flexible wing configurations (#red, #sct) have a slightly lower wing C_L, which is due to the stronger washout. As the required lift for a maneuver flight must per definition remain constant, the loss of lift must be compensated by an additional higher AoA, thus, the fuselage also experiences an increase in lift by implication. Therefore, the differences in ΔS describe the shift in lift between the wing and the fuselage at higher load factors. Transverse load reduction in maneuver flight thus can only be achieved by redistributing the lift between wing and fuselage.

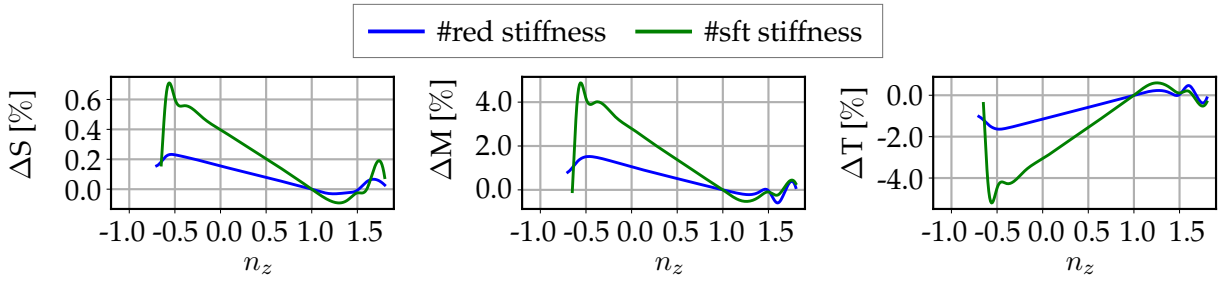

(a) Flight scenario #2.

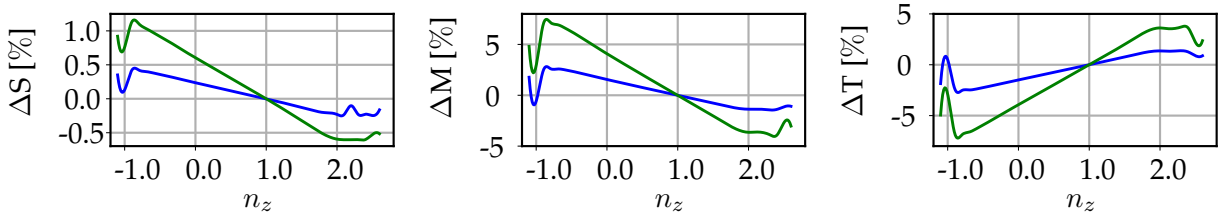

(b) Flight scenario #3.

Figure 5.8.: Difference of the AR-10 wing root section forces, at cruise flight, $\Delta\iota = \frac{\iota_\Upsilon(n_z)-\iota_\Upsilon(n_z=1.0)}{\iota_\Upsilon(n_z=1.0)} - \frac{\iota_{ref}(n_z)-\iota_{ref}(n_z=1.0)}{\iota_{ref}(n_z=1.0)}$, Υ = (red, sft), ι = (S, M, T).

A substantial outcome is the change in bending and torsional moments ΔM and ΔT, respectively. Unlike lift, both quantities are independent of the maneuver trim state and are ideally not increased or maintained low in the sense of a maneuver load reduction. As indicated in the ΔM and ΔT results, these quantities show a load reduction capability with an increasing load factor. With increasing wing flexibility, the load reduction $\Delta\iota$ can be further decreased in maneuver flight. However, all configurations indicate a peak, after which the load cannot be reduced any further. This is followed by a decrease in the reduction and a transition to an unsteady wing flow, which corresponds to the starting of flow separation, indicated by the oscillatory response of the external aerodynamic loads. Furthermore, the wings bending deflection can no longer be increased owing to lift drop. The peak values mark the utmost possible load reduction in a steady-state assessment and defined at the end of the linear range. These values are therefore used to assess the load alleviation potential. Results beyond the limit mark are not considered in the evaluation as these flow conditions have a high unsteady nature, for which the modeling assumptions of a quasi-steady flow reach their limitations. A summary of all flight and fuel scenarios is in Table 5.2 presented.

The results for *cruise-flight* with full wing tanks (#2) show only marginal improvements with varying wing stiffness. Due to the flight at maximum take-off weight, the steady *cruise* C_L at $n_z = 1.0$ is already high and leaves only a minimal possibility to increase the lift further. The correlation between wing deflection and washout, identified in chapter 3 can also be observed between #2 scenario and the empty wing fuel tank in scenario #3. As a result of the decrease in the total weight, the stationary C_L at *cruise* $n_z = 1.0$ decreases. Consequently, the necessary lift for higher n_z maneuvers can be achieved before flow separation occurs on the wing. Therefore, the relative deflections Δz and wing twist $\Delta\theta$ are larger (see Figure 5.6a and Figure 5.6b), and as the washout increases, more maneuver load reduction can be achieved. For load factors smaller than $n_z = 1.0$ the washout kinematic is reversed and the load increases, compared to the reference. The positive effect during positive load factors causes a higher load with more flexible configurations at load factors small than $n_z = 1.0$. As the load factors continue to achieve more negative values, the linear range stops and a transient flow with negative stall occurs.

Low Speed Flight Scenarios

Figure 5.9 shows the wing root section forces at *low-speed* flight. In the *take-off* scenario (#1) with full wing tanks the limit load factor cannot be achieved due to flow separation, resulting in loss of lift. However, in the *approach* flight scenario (#4), no stall or other non-linear dominating phenomena could be identified within the maneuver load envelope. Consequently, a linear correlation is observed between the load factor and the three wing root section forces in the entire maneuver load n_z range. The maximum load reduction for ΔM and ΔT compared to the #ref wing stiffness are summarized in Table 5.2. An improved external load reduction characteristic is observed in both scenarios with a more flexible wing.

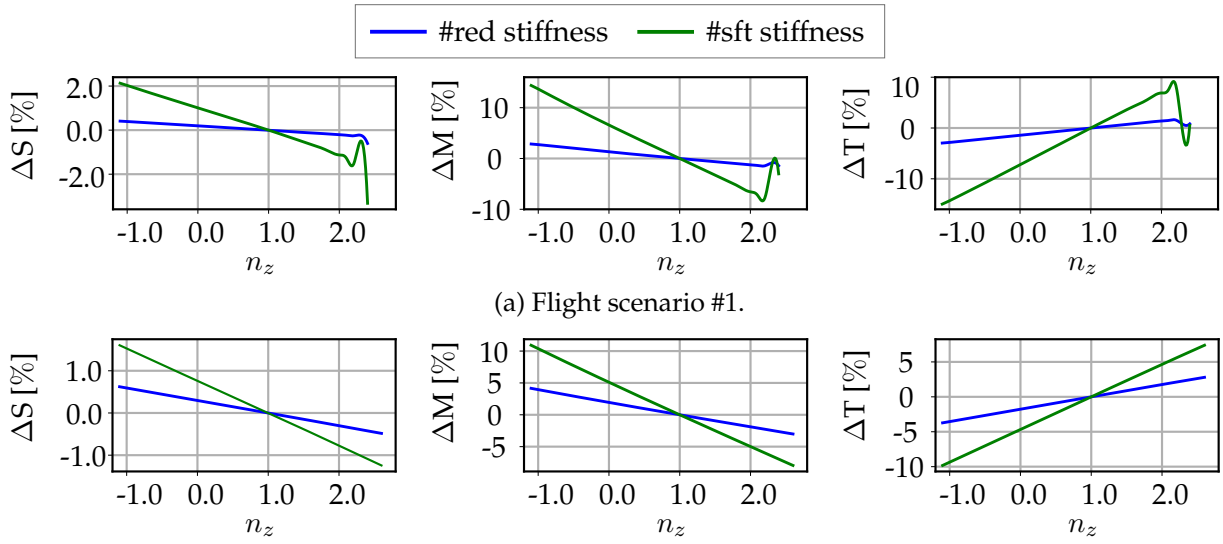

(a) Flight scenario #1.

(b) Flight scenario #4.

Figure 5.9.: Difference of the AR-10 wing root section forces, at low-speed flight, $\Delta\iota = \frac{\iota_\Upsilon(n_z) - \iota_\Upsilon(n_z=1.0)}{\iota_\Upsilon(n_z=1.0)} - \frac{\iota_{ref}(n_z) - \iota_{ref}(n_z=1.0)}{\iota_{ref}(n_z=1.0)}$, Υ = (red, sft), ι = (S, M, T).

Table 5.2.: AR-10, wing root sectional forces peak point summary for the flight scenarios #1-#4.

flight scenario	**#1**		**#2**		**#3**		**#4**	
	#red	#sft	#red	#sft	#red	#sft	#red	#sft
ΔM	−1.50%	−8.36%	−0.22%	−0.53%	−1.38%	−1.45%	−2.8%	−7.5%
n_z	2.171	2.171	1.285	1.25	2.30	2.33	2.5	2.5
ΔT	1.64%	9.18%	0.23%	−0.59%	−3.79%	−4.04%	−2.6%	6.9%
n_z	2.171	2.171	1.274	1.25	2.35	2.33	2.5	2.5

5.3. Aeroelastic Analysis of the AR-13 Wings

The AR-13 wing configuration is subjected to the same analysis and assessment as in the AR-10 wing study. The four flight scenarios introduced in Table 5.1 are used as the basis for the load analysis. Figure 5.3 shows the n_z-AoA and C_L-AoA slopes of the elastic #ref AR-13 configuration. With full fuel tanks (#1, #2), the maximum maneuver load will not be exceeded due to flow separation and related limited lift. Only the flight scenarios with an empty wing tank show the possibility to reach the maximum maneuver load factor, whereas scenario #4 again has a linear C_L-AoA characteristic over the defined range. The C_L-slope results for #red and #sft can be found in section A.9.

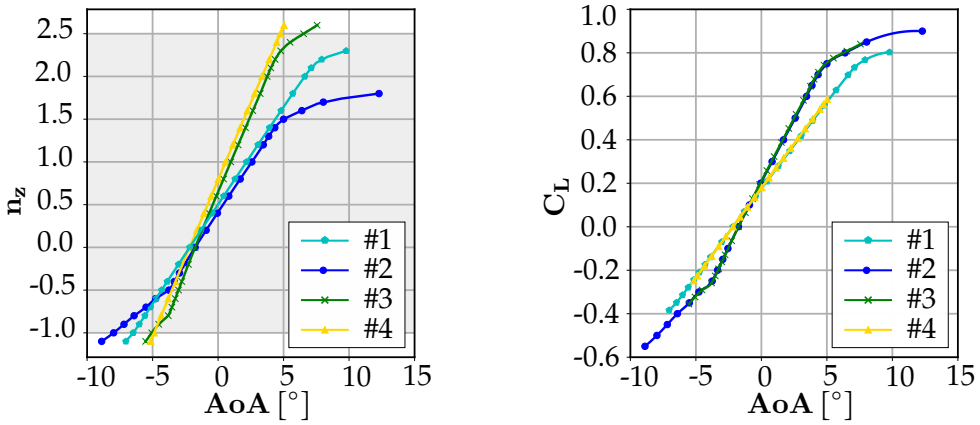

(a) n_z-slope. (b) C_l-slope.

Figure 5.10.: Trimmed quasi-steady maneuver loads of the AR-13 elastic aircraft configuration, wing structure #ref.

As with the AR-10 case study, the loss of lift is noticed in the AR-13 configuration, which in turn is related to the beginning of flow separation on the wing. To illustrate this, the surface friction coefficient C_f is shown in Figure 5.11, where low negative C_f values show areas of detached flow.

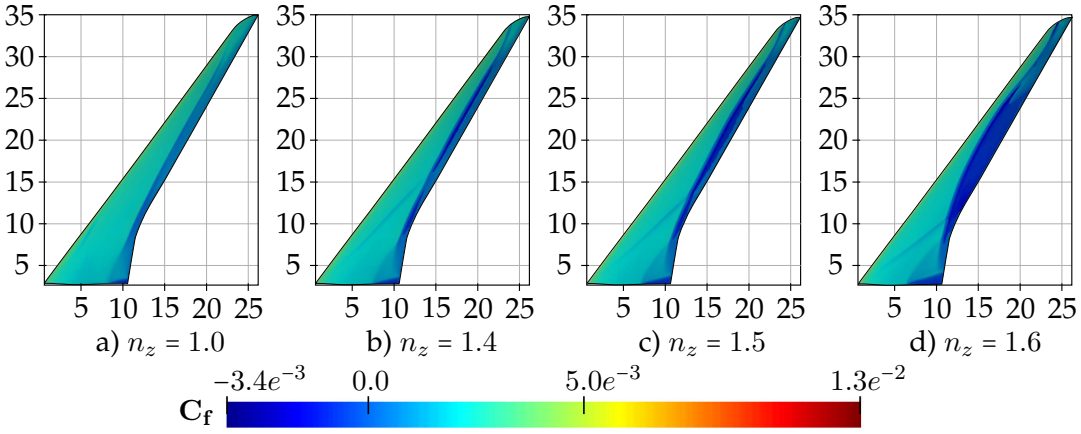

Figure 5.11.: Skin friction coefficient C_f for different load factors n_z at cruise #2.

5.3.1. External Wing Loads Investigation of the Reference Configuration

Figure 5.12 shows the resulting aerodynamic wing root section loads S, M, and T at the wing root reference point for the #ref stiffness configuration at different load factors. Note that due to the larger wingspan, the bending and torsional moments at the wing root are generally higher compared to the AR-10 wing. Similarly, the steady flight point at n_z = 1.0 is in the linear range, and the influence of stall can be recognized by the decreasing slope of the section forces as n_z increases.

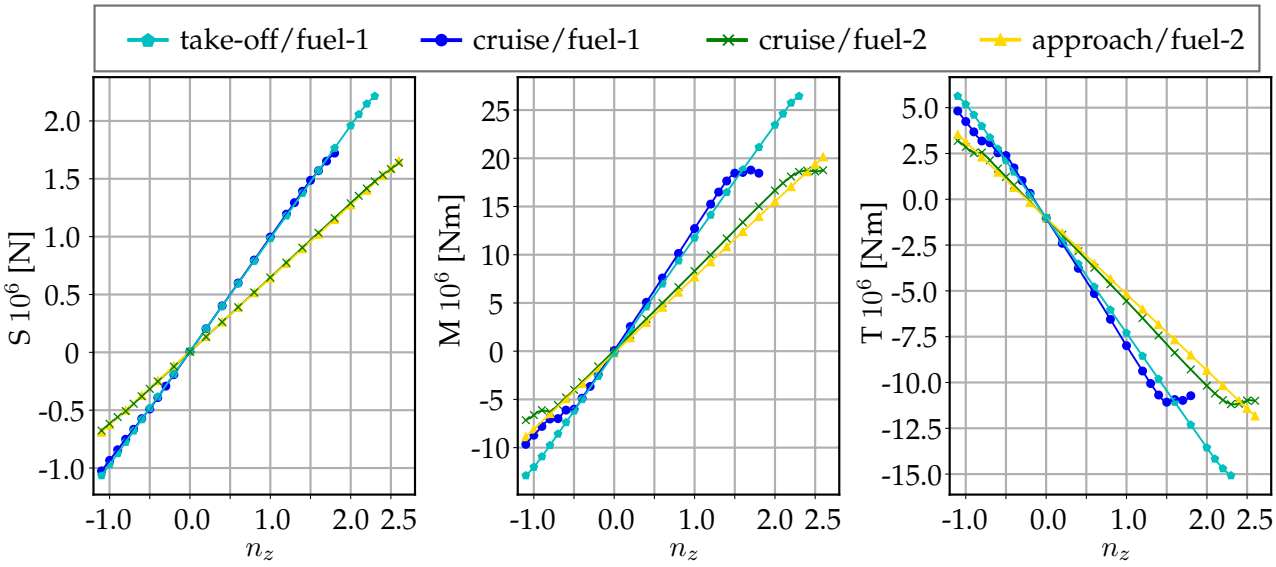

Figure 5.12.: AR-13 configuration wing root section forces for different flight and fuel loading scenarios.

The lift distribution along the span is shown for the selected load factors at *cruise* speed and *low-speed* in Figure 5.13 and Figure 5.14, respectively. For this case study, it can be stated that:

1. The load application center shifts towards the root of the wing as the load factors increase.

2. Compared to the AR-10 configuration, a significantly larger deflection and particularly increased wing twist is observed.

3. The *cruise-flight* load cases show a decrease in lift due to flow separation.

4. For flight case #3, an up twist of the wing is observed. Analyzing this in the context of the C_f plot in Figure 5.11, this occurs in areas of flow separation.

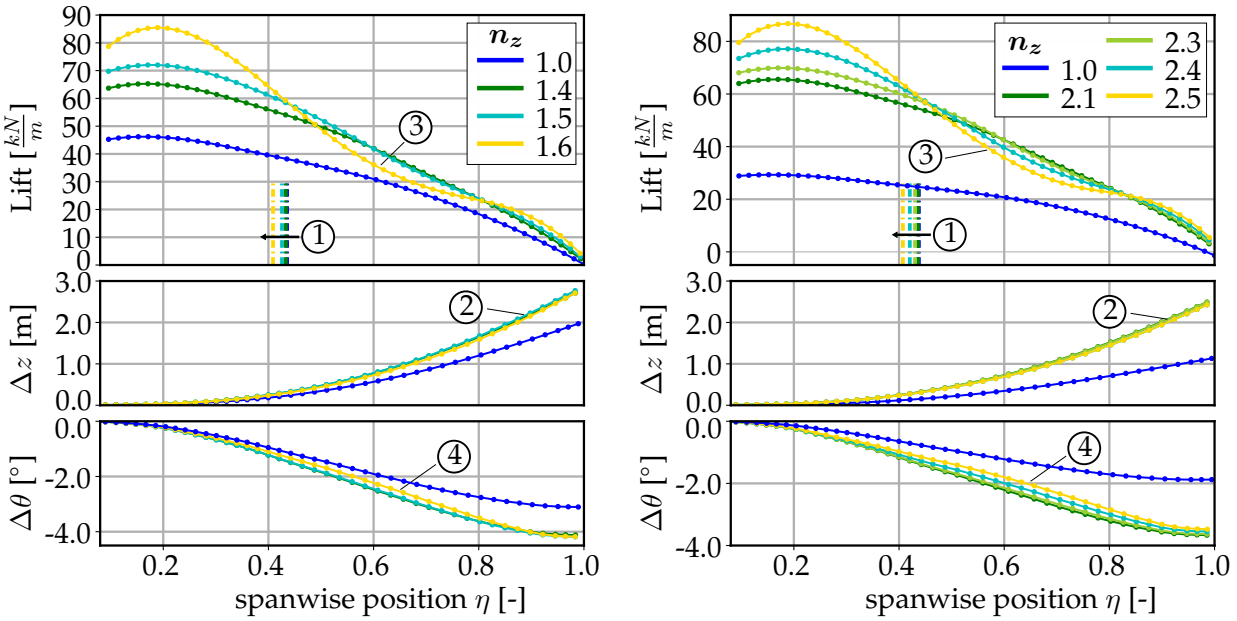

(a) Ma = 0.86, fuel model-1.

(b) Ma = 0.86, fuel model-2.

Figure 5.13.: Wing lift distribution and deformation at trimmed quasi-steady maneuver loads of the AR-13, #ref structural elastic aircraft configuration at cruise (#2, #3).

A particular difference is observed at *low-speed* flight with fuel model-1, shown in Figure 5.14a. The important characteristics are:

1. A comparison of the position of the flow separation to the *cruise-flight* scenario, as shown in Figure 5.13a, reveals that the area of starting separated flow in *approach-flight* shifts towards the fuselage.
2. The wing twist is considerably more negative, so that the flow is restored in the outer part of the wing and does not detach. As the wing increases in stiffness towards the wing root, this effect is progressively reduced, why it comes to flow separation (point 1).
3. The load application point of the lift force, indicated as dashed lines, hardly changes its position in the low speed cases. The same could be observed in the AR-10 configuration.

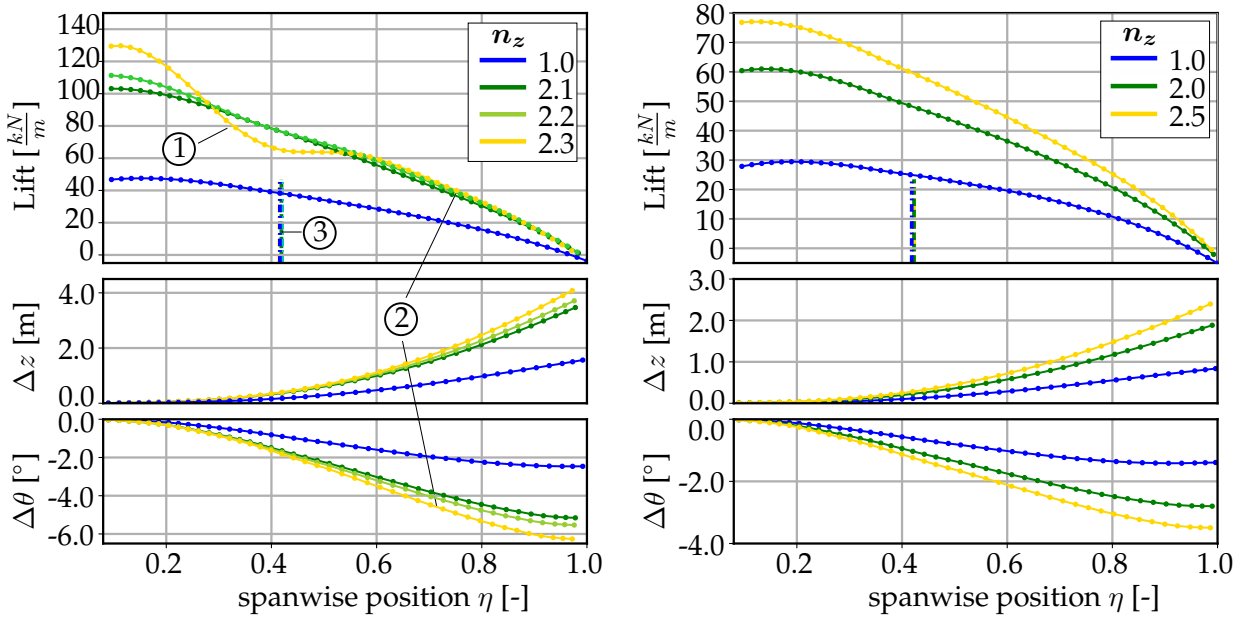

(a) $Ma = 0.5$, fuel model-1. (b) $Ma = 0.5$, fuel model-2.

Figure 5.14.: Wing lift distribution and deformation at trimmed quasi-steady maneuver loads of the AR-13, #ref structural elastic aircraft configuration at low speed flight (#1, #4).

5.3.2. External Load Comparison at Different Wing Stiffnesses

The influence of varying the structural wing stiffness (#ref, #red, and #sft) on the lift distribution and wing washout is studied by comparing the wing root section loading in different flight scenarios. As in the previous AR-10 wing study, the difference between #red and #sct with respect to #ref is studied. Further details, including the absolute root sectional loading, can be found in annex A.10.

Cruise Flight Scenario

The difference in section root forces for different wing stiffnesses at *cruise-flight* are depicted in Figure 5.15. Essentially the same phenomena as for the AR-10 wing can be identified. For transverse wing load S, a lift shift to the fuselage for higher n_z can be observed along with a linear dependency close to the steady-state *cruise-flight* condition, which is stopped by achieving $C_{L,max}$ and the subsequent flow separation. A general difference compared to the AR-10 configuration can be observed in the relative load reduction, which is larger in the case of the AR-13 wing. In the #3 flight scenario, a lower steady C_L at $n_z = 1.0$ leads to more wing bending deflection before stall occurs. The section force peak

load for evaluation of the load reduction characteristic is specified after reaching the end of the linear range, with the results summarized in Table 5.3.

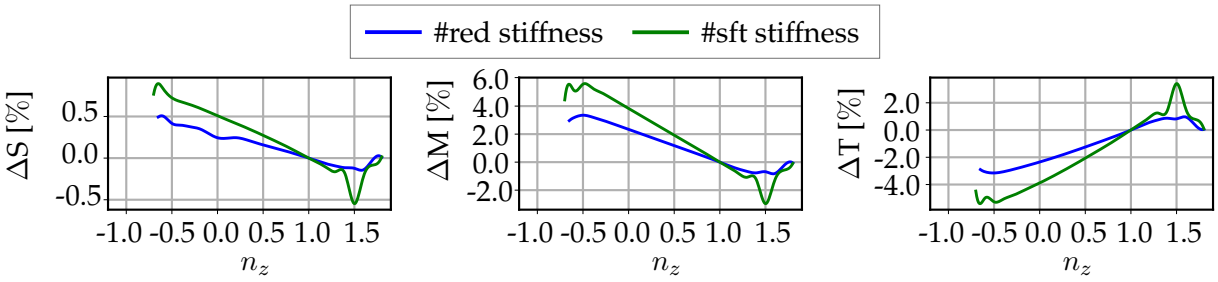

(a) Flight scenario #2.

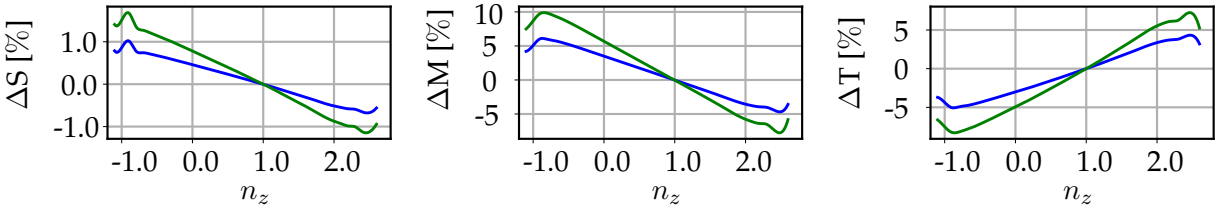

(b) Flight scenario #3.

Figure 5.15.: Difference of the AR-13 wing root section forces, at cruise flight, $\Delta\iota = \frac{\iota_\epsilon(n_z)-\iota_\Upsilon(n_z=1.0)}{\iota_\Upsilon(n_z=1.0)} - \frac{\iota_{ref}(n_z)-\iota_{ref}(n_z=1.0)}{\iota_{ref}(n_z=1.0)}$, Υ = (red, sft), ι = (S, M, T).

Low-Speed Flight Scenario

Figure 5.16 shows the wing root section forces at *low-speed* flight scenario #1 and #4. Generally, a more flexible wing configuration shows a better potential to reduce loads at higher load factors. The results for the *approach* (#4) shows that no flow separation or other non-linear dominant phenomena can be identified within the maneuver load range as with the AR-10 wing. The load reduction characteristic can be enhanced up to $n_z = 2.5$ and has not reached a local optimum.

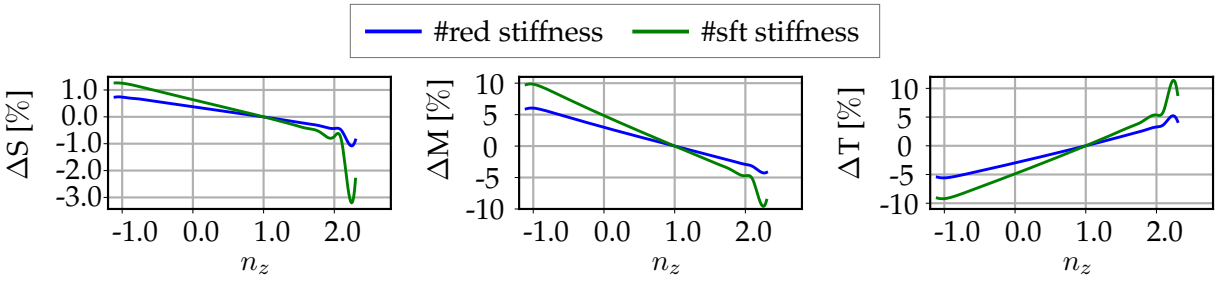

(a) Flight scenario #1.

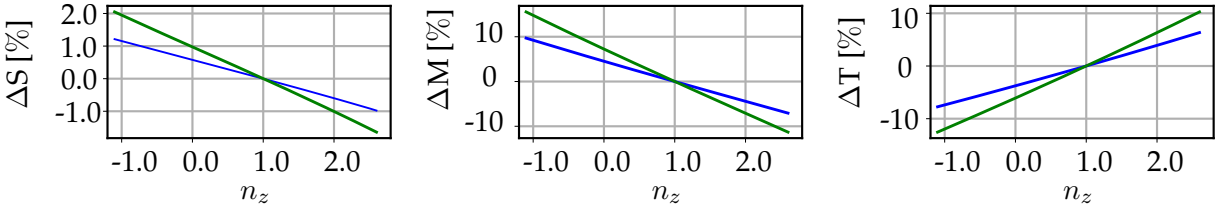

(b) Flight scenario #4.

Figure 5.16.: Difference of the AR-13 wing root section forces, at low-speed flight, $\Delta\iota = \frac{\iota_\Upsilon(n_z)-\iota_\Upsilon(n_z=1.0)}{\iota_\Upsilon(n_z=1.0)} - \frac{\iota_{ref}(n_z)-\iota_{ref}(n_z=1.0)}{\iota_{ref}(n_z=1.0)}$, Υ = (red, sft), ι = (S, M, T).

Table 5.3.: AR-13, wing root sectional forces peak point summary for the flight scenarios #1-#4.

flight scenario	**#1**		**#2**		**#3**		**#4**	
	#red	#sft	#red	#sft	#red	#sft	#red	#sft
ΔM	-4.28%	-9.59%	-0.77%	-1.09%	-4.69%	-7.77%	-6.61%	-10.60%
n_z	2.27	2.25	1.38	1.29	2.48	2.49	2.5	2.5
ΔT	5.23%	11.41%	-0.87%	-1.25%	4.33%	7.24%	5.93%	9.60%
n_z	2.23	2.24	1.39	1.29	2.47	2.46	2.5	2.5

5.4. Summary and Discussion of the Steady Maneuver Load Results

From the quasi-steady maneuver load study, it can be concluded that both wing layouts exhibited similar characteristics in terms of load reduction. The main common aspects due to more flexible wing structures are:

- The ability to reduce the load compared to a steady $n_z = 1.0$ flight depends substantially on how much the wing can deflect. Therefore, a higher load reduction can be achieved with a more bending flexible wing structure.
- Due to the wing washout, the lift distribution of more flexible wings is shifted towards the wing root, with a small amount redistributed to the fuselage.
- The limit load for pull-up maneuver is achieved in the low speed scenario with empty fuel tank. However, the largest external loads occur at low speed and MTOW. This is due to the lower deflection resulting from the higher inertia.

When considering flow separation as load reduction, it follows:

- For *cruise flight* scenarios, flow separation can be identified as a load limiting factor in the bending and torsional moment, characterized by decreasing load gradient at higher load factors.
- The maximum deflection depends on how much lift the wing can provide. Considering washout for passive load alleviation, the load reduction capabilities decrease when wing stall occurs at higher load factors. In combination with more flexible wings, this can have a negative effect on the load alleviation caused by washout.
- With the further increase of the load factors, improvements in the load reduction behavior can occur. This post-stall regime is characterized by a strong unsteady nature, for which a steady modeling approach is inherently limitative in its prediction. The transient flow must be taken into account in steady maneuver flight, in order to reflect the load fluctuations caused by cyclical separations.

The results from the steady-state load reduction from washout are therefore considered. To better illustrate the differences between the wing layouts in terms of load reduction performance, the main results are summarized in Table 5.4. The assessment is conducted by evaluating the wing root section forces M and T, at the steady flight point at $n_z = 1.0$ for the AR-10 and AR-13 wing layouts, as well as their gradients with regards to a change in n_z.

The results show that the AR-13 compared with the AR-10 wing exhibited higher external wing loads for all stiffness configurations and in all flight and fuel loading scenarios. Likewise, the wing root loading gradients $\frac{dM}{dn_z}$, $\frac{dT}{dn_z}$ are greater with respect to a change in the load factor n_z. The induced maneuver loads for the AR-13 are therefore higher, than for the AR-10 wings.

The general positive effect that more flexible wings have a better load reduction potential can be identified when analyzing the gradient of the internal load differences ΔM and ΔT between

Table 5.4.: Summary of the wing root sectional forces at n_z = 1.0.

wing configuration		AR-10				AR-13			
		M [kNm]	$\frac{dM}{dn_z}$	T [kNm]	$\frac{dT}{dn_z}$	M [kNm]	$\frac{dM}{dn_z}$	T [kNm]	$\frac{dT}{dn_z}$
(#1) Ma = 0.5	#ref	10651	10357	-6267	-5193	11759	11873	-7304	-6291
	#red	10678	10246	-6285	-5119	11828	11598	-7352	-6104
	#sft	10723	9729	-6315	-4781	11871	11423	-7381	-5982
(#2) Ma = 0.86	#ref	11400	11464	-6770	-6182	12714	12792	-7994	-7069
	#red	11400	11349	-6770	-6100	12713	12469	-7993	-6841
	#sft	11400	11132	-6770	-5952	12712	12311	-7993	-6726
(#3) Ma = 0.86	#ref	7524	7218	-4742	-3842	8307	8331	-5554	-4599
	#red	7575	7149	-4776	-3797	8442	8170	-5645	-4494
	#sft	7658	7034	-4832	-3722	8527	8068	-5703	-4425
(#4) Ma = 0.5	#ref	7039	6786	-4470	-3398	7692	7864	-5174	-4166
	#red	7115	6723	-4521	-3357	7890	7714	-5308	-4069
	#sft	7242	6617	-4606	-3286	8012	7618	-5392	-4006

the varying stiffness of the wings. The summary of all configurations and flight/fuel scenarios for steady-state flight at n_z = 1.0 is shown in Table 5.5. All configurations show that the passive load reduction improves by increasing the structural flexibility. The more flexible AR-13 wing can make better use of the kinematic washout effect, and thus achieves better characteristics. However, this is not sufficient to compensate for the higher load level resulting from the larger wingspan compared to the AR-10 wing. This means that passive load alleviation of external aerodynamic load through flexible wings is in the first place recommended by structural design with the same planform.

Table 5.5.: Summary: Difference of the change in wing root sectional forces for varying wing stiffnesses at n_z = 1.0.

wing configuration		Ma = 0.5 (#1)		Ma = 0.86 (#2)		Ma = 0.86 (#3)		Ma = 0.5 (#4)	
		#red	#sft	#red	#sft	#red	#sft	#red	#sft
AR-10	$\frac{d(\Delta M)}{dn_z}$	-1.00	-2.91	-1.55	-4.08	-1.91	-5.03	-1.28	-6.51
	$\frac{d(\Delta T)}{dn_z}$	1.21	3.39	1.51	3.99	1.77	4.67	1.42	7.16
AR-13	$\frac{d\Delta M}{dn_z}$	-2.53	-3.76	-3.50	-5.66	-4.47	-7.15	-2.91	-4.74
	$\frac{d\Delta T}{dn_z}$	2.84	4.28	3.19	5.21	3.84	6.20	3.11	5.10

6 Aircraft Gust Load Study

The aeroelastic aircraft models introduced in chapter 4 are used to study the load reduction characteristics under dynamic gust interaction, as shown in Figure 6.1. The influence of gusts is investigated using the *Field-Velocity-Approach*, as introduced in the academic demonstration example (chapter 3). First, the gust model and the setup required for the transient simulation are introduced. In the following study, gusts with short and long gust gradients are considered, in which a distinction is made between the *cruise-* and *approach-flight* scenarios. Under the influence of different gust lengths, the AR-10 and AR-13 wing designs, including different stiffness configurations, are analyzed individually. In conclusion, the two configurations are compared and the gust response is characterized in terms of the external load reduction.

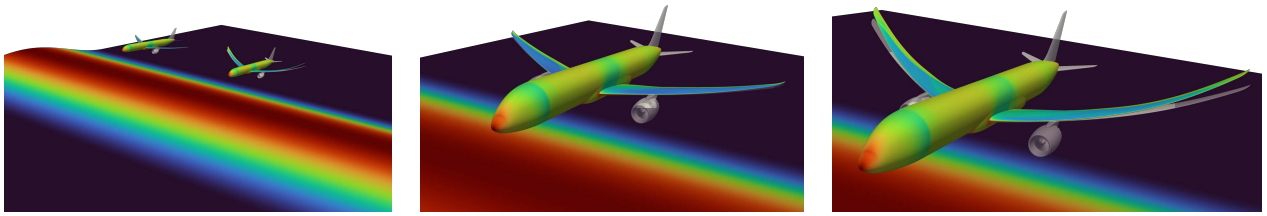

(a) 1-cos gust field. (b) Aspect Ratio 10 configuration. (c) Aspect Ratio 13 configuration.

Figure 6.1.: Transport aircraft gust encounter study.

Contents

6.1. Flight Condition and Computational Setup

The structural and aerodynamic models developed in chapter 4 are used as computational models. Therefore, the simulation setup is the same as in the maneuver load study, with the difference that the pitch angle θ is used for trimming instead of the global AoA. As no external wind is considered, $\alpha = \theta$ applies. As initial solution to the transient simulations, the results of the trimmed steady-state calculation at $n_z = 1.0$ are used. At time t_0, the position of the gust is $100\,\mathrm{m}$ in front of the aircraft wing reference point. The physical time step size used for the transient simulation is $\Delta t = 8.25 \cdot 10^{-4}\,\mathrm{s}$. The choice of the time discretization step is a compromise between the accuracy and the computational

runtime. For the transient gust load analysis, the two flight scenarios *cruise-flight* at $Ma = 0.86$ with fuel model-1 (#2) and *approach-flight* $Ma = 0.5$ with fuel model-2 (#4) are considered, which are further separated into gust load cases with short (case-1) and long gust lengths (case-3). The corresponding flow and gust parameters are listed in Table 6.1. The geometric properties of gust length and aircraft size, herein, the AR-10 wing configuration with #2 *cruise* flight scenario, are plotted in Figure 6.2.

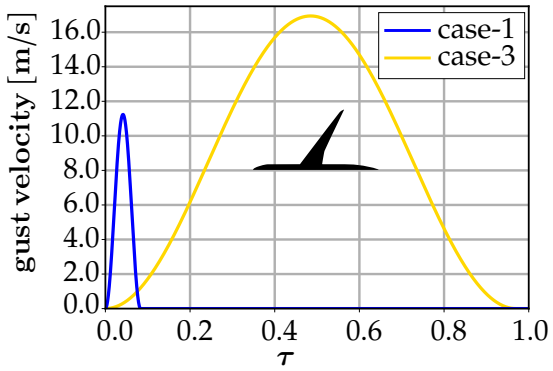

	V_v Gust-A cruise #2	V_v Gust-B approach #4
Ma_∞	0.86	0.5
FL	350	0
ρ_∞	$0.380\,45\,\mathrm{kg\,m^{-3}}$	$1.225\,\mathrm{kg\,m^{-3}}$
T_∞	218.92 K	288.15 K
case-1:		
H = 18.29 m	11.24 $\frac{\mathrm{m}}{\mathrm{s}}$	8.82 $\frac{\mathrm{m}}{\mathrm{s}}$
case-3:		
H = 213.36 m	16.94 $\frac{\mathrm{m}}{\mathrm{s}}$	13.29 $\frac{\mathrm{m}}{\mathrm{s}}$

Figure 6.2 & Table 6.1: Aircraft cruise- and approach-flight gust load cases.

6.2. Aeroelastic Gust Load Response of the AR-10 Wings

The structural AR-10 wing with different structural flexibility are studied based on their load reduction characteristics under an external transient 1-cos gust encounter. The gust loads are obtained by means of a transient Fluid-Structure-Interactions simulation. The loading scenarios are distinguished in a *cruise-* and *approach-flight* scenarios, as described in Table 6.1.

6.2.1. Results for Cruise Flight Condition

The C_L time progression results for gusts with different structural stiffness (#ref, #red, #sft) are given in Figure 6.3. The additional induced lift caused by the gust can be detected in the C_L graph, which then causes the wing structure to deflect and oscillate around the steady state flight condition. The longer gust exposure and higher gust vertical velocity of the case-3 scenario results in a considerably higher induced maximum C_L.

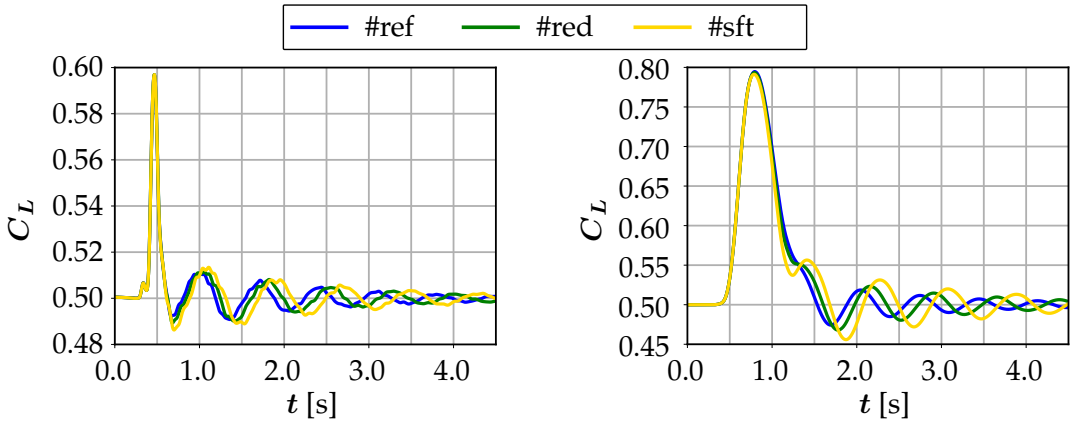

(a) C_L progression case-1.

(b) C_L progression case-3.

Figure 6.3.: AR-10 gust C_L response in cruise flight with different gust lengths.

Wing Deflection Results

The respective deflection of the wing tip over time for the different stiffnesses relative to the undisturbed steady-state flight condition of the gust cases-1 and -3 scenarios are shown in Figure 6.4. Additionally, the deflection u_z and twist θ along the span is shown in Figure 6.5, with the undisturbed steady state condition at t_0 shown in black. The elastic deformation of the case-1 gust is shown in green with the minimum and maximum values indicated as solid lines. The results of the case-3 gusts scenario are plotted in blue. The higher induced C_L in case-3 leads to a higher deflection of the wing in all cases, which becomes more significant with increasing structural flexibility. In case-3, the key difference is that the amount of $\Delta\theta$ increases as the flexibility increases, thereby indicating that washout is increased, and hence more reduction of the local AoA.

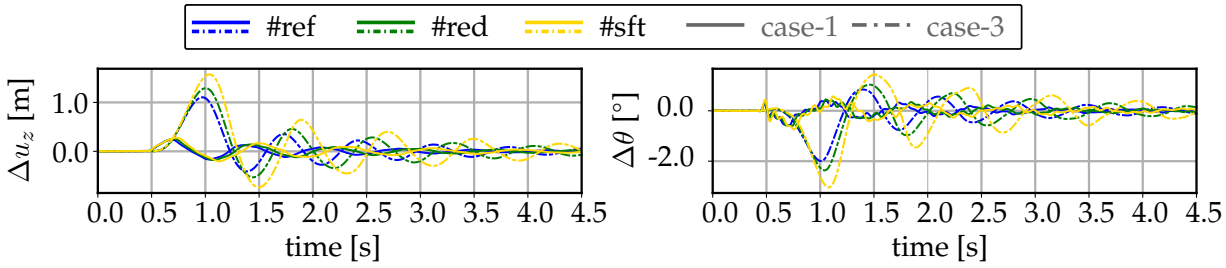

(a) max displacement. (b) max rotation.

Figure 6.4.: AR-10 wing tip deflection relative to cruise steady flight shape during gust encounter case-1, case-3.

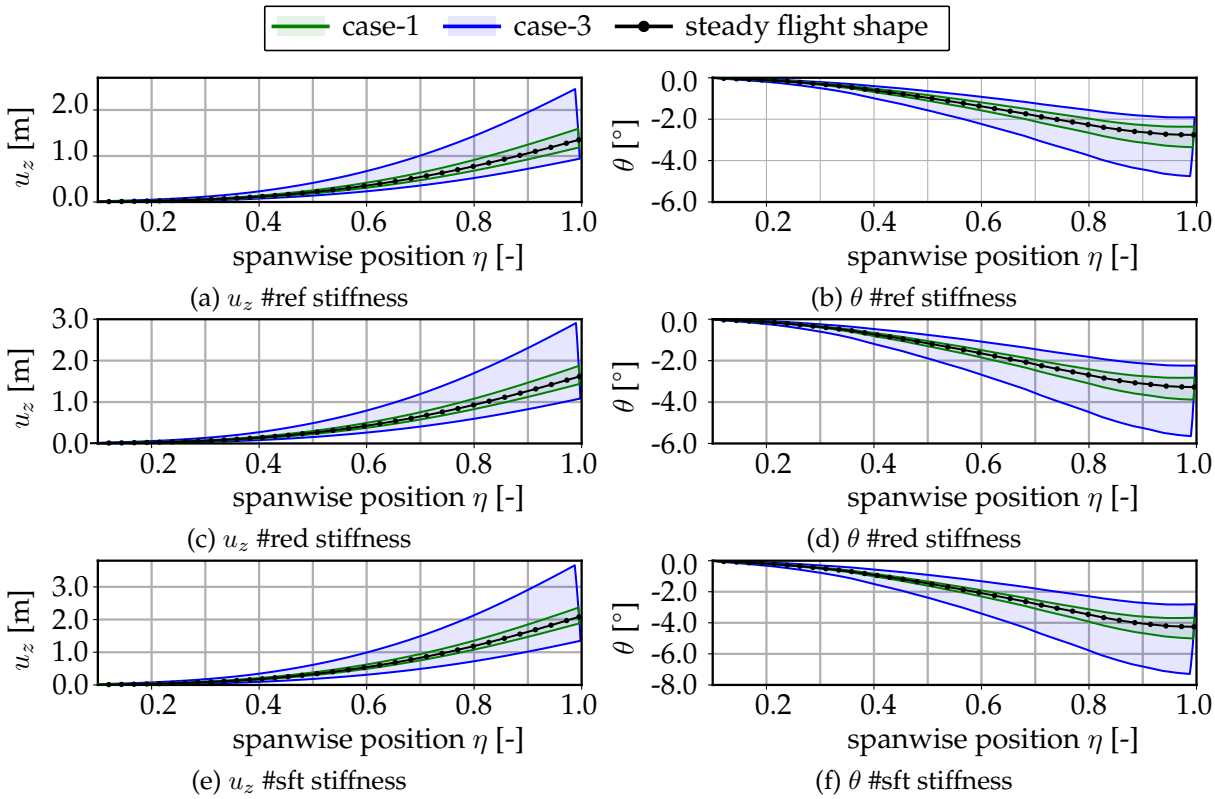

(a) u_z #ref stiffness (b) θ #ref stiffness

(c) u_z #red stiffness (d) θ #red stiffness

(e) u_z #sft stiffness (f) θ #sft stiffness

Figure 6.5.: AR-10 wing reference axis deformation during cruise flight gust encounter.

External Load Results

Due to the wing sweep, the maximum peak loads of the root bending moment M and torsion moment T do not occur simultaneously. Therefore, both are plotted in a bending-torsion diagram, as shown in

Figure 6.6 and Figure 6.7. The initial state at t_0 is given by markers, with the transient evolution along the hystereses indicated by the arrow.

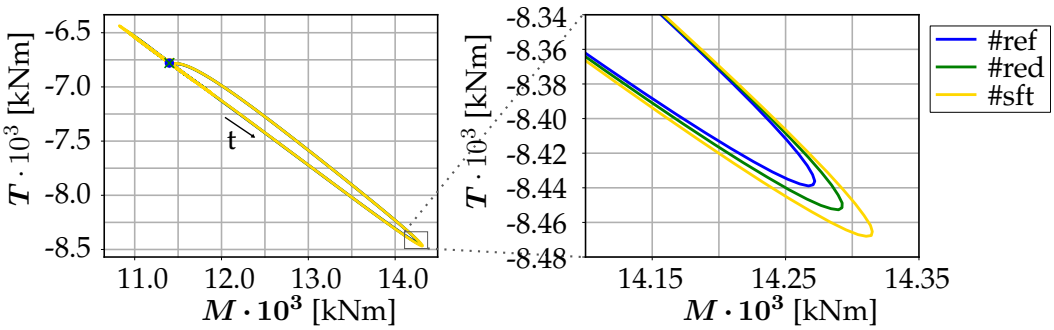

Figure 6.6.: AR-10, bending-torsion diagram in cruise flight for gust length case-1.

For the case-1 scenario, it can be noted that the more flexible wing leads to an increased external load. By comparing the results with the deformation plot in Figure 6.5, it is observed that the reduction of the local AoA is not sufficiently strong to reduce the additionally lift. Additionally, due to the position of the neutral point, which is in front of the elastic axis, the extra induced lift causes the wing to twist up. In the absence of wing bending, due to the wing's inertia, the wing twists up and thus results in an increase of the local AoA. As the torsional stiffness counteracts the up twist, this becomes more pronounced with reduction of the torsional stiffness of the wing. Therefore, the load reduction behavior for small gust lengths is affected negatively by a more flexible wing structure. This is in contrast to the steady state results conducted in the previous maneuver load study in chapter 5 and means further, that the gust-aircraft interaction time has an effect on the load reduction characteristic. These findings are in agreement with the 2-DoF model studied in chapter 3.

The evaluation of the case-3 bending-torsion load in Figure 6.7 shows that the peak load of all three stiffnesses is close to each other. The reason for this can be determined from the C_L curve in Figure 6.3b and the steady elastic C_L slope determined in Figure 5.3b. With $C_L \approx 0.6$ the first non-linearities due to flow separation can be noted, and as in the steady state analysis, the load reduction depends on the deflection of the wings. If this is limited by the stall boundary, the washout of the wing also stops. To investigate the drop in lift owing to flow separation, the lift distribution during the gust encounter of scenario case-3 is analyzed in detail.

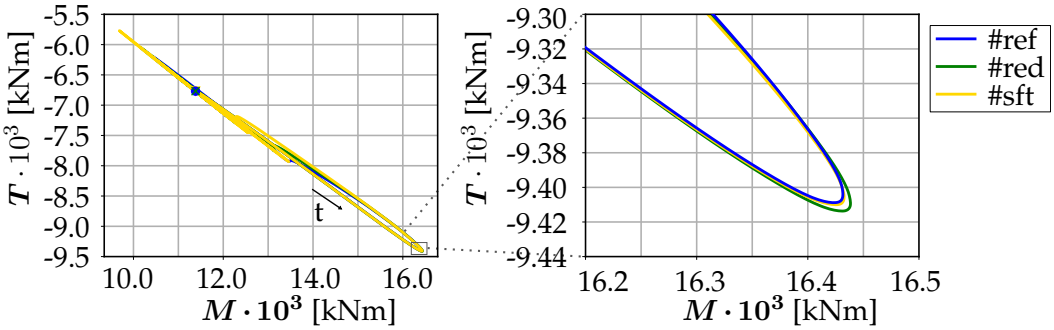

Figure 6.7.: AR-10, bending-torsion diagram in cruise flight for gust length case-3.

The lift distribution for different time steps is shown in Figure 6.8. The undisturbed steady distribution at t_0 is plotted in blue. At time $t = 0.724\,35\,\mathrm{s}$, displayed in green, the maximum bending moment is reached. The maximum C_L is reached at $t = 0.794\,475\,\mathrm{s}$ (cyan), where the first reductions in lift due to flow separation can be identified. When the maximum deflection is reached at $t = 0.974\,325\,\mathrm{s}$ (yellow), the decrease in outboard lift is progressing.

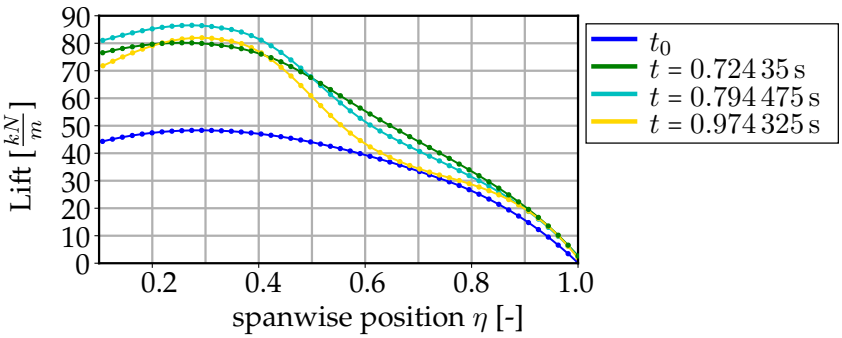

Figure 6.8.: AR-10 lift distribution, #ref configuration at cruise flight, case-3.

The flow separation occurring on the wing can also be quantified via the surface friction coefficient C_f between n_z = 1.0, as shown in Figure 6.9a and the maximum wing tip deflection, plotted in Figure 6.9b. Additionally, for the structural configurations #red and #sft the surface friction C_f at maximum deflection are shown in Figure 6.9c and Figure 6.9d, respectively. In comparison, the separation is slightly washed out when the wing becomes more flexible. The time of maximum deflection is also considerably delayed. This explains why the maximum bending moment M does not differ much in *cruise-flight* gust case-3, as it is dominated and limited by the flow separation. Compared to the gust encounter scenario of the 2-DoF system analysis, no recovery of the flow without drop below steady flight C_L is observed.

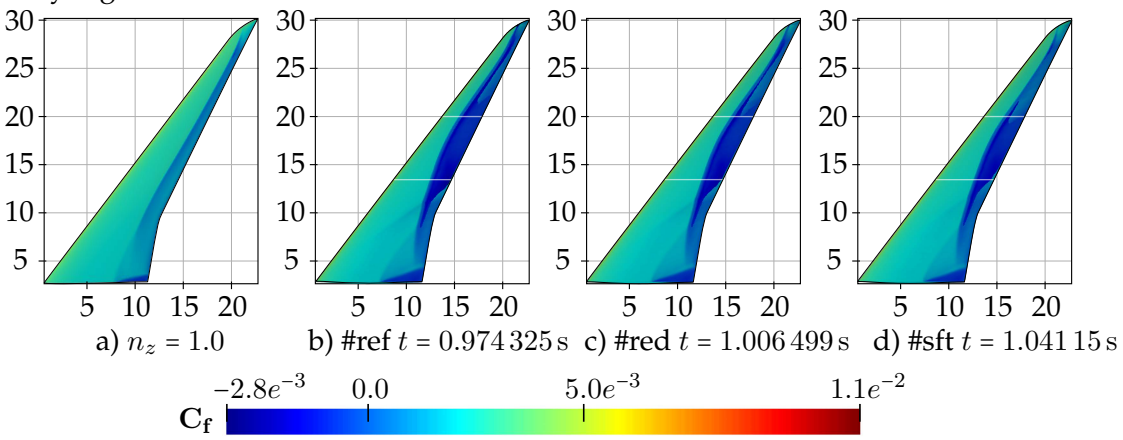

Figure 6.9.: AR-10 wing friction coefficient C_f for different wing stiffnesses #ref, #red and #sft in cruise flight scenario #2, at maximum wing tip deflection.

6.2.2. Results for Approach Flight Condition

Figure 6.10 shows the C_L results for gust case-1 and case-3 at *approach-flight* condition. Differences are observed in the gust scenario case-3, in which the maximum induced C_L is lower for a structurally more flexible wing. Furthermore, the oscillation is more dampened due to the higher air density.

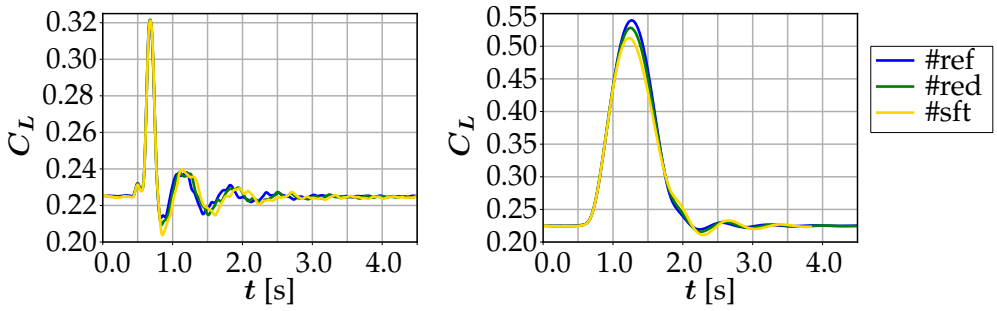

(a) C_L progression case-1 (b) C_L progression case-3

Figure 6.10.: AR-10, gust C_L response in approach flight at different gust lengths and structural stiffnesses.

Wing Deflection Results

The results of the wing tip deflection, Δu_z, relative to the undisturbed shape during *approach-flight* condition are shown in Figure 6.11. Compared to the *cruise-flight* scenario, the wing deflects noticeably more, owing to the lower fuel mass of the wing, which decreases the inertia forces acting against the lift. In addition, no lift limiting effect like flow separation occurs. Comparing the twists $\Delta\theta$ in gust case-3 with respect to the undisturbed flight shape, it is observed that the wing achieves more washout in *approach-flight*. Likewise, for small gust lengths (gust-1), the wing twists up as in *cruise-flight*.

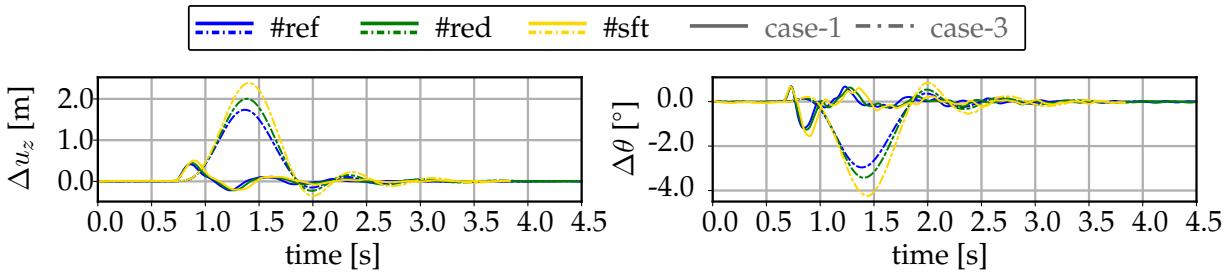

(a) max displacement (b) max rotation

Figure 6.11.: AR-10 wing tip deflection relative to approach steady flight shape during gust encounter case-1, case-3.

Deflection u_z and θ along the normalized wing span η is shown in Figure 6.12, with the undisturbed steady state flight shape at t_0 plotted as black line. The elastic deformations of the case-1 and case-3 gust are shown in green and blue, respectively. The generally increasing deflection with increasing structural flexibility can also be identified in this plot.

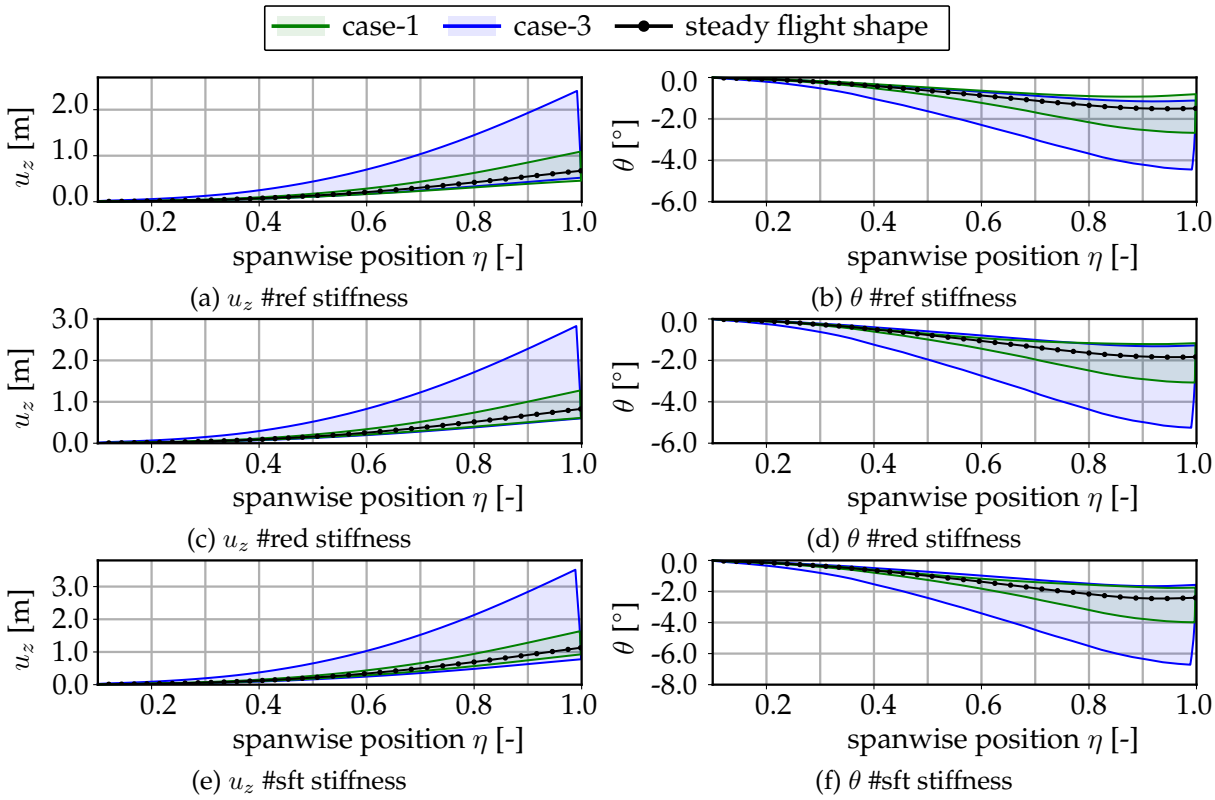

(a) u_z #ref stiffness (b) θ #ref stiffness

(c) u_z #red stiffness (d) θ #red stiffness

(e) u_z #sft stiffness (f) θ #sft stiffness

Figure 6.12.: AR-10 wing reference axis deformation during approach flight gust encounter.

External Load Results

The analysis of the external loads in *approach-flight* case-1, plotted in Figure 6.13, shows that the peak level loading is lower. As for the *cruise-flight* case, the structurally more flexible wing configurations do not provide beneficial alleviation of the additional induced loads at small gust lengths. The deformation analysis, in which the wing twists up at small gust lengths, reveals that the loads cannot be reduced. Furthermore, as the absolute twist up $\Delta\theta$ is larger compared to *cruise-flight*, higher load amplitudes, especially in the root bending moment, are induced.

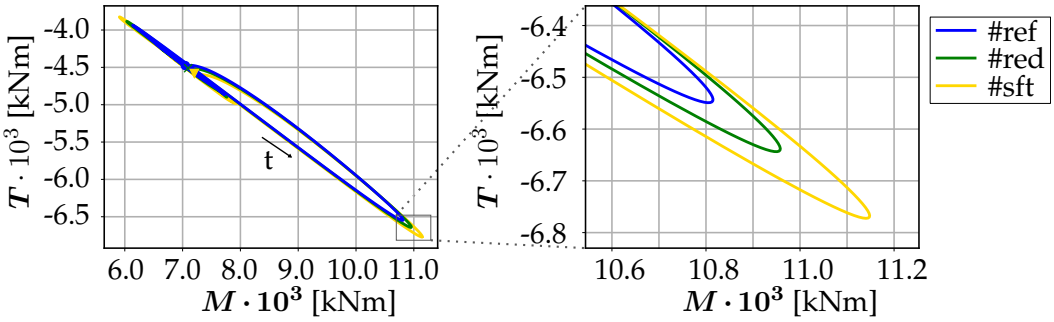

Figure 6.13.: AR-10, bending-torsion diagram in approach flight with gust length case-1.

For gust load case-3, shown in the Figure 6.14, the maximum gust loads M and T at the wing root can be reduced with increasing flexibility of the structure. Although the absolute external loads values are lower than in the case of *cruise-flight*, the peak load amplitude can be reduced significantly. This could also be observed in the steady-state maneuver load study, where no stall occurs on the wing in the *approach-flight* scenario. Due to the progressive increase in lift, the wing can consistently progress the washout and effectively reduce the load.

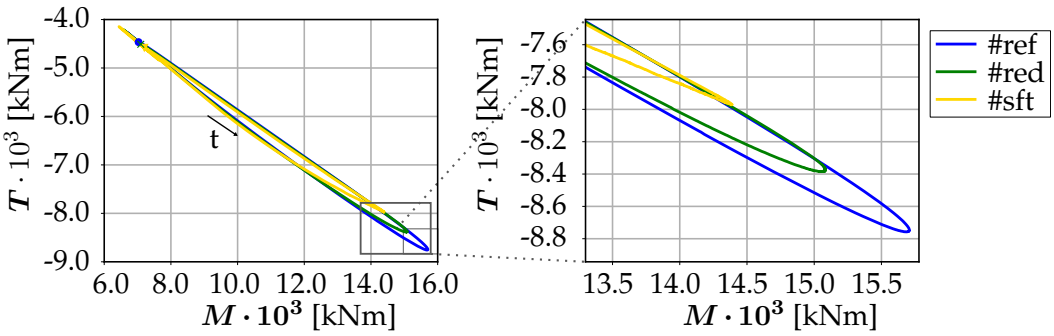

Figure 6.14.: AR-10, bending-torsion diagram in approach flight with gust length case-3.

6.3. Aeroelastic Gust Load Response of the AR-13 Wings

In this section, the load reduction of the AR-13 wing layout with different structural stiffnesses encountering the gust lengths of case-1 and case-3 is investigated. As for the AR-10 wing, the results are presented for a *cruise-* (#2) and *approach-flight* (#4) scenario from Table 6.1.

6.3.1. Results for Cruise Flight Condition

The time progression of C_L for the three stiffness configurations (#ref, #red, #sft) at gust load case-1 and case-3 at *cruise-flight* is shown in Figure 6.15. As with the AR-10 configuration, the additional induced lift causes the wing structure to deflect and oscillate around the stationary flight condition, with the load of case-3 in turn achieving the largest C_L values. Additionally, C_L could not be increased above a maximum value, thereby indicating that a lift-limiting effect occurs.

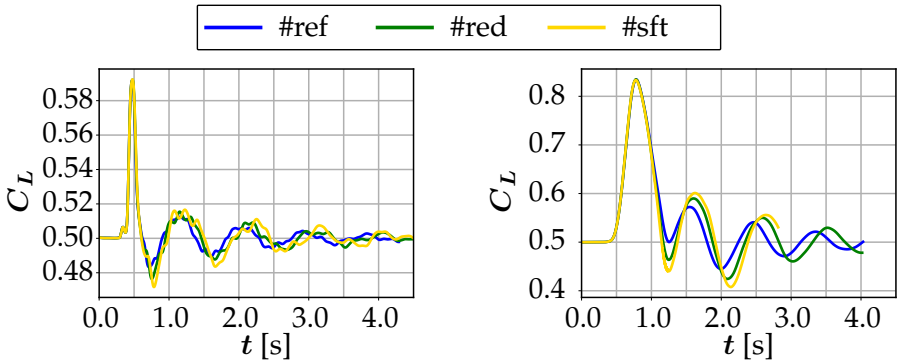

(a) C_L progression case-1. (b) C_L progression case-3.

Figure 6.15.: AR-13 gust C_L response in cruise flight with different gust lengths.

Wing Deflection Results

The wing tip deformation over time for the different stiffnesses compared to the undisturbed steady state flight condition of the gust scenarios case-1 and case-3 are presented in Figure 6.16. As for the AR-10 configuration, the wing twists up in the event of small gust lengths. A clear difference can be observed in the case-3 gust scenario, wherein the wing considerably twists up as well. The wing structures used here do not have sufficient torsional stiffness, so that the targeted washout only occurs after a more severe wing bending deflection. Therefore, the wings inertia has a dominant influence in both gust cases.

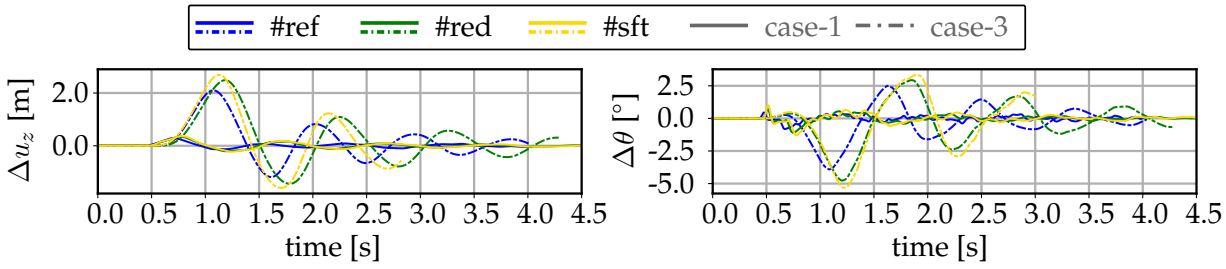

(a) max displacement (b) max rotation

Figure 6.16.: AR-13 wing tip deflection relative to cruise steady flight shape during gust encounter case-1, case-3.

Additionally, the deformations u_z and θ along the span are illustrated in Figure 6.17, with the undisturbed steady state condition at t_0 indicated in black. The elastic deformations of case-1 and case-3 gusts are plotted in green and blue, respectively. The minimum and maximum deformations are marked as solid lines. Compared to the AR-10 wing, all AR-13 configurations achieve significantly larger deformation amplitudes due to an increase in structural flexibility.

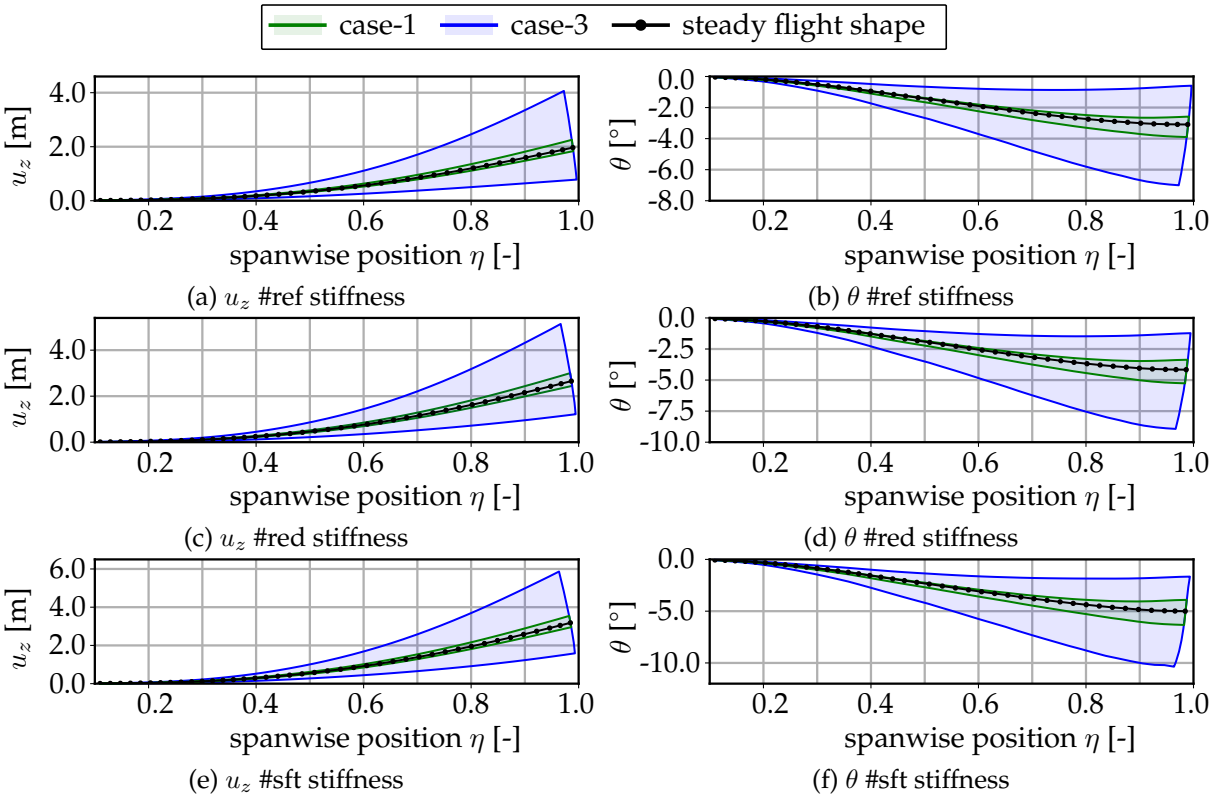

Figure 6.17.: AR-13 wing reference axis deformation during gust encounter.

External Load Results

The external loads as root bending-torsion diagram for *cruise flight* case-1 and case-3 are depicted in Figure 6.18 and Figure 6.19. The markers indicate the initial state at t_0 and the development with time is indicated by the arrow. Generally, a substantially higher load level occurs in the root bending moment M and torsion moment T. In both gust load case-1 and case-3, the AR-13 wing design shows a less effective load reduction characteristic for the structurally more flexible configuration in the *cruise* scenario.

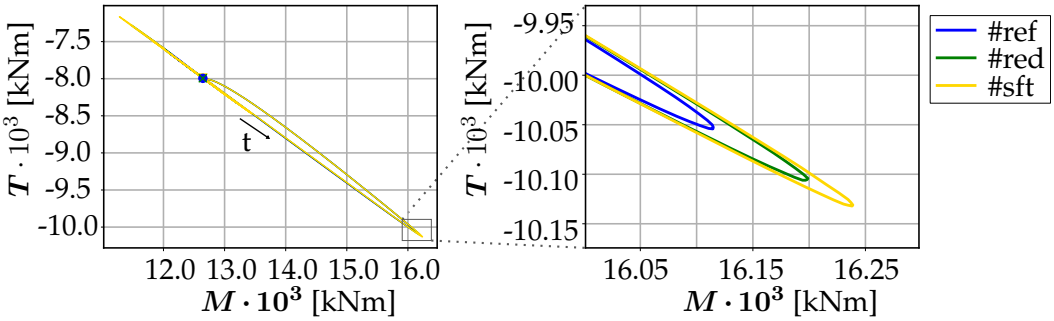

Figure 6.18.: AR-13, bending-torsion diagram in cruise flight with gust length case-1.

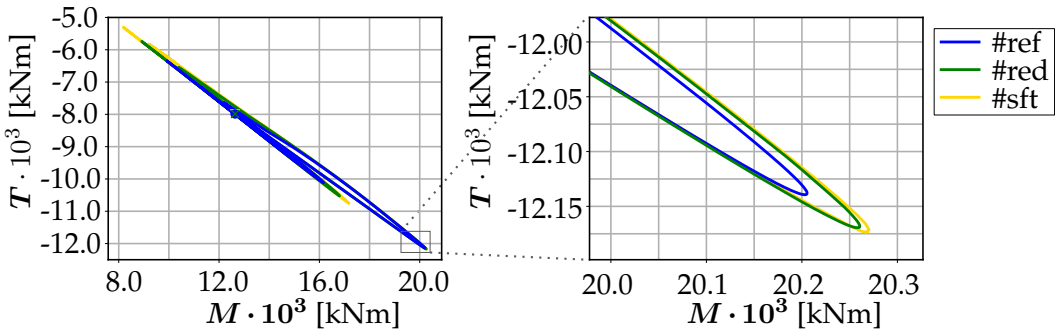

Figure 6.19.: AR-13, bending-torsion diagram in cruise flight with gust length case-3.

The wing lift distribution at different time steps for the AR-13 #ref configuration, gust case-3, is shown in Figure 6.20. The undisturbed steady distribution at t_0 is plotted in blue. The additional time steps are again plotted for the peak values of C_L (cyan), M (green), and $u_{z,max}$ (yellow). The lift distribution at the time of maximum lift (cyan) shows a slight decrease in lift between $\eta = 0.6 - 0.8$, although this is not as dominant as in the AR-10 configuration. Furthermore, the time between reaching the maximum load and the maximum deflection is noticeably shorter than that in the AR-10 configuration. When reaching the maximum wing deflection, the aerodynamic load has already decreased significantly and no noticeable stall indications are observed. In contrast to the AR-10 wing, flow separation occurs when the load maximum is reached and starts to reattach.

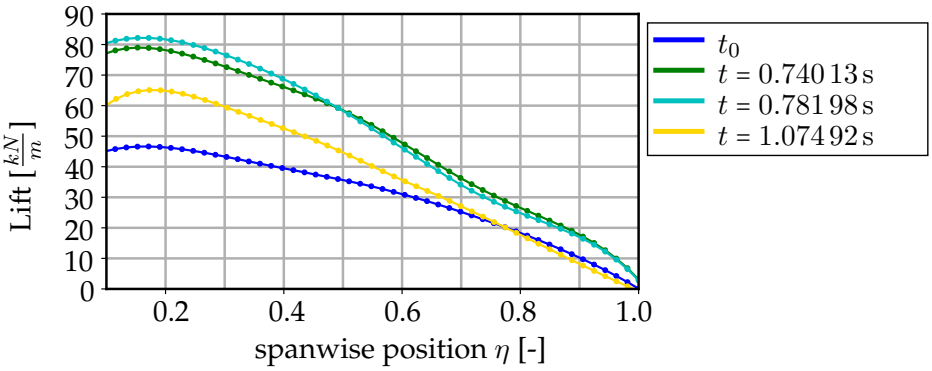

Figure 6.20.: AR-13 lift distribution, #ref configuration at cruise flight, case-3.

The AR-13 wing shows a phase shift between deflection and maximum lift due to inertia. Maximum lift and the time of maximum deflection is significant delayed. The surface friction coefficient C_f contour plot in Figure 6.21 illustrates the detached flow for the three wing stiffnesses #ref, #red, and #sft at maximum C_L during the gust case-3 encounter. At maximum lift, the AR-13 wing shows stall in the *cruise-flight* scenario, but not to the same extent as in the AR-10 layout.

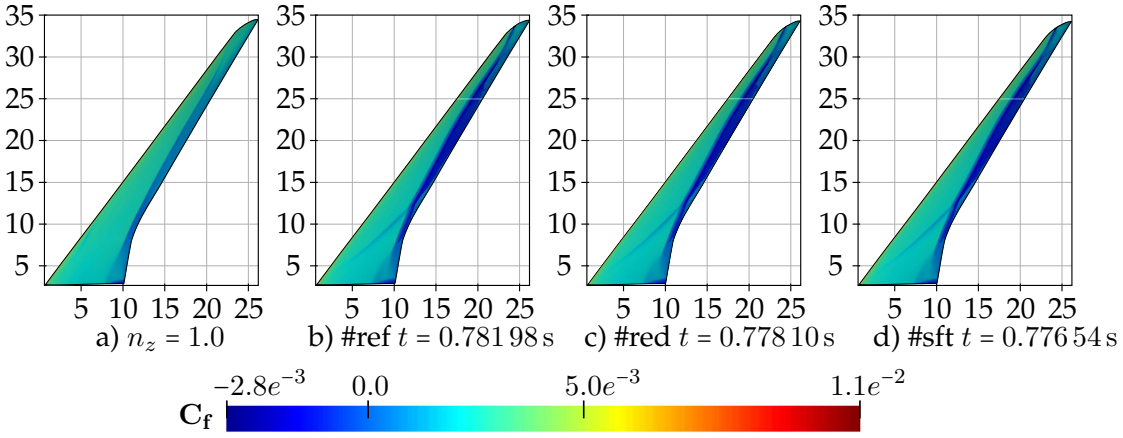

Figure 6.21.: AR-13 wing friction coefficient C_f for different wing stiffnesses #ref, #red and #sft in cruise flight scenario #2, at maximum lift.

6.3.2. Results for Approach Flight Condition

The time progression of C_L for the three stiffness configurations (#ref, #red, and #sft) at gust load case-1 and case-3 for *approach flight* is shown in Figure 6.22. Similar to the AR-10 wing, a difference in the maximum induced C_L for the varying stiffness versions is observed in case-3. The same is true for the vibration, which is more strongly damped due to the higher air density.

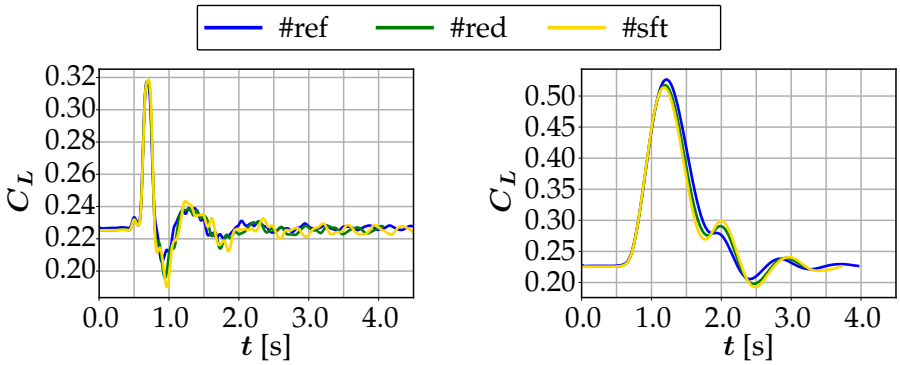

(a) C_L progression case-1. (b) C_L progression case-3.

Figure 6.22.: AR-13 gust C_L response in approach flight at different gust lengths and structural stiffnesses.

Wing Deflection Results

The deflections of the wing tips can be found in Figure 6.23. As in *cruise-flight*, an initial turn up of the wing tip can be observed in the *approach-flight* scenario when interacting with the gust field. The corresponding u_z deflection and twist distribution θ of the reference axis is illustrated in Figure 6.24. The amplitudes of case-1 and case-3 are shown in green and blue, respectively. Again, the maximum and minimum deformations are indicated by solid lines, and the steady flight shape is indicated in black.

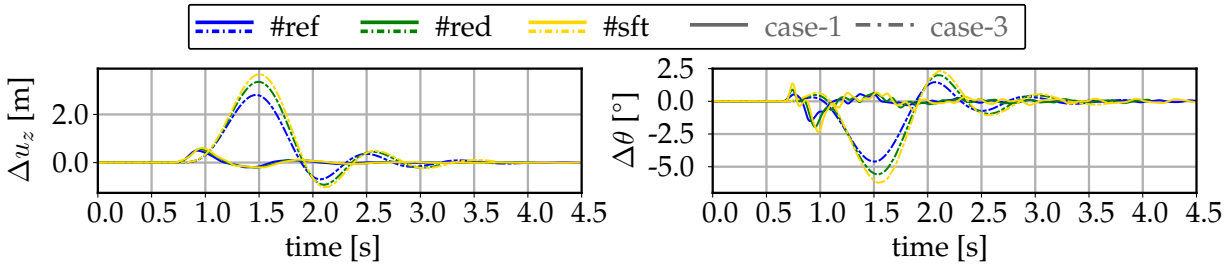

(a) max displacement (b) max rotation

Figure 6.23.: AR-13 wing tip deflection relative to approach steady flight shape during gust encounter case-1, case-3.

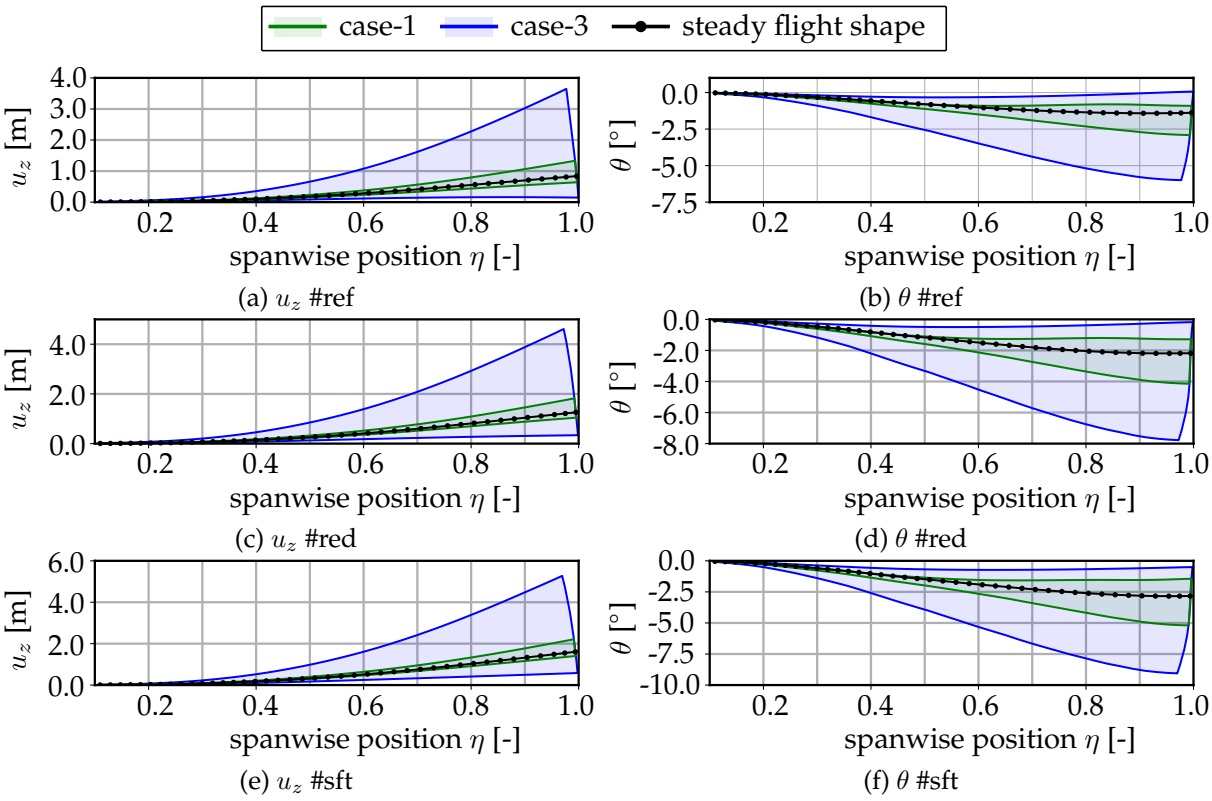

Figure 6.24.: AR-13 wing reference axis deformation during gust encounter.

External Load Results

The external loads as root bending-torsion diagram are depicted in Figure 6.25 and Figure 6.26 for case-1 and case-3, respectively. For the short gust length case-1, the same conclusions can be drawn as in the *cruise* case. Due to the lower stiffness and the associated twist up of the wing, the wing root section loads M and T increase. However, in load case-3, a trend change is observed. The #red structural design showed a slightly reduced bending moment with comparable maximum torsional moment T. The even more flexible #sft wing does not show this advantage, thereby resulting in an increased torsional moment. No clear trend statement is found between wing stiffness and external load reduction for the last load case.

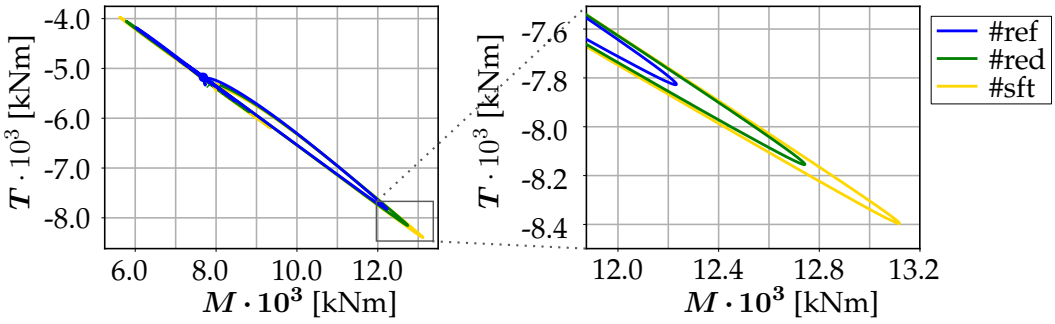

Figure 6.25.: AR-13, bending-torsion diagram in approach flight with gust length case-1.

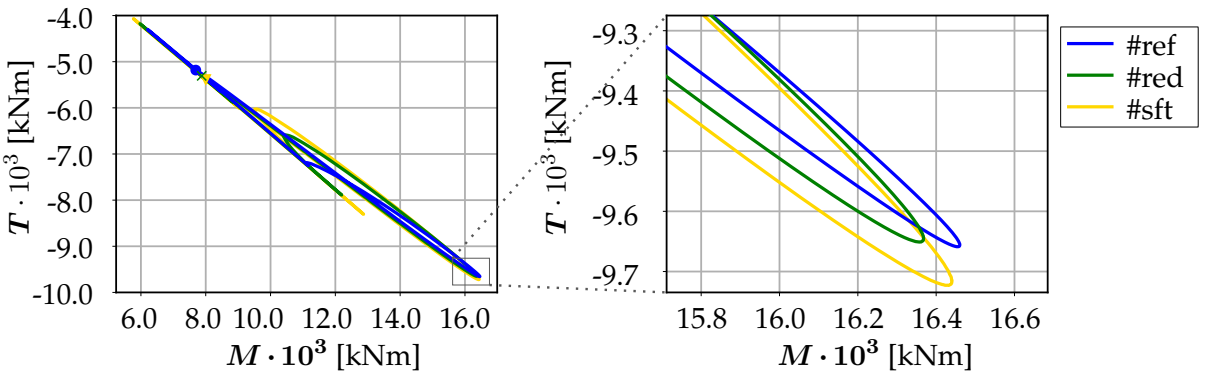

Figure 6.26.: AR-13, bending-torsion diagram in approach flight with gust length case-3.

6.4. Classification of the Wing's Gust Response Characteristics

In the previous chapters, the fundamental results on the gust behavior of the AR-10 and AR-13 aircraft wings are presented. The results of the wing structural deformation and induced external loads are analyzed in detail with the aim to list the individual effects and categorize the load-reduction characteristics.

6.4.1. Standard Case

This analysis begins with the *approach-flight* scenario #4 of the AR-10 wing as it shows the characteristics of load reduction performance that are generally considered to be beneficial. Figure 6.27 shows the results for transverse section load S, root bending moment M, wing tip deflection u_z, and tip rotation θ at the time when the wing begins to encounter the gust. The three stiffness versions, #ref, #red, and #sft, are individually represented by different line types. For a better representation of all quantities in a common diagram, each is normalized with the maximum amplitude of the respective reference stiffness (#ref) result. The most significant correlations are as follows:

1. The time transient behavior of the external shear force, S, at the wing root corresponds to the lift force generated by the wing. The gust response of a rigid wing, as reference, and the flexible wing's response are illustrated in light blue and black, respectively. Compared to the maneuver flight, the additional lift in a gust load case is not desired. As seen from the #red and #sft results, the load decreased with a more flexible wing.

2. The progression of the bending moment M is indicated in yellow. As with the transverse force S, a load-reducing is observed with a more flexible structural design. Due to the wing sweep, the gust peak does not occur uniformly on the wing, so that the moment peak load occurs with an offset.

3. With a more flexible wing, considerably more negative twist θ is achieved, which indicates that the local AoA is reduced by a greater magnitude. The lower AoA in turn decreases the lift, which decreases the external loads (S, M).

4. The more flexible wings leads to increased bending deflections. The correlation between deflection and washout is explained in the 2-DoF model of chapter 3. Similarly, in this study, a link between deflection and washout (twist) is observed.

5. Due to the inertia of the wing, the deflection only sets in with considerable time offset.

6. At the beginning of the gust encounter, the wing twists upwards, thereby increasing the AoA. This corresponds to the opposite characteristic, which is not intended in the design. This negative effect increases slightly with a lower wing stiffness owing to the lift force, which is in front of the elastic wing axis and, thus, creates a positive torsional moment. However, the washout from the wing bending is not yet active (Point 5)

7. Due to the twist up at the beginning of the gust encounter (Point 6), the external loads are higher than in the rigid wing case.

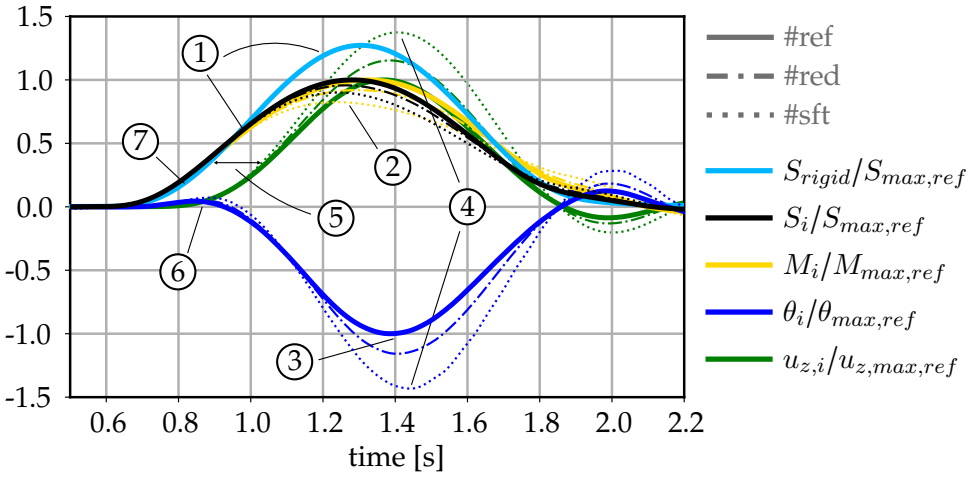

Figure 6.27.: AR-10 wing gust interaction, approach #4 scenario, gust case-3.

6.4.2. Short Excitation Case

The second category is a gust scenario with a short wave length, causing a short excitation of the structure. The applied study case is *approach-flight* scenario #4 of the AR-10 wing. Similarly, the transverse root force S, root bending moment M, and the wings tip deflection u_z, as well as rotation θ are evaluated for the different wing stiffnesses. The results for the case-1 gust is presented in Figure 6.28. The key correlations identified are:

1. Between the maximum transverse force, S, and bending moment M peak point, an offset in time is observed. Compared to the rigid-body gust, the lift induced trough the gust up wind increases faster. The external load increases with a more flexible wing configuration. The higher transverse peak load in the elastic configuration compared with the rigid wing indicates that the local AoA is increased.

2. In terms of the wing twist, the more flexible configurations twist up more, increasing the local AoA and thus the external loading.

3. By the time the wing achieves any washout reaction, the gust and the maximum load point are already exceeded.

4. The correlation between wing deflection and washout can also be observed in this scenario, however, the inertia leads to a significantly strong time lag, so that no load alleviation advantage can be achieved. The only way to alleviate the peak loads is to have a higher wing torsional stiffness, to reduce the twist up.

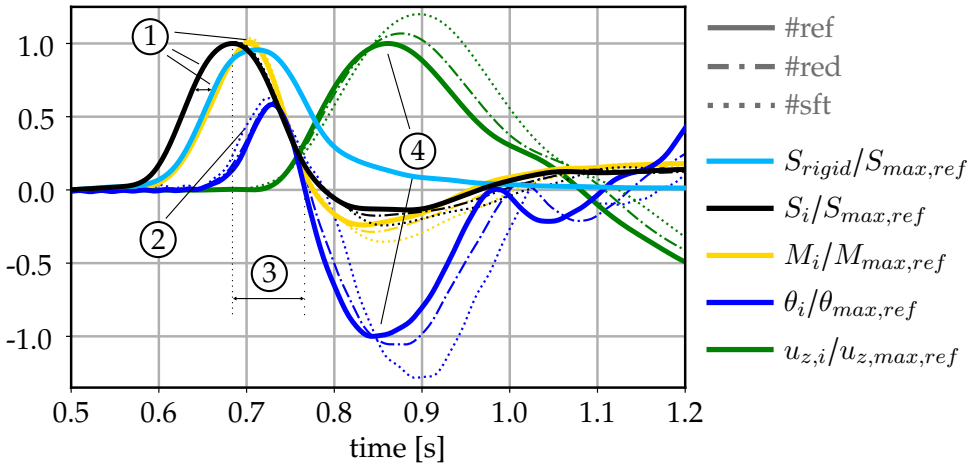

Figure 6.28.: AR-10 wing gust interaction, approach #4 scenario, gust case-1.

6.4.3. Special Case of Highly Flexible Wing

Furthermore, a gust scenario with large wing flexibility is discussed, such as the AR-13 configuration at gust load case-3 in *approach*. The transverse root force S, root bending moment M, wing tip deflection u_z, and rotation θ for the different wing stiffnesses are shown in Figure 6.28. The main interactions identified are:

1. It is noticeable that the phase between maximum wing lift (shear force S) and bending moment is shifted, which indicates that the lift increases faster in the span wise direction towards the wing tips than in the root position.

2. Additionally, the wing showed a distinct twist up at the beginning of the gust encounter, which indicates the already described reduced torsional wing stiffness. This further induces higher loads compared to the rigid body solution. This observation is in line with the observation in point 1, that the wings torsional stiffness is more soft.

3. With more structural flexibility, the twist up is further intensified. When reaching the bending maximum, the wing has not yet achieved a clearly recognizable washout for load reduction.

4. Comparing the peak position between the elastic wing and rigid-body wing, it is observed that the peak load is reached much earlier during the gust encounter. The highly flexible wing shows a significantly different response when determining the peak load point compared to the standard case, which is based on the AR-10 wing. The peak load is dominated by the interaction at gust initiation, when no washout is achieved (point 3).

5. In the further progression, the correlation between wing deflection and washout gets noticeable.

6. Under sufficient wing deflection, the washout can be increased with a more flexible wing, and hence, a lower load level can be achieved.

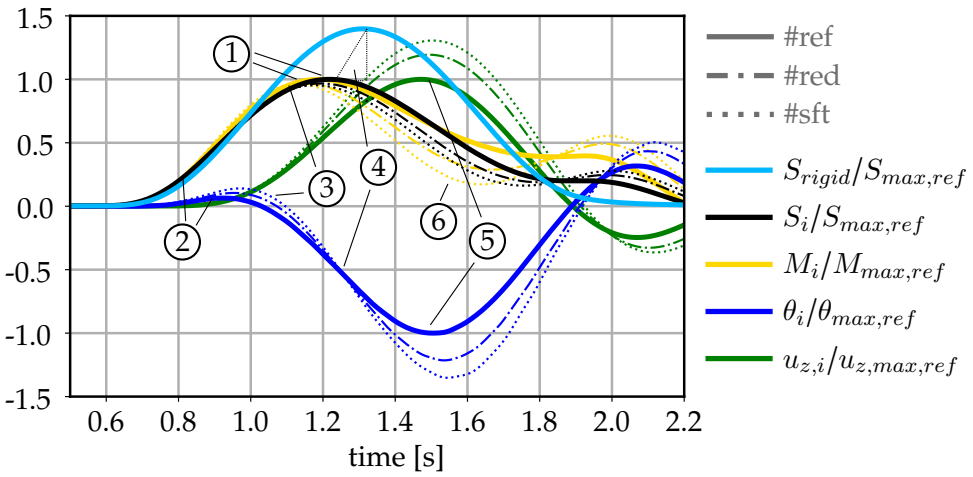

Figure 6.29.: AR-13 wing gust interaction, approach #4 scenario, gust case-3.

6.4.4. Special Case of Flow Separation

The last special case considered involves the occurrence of flow separation, which is strongly dependent on the wing and airfoil design. What is observed in this study is discussed based on the AR-10 configuration at *cruise-flight* (#2), shown in Figure 6.30.

1. Only small differences are observed between the elastic and rigid wing with regards to the maximum shear force, S. However, the elastic configuration still has slightly lower load amplitudes since not the entire wing is affected by flow separation, meaning there are still areas where the flow is attached and load reduction can be achieved by washout.

2. Once more, an twist up of the wing at the entry point of the gust upwind field is noted.

3. In this case, the bending moment accumulates faster than the additional lift. Due to the limitation in lift, the bending moment ultimately drops.

4. A coupling between wing bending deflection and washout is detected. However, there are no noticeable positive effects, as the peak load has already been exceeded. The more flexible wing configurations shows a load-reducing effect, but it no longer influences the exceeded peak load.

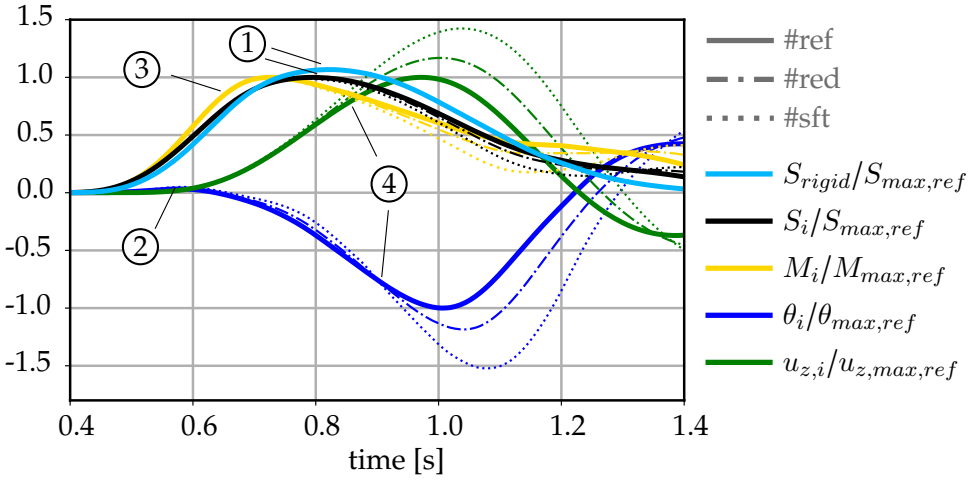

Figure 6.30.: AR-10 wing gust interaction, cruise #2 scenario, gust case-3.

6.5. Summary and Discussion of the Gust Load Results

The results of the transient gust load simulation show a number of variations in the external load reduction characteristic compared to the quasi-steady analysis. The most important aspects that are identified are:

- Similar to chapter 3, the reduction of the external aerodynamic loads depend on the gust gradient. Short gust lengths in combination with more flexible wings decrease the load alleviation performance.
- For load cases with insufficient deflection, no desired washout effect is achieved. The deformation analysis showed that the wing twists up, and hence, the local AoA increases. With a more flexible wing, this effect dominates and results in a lower load reduction effect.
- The AR-10 wing produces sufficient washout for long gust lengths at *approach-flight* condition, which can reduce the external gust peak loads. With increasing structural flexibility, this effect can be increased.
- In *cruise-flight*, the AR-10 wings deflection is stopped by the decreasing lift due to stall. In the three stiffness configurations studied, the load is limited by flow separation. Influences of structural stiffness cannot be identified.
- The characteristics of the AR-13 wing layout shows a clear difference to the AR-10 configuration. All structural configurations considered at different gust load cases and flight scenarios show a lower load reduction performance owing to the insufficient torsional stiffness, which dominates at the beginning of the gust encounter. As no washout occurs from bending deflection, no effective load reduction is achieved. This confirms the results presented in chapter 3 with the reduced order 2-DoF modeling example. Subsequently, this aspect confirms its usability for fundamental design investigations.
- Once the AR-13 wing reaches a minimum deflection, significantly higher reductions in the local AoA can be achieved.

The results obtained from the 3D wing gust calculation are consistent with the conclusions of the simplified 2-DoF model from chapter 3, which are:

- Without existing wing deflection, the kinematic relation causing the washout does not occur, and hence, the load reduction caused by a reduced local AoA is not effective.
- A reduced torsional wing stiffness leads to a twist up of the wing, and hence, to the opposite effect.

In the characterization referred to as the standard case, the peak loads can be reduced with a more flexible wing design. However, in short-wave gusts and with extremely flexible wings, such as the AR-13 configuration, the load reduction behavior is dominated by the torsional stiffness due to the wing inertia at the time of the peak load, when the corresponding load-reducing washout has not been sufficiently established.

Therefore, the correlation between deflection and load reduction is a point worth mentioning in the context of research conducted on aeroelastic tailored wings. The studies shown here reveal that back-swept wings have a natural load reduction when sufficient bending is achieved. Specific methods for aeroelastic tailoring are not used in the structural design process. Composite structures or tow-steered composite technologies can enhance the effect of washout. However, the activating mechanism is a coupling between bending and twist. Thus, a perspective of the application of aeroelastic tailoring includes both:

- Adjustment of the stiffness along the load paths, also known as stiffness tailoring, to implement an optimal lightweight design.
- Using additional coupling possibilities, material or geometrical, to improve the washout, especially with small deflections.

Therefore, aeroelastic tailoring can help to achieve the effective changes in the local AoA with smaller bending deflections. The latter plays a major role in the development of extremely flexible wings, as peak loads occur in the critical range where, at least for the examples used in this study, insufficient washout is observed.

7 Discussion and Conclusions

This chapter summarizes the research carried out. First, the results and findings of this study are presented. To conclude, an outlook on further research perspectives is given.

Contents

7.1. Summary and Conclusion of the Research Work

To achieve the goals of sustainable aviation industry, there is a need for new and innovative aircraft concepts that are superior to the present transport aircraft in terms of performance and environmental footprint. Both the academic and industrial research sectors are aiming to achieve these goals by reducing induced drag by using higher aspect ratio wings. However, such configurations also bring a number of aeroelastic disadvantages. As these are still difficult to predict and solve, it is not yet possible to implement them efficiently for transonic civil transport aircraft. The investigations carried out in this study contribute to more detailed high fidelity aeroelastic simulations of flexible wings. By applying advanced computational methods, a better understanding of the characteristics of elastic backward swept wings under maneuver loading and gust response was achieved. Besides the general aeroelastic response, the impact of the wing stiffness and the wing flexibility was of particular interest and therefore, the primary focus in this study.

A fundamental requirement for extending the work beyond the current state of the art of conventional aeroelastic design methods was the use of *CFD* methods, which consider non-linearities, such as strong compressibility, shock or flow separation. Therefore, for the entire study, higher-fidelity methods based on RANS and URANS equations were used for aerodynamic modeling. In addition, the *Field Velocity Approach* was applied to calculate the gust loads with a *Fluid Structure Interaction* aeroelastic modeling approach.

7.1.1. 2-DoF Demonstration Model

First, a reduced 2-DoF demonstration example was presented to demonstrate the modeling approach. Furthermore, the demonstration example was utilized to study the aerodynamic and structural influences on the aeroelastic behavior. For this purpose, existing methods from the literature were combined to set up a 2D computational aeroelastic model of a backward swept wing segment. In the structural model, the structural stiffness was defined by means of discrete translational and torsional springs, representing the wings bending and torsional stiffness. Busemanns *Infinite Swept Wing Theory* was applied to extend the structural mechanical model with an aerodynamic model and used for steady-state and transient aeroelastic simulations in the transonic and subsonic flight regime.

The first question was to investigate the influences of the bending and torsional stiffnesses, while considering a *cruise-flight* at $Ma = 0.86$ and subsonic *approach-flight* scenario at $Ma = 0.5$. For this purpose, static and transient gust response simulations with three different gust lengths were conducted. In both analyses, the same fundamental statements were found.

- The ability to reduce the loads depend significantly on the ability of a sufficient bending deflection, which activates the dominating kinematic bending-torsion coupling and decreases the angle of attack of the segment during any additional loading. Therefore, a wing that is more flexible in bending has a positive influence on the load reduction performance.
- As the aerodynamic lift force is in all cases in front of the elastic axis, a torsional moment is induced, which twists up the airfoil, thereby inducing higher angles of attack. Torsionally stiffer configurations that can counter this additional moment show a positive load reduction effect.

In this context, the influence of different gust lengths was analyzed. For the gust load model, the 1-cos gust defined according to CS-25 was used. The three gust profiles considered had different gust lengths: a short gust length with an impulse like characteristic, a long gust length, and a medium gust length as an intermediate step. The maximum vertical gust speeds were adjusted according to the CS-25 gust profile. The main results are:

- The gust exposure time is essential to overcome inertia forces and generate sufficient bending deflection. The effect of long gust length is advantageous as it allows sufficient bending deflection, and hence, washout to reduce the additional induced angle of attack.
- Short gust lengths achieve insufficient bending deflection, and hence, the twist up effect dominates. Consequently, torsionally stiff configurations show better load reduction performance for small gust lengths.

In the 2-DoF demonstration example, the basic assumption was that the torsional and bending stiffnesses can be adjusted individually. Accordingly, with regard to the possibility of load reduction, a design that is more flexible in bending and stiffer in torsion is preferred.

Furthermore, studies on load reduction performance exploiting flow separation were conducted. Besides the flow conditions in the transonic flight regime, the motivation of this study was also to capture the possibility of flow separation in the basic model assumption. This explains the decision to apply RANS or URANS models to make such studies possible. To allow the stall influence to become apparent, the flight conditions were changed in two ways. In study one, the steady aerodynamic load level was incrementally lifted to operate the airfoil closer to $C_{l,max}$, whereas in the second study, the gust velocities were scaled so that $C_{l,max}$ was induced by the additional AoA of the gust upwind field. The core statements acquired from this study are:

- Stall can be used effectively to limit the load generated by lift. If a higher vertical speed is introduced by the gust or increased through the mean steady lift, no major differences were observed in the aerodynamic peak load. This effect can be applied irrespective of the structural stiffness.
- Significant differences were observed in the post-stall behavior. Herein, cases could be identified where the detached flow recovered rapidly and the airfoil slowly reverted to steady flight conditions. The decisive factor was the upstream flow condition and the lift increment between steady-state flight and $C_{l,max}$. Such moderate post stall configuration could be identified at *cruise* speed.
- Especially in the *approach-flight* configurations, the lift collapsed and drops below the lift required for steady-state flight. Accordingly, the structure responds with strong oscillations in the torsional and bending degrees of freedom.

- For that specific case, providing a final assessment is difficult, as the 2-DoF model does not reflect the full complexity of a 3D wing. If the airfoil represents the entire wing, a drop in lift below necessary steady flight level is not tolerable, as that the aircraft could no longer keep the trim attitude and maintain altitude.
- Stall typically does not have to occur abruptly on the entire 3D wing. However, load limiting of the load through partial wing stall might be possible.

When analyzing the influence of different gust vertical speeds, the following observations were made:

- As the vertical speed increases, the load reduction characteristic can be scaled linearly until flow separation is achieved. If the critical lift is exceeded, it is limited by the stall, regardless of whether a higher angle of attack is induced by gusts.
- The passive load reduction performance depends on the gust length. For small gust lengths, only minor reductions can be achieved. A wing configuration being more flexible in bending shows a better possibility to reduce additional lift. Therefore, the statements made at the beginning could be confirmed for the more general study with different gust lengths and vertical speeds.

7.1.2. Civil Transport Aircraft Simulation

In the second part of this work, aeroelastic models of two civil transport aircraft configurations were investigated to determine the influence of wing configurations with different stiffness characteristics using simulations of steady-state maneuver and transient gust response. An aircraft with an aspect ratio of 10 and 13 (novel) wing planform were implemented. As far as possible, both configurations were developed to meet the same operational parameters. To influence the stiffness of the wings, different pseudo artificial materials were introduced. The stiffness of the wing was influenced by changing the material properties, so that wings with the same planform but different stiffnesses could be realized. Geometric influences were studied directly between the AR-10 and AR-13 configurations. The modeling of the wing structure and its deformations was carried out using FEM. For this, a simplified pre-sizing process was implemented so that the structural design corresponded to the predefined load specifications. A special feature of this work is that the structure is not developed from the stress-free unloaded jig-shape, but around a predefined target flight shape. Therefore, all wing configurations with the same planform were ensured to have the same lift distribution in the design point despite different stiffnesses. Therefore, determining the corresponding jig-shape required to fulfill the intended flight shape was part of the design process. Finally, the resulting models were used for quasi-steady pull up maneuver studies and transient gust response analyses.

In the maneuver load study, the different wing planforms with different structural stiffness were investigated for their passive aerodynamic load reduction potential at higher load factors. For this purpose, a trimmed quasi-steady pull up maneuver flight was considered at different flight speeds, including two low speed (Ma = 0.5, FL = 0) and two cruise flight scenarios (Ma = 0.86, FL = 350), with different fuel loading conditions. The essential findings are:

- The wings in both AR-10 and AR-13 configurations reached the limit load only with *approach-flight* conditions. In the *cruise-flight* case, the wings could not provide sufficient lift, and stall occurs before design limit load n_z = 2.5 is reached.
- The transverse shear force and the bending and torsional moments resulting from the aerodynamic forces were evaluated for the load reduction ability with different stiffnesses. The reduction of the transverse shear forces was only possible to a small extent because the necessary lift must be generated for a given maneuver flight. Therefore, in maneuver flight, the transverse force can only be reduced by transferring it partially from the wing to the fuselage.

- In the pull-up maneuver flight cases with flow separation, the load reduction potential decreases due to the lower bending deflection caused by the lower lift. This negatively impacts the wing sections where the flow is still attached. The reduction in load was stopped and the local angle of attack increased. Therefore, the occurrence of stall can be classified as a limiting factor of load reduction trough washout.

- More flexible wing configurations were able to generate a higher load reduction potential in all studies. Compared with steady-state flight, the best results for the AR-10 wing load reduction are obtained in the take-off scenario. The bending and torsional moments are decreased by 8.36% and 9.18%, respectively. For the AR-13 configurations, the best reduction in bending moment were achieved during approach with up to 10.6%, and for the torsional moment in take-off with 11.41%.

- The best results were obtained for the *take-off* and *approach-flight* scenarios, which was consistent with the observations from the 2-DoF demonstrator study. In both flight conditions, the bending deflection between maximum load and flight shape of the wing was the largest. Therefore, in relative terms, more washout can be generated.

From a relative point of view, the AR-13 wing had a slightly better maneuver load reduction capability. However, the absolute loads must be considered. Here, the following can be stated:

- The AR-13 wing generally has higher root bending and torsional moments owing to its geometric features. The mean loading level at $n_z = 1.0$ is considerably lower for the AR-10 planform, and hence, the external aerodynamic peak loads are smaller.

- *Take-off* and *approach-flight* scenarios do not represent the load cases with the highest external forces. In this study, *cruise-flight* with full wing tank was identified as the load case, for which the external aerodynamic peak load reduction was significantly lower.

In the second part, the different wing types were analyzed based on their gust response characteristics under both the *cruise-* and *approach-flight* scenarios. The effect of varying wing stiffness on the load reduction potential under different gusts length was investigated. Four possibilities of gust responses were identified as they may occur in a gust exposure with a flexible wing. The essential findings are:

- The load reduction potential was in turn strongly linked to the wing bending deflection. For all gust load cases, the local angle of attack initially increased upon gust initiation because the wing did not have any bending deflection due to its inertia. Due to the extra induced lift, the wing started to twist up.

- Whether a load reduction is possible depends on the relative phase of induced lift and the washout.

- For long gusts lengths, the duration of the gust action is sufficient to produce sufficient wing bending so that the washout begins before the aerodynamic peak load is reached. In this case, the peak load can be reduced and improved using more flexible wings.

- For short gust lengths, flow separation or extremely flexible configurations such as the AR-13 planform, the load reduction behaviour is determined at the beginning of the gust encounter. In this case, the aerodynamic peak loads were reached before sufficient deflection was achieved, that is, when the wing was still in an unfavorable condition, where the local AoA is increased due to the up twist. For all cases, the stiffer wing configurations showed a better load reduction performance as the wing twist-up is counteracted.

The evaluations of the AR-13 configuration showed that after reaching the significantly higher wing deflections, the reduction through washout dominated. However, due to inertia and lower torsional stiffness, the configuration in this study do not show an advantage. Therefore, the results of the aerodynamic peak loads, were characterized by the initial gust interaction.

7.2. Future Research

The results of this thesis show that flexible swept-back wings can inherently alleviate external aerodynamic loads passively through bending-torsion coupling. In order to use simulation techniques to predict the complexity of elastic wings and improve their design, the results obtained provide a direction for further developments and discussions:

- The use of a further optimized structural design can indicate further optimization potentials, especially with regard to gust load reduction. The primary focus is to investigate how aeroelastic tailoring can help to reduce the initial twist up of the wing, that occurs during gust initiation. This can be achieved either by counter-acting (aeroelastic tailoring) or by maximizing torsional stiffness while maintaining flexible in bending (stiffness tailoring). To investigate these effect, more detailed methods of structural design may be applied.
- The focus in this work was the possibility of external aerodynamic load reduction by washing-out the additionally induced angle of attack. In order to take into account the inertia effects of the structure, the evaluation of the load reduction can be done by assessing the internal structural loads.
- The ability of the wing to deflect has a noticeable effect on the ability to decrease the local angle of attack. Therefore, the fuel distribution in the wing is relevant for influencing the inertia. From an operational perspective, an assessment must be made to determine if the effect of load counterbalance (lift vs. inertia) or the washout due to deflection is favorable.
- Including transient simulation can help to evaluate the post stall characteristic of the wing and support the assessment whether flow separation can be used to limit the load peaks during maneuver flight.

A | Appendix

A.1. Aerofoil Grid Resolution Study

Because many computationally intensive simulations must be performed, the grid resolution should offer a sufficient solution quality with adequate computing effort. Hence, stationary solutions based on grids with different resolutions are evaluated with respect to the convergence trend over the number of cells. For this purpose, the number of grid points along the chord direction is used as the grid control parameter. As the solver termination criterion, the force F_z and moment M_y are used with a Cauchy convergence of $1.0 \cdot 10^{-5}$ over 20 iterations. Four grids with chord resolutions N_{nodes} 150, 300, 600 and 900 under *cruise* flight conditions are used. The change in C_L for the different resolutions is shown in Figure A.1a, with medium-resolution N_{knodes} = 300 as a reference.

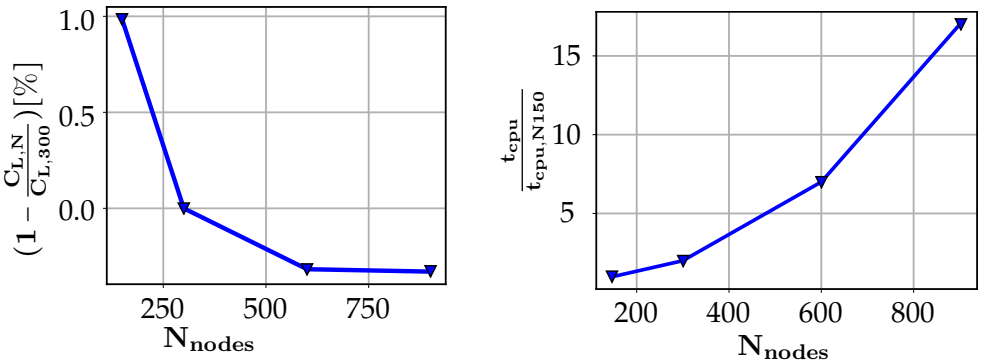

(a) C_L variation, with N_{300} as Reference.

(b) Computational time with, N_{150} as reference.

Figure A.1.: Variation of the lift coefficient C_L and computational time t due to different mesh resolutions.

A relatively significant change in the lift derivative is observed when the cell resolution is increased from 150 to 300. Resolutions of more than 300 lead to only minor changes, whereas the computing time increases significantly, as shown in Figure A.1b.

The C_P distribution, shown in Figure A.2, is used as an additional assessment criterion. The pressure distribution is measured similarly for all grids except for the shock at $\frac{x}{c_{ref}}$ = 0.7. Finer grids offer improved resolution as the mesh size increases. A grid with N_{knot} = 300 is selected for the aeroelastic tests presented in this study.

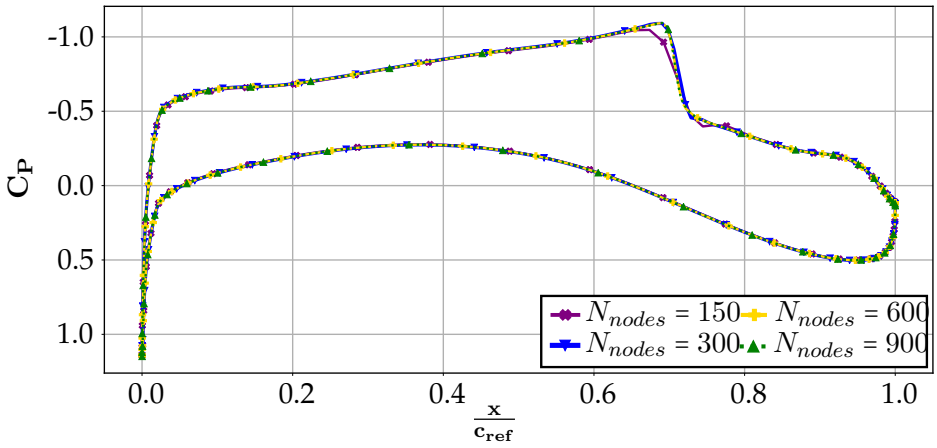

Figure A.2.: Chordwise C_p distribution for different mesh resolutions at cruise flight condition.

A.2. Steady Trim Points Academic Example Problem

Table A.1 below shows the trim points for the different stiffness configurations. The structural stiffness parameters and jig-shape of the *cruise* configuration are the same for the steady-state *approach* simulation. To achieve the same lift L in the *cruise* and *approach*, AoA is adjusted accordingly.

Table A.1.: 2d steady trim points for cruise and approach flight.

		jig shape		cruise initial deflection			approach initial deflection			approach AoA
$\frac{\mathbf{K_h}}{\mathbf{K_{h,ref}}}$	$\frac{\mathbf{K_\theta}}{\mathbf{K_{\theta,ref}}}$	$\mathbf{h_{jig}}\,[m]$	$\theta_{\mathbf{jig}}\,[^o]$	$\mathbf{h_0}[m]$	$\mathbf{\Phi_0}\,[^o]$	$\theta_\mathbf{0}\,[^o]$	$\mathbf{h_0}[m]$	$\mathbf{\Phi_0}\,[^o]$	$\theta_\mathbf{0}\,[^o]$	$\alpha\,[^o]$
1.0	1.0	0.0	1.375	0.8	2.265	−1.567	0.793	2.240	−1.927	−0.147
0.5	1.0	−0.8	2.683	1.6	4.530	−1.567	1.587	4.481	−1.927	−0.160
0.75	1.0	−.267	1.812	1.067	3.02	−1.568	1.058	2.988	−1.927	−.152
1.25	1.0	0.16	1.114	0.64	1.812	−1.568	0.635	1.793	−1.927	−0.146
2.5	1.0	0.48	0.591	0.32	0.906	−1.568	0.317	0.896	−1.927	−0.141
4.0	1.0	0.6	0.395	0.2	0.566	−1.568	0.198	0.56	−1.927	−0.139
1.0	0.5	0.0	2.944	0.8	2.265	−3.136	0.794	2.241	−3.854	0.163
1.0	0.75	0.0	1.898	0.8	2.265	−2.091	0.794	2.241	−2.57	−0.044
1.0	1.25	0.0	1.062	0.8	2.265	−1.254	0.794	2.241	−1.542	−0.210
1.0	2.5	0.0	0.435	0.8	2.265	−0.627	0.794	2.241	−0.771	−0.335
1.0	4.0	0.0	0.2	0.8	2.265	−0.392	0.794	2.241	0.2	−0.381

A.3. Definition of the Gust Load Cases

The selection of test cases are aligned with the AeroGust [27] test conditions case-F, case-H, and case-I/D. In accordance with the admission regulations [29, 44], the design gust velocity V_v is calculated from the gust gradient H as follows:

$$V_v = U_{ref} \cdot F_g \cdot \left(\frac{H}{350}\right)^{\frac{1}{6}}. \tag{A.1}$$

The corresponding reference gust velocity U_{ref} and alleviation factor F_g for the gust models used in this thesis are listed in Table A.2.

Table A.2.: 1-cos gust parameters, $U_{ref} \cdot F_g$.

	Gust-A	**Gust-B**	**Gust-C**	**Gust-D**	**Gust-E**
$U_{ref} \cdot F_g$	18.3826 $\frac{\mathrm{m}}{\mathrm{s}}$	14.4248 $\frac{\mathrm{m}}{\mathrm{s}}$	24.8100 $\frac{\mathrm{m}}{\mathrm{s}}$	31.1556 $\frac{\mathrm{m}}{\mathrm{s}}$	35.1952 $\frac{\mathrm{m}}{\mathrm{s}}$

A.4. Unsteady FSI Time Discretization Evaluation

The time response of the lift distribution for the three gust gradients 1-3 under *cruise* conditions (Gust-A) is shown in Figure A.3 for the rigid-body case and Figure A.4 for the elastic aerofoil segment. In general, it can be seen that the progression is similar for the four different time steps. However, for $\mathcal{C} = 8$, in gust gradient case-1, the gust shape is only roughly resolved, and further larger deviations can be observed in the elastic simulation for case-3. Because the maximum lift or pitch moment is used as an evaluation criterion for load reduction, the change in $C_{l,max}$ and $C_{m,max}$ with respect to the time step size is used as an assessment. In this respect, a change of $epsilon < 10^{-}4$ for the derivatives is considered to be sufficiently accurate. Considering the required computational simulation time, shown in Figure A.7, $\mathcal{C} = 2$ is selected for the parameter study. The option fulfills the specified convergence criterion, except for the rigid case with gust gradient case-3. In this case, the time step size must be adjusted accordingly, which is why $\mathcal{C} = 2$ is evaluated as an acceptable compromise between accuracy and computational effort for mainly elastic simulations.

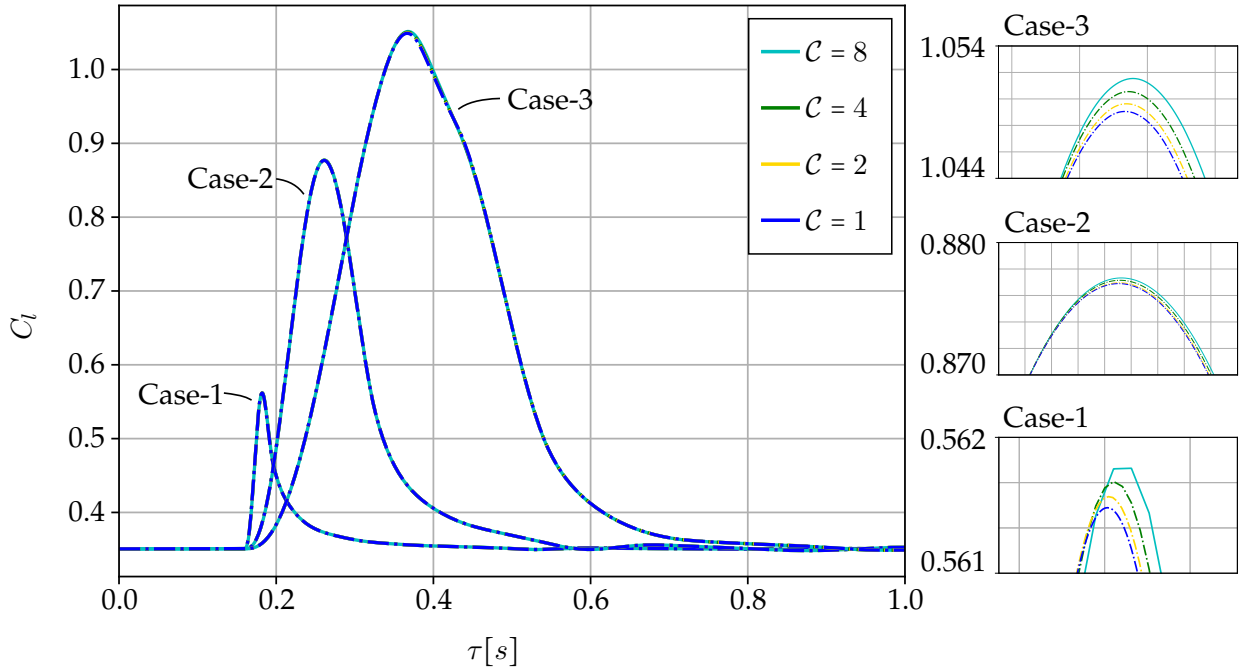

Figure A.3.: Rigid aerofoil gust response comparison of C_l progression over nominalized time τ with different time step resolutions.

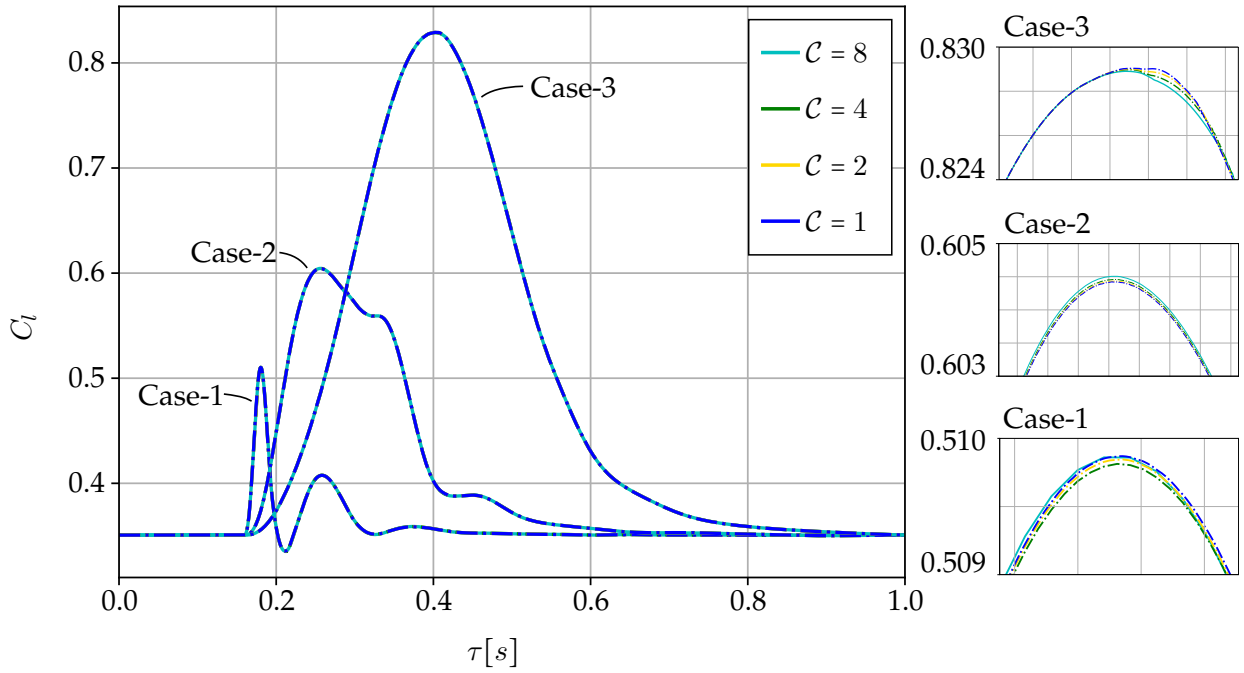

Figure A.4.: Aeroelastic gust response comparison of C_l progression over nominalized time τ with different time step resolutions.

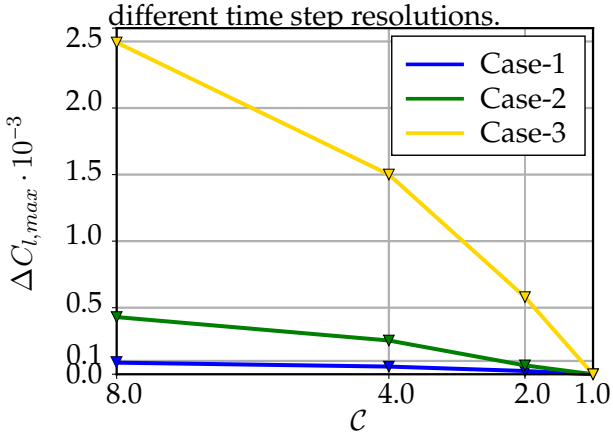

(a) Rigid aerofoil gust response.

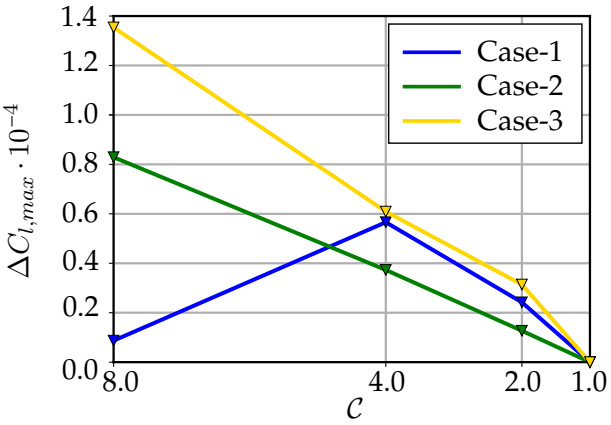

(b) Aeroelastic gust response.

Figure A.5.: Influence of the time step resolution on the absolute change of $\Delta C_{l,max} = \|C^{\mathcal{C}}_{l,max} - C^{\mathcal{C}=2.0}_{l,max}\|$.

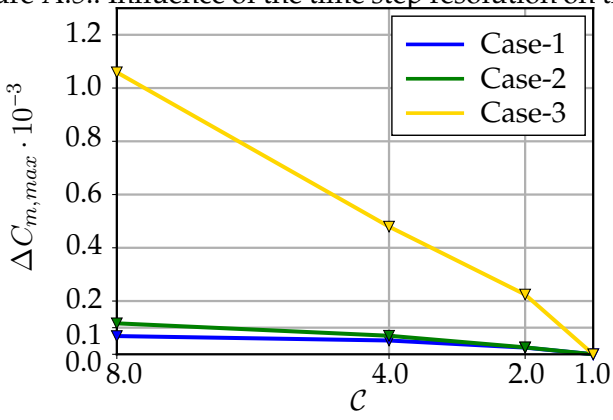

(a) Rigid aerofoil gust response.

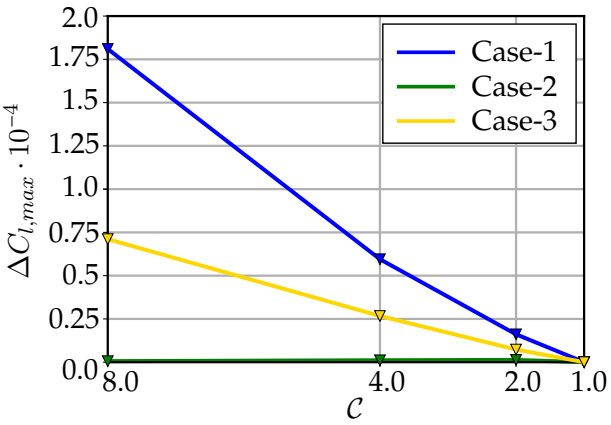

(b) Aeroelastic gust response.

Figure A.6.: Influence of the time step resolution on the absolute change of $\Delta C_{m,max} = \|C^{\mathcal{C}}_{m,max} - C^{\mathcal{C}=2.0}_{m,max}\|$.

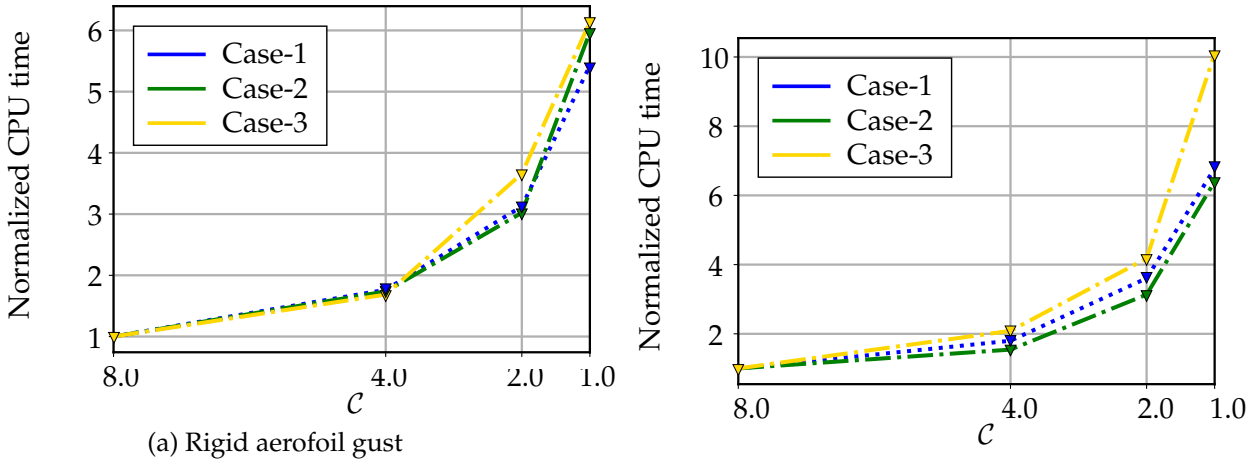

(a) Rigid aerofoil gust response.

(b) Aeroelastic gust response

Figure A.7.: Influence of the time step resolution on computing time, normalized $\frac{t_{CPU}}{t_{CPU}^{S=4}}$.

A.5. Influence of the Design Gust Velocities

Figure A.8 shows ΔC_l of the reference and $0.75 \cdot K_h$ stiffness configurations. The results are plotted for the different design gust velocities V_v and different gust length H. The nonlinear characteristic for long gusts lengths H is well visible, while for small gust lengths, the responses vary linearly. Although in a different context, this agrees with the findings of Kaiser [22], that gust loads are influenced by nonlinear phenomena, especially in the case of long gust lengths.

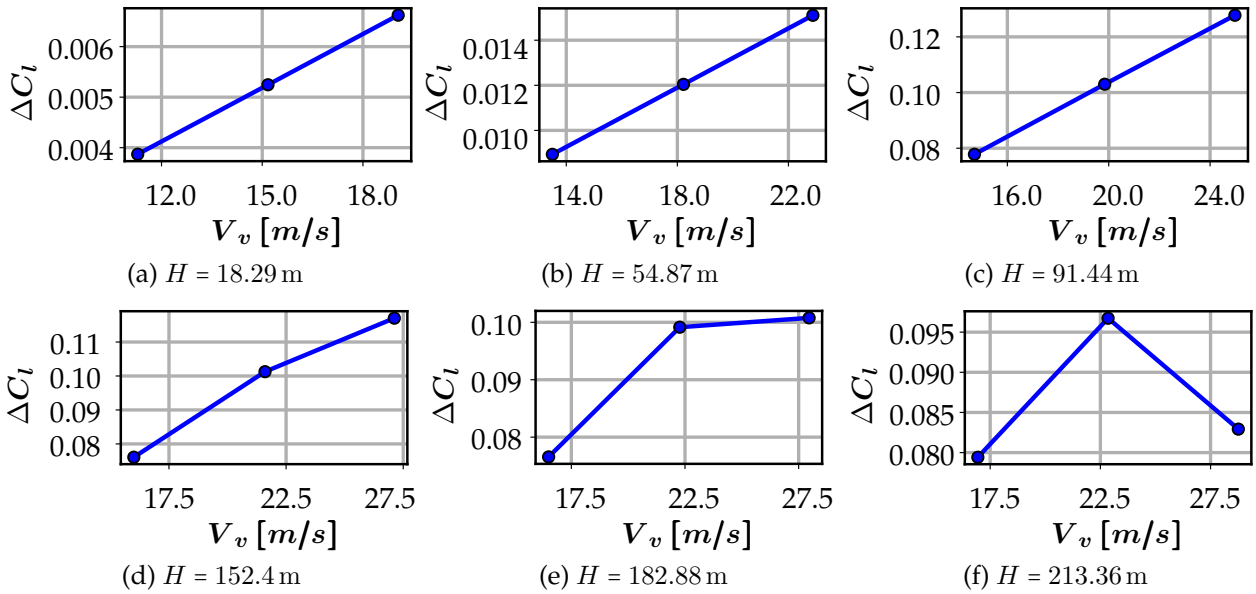

(a) H = 18.29 m (b) H = 54.87 m (c) H = 91.44 m

(d) H = 152.4 m (e) H = 182.88 m (f) H = 213.36 m

Figure A.8.: Comparison of the C_l difference with different design gust speeds V_v.

The C_l difference at different gust lengths for different gust velocities for *approach-flight* is shown in Figure A.9. In comparison with the *cruise* flight condition, no nonlinearities can be identified. This means that for the analyzed example, even with a significantly increased design gust speed, possible flow separations could not be identified as an option for lift reduction.

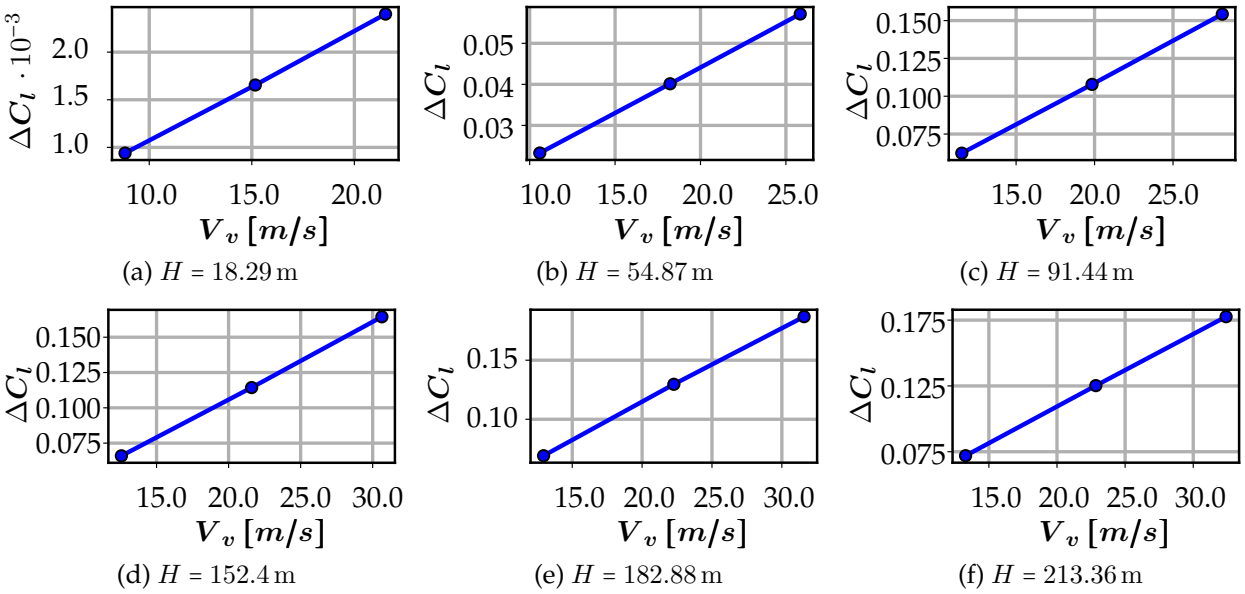

(a) H = 18.29 m (b) H = 54.87 m (c) H = 91.44 m

(d) H = 152.4 m (e) H = 182.88 m (f) H = 213.36 m

Figure A.9.: Comparison of the C_l difference with different design gust speeds V_v.

A.6. Structural Design Optimization Convergence Results

The dimensioning of the wing structure is solved, as described in chapter 4, by formulating it as an optimization problem, where the total mass of the structure is chosen as the target value to be minimized. The solution is considered to converge if the relative change in the target variable is less than $\frac{m^{(p)}-m^{(p-1)}}{m^{(p-1)}} < 10^{-5}$. The constraints are considered satisfied if $max(g(x)) < 0.005$ holds. The progression of the structural mass over the iteration for the AR-10 configuration is shown in Figure A.10 - Figure A.12. The respective convergence progressions for the AR-13 wing layout are shown in Figure A.13 - Figure A.15.

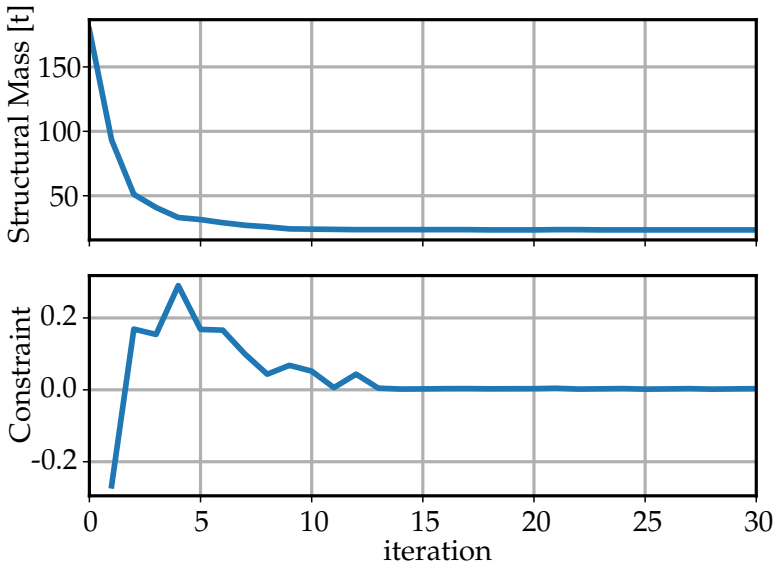

Figure A.10.: AR-10 #ref, structural mass and constraint value progression.

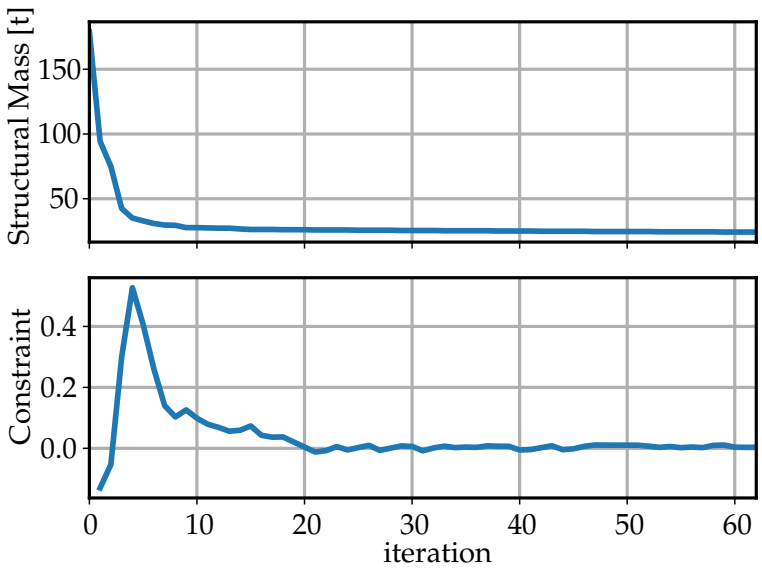

Figure A.11.: AR-10 #red wing stiffness, structural mass and constraint value progression.

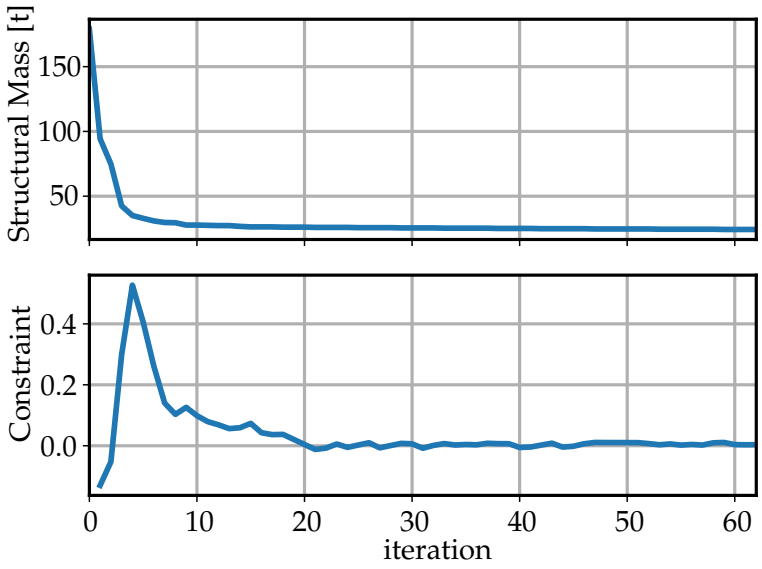

Figure A.12.: AR-10 #sft wing stiffness, structural mass and constraint value progression.

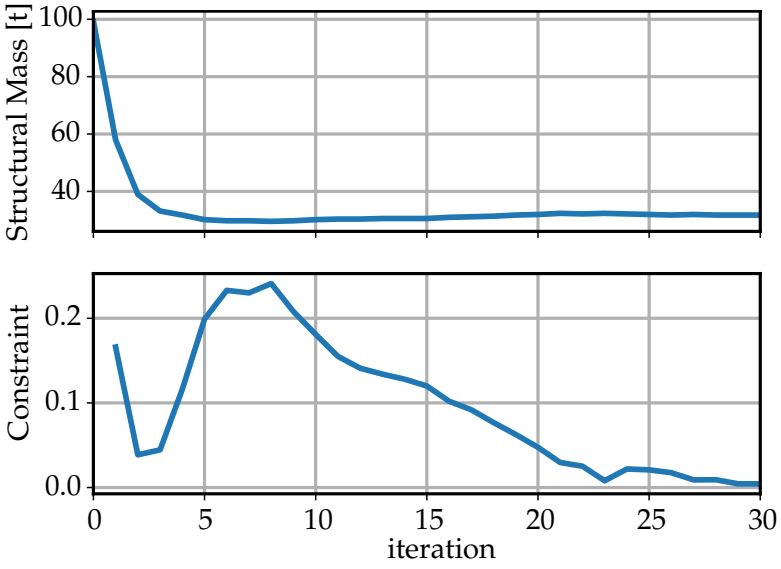

Figure A.13.: AR-13 #ref, structural mass and constraint value progression.

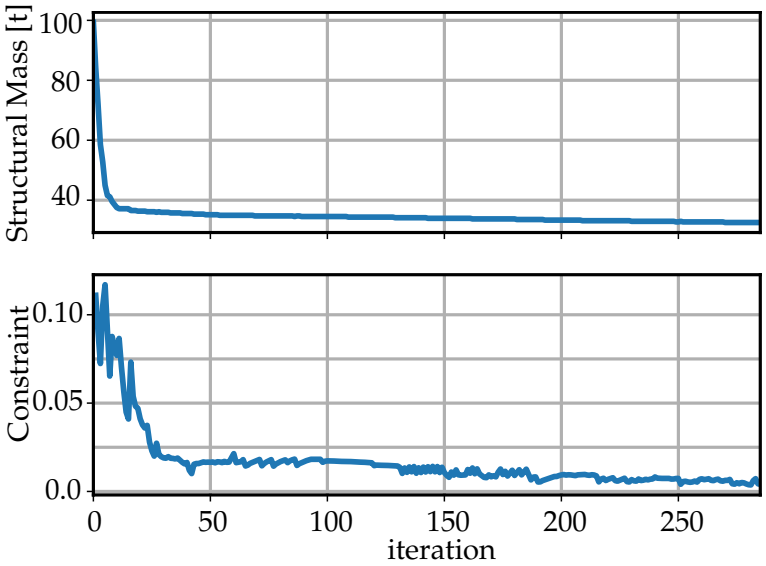

Figure A.14.: AR-13 #red, structural mass and constraint value progression.

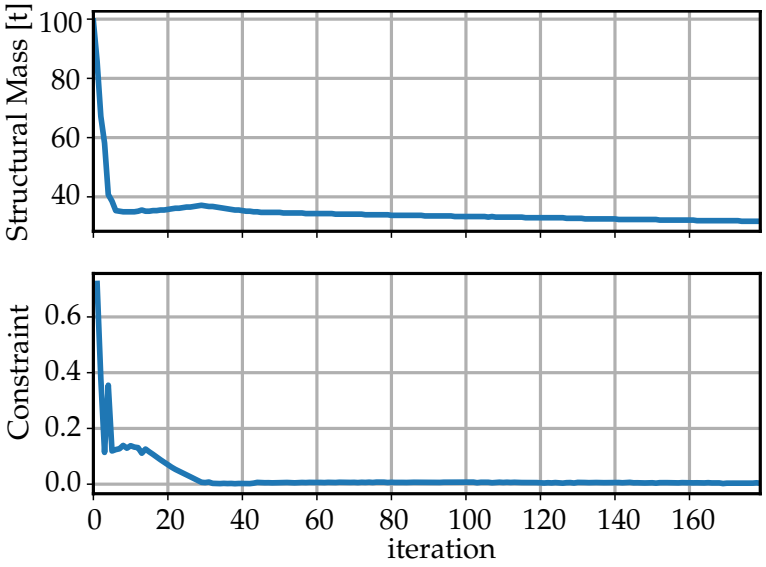

Figure A.15.: AR-13 #sft, structural mass and constraint value progression.

A.7. Modal Properties under Preloading

Structural prestressing can play a role in elastic wing structures, which has been investigated in other contexts in [5]. In particular, when the structural dynamic equations of motion are expressed in modal coordinates, the shifting of eigenmodes can change system behavior. An overview of the shift in the individual structural eigenfrequencies is presented in Table A.3. The natural frequencies in the flight shape at n_z = 1.0 and n_z = 1.6 and the stress-free state, that is, jig-shape, are compared. Different levels of frequency variation can be observed depending on the wing design and structural mode number. In the present study, the structural dynamic equilibrium equations are consequently solved using physical coordinates in the time domain. Changes due to large deformations or prestressing effects are considered.

Table A.3.: Structural eigenfrequencies, #ref-material, symmetric-modes.

mode	**AR-10**			**AR-13**		
number	jig	cruise n_z = 1.0	cruise n_z = 1.6	jig	cruise n_z = 1.0	cruise n_z = 1.6
1	1.172	1.172	1.173	0.686	0.683	0.682
2	2.966	2.959	2.959	1.950	1.939	1.925
3	4.041	4.038	4.034	2.746	2.642	2.557
4	5.091	5.106	5.109	3.868	3.871	3.857
5	7.099	7.070	7.066	5.628	5.691	5.713
6	9.330	9.226	9.208	6.829	6.578	6.367
7	10.168	10.293	10.309	7.533	7.362	7.280
8	10.581	10.535	10.527	9.681	9.735	9.685
9	13.573	13.591	13.589	10.334	10.835	10.988
10	15.585	15.596	15.584	11.287	11.451	11.800
11	17.560	17.543	17.537	13.090	13.103	13.191
12	17.750	17.845	17.882	15.673	15.457	15.341
13	22.038	22.057	22.060	16.538	16.582	16.543
14	25.617	25.513	25.474	17.074	17.385	17.728
15	27.145	27.166	27.183	19.958	19.924	19.877
16	28.491	28.644	28.686	23.354	23.350	23.315
17	32.974	32.967	32.950	23.782	23.879	23.948
18	33.990	33.994	33.990	25.387	25.461	25.568
19	37.278	37.124	37.084	27.991	27.965	27.910
20	38.447	38.504	38.520	30.869	30.916	30.993
21	40.155	40.161	40.152	33.273	33.474	33.544
22	40.732	40.881	40.914	33.712	33.711	33.783
23	46.139	46.146	46.143	36.983	36.851	36.687
24	47.251	47.242	47.243	37.963	38.126	38.240
25	48.744	48.617	48.591	41.165	41.225	41.268

A.8. Lift Distribution under Steady Pull-Up Maneuver

Figure A.16 shows a pull-up maneuver in which the aircraft is no longer considered as point. In this case, it must be considered that the pitch rate q and its associated rigid-body rotation leads to an induced relative flow velocity. This influence becomes more significant the further the lifting surfaces are away from the C.G. Although this is strictly speaking of a transient flight maneuver, the flow can be considered as quasi-stationary problem if a constant pitch rate is assumed and the body-fixed coordinate system is used as the solution coordinate system. For a symmetrical pull-up maneuver the following relation $q = \frac{g}{V}(1 - n_z)$ between pitch rate q, load factor n_z and flight speed V applies accordingly [79]. However, as can be noted in the plotted resulting lift distributions between steady and quasi-steady at $n_z = +2.5g$, there are no significant differences. Only the global AoA, which is influenced by the relative induced AoA, is reduced.

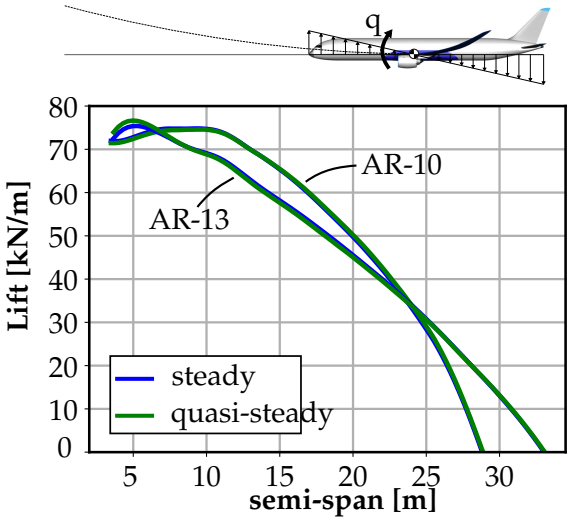

Figure A.16.: Quasi-steady symmetric pull-up maneuver.

A.9. Elastic Aircraft C_L Slope at Different Wing Stiffnesses

Figure A.17 and Figure A.18 show the trimmed flight conditions of the AR-10 and AR-13 wings for different load factors n_z at *cruise-#2* flight with corresponding AoA. The results of the elastic wing configurations with different stiffnesses (#ref, #red, #sft) with the rigid body solution as reference are shown. As the *cruise-#2* flight shape is selected as the common reference design shape, all configurations have the same trimmed state at $C_L = 0.5$ or $n_z = 1.0$. Comparing the changes in C_L, a clear difference between the rigid and flexible wings can be observed. Furthermore, for all flexible configurations $C_{L,\alpha}$ are lower. The different wing structural stiffnesses show only slight variations, which are due to the evaluation of the integral quantity C_L. Because the information of the lift distribution is not mapped, there are only slight differences in the AoA. This is due to the varying stiffness of the wings and the resulting reduction in the total wing lift (wash-in and wash-out). Because the total lift must be maintained, it is is proportionally transferred to the fuselage by changing the AoA.

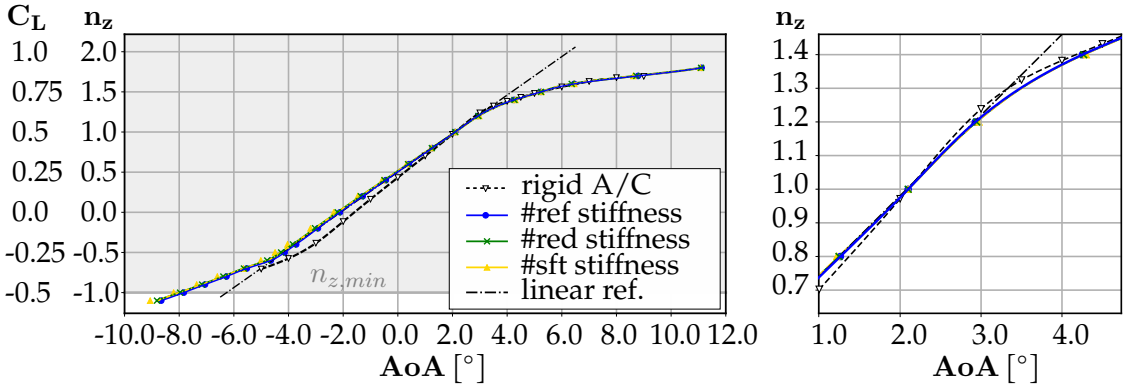

Figure A.17.: AR-10 wing configuration lift slope of the elastic aircraft configuration in cruise flight (#2), and different structural stiffnesses.

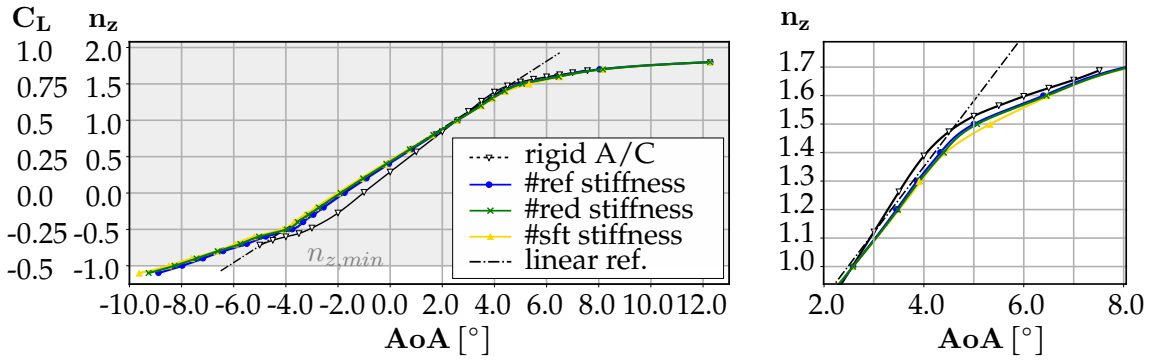

Figure A.18.: AR-13 wing configuration lift slope of the elastic aircraft configuration in cruise flight (#2), and different structural stiffnesses.

The steady flow results for C_L in the *approach* flight condition (#4) are shown in Figure A.19 for AR-10 and in Figure A.20 for the AR-13 wing. It should be noted that the different elastic configurations have different wing jig shapes. These are designed in such a way that, in design *cruise* flight, all wings have the same shape. Because the structural wing design is not changed, only the flight condition, inherently all wings exhibits different *approach* flight shapes. For this reason, no rigid wing solution is provided, as a conclusive comparable link between the wings is missing. Compared with the transonic airspeed at *cruise*, the *approach* flight for the configuration shows that a full load range can be achieved for all structural stiffness variations and a linear C_L-to-AoA gradient can be found.

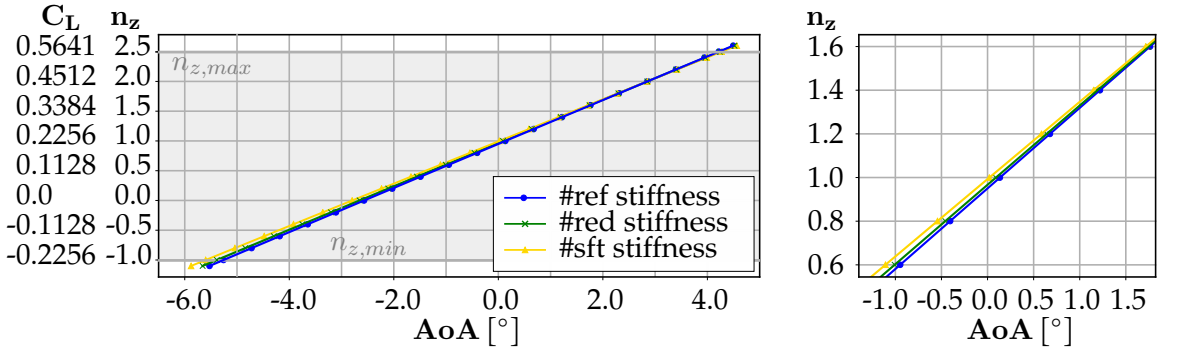

Figure A.19.: AR-10 wing configuration lift slope of the elastic aircraft configuration in approach flight (#4), and different structural stiffnesses.

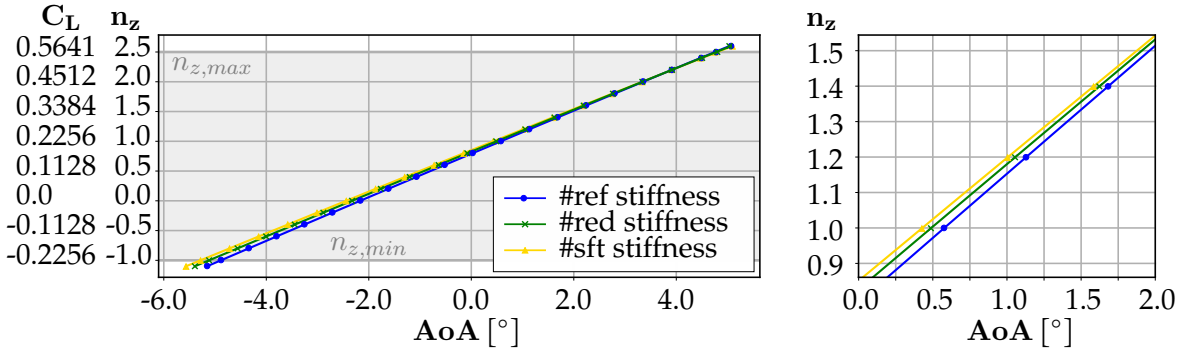

Figure A.20.: AR-13 wing configuration lift slope of the elastic aircraft configuration in approach flight (#4), and different structural stiffnesses.

A.10. External Load Results at Different Wing Stiffnesses

The following section provides the results of external loads with different structural stiffnesses and variations. The results are presented as relative differences, with reference to the loading condition at $n_z = 1.0$ for the *cruise* and *low-speed* flight scenarios. Because the absolute root loads of the different wing structures are close together, the variation in the #red and #sft stiffness configurations compared with the #ref configuration are plotted separately.

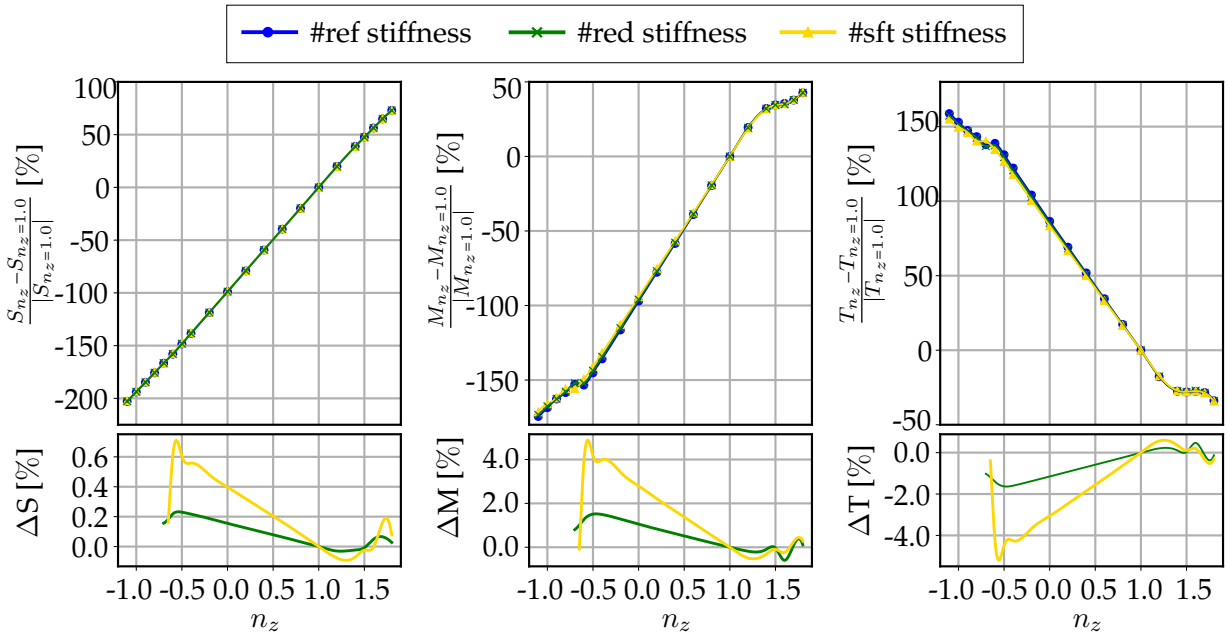

(a) Flight scenario #2.

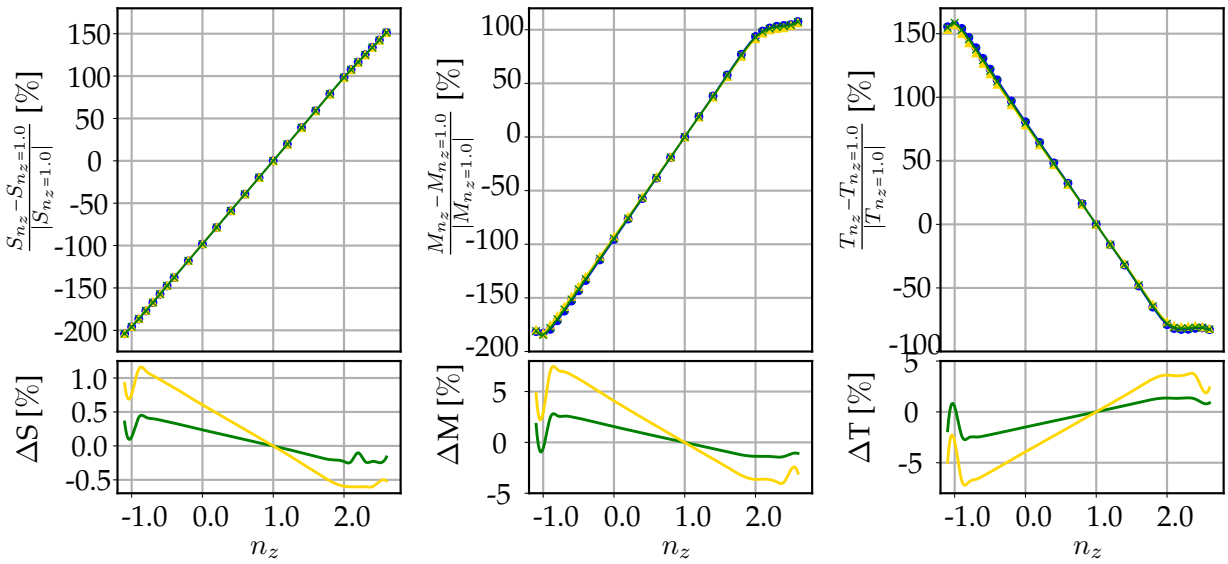

(b) Flight scenario #3.

Figure A.21.: Wing root section forces, AR-10 configuration at cruise flight.

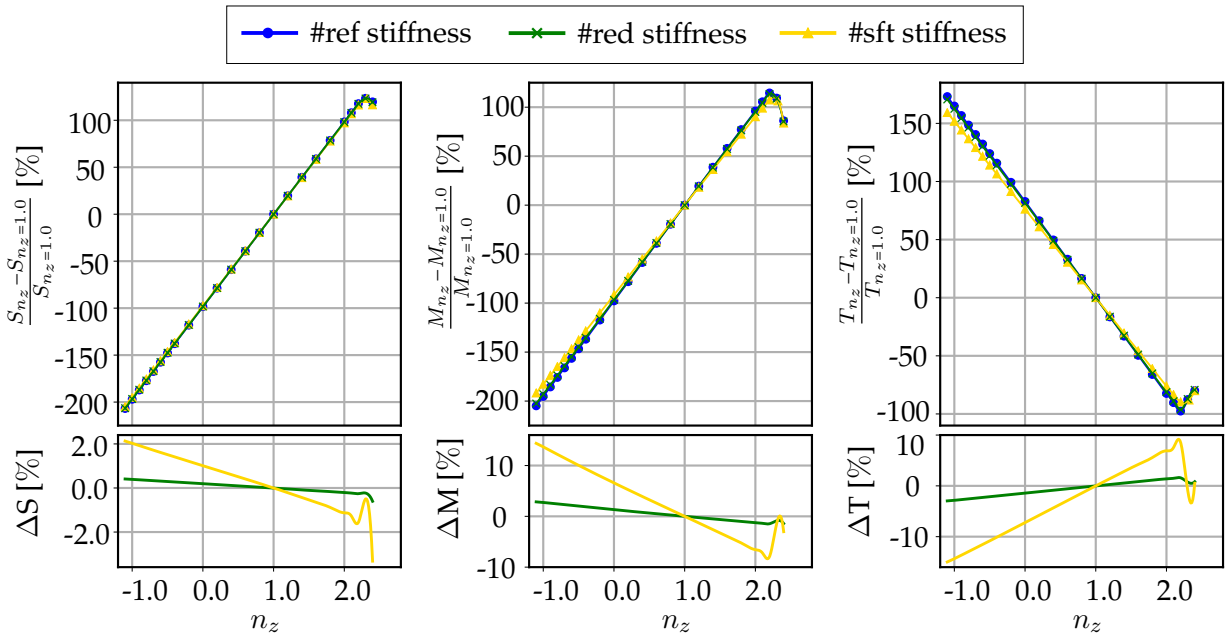

(a) Flight scenario #1.

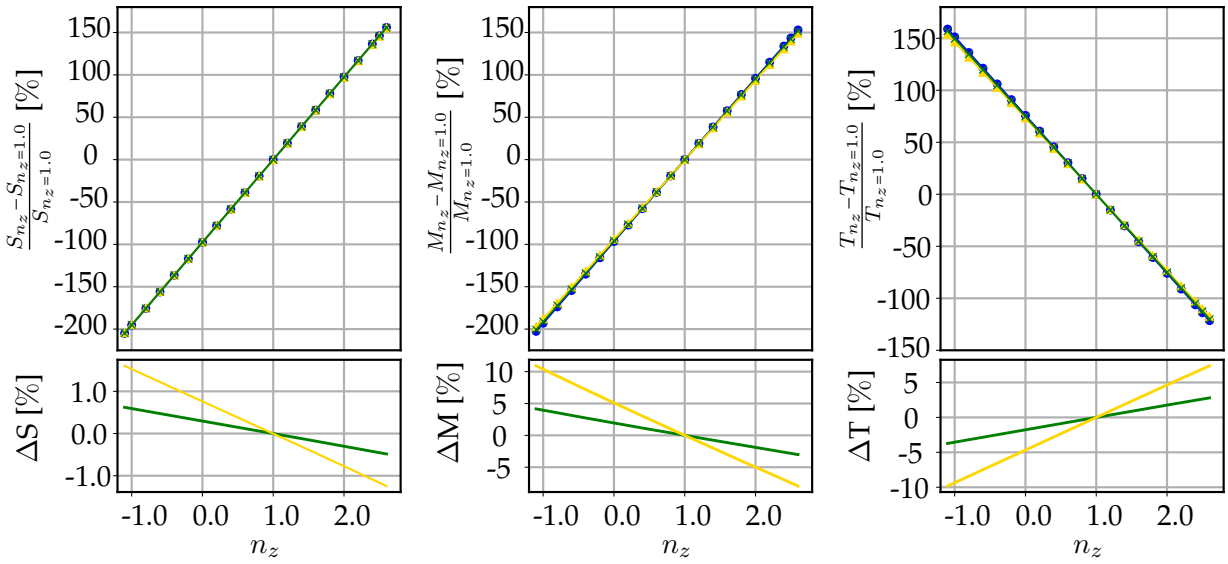

(b) Flight scenario #4.

Figure A.22.: Wing root section forces, AR-10 configuration at low speed flight.

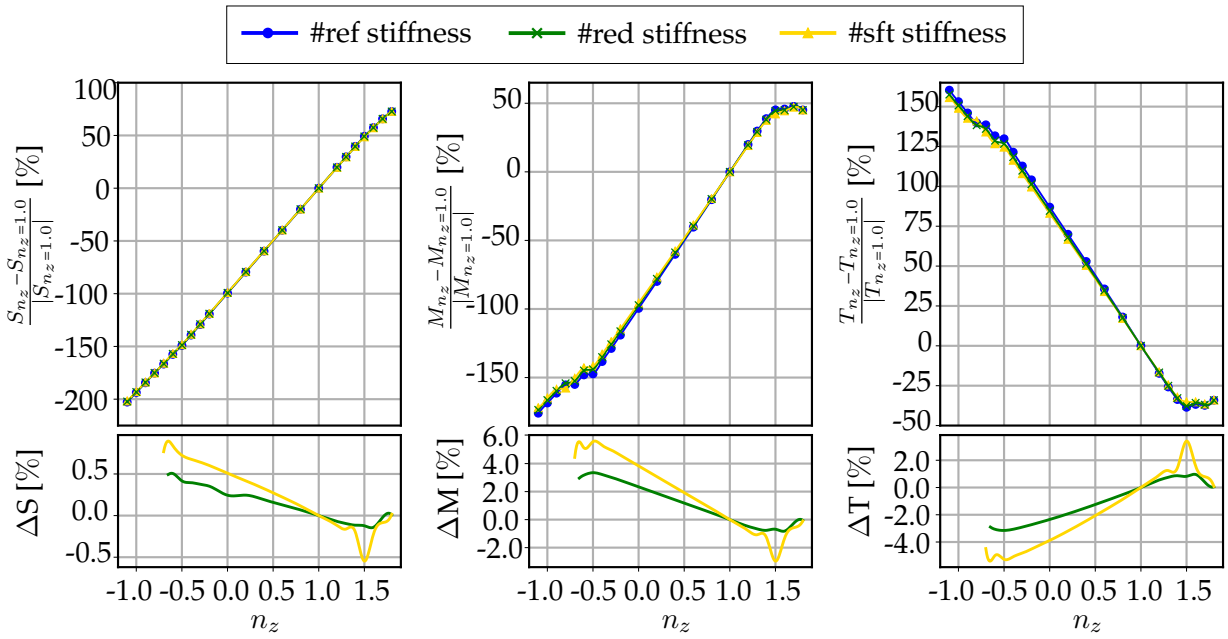

(a) Flight scenario #2.

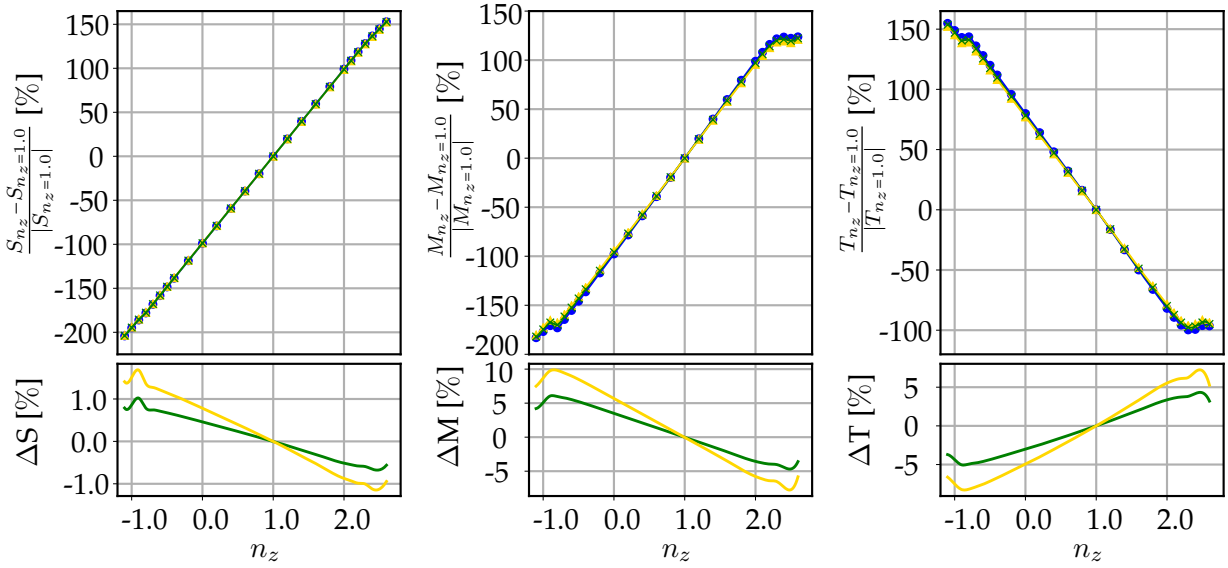

(b) Flight scenario #3.

Figure A.23.: Wing root section forces, AR-13 configuration at cruise flight.

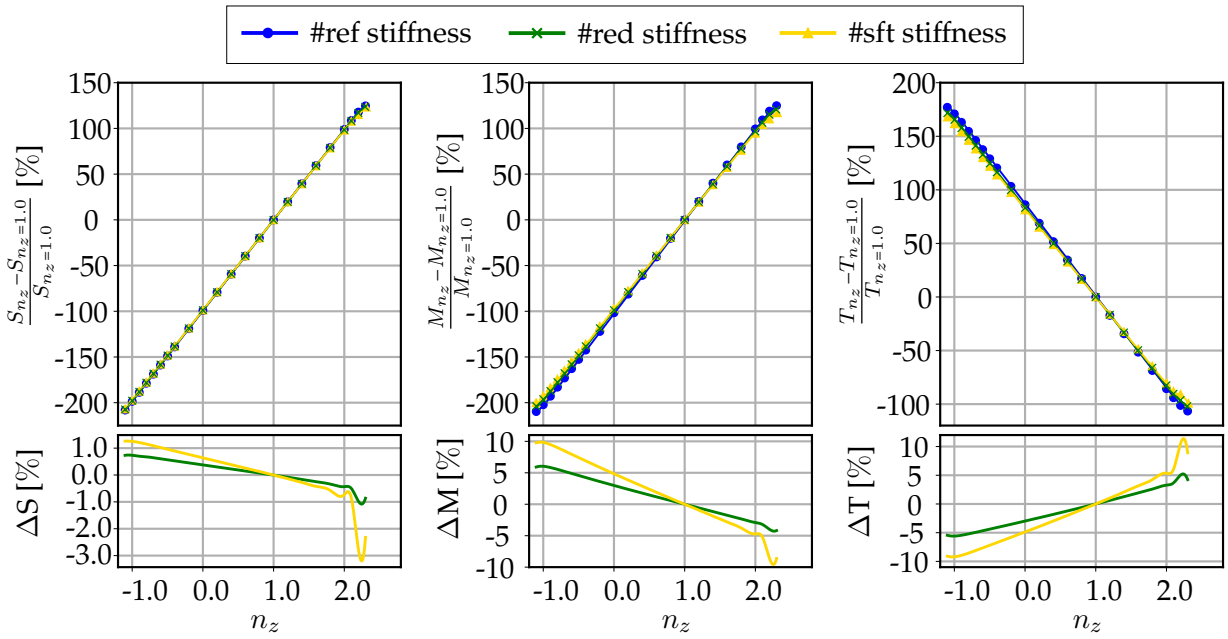

(a) Flight scenario #2.

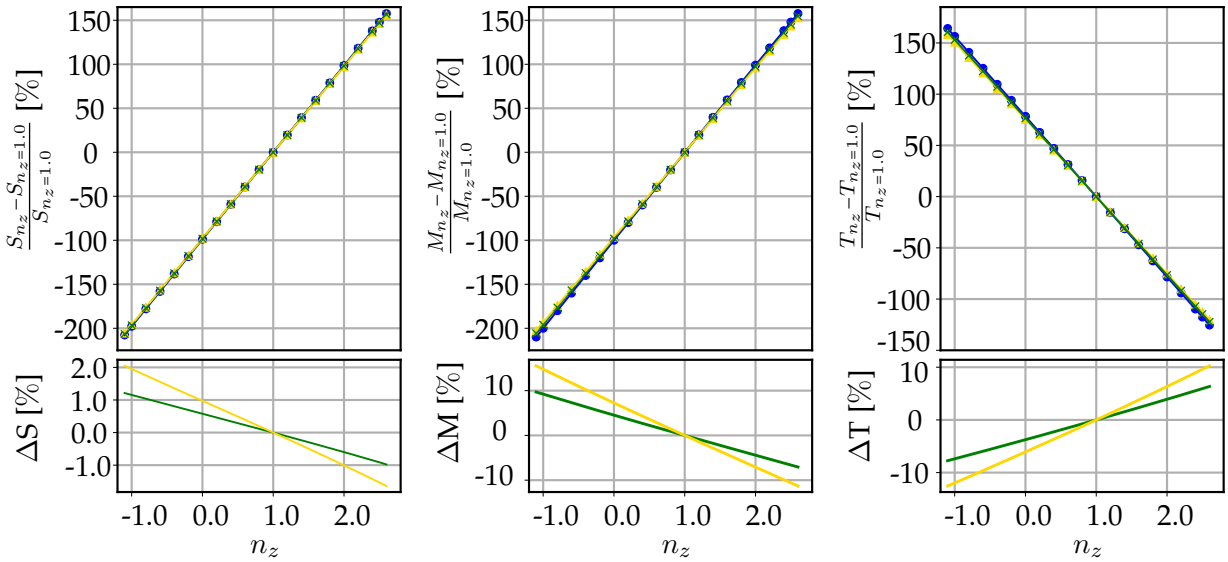

(b) Flight scenario #3.

Figure A.24.: Wing root section forces, AR-13 configuration at low speed flight.

B Bibliography

[1] Air Travel – Greener by Design Mitigating the environmental impact of aviation: Opportunities and priorities. In: *The Aeronautical Journal* (2005), S. 361–416

[2] A., Abbas ; J., Vicente ; E., Valero: Aerodynamic Technologies to Improve Aircraft Performance. In: *Aerospace Science and Technology* 28 (2012), S. 100–132

[3] A., Felippa C. ; C., Park K. ; FARHAT, C.: Partitioned analysis of coupled mechanical systems. In: *Computer Methods in Applied Mechanics and Engineering* 190 (2001), S. 3247–3270

[4] A., Hauffe: Expandable Laminate Explorer. In: *Lehrstuhl fuer Luftfahrzeugtechnik - TU-Dresden* (2020)

[5] A., Hermanutz ; M., Hornung: Influence on the Flutter Behavior of Pre-Stressed Wing Structures Under Aerodynamic Loading. In: *IFASD* (2019)

[6] A., Jameson: Time Dependent Calculations Using Multigrid, with Applications to Unsteady Flows Past Airfoils and Wings. In: *AIAA* (1991)

[7] A., Weisshaar: Aeroelastic Tailoring, Creative Uses of Unusual Materials. In: *AIAA* (1987)

[8] AIRBUS: *Inovation: Airbus reveals new zero-emission concept aircraft*. `https://www.airbus.com/newsroom/press-releases/en/2020/09/airbus-reveals-new-zeroemission-concept-aircraft.html`. 2020

[9] B., Stanford ; C., Jutte: Aeroelastic Tailoring via Tow Steered Composites. In: *NASA Technical Memorandum* (2014)

[10] B., Yang ; T.A., Laursen ; X., Meng: Two dimensional mortar contact methods for large deformation frictional sliding. In: *International Journal for Numerical Methods in Engineering* 62 (2005), S. 1183–1225

[11] BOEING: *Introducing the 777X, Technical Specs*. `https://www.boeing.com/commercial/777x/`. 2020

[12] BOEING, Commercial: *777X Low Speed Taxi Test*. `https://www.boeing.com/777x/reveal/video-777x-low-speed-taxi-test/`. 2019

[13] BOEING, Technology: *Spreading our wings: Boeing unveils new Transonic Truss-Braced Wing*. `https://www.boeing.com/features/2019/01/spreading-our-wings-01-19.page`. 2019

[14] C., Cesnik ; R., Palacios ; E., Reichenbach: Re-examined structural design procedures for very flexible aircraf. In: *Journal of Aircraft* 51 (2014), S. 1580–1591

[15] C., Farhat ; M., Lesoinne: Two efficient staggered algorithms for the serial and parallel solution of three-dimensional nonlinear transient aeroelastic problems. In: *Computer Methods in Applied Mechanics and Engineering* 182 (2000), S. 499–515

[16] C., Farhat ; M., Lesoinne ; N., Maman: Mixed explicit/implicit time integration of coupled aeroelastic problems: Three-field formulation, geometric conservation and distributed solution. In: *International Journal for Numerical Methods in Fluids* 10 (1995), S. 807–835

[17] C., Farhat ; M., Lesoinne ; P.L., Tallec: Load and motion transfer algorithms for fluid/structure interaction problems with non-matching discrete interfaces: Momentum and energy conservation, optimal discretization and application to aeroelasticity. In: *Computer Methods in Applied Mechanics and Engineering* 157 (1998), S. 95–114

[18] C., Farhat ; ZEE K. G. van der ; P., Geuzaine: Provably second-order time-accurate loosely-coupled solution algorithms for transient nonlinear computational aeroelasticity. In: *Computer Methods in Applied Mechanics and Engineering* 195 (2006), S. 1973–2001

[19] C., Felippa: *Introduction to Finite Element Methods*. 1. University of Colorado, Department of Aerospace Engineering Sciences and Center for Aerospace Structures, 2004

[20] C., Hirsch: *Numerical Computation of Internal and External Flows: The Fundamentals of Computational Fluid Dynamics*. Elsevier, 2007. – ISBN 978-0-7506-6594-0

[21] C., Hirt ; A., Amsden ; J., Cook: An Arbitrary Lagrangian-Eulerian Computing Method for All Flow Speeds. In: *Journal of Computational Physics* 14 (1974), S. 227–253

[22] C., Kaiser ; D., Quero ; J., Nitzsche: Quantification of Nonlinear Effect in Gust Load Prediction. In: *IFASD* (2019)

[23] C., Schlemmer: Verwendung verschiedener Steuerflächenkonfigurationen zur Böenlastabminderung. In: *Luft und Raumfahrt* 3 (2018), S. 42–45

[24] C., Wales ; C., Valente ; R., Cook ; A., Gaitonde ; D., Jones ; J., Cooper: The future of non-linear modelling of aeroelastic gust interaction. In: *AIAA Aviation Forum* (2018)

[25] C.-Y., Niu M.: *Aircraft Structural Design: Practical Design Information and Data on Aircraft Structures*. Hong Kong: Conmilit Press Ltd, 1988

[26] C.D., Regan ; C.V., Jutte: Survey of Applications of Active Control Technology for Gust Alleviation and New Challenges for Lighter-weight Aircraft. In: *Dryden Flight Research Center* (2012)

[27] CONSORTIUM, Aerogust: Aeroelastic Gust Modelling, Final summary of the AEROGUST project. In: *www.aerogust.eu* (2018)

[28] C.P., Szczyglowski ; S.A., Neild ; B., Titurus ; J.Z., Jiang ; E., Coetzee: Passive Gust Loads Alleviation in a Truss-Braced Wing Using an Inerter-Based Device. In: *Journal of Aircraft* (2019)

[29] CS25: *European Aviation Safety Agency*. – 25.341 S

[30] D., Raveh: Gust Response Analysis of Free Elastic Aircraft in the Transonic Flight Regime. In: *Journal of Aircraft* 48 (2011), S. 1204–1211

[31] D., Schuster ; D., Liu ; L., Huttsell: Computational Aeroelasticity: Success, Progress, Challenge. In: *Journal of Aircraft* 40 (2003), S. 843–856

[32] D., Schwamborn ; A., Gardner ; A., Krumbein ; H., Lüdeke ; A., Stürmer: Development of the DLR TAU-Code for aerospace applications. In: *International Conference on Aerospace Science and Technology* (2008)

[33] D.A., Burdette ; J.R.R.A., Martins: Design of a transonic wing with an adaptive morphing trailing edge via aerostructural optimization. In: *Aerospace Science and Technology* 81 (2018), S. 192–203

[34] D.C., Wilcox: *Turbulence Modeling for CFD*. 3. DCW Industries, 2006

[35] DLR: Technical Documentation of the DLR TAU-Code Release 2018.1.0. (2018)

[36] D.S., Lee ; D.W., Fahey ; A., Skowron ; M.R., Allen ; U., Burkhardt ; Q., Chen ; S.J., Doherty ; S., Freeman ; P.M., Forster ; J., Fuglestvedt ; A., Gettelman ; R.R., De León ; L.L., Lim ; M.T., Lund ; R.J., Millar ; B., Owen ; J.E., Penner ; G., Pitari ; M.J., Prather ; R., Sausen ; L.J., Wilcox: The contribution of global aviation to anthropogenic climate forcing for 2000 to 2018. In: *Atmospheric Environment* 244 (2021)

[37] E., Livne: Aircraft Active Flutter Suppression: State of the Art and Technology Maturation Needs. In: *Journal of Aircraft* 55 (2018)

[38] EASA: *Certification Specification and Acceptable Means of Compliance for Large Aeroplanes CS-25 - Amendment 24*. https://www.easa.europa.eu/sites/default/files/dfu/CS-25%20Amendment%2024.pdf. 2020. – Accessed: 2020-04-06

[39] E.H., Dowell: *A Modern Course in Aeroelasticity. Solid Mechanics and Its Applications*. Springer, Dordrecht, 2005. – 275–297 S. – ISBN 978-1-4020-2039-1

[40] EUROPEAN, Commission: *Flightpath 2050 Europes Vision for Aviation, Report of the High Level Group on Aviation Research*. https://www.easa.europa.eu/system/files/dfu/CS-25%20Amendment%2018_0.pdf. 2011

[41] EUROPEAN, Commission: *Strategic research and innovation agenda: The proposed European Partnership for Clean Aviation*. https://ec.europa.eu/info/sites/default/files/research_and_innovation/funding/documents/ec_rtd_he-partnerships-clean-aviation.pdf. 2020. – Accessed: 2022-02-06

[42] EUROPEN UNION, Clean S.: *Smart Fixed Wing Aircraft*. https://www.cleansky.eu/smart-fixed-wing-aircraft-sfwa. 2014

[43] F., Afonso ; J., Vale ; É., Oliveira ; F., Lau ; A., Suleman: A review on non-linear aeroelasticity of high aspect-ratio wings. In: *Progress in Aerospace Sciences* 89 (2017), S. 40–57

[44] FAA25: *Federal Aviation Administration*. – 25.341–1 S

[45] G., Fujiwara ; N., Nguyeny: Adaptive Aeroelastic Wing Shape Optimization for High-Lift Configurationgurations. In: *AIAA Aviation* (2015)

[46] G., Kenway ; J., Martins: Multipoint High-Fidelity Aerostructural Optimization of a Transport Aircraft Configuration. In: *Journal of Aircraft* 51 (2014), Nr. 1, S. 144–160

[47] H., Altenbach ; J., Altenbach ; K., Naumenko: *Ebene Flaechentragwerke*. 2. Springer Vieweg, 2016. – 327–375 S

[48] H., Jaeger ; R., Mastel ; M., Knaebel: *Technische Schwingungslehre*. Springer Vieweg, 2016. – 90–95 S. – ISBN 978-3-658-13792-2

[49] H., Schlichting ; E., Truckenbrodt: *Aerodynamik des Flugzeugs, Zweiter Band*. 3. Springer, 2001

[50] H., Schlichting ; K., Gersten ; E., Krause: *Grenzschicht-Theorie*. 10. Springer, 2006

[51] H.P., Monner ; M., Kintscher ; T., Lorkowski ; S., Storm: Design of a Smart Droop Nose as Leading Edge High Lift System for Transportation Aircrafts. In: *AIAA* (2009)

[52] I., Pai S. ; R., Sears W.: Some Aeroelastic Properties of Swept Wings. In: *Journal of the Aeronautical Sciences* 16 (1949), Nr. 2, S. 105–115

[53] J., Bachmann ; C., Hidalgo ; S., Bricout: Environmental analysis of innovative sustainable composites with potential use in aviation sector — A life cycle assessment review. In: *SCIENCE CHINA Technological Sciences* 60 (2017), S. 1301–1317

[54] J., Blazek: *Computational Fluid Dynamics, Principles and Applications*. 3. Butterworth Heinemann, 2015. – ISBN 978-012-801-172-0

[55] J., Dillinger: Static Aeroelastic Optimization of Composite Wings with Variable Stiffness Laminates. In: *Deutsches Zentrum für Luft und Raumfahrt e.V.* (2015)

[56] J., Donea ; A., Huerta ; J.Ph., Ponthot ; A., Rodriguez-Ferran: *Encyclopedia of Computational Mechanics - Arbitrary Lagrangian–Eulerian Methods*. John Wiley, 2004. – 413–437 S. – ISBN 0-470-84699-2

[57] J., Donea ; S., Giuliani ; J., Halleux: An Arbitrary Lagrangian-Eulerian Finite Element Method for Transient Dynamic Fluid-Structure Interactions. In: *Computer Methods in Applied Mechanics and Engineering* 33 (1982), S. 689–723

[58] J., Katz ; A., Plotkin: *Low-Speed Aerodynamics*. 2. Cambridge University Press, 2001

[59] J., Kenway ; G., Kenway ; J., Martins: High Aspect Ratio Wing Design: Optimal Aerostructural Tradeoffs for the Next Generation of Materials. In: *AIAA SciTech* (2014)

[60] J., Miles: A Formulation of the Aeroelastic Problem for a Swept Wing. In: *Journal of the Aeronautical Sciences* 16 (1949), S. 477–490

[61] J., Pattinson ; T., Wilson ; M., Herring: High Fidelity Simulation of the Folding Wing Tip for Loads Alleviation. In: *IFASD* (2015)

[62] J., Scheelhaase ; W., Grimme ; M., O'Sullivan ; T., Naegler ; M., Kloetzke ; U., Kugler ; B., Scheier ; T., Standfuss: *Klimaschutz im Verkehrssektor - Aktuelle Beispiele aus der Verkehrsforschung*. 9. Wirtschaftsdienst, 2018

[63] J., Sitaraman: *CFD Based Unsteady Aerodynamic Modeling for Rotor Aeroelastic Analysis*, Univ. of Maryland, Dissertation, 2003

[64] J., Slotnick ; A., Khodadoust ; D., Darmofal ; W., Gropp ; E., Lurie ; D., Mavriplis: CFD Vision 2030 Study: A Path to Revolutionary Computational Aerosciences. In: *NASA Center for AeroSpace Information* (2014)

[65] J., Wright ; J., Cooper: *Introduction to Aircraft Aeroelasticity and Loads*. 2. Wiley, 2015

[66] J.H., Ferziger ; M., Peric ; R.L., Street: *Computational Methods for Fluid Dynamics*. 4. Springer, 2020. – ISBN 978-331-999-693-6

[67] John, Anderson D.: *Fundamentals of Aerodynamics*. McGraw-Hill Education, 2015. – 711–776 S. – ISBN 0073398101

[68] K., Risse: Das Viertuelle Flugzeug. In: *Luft und Raumfahrt* 3 (2018), S. 14–17

[69] K.J., Bathe: *Finite-Elemente-Methoden*. Springer, 2002. – ISBN 3540668063

[70] L., Reimer ; M., Ritter ; R., Heinrich ; W., Krueger: CFD-based Gust Load Analysis for a Freeflying Flexible Passenger Aircraft in Comparison to a DLM-based Approach. In: *AIAA Aviation* (2015)

[71] L., Reimer ; R., Heinrich ; M., Ritter: *Towards Higher-Precision Maneuver and Gust Loads Computations of Aircraft: Status of Related Features in the CFD-Based Multidisciplinary Simulation Environment Flow Simulator*. 89. Springer International Publishing, 2020. – 597–607 S

[72] M., Kier T.: An Integrated for Lateral Gust Loads Analysis and Dutch Roll Flight Dynamics Using a 3D Panel Method. In: *IFASD* (2017)

[73] M., Kier T.: An Integrated Analysis Model For Assessment of Critical Load Conditions for the Vertical Tail Plane. In: *IFASD* (2019)

[74] M., Kier T. ; N., Looye G. H.: Unifying Manoeuvre and Gust Loads Analysis Models. In: *IFASD* (2009)

[75] M., Sensmeier ; J., Samareh: A Study of Vehicle Structural Layouts in Post-WWII Aircraft. In: *Structures, Structrual Dynamics, and Materials Conference* 45 (2004)

[76] M.M.J., Opgenoord ; M., Drela ; K.E., Willcox: Influence of Transonic Flutter on the Conceptual Design of Next-Generation Transport Aircraft. In: *AIAA Journal* 57 (2019), Nr. 5, S. 1973–1987

[77] M.N., Newmark: A Method of Computation for Structural Dynamics. In: *Journal of the Engineering Mechanics Division* 8 (1959), S. 67–94

[78] M.T., Bordogna ; P., Lancelot ; D., Bettebghor ; R., De B.: Static and dynamic aeroelastic tailoring with composite blending and manoeuvre load alleviation. In: *Structural and Multidisciplinary Optimization* (2019)

[79] M.V., Cook: *Flight Dynamics Principles*. Butterworth-Heinemann, 2013. – 221–223 S. – ISBN 978-0-08-098242-7

[80] N., Kroll: DLR project Digital-X: towards virtual aircraft design and flight testing based on high-fidelity methods. In: *CEAS* (2015)

[81] NASTRAN, MSC: *NonLinear (SOL 400) User's Guide*. 2019

[82] NASTRAN, MSC: *Reference Guide*. 2019

[83] O., Stodieck ; J.E., Cooper ; P.M., Weaver: On the Interpretation of Bending-Torsion Coupling for Swept, Non-Homogenous Wings. In: *AIAA* (2015)

[84] P., Causin ; J.F., Gerbeau ; F., Nobile: Added-mass effect in the design of partitioned algorithms for fluid–structure problems. In: *Computer Methods in Applied Mechanics and Engineering* 194 (2005), S. 4506–4527

[85] P., Spalart ; S., Allmaras: A One-Equation Turbulence Model for Aerodynamic Flows. In: *30th AIAA Aerospac Science Meeting* (1992)

[86] P., Wriggers: *Nichtlineare Finite-Element-Methoden*. Springer, 2001. – ISBN 978-3-540-67747-5

[87] R., Cambell ; M., Lynde: Natural Laminar Flow Design for Wings with Moderate Sweep. In: *AIAA Aviation* (2016)

[88] R., Heinrich: *New Results in Numerical and Experimental Fluid Mechanics IX, Simulation of Interaction of Aircraft and Gust Using the TAU-Code*. Springer International Publishing Switzerland, 2014. – 503–511 S. – ISBN 3319031570

[89] R., Heinrich ; L., Reimer: Comparison Of Different Approaches for Gust Modeling in the CFD Code TAU. In: *IFASD* (2013)

[90] R., Rosario ; R., Wahls ; G., Follen ; N., Madavan: Subsonic Fixed Wing Project. In: *Technical Conference* (2011)

[91] R., Singh ; J.D., Baeder: Generalized Moving Gust Response Using CFD with Application to Airfoil-Vortex Interaction. In: *AIAA* (1997), S. 1997–2208

[92] R., Slayton ; G., Spinardi: Radical innovation in scaling up: Boeing's Dreamliner and the challenge of socio-technical transitions. In: *Technovation* 47 (2016), S. 47–58

[93] R., Vries ; R., Vos: Aerodynamic Performance Benefits of Over-the-Wing Distributed Propulsion for Hybrid-Electric Transport Aircraft. In: *AIAA SCITECH* (2022)

[94] R.G., Cook ; D.E., Calderon ; J.E., Cooper ; M.H., Lowenberg ; S.A., Neidl: Industrially Inspired Gust Loads Analysis of Various-Aspect-Ratio Wings Featuring Geometric Nonlinearity. In: *Journal of Aircraft* (2019)

[95] R.M., Jones: *Mechanics of Composite Materials*. Taylor and Francis, 1999. – 55–275 S. – ISBN 1-56032-712-X

[96] S., Binder ; A., Wildschek ; R., Breuker: The interaction between active aeroelastic control and structural tailoring in aeroservoelastic wing design. In: *Aerospace Science and Technology* 110 (2021)

[97] S., Tsai ; E., Wu: General Theory of Strength for Anisotropic Materials. In: *Journal of Composite Materials,* 5 (1971), S. 58

[98] SCIENCES, National A. of: *Commercial Aircraft Propulsion and Energy Systems Research: Reducing Global Carbon Emissions*. The National Academies Press, 2016

[99] T., Brooks ; G., Kenway ; J., Martins: Undeflected Common Research Model (uCRM): An Aerostructural Model for the Study of High Aspect Ratio Transport Aircraft Wings. In: *AIAA AVIATION Forum* (2017)

[100] T., Brooks ; J., Martins ; G., Kenway: Aerostructural Tradeoffs for Tow-Steered Composite Wings. In: *Journal of Aircraft* (2020)

[101] T., Gerhold: *"Overview of the Hybrid RANS Code TAU". In: MEGAFLOW - Numerical Flow Simulation for Aircraft Design. Notes on Numerical Fluid Mechanics and Multidisciplinary Design*. 89. Springer, 2005

[102] T., Klimmek ; P., Ohme ; D., Ciampa P. ; V., Handojo: Aircraft Loads – An Important Task From Pre-Design to Loads Flight Testing. In: *Deutscher Luft- und Raumfahrtkongress* (2016)

[103] T., Wunderlich: Methoden der Simulationsbasierten Tragfluegeloptimierung. In: *Deutscher Luft- und Raumfahrtkongress* (2017)

[104] T.R., Brooks ; R., Timothy ; G.K.W., Kenway ; J.R.R.A., Martins: Benchmark Aerostructural Models for the Study of Transonic Aircraft Wings. In: *AIAA Journal* 56 (2018), Nr. 7, S. 2840–2855

[105] V., Handojo: Investigation of Load Alleviation in Aircraft Pre-Design and its Influence on Structural Mass and Fatigue. In: *Aerospace Science and Technology* 122 (2022), S. 1270–9638

[106] W., Krueger ; J., Dillinger ; R., Breuker ; K., Haydn: Investigations of passive wing technologies for load reduction. In: *CEAS* 10 (2019), S. 977–993